DEPARTAMENT D'ASTRONOMIA I ASTROFÍSICA

Universitat de València

# Estudio de pequeños elementos magnéticos en la fotosfera y cromosfera solar con telescopios en tierra y espaciales

# Study of small magnetic elements in the solar photosphere and chromosphere with ground-based and space-borne telescopes

Memoria que presenta
Judit Palacios Hernández
para optar al grado de
Doctora en Física
Mención *Doctor Europeus*

Dirigida por Dr. Vicente Domingo Codoñer


VNIVERSITAT DE VALÈNCIA



UNIVERSITAT Ð VALÈNCIA
Febrero de 2012

Thesis supervisor: Dr. Vicente Domingo Codoñer



Some of the material included in this document has been already published in *The Astrophysical Journal Letters*, *Astronomy & Astrophysics* and *Astronomical Society of the Pacific Conference Series*.

**Dr. Vicente Domingo Codoñer,**
Profesor de la Universidad de Valencia,

CERTIFICA:

Que la presente Memoria, *" Estudio de pequeños elementos magnéticos en la fotosfera y cromosfera solar con telescopios en tierra y espaciales " / " Study of small magnetic elements in the photosphere and chromosphere with ground-based and space-borne telescopes "* ha sido realizada bajo su dirección, por Judit Palacios Hernández, y que constituye su tesis doctoral para optar al grado de Doctora en Física, Mención *Doctor Europeus*.

Y para que quede constancia y tenga los efectos que corresponda, firma el presente certificado en Valencia, a 1 de febrero de 2012.

Firmado: Dr. Vicente Domingo Codoñer

Este trabajo de tesis doctoral ha sido posible gracias a:

la ayuda-contrato de Formación de Personal Investigador (FPI), código BES-2007-16384, del Ministerio de Ciencia e Innovación (MICINN) de la cual la autora ha disfrutado desde 2007 hasta 2011, y también de su Programa de Estancias Breves,

además del Programa de Acceso a Grandes Instalaciones Científicas del MICINN en IAC para las observaciones en SST durante 2007 y 2008,

y a los proyectos dependientes del Programa Nacional del Espacio (MICINN): 'Integración y vuelo de SUNRISE/IMaX. Fase conceptual de Solar Orbiter/VIM', con código ESP2006-13030-C06; y 'Diseño preliminar de SO/PHI. Explotación científica de SUNRISE', código AYA2009-14105-C06-04.

*A los que creen que todo es posible. Sigamos luchando por ello.*

I have ceased to question stars and books; I have begun to listen to the teachings that my blood whispers to me.

*Demian (1919). Hermann Hesse.*

うえお むぃて あるこい

*Kyu Sakamoto (1961)*

# Contents

**Abstract** xxvii

**Resumen** xxix

**1 Introduction** 1
- 1.1 Aims of the present study and overview . . . 1
- 1.2 Structure of the Sun . . . 2
  - 1.2.1 Solar magnetic features . . . 7
  - 1.2.2 Magnetic elements in the photosphere . . . 9
    - 1.2.2.1 Flux tube models . . . 9
    - 1.2.2.2 G-band bright points . . . 10
    - 1.2.2.3 Faculae . . . 13
- 1.3 Image processing . . . 15
  - 1.3.1 Image formation . . . 15
  - 1.3.2 Diffraction limit and Point Spread Function . . . 17
  - 1.3.3 Phase Diversity . . . 19
  - 1.3.4 Wiener filter . . . 22
  - 1.3.5 General reduction and post-processing . . . 23
- 1.4 Spectropolarimetry . . . 24
  - 1.4.1 Basics of polarimetry . . . 25
    - 1.4.1.1 Polarization optics . . . 25
    - 1.4.1.2 The Zeeman effect . . . 28
    - 1.4.1.3 Measurement techniques and instruments . . . 31
  - 1.4.2 Retrieval of magnetic fields from observed polarization signals . . . 33
    - 1.4.2.1 Weak magnetic field approximation . . . 33

1.4.2.2 Centre-of-gravity method . . . 34
1.4.2.3 Inversion codes . . . 35

**2 Missions and data acquisition 39**
2.1 Ground-based telescopes . . . 39
2.1.1 Swedish Solar Telescope . . . 39
2.2 Space missions . . . 42
2.2.1 HINODE . . . 42
2.2.1.1 Solar Optical Telescope . . . 44
2.2.1.2 Filters and spectral lines of interest . . . 46
2.2.1.3 SOT-SP: Spectro-Polarimeter . . . 46
2.2.1.4 X-Ray Telescope . . . 46
2.2.2 SUNRISE . . . 48
2.2.2.1 Mission concept . . . 48
2.2.3 SUNRISE flight . . . 53
2.2.4 SuFI/SUNRISE . . . 55
2.2.5 IMaX/SUNRISE . . . 57
2.2.5.1 Introduction . . . 57
2.2.5.2 IMaX optical setup . . . 57
2.2.5.3 IMaX electronics . . . 66
2.2.6 IMaX instrumental calibrations . . . 67
2.2.6.1 Polarimetric description of the instrument . . . 67
2.2.6.2 IMaX Spectroscopic calibration . . . 68
2.2.7 IMaX Observing Modes and data processing . . . 69

**3 Dynamics of small magnetic elements with HINODE and SST 81**
3.1 Introduction and historical overview . . . 81
3.2 Methods applied to the analysis of vortices . . . 83
3.3 Multi-wavelength observations of a vortex-like flow . . . 86
3.4 Spectropolarimetric analysis of the event . . . 89
3.5 Photospheric plasma flows . . . 91
3.6 Statistics of small magnetic elements . . . 95
3.7 Other spectropolarimetric studies . . . 97
3.7.1 Comparison with magnetograms and weak-field approximation . . . 97
3.7.2 Magnetic field intensification . . . 99

**4 Vortex flows observed by IMaX** **103**
4.1 Introduction . . . 103
4.2 Data . . . 103
4.3 Methods . . . 104
4.3.1 General properties of the estimated magnitudes by Local Correlation Tracking over the whole field-of-view . . . 104
4.3.1.1 Effects of windows size and averaging on LCT . 104
4.3.1.2 Effects on magnetic field thresholding for LCT and comparison to different simulations . . . 108
4.3.1.3 Another coordinate system for divergence and vorticity . . . 111
4.3.1.4 Zero-velocity and azimuth computation . . . 114
4.3.2 Analysis of small vortical events . . . 115
4.3.2.1 Statistics of small vortex-like flows . . . 116
4.3.2.2 Centre of rotation and zero-velocity points on LCT . . . 120
4.3.2.3 Magnetic centroids . . . 120
4.4 Discussion and conclusions . . . 121

**5 Study of mesogranular flows in IMaX data** **125**
5.1 Introduction . . . 125
5.2 Observations . . . 127
5.3 Analysis . . . 129
5.3.1 Host exploding granules . . . 129
5.3.2 Associated magnetic field emergences . . . 131
5.3.3 Flow maps of the magnetic and non-magnetic features . 135
5.3.4 Simulations . . . 137
5.4 Discussion and conclusions . . . 140
5.5 Flow maps over the field-of-view . . . 141

**6 Conclusions** **147**
6.1 Future work . . . 149

**A Data mining June 10, 2009** **151**

**B Data mining June 11, 2009** **155**

**C Resumen en español** **159**
C.1 Introducción . . . 159
C.1.1 Objetivos de esta Tesis . . . 159
C.1.2 Estructura del Sol . . . 159
C.1.3 Procesado de imagen . . . 160
C.1.4 Espectropolarimetría . . . 161
C.2 Misiones y adquisición de datos . . . 161
C.2.1 Telescopio Solar Sueco . . . 161
C.2.2 HINODE . . . 162
C.2.3 SUNRISE . . . 162
C.2.3.1 Descripción . . . 162
C.2.3.2 Reducción de datos de IMaX . . . 164
C.3 Dinámica de elementos magnéticos con datos de HINODE y SST 164
C.3.1 Introducción y métodos . . . 164
C.3.2 Datos . . . 165
C.3.3 Análisis de datos espectropolarimétricos . . . 166
C.3.4 Estructura vortical con mapas de flujo y centroides . . . 166
C.3.5 Conclusiones . . . 167
C.4 Vórtices observados con datos de IMaX . . . 167
C.4.1 Introducción . . . 167
C.4.2 Datos . . . 167
C.4.2.1 Métodos: efectos del promediado espacio-temporal 168
C.4.2.2 Métodos: efectos de la eliminación de ruido en magnetogramas en el LCT y comparación con simulaciones . . . 168
C.4.2.3 Otro sistema de coordenadas para la divergencia y vorticidad . . . 169
C.4.2.4 Análisis de pequeños vórtices . . . 169
C.5 Emergencias de campo magnético en gránulos de escala mesogranular . . . 170
C.5.1 Introducción . . . 170
C.5.2 Análisis . . . 170
C.5.2.1 Descripción de los gránulos explosivos . . . 171
C.5.2.2 Emergencias de campo magnético asociadas a los gránulos . . . 171
C.5.2.3 Mapas de flujo de las estructuras . . . 172
C.5.2.4 Simulaciones . . . 172
C.5.3 Conclusiones . . . 172

C.5.4 Mapas de flujo sobre todo el campo . . . . . 173
C.6 Conclusiones finales . . . . . 173
C.6.1 Trabajo futuro . . . . . 175

**Bibliography** **177**

# List of Figures


1 . . . . . xxxi

1.1 Ulugh Beg observatory in Samarqand . . . . . 3
1.2 Diagram of the Sun showing its different layers and features . . . . 4
1.3 SDO Helium image of the chromosphere . . . . . 6
1.4 Sunspot depicted by John of Worcester . . . . . 7
1.5 Ground-based magnetometer record of the Carrington's 'white light flare' . . . . . 8
1.6 Different magnetic flux tube models . . . . . 11
1.7 Image formation process diagram . . . . . 16
1.8 SST OTF and HINODE OTF . . . . . 19
1.9 Wedge filter in the $k-\omega$ space . . . . . 25
1.10 Sketch of a retarder-polarizer set . . . . . 27
1.11 One-dimensional magnetogram . . . . . 31
1.12 Scheme of a simple spectropolarimeter . . . . . 32

2.1 Artistic view of HINODE . . . . . 42
2.2 MV2 rocket . . . . . 43
2.3 Transmission functions of different filters for HINODE . . . . . 45
2.4 XRT effective area and temperature response . . . . . 47
2.5 SUNRISE field-of-view . . . . . 50
2.6 Integration and final testing site in Kiruna . . . . . 53
2.7 SUNRISE trajectory over the Arctic Circle . . . . . 54
2.8 Schwarzschild microscope optical setup, like SuFI's . . . . . 55
2.9 IMaX optical setup diagram . . . . . 59
2.10 Setup of IMaX . . . . . 60
2.11 IMaX prefilter and spectral lines . . . . . 61

2.12 Point Spread Function of IMaX . . . 61
2.13 Sketch of the transmission and reflection in a single etalon . . . 62
2.14 Different Fabry-Pérot setups . . . 63
2.15 Example of 'blueshift' . . . 64
2.16 Intensity versus time, 2009 June10 . . . 70
2.17 Intensity versus time, 2009 June 11 . . . 71
2.18 Example of line fitting for a flat-field . . . 73
2.19 Example of a bad line fitting for a flat-field . . . 74
2.20 Mean power spectrum in Cam1 and Cam2 . . . 75
2.21 Details of the power spectrum . . . 75
2.22 Weak field approximation vs. IMaX calibration. . . . 78
2.23 Restored and non-restored IMaX images . . . 79

3.1 Several sequences of vortices in the literature . . . 83
3.2 Divergence and vorticity diagrams . . . 85
3.3 MDI full disk showing NOAA 10971 . . . 87
3.4 Multiwavelength maps of the event . . . 88
3.5 Image with different noise masks . . . 89
3.6 Spectropolarimetric map series of a vortex . . . 90
3.7 Maximum and unsigned values of Stokes $V$ maps . . . 92
3.8 Map of LCT horizontal velocities and divergence . . . 94
3.9 Temporal evolution of the magnetic centroids . . . 95
3.10 Comparison of longitudinal magnetograms from inversions and SOUP 97
3.11 Histogram of a SST-SOUP magnetogram . . . 98
3.12 Weak field approximation ratio for Fe I lines . . . 98
3.13 Velocity and magnetic field maps for two convective collapses . . . 101

4.1 Divergence maps for different parameters . . . 106
4.2 Vorticity maps for different parameters . . . 107
4.3 PDFs of the divergence and vorticity with *FWHM*=1″ . . . 108
4.4 PDFs of the divergence and vorticity with *FWHM*=1.″5 . . . 108
4.5 Proportion of surface with negative divergence and non-zero vorticity depending on time average with *FWHM*=1″ . . . 109
4.6 Proportion of surface with negative divergence and non-zero vorticity depending on time average with *FWHM*=1.″5 . . . 109
4.7 Histograms of divergence and vorticity for thresholded magnetic maps . . . 110
4.8 Histograms of divergence and vorticity in synthetic magnetograms . 111

4.9 Histograms of divergence and vorticity in synthetic continuum images . . . 111
4.10 Reference system for velocity . . . 112
4.11 Curvature and confluence . . . 113
4.12 Azimuth angle of the horizontal flows for continuum and longitudinal magnetic field. . . . 114
4.13 Zero-velocity points calculated for continuum and longitudinal field maps . . . 115
4.14 Map of the vortices found . . . 117
4.15 Divergence and vorticity of the small events . . . 118
4.16 Vortex lifetime histogram . . . 118
4.17 LCT flow maps, divergence and vorticity of longitudinal field . . . 119
4.18 LCT flow maps, divergence and vorticity of continuum . . . 119
4.19 Trajectories of the magnetic centroids . . . 121

5.1 Context images for the events $v10$ and $\ell 10$ . . . 128
5.2 Binary mask of granulation . . . 129
5.3 Radius and area histograms of the previous image . . . 130
5.4 Expansion velocities for granules and magnetic patches . . . 131
5.5 Sequence of the emergence event $\ell 10$ . . . 132
5.6 Sequence of the emergence event $v10$ . . . 133
5.7 Flow maps of the $\ell 10$ case . . . 134
5.8 Divergence maps of the $\ell 10$ case . . . 135
5.9 Local Correlation Tracking flow maps of the case $v10$ . . . 136
5.10 Divergence maps of the case $v10$ . . . 136
5.11 Continuum snapshot of the simulation . . . 138
5.12 Expansion velocity on synthetic images . . . 139
5.13 Local Correlation Tracking flow maps of the synthetic images . . . 140
5.14 Flowmaps for five series. . . . 144
5.15 *Cancellation magnetograms* for five series. . . . 145

A.1 Stokes $I$ continuum and Stokes $V$ continuum, L3_2 images . . . 151

C.1 . . . 199

# List of Tables


1.1 States of polarization observed with dependence of the line-of-sight direction . . . . . 31

2.1 Main IMaX specifications . . . . . 57
2.2 IMaX Observing Modes . . . . . 70

3.1 Multi-wavelength data time series description . . . . . 88
3.2 Summary table of properties of GBPs . . . . . 96

4.1 Table summarising the bin sizes of histograms in Figure 4.3 and Figure 4.4. . . . . 105

5.1 Data series description for the events $v10$ and $\ell 10$ . . . . . 142

A.1 10 June data reduction table . . . . . 152
A.2 Continued . . . . . 153
A.3 Continued . . . . . 154

B.1 11 June data reduction table . . . . . 156
B.2 Continued . . . . . 157
B.3 Continued . . . . . 158

# List of Acronyms

——— INSTITUTIONS ———

| | |
|---|---|
| GACE | Grupo de Astronomía y Ciencias del Espacio |
| IPL/LPI | Image Processing Laboratory |
| UV | Universidad de Valencia |
| IAC | Instituto de Astrofísica de Canarias |
| IAA | Instituto de Astrofísica de Andalucía |
| MPS | Max Planck Institut für Sonnensystemforschung (MPS) |
| LMSAL | Lockheed Martin Solar and Astrophysics Laboratory |
| KIS | Kiepenheuer Institut für Sonnenphysik |
| HAO | High Altitude Observatory |
| | |
| ISAS | Institute of Space and Astronautical Science |
| JAXA | Japanese Aerospace Exploration Agency |

——— GROUND BASED TELESCOPES ———

| | |
|---|---|
| SST | Swedish Solar Telescope |
| VTT | Vacuum Tower Telescope |

—— INSTRUMENTS AT GROUND BASED TELESCOPES ——

| | |
|---|---|
| SOUP | Solar Optical Universal Polarimeter |
| CRISP | CRisp Imaging SpectroPolarimeter |
| KAOS | Kiepenheuer Adaptive Optics System |

——— SPACE MISSIONS ———

| | |
|---|---|
| SDO | Solar Dynamics Observatory |
| SoHO | Solar Heliospheric Observatory |

— HINODE and SUNRISE INSTRUMENTATION AND ELEMENTS —

| | |
|---|---|
| SOT | Solar Optical Telescope of HINODE |
| EIS | EUV Imaging Spectrometer |
| XRT | X-Ray Telescope |
| NFI | Narrowband Filter Imager |
| BFI | Broadband Filter Imager |
| SP | Spectro-polarimeter |
| CT | Correlation Tracking/Tracker |
| IMaX | Imaging Magnetograph of SUNRISE |
| ISLiD | Image Stabilization and Light Distribution System |
| SuFI | SUNRISE Ultraviolet Imager |
| LISS | Lockheed Intermediate Sun Sensor |
| CWS | Correlating Wavefront Sensor |
| AIV | Assembly, Integration and Verification |
| PFI | PostFocus Instrumentation of SUNRISE |
| ICS | Instrument Control System of SUNRISE |
| ICU | Instrument Control Unit of SUNRISE |
| DSS | Data Storage Subsystem of SUNRISE |
| HVPS | High Voltage Power Supply of SUNRISE |
| HRW | Heat Rejection Wedge of SUNRISE |
| ME | Main Electronics of IMaX |
| PE | Proximity Electronics of IMaX |
| I/F | IMaX interface |
| IPB | Image Processing Board |
| OBE | Optical Bench Electronics |
| TCPE | Thermally Controlled Pressurized Enclosures |
| LDB | Long Duration Balloon |
| FPI | Fabry Pérot Interferometer |
| LCVR | Liquid Crystal Voltage Retarder |
| AO | Adaptive Optics |
| SH | Shack-Hartmann |

## COMMON DEFINITIONS

| | |
|---|---|
| S/N | Signal-to-Noise ratio |
| LOS | Line-of-Sight |
| FOV | Field of View |
| PSF | Point Spread Function |
| OTF | Optical Transfer Function |
| PD | Phase Diversity |
| WFE | Wavefront error |
| LCT | Local Correlation Tracking |
| MOMFBD | Multi-Object Multi-Frame Blind Deconvolution |
| IDL | Interactive Data Language |
| SSW | SolarSoftWare |
| FWHM | Full Width at Half Maximum |
| TSI | Total Solar Irradiance |
| LTE | Local Thermodynamic Equilibrium |
| RTE | Radiative Transfer Equation |
| CF | Contribution Function |
| RF | Response Function |
| UT | Universal Time |
| GBP/BP | G-band Bright Point/bright point |

# Abstract

The photosphere is the best known layer of the Sun, as it delimits its surface and furthermore, it has been observed in detail since the beginning of the telescopic era. The convection zone redistributes the magnetic field over the photosphere and the upper layers. On the many scales of the solar surface magnetism, the smallest elements seen in the photosphere are the most unknown, due to the limit in resolution of a finite telescope. The structures that are smaller than typically 100 km are smeared out. In this Thesis, the small bright features of the magnetic network and internetwork over the resolution limit are analysed from the dynamical point of view, and linked with their physical properties as the magnetic field and intensity.

The instruments used in this text for data acquisition are the Swedish Solar Telescope, the spatial telescope HINODE and the balloon-borne solar telescope SUNRISE. From this suite of instruments, the disk centre of the Sun have been explored with the aim of studying these smallest blocks of the solar magnetism. Magnetic field densities have been estimated by inversions, weak-field approximation and center-of-gravity method.

The observatory SUNRISE and its magnetograph IMaX, completed its first flight on 2009, from June 8 to June 13. It acquired high-quality data on the Stokes parameters $I, Q, U, V$ from where different physical parameters, namely the line-of-sight velocity, longitudinal and transverse magnetic field density and line minimum can be extracted. In this Thesis, the data mining of 2009 June 10 and 11 is carried out, and all the subsequent reduction, such as the flat-field correction, spectral line removal, dark current correction, and image restoration by the Phase Diversity method. The data products are available to the scientific community for public use.

One of the results of this Thesis is a multi-wavelength description of a vortex-like flow is performed. The small magnetic features are bright in CN, Ca II H and G-band (from HINODE and the Swedish Solar Telescope) that correspond to a magnetic region, studied in Mg I magnetograms. The vortex-like flow is traced by magnetic centroids and divergence, where the turning motion in a downdraft is noticeable. The downdrafts are also confirmed by spectropolarimetric data, which not only allow us to estimate the magnetic field vector, but also the line-of-sight velocity. These magnetic structures evolve along $\sim$1 hour and convective collapses can occur in the magnetic areas, having some minutes of duration. The signatures of the magnetic intensification, such large downflows and abnormal Stokes $V$ profiles, are found in the bright points.

The study of photospheric flows is significant for many parts of this Thesis: methods like the Local Correlation Tracking allows us to analyse the development of flows, to estimate magnitudes as the divergence and vorticity on a field of view, or to inspect the interaction of flows and different magnetic structures. We examine with different time averages and correlation window sizes of the Local Correlation Tracking, the divergence and vorticity along a given field of view observed by IMaX/SUNRISE on 2009, June 9. We also examined the effects of magnetogram thresholding on the calculation of divergence and vorticity. Again, the Local Correlation Tracking method allows us to study small vortex-like flows, and comparing them with another techniques: the passive advected tracers, the zero-velocity computation, and the study of the vorticity by decomposing the horizontal velocity field in two components.

The magnetic features in the photosphere are not only bright points located in the intergranular lanes. We have investigated flux emergence processes in two large exploding granules with IMaX/SUNRISE data. These granules reach mesogranular sizes (5-8 Mm). The typical expansion velocity of the granules is 0.6 $\mathrm{km\,s^{-1}}$ and 1 $\mathrm{km\,s^{-1}}$ for the magnetic patches that cover the mesogranular-sized granules. Divergence maps confirm the mesogranular scale. Some magnetic loops, featured as two opposite polarity patches linked by a transverse field magnetic patch are detected in the field of view. These magnetic field emergence cases are compared to magnetohydrodynamic simulation in continuum and longitudinal magnetic field, yielding to similar results.

# Resumen

La fotosfera es la capa más conocida del Sol, ya que delimita su superficie y se ha observado en detalle desde el inicio de la era telescópica hasta ahora. La capa convectiva redistribuye el campo magnético sobre la fotosfera y capas superiores. De todas las escalas diferentes del magnetismo solar de la superficie, los pequeños elementos magnéticos son los más desconocidos, debido a que la dependencia del límite de resolución del instrumento que observa puede hacer que estas estructuras se desvirtúen y pierdan intensidad. Los elementos de menos de 100 km aparecen no resueltos. En esta tesis, estas estructuras brillantes de la red e *internetwork* solar de tamaño ligeramente mayor al límite son analizados desde el punto de vista de la dinámica, uniéndolo con propiedades físicas como la intensidad y el campo magnético.

Los instrumentos usados en este texto para adquisición de datos son el Telescopio Solar Sueco, el telescopio espacial HINODE y el telescopio montado en un globo estratosférico, SUNRISE. Con este conjunto de instrumentos, se ha explorado el centro del disco solar para analizar estos bloques estructurales del magnetismo solar. La densidad de campo magnético se ha estimado a través de inversiones, aproximación de campo débil y método de centro de gravedad.

El observatorio SUNRISE y su magnetógrafo IMaX completaron su primer vuelo en 2009, del día 8 al 13 de Junio. Este observatorio logró adquirir datos de alta calidad de los parámetros de Stokes $I, Q, U, V$ de los cuales se pueden extraer diferentes parámetros físicos, como la velocidad en la línea de visión, magnetogramas longitudinales y transversales,y mínimo de la línea. En esta tesis, el ha llevado a cabo análisis de datos de los días 10 y 11 con toda su reducción posterior, correcciones de campo plano y corriente de oscuridad, hasta la fase de restauración de

imágenes por el método de la Diversidad de Fase. Los datos reducidos son accesibles para toda la comunidad científica.

Uno de los resultados de esta tesis es una descripción multiespectral de un flujo vortical. Los pequeños elementos magnéticos son brillantes en CN, Ca II H y banda G (en HINODE y el Telescopio Solar Sueco) que corresponden a una región magnética, que aparece en magnetogramas de Mg I. El flujo en forma de vórtice se traza con centroides magnéticos y cálculo de divergencias, donde el flujo que retorna hacia el interior es importante, y aparece también datos espectropolarimétricos, que no sólo permiten estimar el vector campo magnético, sino también velocidades en la línea de visión. Estas estructuras magnéticas evolucionan durante $\sim$1 hora y también hay signos de intensificación magnética, como intensos flujos hacia abajo y perfiles $V$ de Stokes anormales sobre los puntos brillantes.

El estudio de flujos fotosféricos es fundamental en diferentes partes de esta tesis: métodos como el Seguimiento de Correlación Local nos ayuda a analizar el desarrollo de flujos, a estimar magnitudes como la divergencia y vorticidad en un campo de visión, o inspeccionar la interacción de flujos y las estructuras magnéticas. Examinamos con diferentes promedios temporales y tamaños de ventanas de correlación el resultado de los cálculos de divergencia y vorticidad en imágenes de IMaX/SUNRISE del 9 de junio de 2009. De nuevo, el Seguimiento de Correlación Local sirve para detectar los flujos vorticales más pequeños, y compararlos con diferentes técnicas, como los trazadores pasivos, el cálculo de la velocidad donde es nula, y el estudio de la vorticidad a través de la descomposición del campo de velocidades horizontales en dos componentes.

Las estructuras magnéticas en la fotosfera no son sólo puntos brillantes localizados en las zonas intergranulares. Hemos investigado procesos de emergencia magnética sobre dos grandes gránulos con datos de IMaX/SUNRISE. Estos gránulos alcanzan tamaños mesogranulares (5-8 Mm). La velocidad de expansión típica de los gránulos es 0.6 $\mathrm{km\,s^{-1}}$ y de 1 $\mathrm{km\,s^{-1}}$ para las zonas magnéticas que cubren los gránulos. Los mapas de divergencia confirman la escala mesogranular. También se han encontrado bucles magnéticos, que presentan dos polaridades en el magnetograma longitudinal unidas por una zona de campo magnético transversal. Estos casos de emergencia magnética se ha comparado con con simulaciones magnetohidrodinámicas, con resultados similares a los de las observaciones de IMaX.


FIGURE 1— Artistic photographic rendition of the SUNRISE balloon before its launching on June 8, 2009. Original image from *Barthol et al. (2011)*. Included also in the back cover.

# 1

# Introduction

An introduction about the Sun and its main characteristics are presented in this Chapter, along with some basic tools for its study and techniques regarding the observation process.

All the right reasons. (Nickelback, 2005)

## 1.1 Aims of the present study and overview

The goal of this work is the detailed study of small magnetic structures in the photosphere and low chromosphere. These elements are fundamental to understand the smallest blocks of the solar magnetism. High resolution and polarimetric accurate observations are highly needed in order to understand the quiet Sun magnetism. In this Thesis, magnetic fields and dynamics are studied for different events where small magnetic flux concentrations are involved. For the study of these events, data from ground-based instruments are used, as the Swedish Solar Telescope, and from space-borne telescopes, as HINODE and SUNRISE. The data employed are acquired in different wavelengths, aiming to generate a complete picture, and complemented with spectropolarimetric observations. Furthermore, the work on SUNRISE data constituted a significant part of the thesis work, as data were fully reduced and used in this text.

The summary of this Thesis and its contents are described below:

In Chapter §1 includes an introduction covering different topics, such as solar structure, along with historical aspects. Also a review of image formation and filtering is presented. An extensive part is devoted to magnetic flux tubes, highlighting the importance of having a better knowledge of the smallest structures found in the

Sun. A Section revisiting polarimetry basics, spectropolarimetric instrumentation, and methods to estimate magnetic fields through polarized light is included.

Chapter §2 describes the different telescopes used in this work, as the Swedish Solar Telescope and HINODE. The instrument IMaX/SUNRISE is reviewed in detail, from pre-flight calibration to the final data reduction and image restoration process.

Chapter §3 deals with the multi-wavelength analyses of the dynamics of small elements dragged by convective vortex-flow motions, observed with space-borne telescopes. The vortical motion is found by different methods. Some events on these magnetic structures, as convective collapse, are studied.

Chapter §4 extends the study of the previous Chapter and presents an evaluation and interpretation of the usual methods for finding convective vortices in the solar photosphere in IMaX data, along with new ones.

Chapter §5 details the study of flux emergence on mesogranular-sized granules in IMaX data. The mesogranular scale is estimated by different methods, and the resulting horizontal flows are analysed. These data are compared to a numerical simulation, yielding similar results.

In Chapter §6, conclusions and outlook are drawn.

On Appendix A and B, Tables of data reduction of the magnetograph IMaX from SUNRISE are available.

## 1.2 Structure of the Sun

The Sun is a typical G2V star, the closest to Earth, and this fact allows us to study its structure. From 4000 years ago until now, people noticed the most conspicuous structures on the Sun's surface, such as sunspots. Its obvious influence on the Earth's seasons, climate and life made our star the leading celestial body of the first astronomical cults and of the earliest attempts at astronomical studies. To cite some of the best known: the heliacal rising of Sirius which coincides with the season of flooding of fertile lands and its economic raising for the Egyptian people, 4000 years ago, or measuring the exact moment where midday happened making use of the big semicircular walls around 1400 A.C. in Samarqand (Figure 1.1). This simple instrument is a large arch that was used to determine the moment when the Sun passed the local central meridian. A trench of about 2 metres wide was dug in a hill along the line of the meridian and the arc of a sextant was placed in it. Today, there is a circular base showing the outline of the original structure.

Our closest star whose radius is $R_\odot = 700\,000$ km, has an absolute magnitude of $M_\odot$=4.74 and a luminosity of $L_\odot$=4 $10^{26}$ W. The spectral energy distribution ranges

from radio to X-rays; these upper and lower limits in wavelength actually belong to coronal emissions. The bulk of the energy corresponds to visible wavelengths emitted from the photosphere.

The Sun's structure can be divided in different layers, from inner to outermost: the core, the radiative zone, the convective zone, the photosphere, the chromosphere, the transition region, and the corona. These layers are depicted in Figure 1.2. The core is where all nuclear reactions take place, fusing hydrogen into helium by the process called p-p chain. Its temperature reaches about 16 million Kelvin, and it is located from the centre to about 0.2 to 0.25$R_\odot$. It has a density of up to $1.5\times10^5$ kg $m^{-3}$. The high-energy photons (gamma rays and X-rays) released in fusion reactions take a long time – roughly 200 000 years – to reach the surface, slowed by scattering and thermalized and converted into visible-light photons.

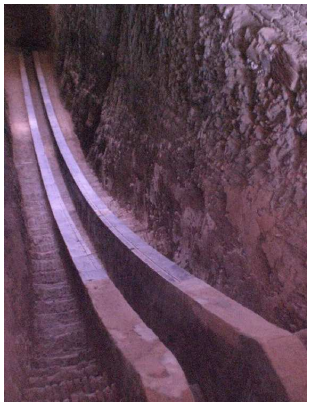

FIGURE 1.1— Ulugh Beg observatory in Samarqand and its meridian circle.This is a large arch that had been used to determine midday. Courtesy and credits of Jesús Mayordomo Sánchez.

Once the energy is produced in the core of the Sun, it has to travel from the core to the outer regions. This layer, the radiative zone, ranges from 0.2$R_\odot$ to about 0.7$R_\odot$. The temperature in the radiation zone of the Sun is lower than in the core, and its density is thus lower, which allows thermal radiation to transfer the intense heat of the core outward. The heat is transferred by ions of hydrogen and helium emitting photons, which travel a brief distance before being re-absorbed by other ions.

The convection zone has a height range between 0.7$R_\odot$ to 1.0$R_\odot$. In this region, the temperature, lower than in the central layers, causes an increase of the amount of $H^-$, raising the opacity due to this ion. Convection, the energy transport by mass motions, becomes a more efficient way of transporting energy rather than radiation in this particular layer. Therefore, thermal convection occurs as thermal columns carry hot material to the surface (photosphere) of the Sun. As soon as the material cools off at the surface, it dips downward to the base of the convection zone, to obtain more heat from the top of the radiative zone. The photosphere, the top of the convection zone and the region of interest of this work, is where the core photons become thermalized and the matter becomes transparent. The definition of the surface of a star is important and may vary depending on

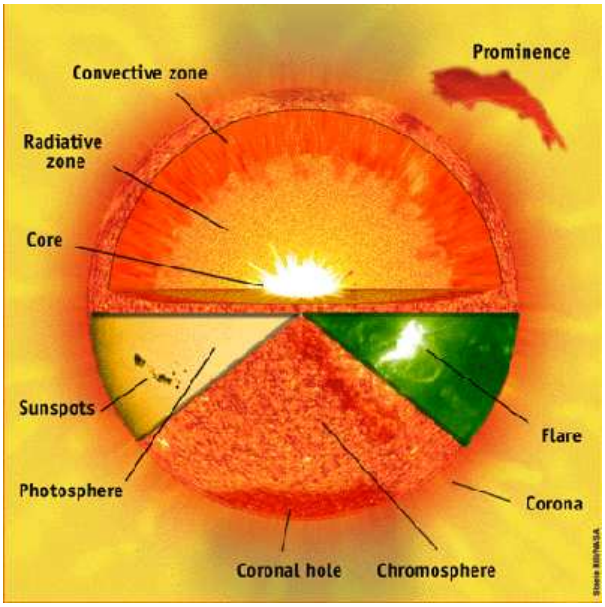


FIGURE 1.2— Diagram of the Sun showing its different layers and features. Adopted from http://sohowww.nascom.nasa.gov/explore/.

the parameters used for this definition. One way to define the surface is to use the layer where the temperature equals the effective temperature in the Stefan-Boltzmann law. Hence, the photosphere is typically used to describe the Sun's or another star's visual surface. The geometrical thickness of the Sun's photosphere is about 500 km and has an effective temperature of 5778±3 K (Stix, 2002), with a range between 4500 and 6000 K and a density of about $2\times10^{-4}$ kg m$^{-3}$. The turbulent convection of this outer part of the solar interior gives rise to a 'small-scale' dynamo that produces magnetic north (positive) and south (negative) poles all over the surface of the Sun. A good amount of magnetic features are observable in this layer, as sunspots, faculae, bright points in G-band, etc. The Sun's photosphere is composed of convection cells called granules, which are cells of gas each approximately 1000 kilometres in diameter – defining a very useful unit in comparison with the granular average size, that is a megametre or Mm – with hot rising gas in the centre and cooler gas, which defines the granule wall, falling in the intergranular lanes. These gas parcels are adiabatically lifted from their equilibrium position. Each granule has a lifetime of only about ten minutes, resulting in a continually *boiling* pattern. The phenomenon of *overshooting* – penetration of the

convective motion into an stably stratified layer – happens at the top and base of the convection zone. Grouping the typical granules are supergranules of up to 30 000 kilometres in diameter with lifespans of up to 24 hours. An intermediate scale of the granulation is the *mesogranulation*, that will be examined in Chapter §5 in more detail.

At the solar surface, we can see also some variations of contrast over portions of thousands of kilometres. These are the *p-modes*, a kind of acoustic waves that have the pressure as their restoring force. P-mode oscillations have frequencies larger than 1 mHz and are very strong in the 2-4 mHz range, so they may also be called 5-minute oscillations. Waves are common features in the photosphere, and even more at highest layers. But not only they are found in the upper layers: to probe the solar interior, unaccesible by any other means, helioseismology is used. The measurements of different waves give constraints of density and distance of the inner parts from the surface.

The chromosphere is more visually transparent than the photosphere, and it extends from 700 to 2000 km above the photosphere. Furthermore, the minimum and maximum heights of the chromosphere are defined from the solar temperature profile: a temperature minimum occurs just above the photosphere; then the lower limit of the chromosphere is the temperature minimum, and the maximum is the level where the temperature reaches 25 000 K. The name 'chromosphere' comes from the fact that it has a reddish colour, as the visual spectrum of the chromosphere is dominated by H$\alpha$ at 656 nm, which is clearly visible in a total solar eclipse at the Sun's limb as a red rim.

The photospheric temperature is about 4000 K to 6400 K but the chromosphere temperature ranges from about 4500 K to 25 000 K. This increasing temperature produces emission reversal of lines, for example of the typical chromospheric lines Ca II H and K. The low density, high temperature and the low collisional rates induce departures of the local thermodynamic equilibrium (LTE)[1].

The layer between the top of the chromosphere ($\sim 10^4$ K) and the corona ($\sim 10^6$ K) is called the transition region. It is appropriate to think of it as a temperature regime rather than a geometric layer. The ultraviolet (UV) spectrum from 50 nm to 160 nm is suited to explore this region, with missions like TRACE (Transition Region and Coronal Explorer) and nowadays SDO (Solar Dynamic Observatory).

[1] LTE implies that two variables uniquely define state of gas: temperature and density, via equilibrium relations of statistical mechanics. All atomic, ionic, and molecular level populations are given by Maxwellian-like Saha-Boltzmann statistics defined by local temperature. The local temperature is defined for a volume with a radius smaller than the thermalization length.

One image obtained by this telescope is shown in Figure 1.3.

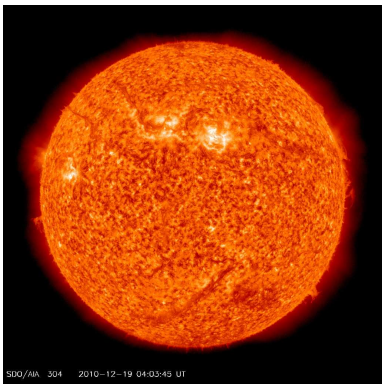


FIGURE 1.3— *Solar Dynamics Observatory* (*SDO*) He II 304 Å image of the chromosphere showing prominences, active regions and filaments. Adopted from http://sdo.gsfc.nasa.gov/.

The corona extends millions of kilometres into space, most easily seen during a total solar eclipse, but also observable with a coronagraph. Unusual spectral features are evinced, due to the high temperature of the corona. These spectral features have been observed in Fe XIV, which indicates a plasma temperature in excess of $10^6$ K. The Sun has a million degree corona, that was first discovered by Grotrian in 1939 by identifying the coronal lines as transitions from low metastable levels of the ground configuration of highly ionized metals (the Fe XIV line at 5303 Å, but also the line Fe X at 6374 Å).

Light from the corona comes from three primary sources. The K-corona – K for kontinuierlich – is created by Thomson scattering by free electrons, therefore it is partially polarized; Doppler broadening of the reflected photospheric absorption lines completely obscures them, giving the spectral appearance of a continuum with no absorption lines. It is dominating at a distance of $0.3R_\odot$. The F-corona – F for Fraunhofer – is created by photospheric light scattered on dust particles, observable because its light contains the Fraunhofer absorption lines that are seen in raw sunlight, and it extends to 2-3 $R_\odot$ (Aschwanden, 2005). The E-corona – E for emission – is due to spectral emission lines produced by ions that are present in the coronal plasma; it may be observed in broad or forbidden or hot spectral emission lines and is the main source of information about the corona's composition.

The solar magnetic activity cycle causes the 11-year periodic solar variation (changing the level of irradiation experienced on Earth) which also drives variations in the interplanetary medium. The solar cycle was discovered in 1843 by Samuel Heinrich Schwabe, who noticed a periodic variation in the average number of sunspots seen from year to year on the solar disk. Rudolf Wolf compiled and studied these and other observations, reconstructing the cycle back to 1745, eventually pushing these reconstructions to the earliest observations of sunspots by Galileo and contemporaries in the early seventeenth century.

The total solar irradiance (TSI) is the amount of solar radiative energy incident on the Earth's upper atmosphere. TSI variations were undetectable until satellite

observations began in late 1978. The major finding of satellite observations is that TSI varies in phase with the solar magnetic activity cycle with a variation of about 0.1% and an average value of TSI about 1366 W $m^{-2}$. It has been determined that variations about the average up to -0.3% are caused by large sunspot groups and of +0.05% by large faculae and bright network on a week to 10-day timescale. Recent studies, as Balmaceda (2007), estimate a secular increase of the TSI of about 1.3 W $m^{-2}$ since Maunder's Minimum.

### 1.2.1 Solar magnetic features

Sunspots have been observed by most civilizations. The earliest surviving report of sunspot observation dates from IV century BC. By 28 BC, Chinese imperial astronomers documented observations regularly. Pliny the Elder mentioned dark structures on the Sun circa 77 AC. In 1129, sunspot activity was described by John of Worcester – shown in Figure 1.4 – and Averroes provided a description of sunspots in the end of the XII century. Sunspots were first observed telescopically in late 1610 by Thomas Harriot (199 drawings of sunspots were found from 1610 to 1613) and Johannes and David Fabricius, who published a description in June 1611. Johannes Hevelius listed his daily solar observations from 1653 to 1679 in Machina Coelestis (1679) (Hoyt and Schatten, 1995). At that time Galileo had been showing sunspots to astronomers in Rome, and Christoph Scheiner had probably been observing the spots for two or three months using an improved helioscope of his own design. A fundamental instrument for solar observations was the *camera obscura* (Casanovas, 1997), used by Kepler in a mercury transit, when he spotted other dark structures, and by Scheiner, who used a telescope with an equatorial mounting and could determine the Sun's rotation axis. All his results were presented in his book Rosa Ursina (1626-1630).

FIGURE 1.4— Sunspot depicted by John of Worcester in 1129. Adopted from http://sunearthday.nasa.gov/.

Sunspots are the largest coherent manifestation of the photospheric magnetic fields. These phenomena appear conspicuously as dark spots compared to their surroundings, with lifetimes of days. They are caused by intense magnetic activity, which inhibits convection, forming areas of reduced surface temperature. Although they are at temperatures of roughly 3000-4500 K, the contrast with the surrounding material at about 5780 K leaves them clearly visible as dark spots, in contrast with the brighter photosphere. Sunspots display two different regions: more vertical

magnetic field in the dark core or umbra, and horizontal fields in a filamentary structure called penumbra. Sunspots expand and contract as they move across the surface of the Sun and can be as large as 80 000 kilometres. Manifesting intense magnetic activity, sunspots host secondary phenomena such as coronal loops and reconnection events, as well as small magnetic features like umbral and penumbral dots. Most solar flares and coronal mass ejections originate in magnetically active regions around visible sunspot groups. Similar phenomena indirectly observed on stars are commonly referred to as starspots.

Other very conspicuous feature are the faculae. These large bright extensions of solar surface covered by magnetic fields are described at Section §1.2.2.3. Some of the features appearing in the chromosphere are plages. These structures of high contrast regions correspond to active regions (faculae and sunspots) in the photosphere and present strong magnetic fields. Their large extension and long lifetime play an important role in the estimation of the TSI.

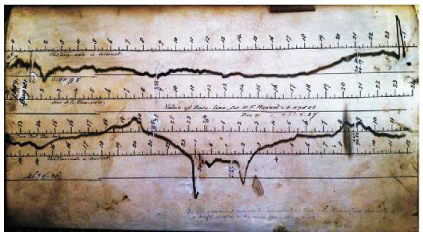

FIGURE 1.5— Effects of the space weather: Ground-based magnetometer record of the Carrington's 'white light flare', happened in 1859. http://sdoisgo.blogspot.com/

The most common solar feature within the chromosphere are spicules, long thin fingers of gas of 5000 km height which appear like grass, growing upwards from the photosphere below. Spicules (type I) rise to the top of the chromosphere and then sink back down again over the course of about 10 minutes on parabolic trajectories with a non-ballistic motion. They also can display transverse motion due to waves (de Pontieu et al., 2007). Type II spicules show shorter lifetimes, around 1 min. Also macrospicules (sized four times larger than spicules) are found close to the solar poles. Other structures, as fibrils, individual short-lived active-region chromospheric jet-like features in H$\alpha$ appear in this very dynamic layer. In addition, there are also large-scale feature, as solar prominences, that rise up through the chromosphere from the photosphere, and sometimes they reach altitudes of 150 000 kilometres. Some of them are displayed in Figure 1.3. However, probably the most relevant features are flares. These sudden brightenings observed over the Sun surface are large energy releases of up to $6\times10^{25}$ J, involving different physical mechanisms (magnetic reconnection, electron acceleration and braking, material evaporation and shocks) that imply energy release in all wavelengths, from radio to X-rays.

Some features present in the corona are the coronal holes. These structures

are low density and temperature regions which appear dark in EUV and X-rays. These are wide zones of the Sun where the magnetic field is unipolar and opens towards the interplanetary space. There are different types of coronal holes. Polar coronal holes have long durations and the high speed solar wind arises mainly from these polar coronal holes. Non-polar coronal holes are related to remnants of active regions and can persist during several solar rotations. Transient coronal holes are associated with eruptive events, as coronal mass ejections (CMEs) and filament eruptions (Zhang et al., 2006). But not everything is quiescent in the corona. A whole zoo of very dynamic events (nanoflares, microflares) derived from magnetic reconnection provoke energy release of about $10^{17}$ J in X-rays for each of these events.

The interactions of the Sun-Earth interplanetary medium and its forecasting, commonly known as space weather, are usually driven by the solar wind or interplanetary coronal mass ejections that interact with the geomagnetic field and originate geomagnetic storms. These storms can be measured with different indices, being the $Dst$ index of the most usual. The disturbance storm time index ($Dst$) is a measure of geomagnetic activity used to assess the severity of magnetic storms. It is expressed in nanoteslas (nT) and is based on the average value of the horizontal component of the Earth's magnetic field measured hourly at four near-equatorial geomagnetic observatories.

### 1.2.2 Magnetic elements in the photosphere

Small-scale magnetic field features are main topic of this Thesis. A good knowledge of their size, lifetime, and coverage are parameters that can help us to understand their role on the TSI, local dynamo, etc. These structures can be found ubiquitously in the solar surface, being accumulations of magnetic field located in the intergranular lanes between granules. In the following Subsections, flux tube models and their observational photospheric manifestations, which are G-band bright points and faculae, are described. First detailed observations of these magnetic concentrations were made by Dunn and Zirker (1973); Mehltretter (1974), observing both faculae, GBPs, 'filigree', 'crinkles', micropores, etc.

#### 1.2.2.1 Flux tube models

In this Section, a basic flux tube model suitable for modelling facular points and GBPs is explained, plus some different versions. According to Spruit's model, magnetic flux tubes (basic elements of faculae and GBPs) are considered to be evacuated flux tubes with hot walls and a hot or cool floor (corresponding to an

optical depth $\tau = 1$, as definition of photosphere) depending on the evacuation and diameter of the flux tube. This model (Spruit, 1976) is presented in Figure 1.6(a). Horizontal arrows mark the lateral heat influx/outflux under/over the photosphere (level $Z = 0$ in the Figure 1.6). Strong fields inhibits horizontal convective exchange while the vertical convective transport is partially reduced (Deinzer et al., 1984). This model assumes that inside each small flux tube the magnetic field is of the order of kilogauss, but practically zero outside. Due to the magnetic pressure the flux tube interior is evacuated, and tube walls are bright due to radiation leaking in from the surroundings, meaning there is a horizontal flux of energy into the tube. When the tube is sufficiently broad, the horizontal optical depth between the wall and the tube centre is large and most of the radiation cannot reach the centre. In this case, the tube floor remains dark at its centre. But if the tube is narrow enough, the horizontal flux of energy can reach the centre of the tube; then, the interior of the tube is heated, the vertical energy flux increases, and the tube turns bright, even at disk centre.

Topka's model (Topka et al., 1997) describes a flux tube by three parameters: the Wilson depression – because the gas pressure is lower, the opacity is lower, so that the tube looks like a depression, called, by analogy to sunspots, the Wilson depression $Z_w$ – the lateral heat influx and the radius. A sketch is presented in Figure 1.6(b). Convective transport is not allowed across the field lines.

#### 1.2.2.2 G-band bright points

Bright points in G-band (GBPs) are identified with small magnetic concentrations that look as sharp bright point-like features. Ubiquitous over the Sun's surface, they can be found in the network, forming long structures and tracing supergranules, isolated in the internetwork or close to sunspots. As slender flux tubes, these structures follow the models of magnetic tubes (see next Subsection). Typical magnetic fields strength range from hG to kG (Sánchez Almeida et al., 2004).

The way of quantifying the brightening of these features is defining the contrast normalized to a Quiet Sun intensity value:

$$C(x,y) = \frac{I(x,y) - \langle I_{quietsun}(x,y)\rangle}{\langle I_{quietsun}(x,y)\rangle}. \tag{1.1}$$

The maximum contrast is about $1.8I_c$, where $I_c$ is the continuum intensity. The most usual way of observing these magnetic structures is G-band, but they also can be studied in CN band or other wavelengths as in Leenaarts et al. (2006), who affirm that the highest contrast can be found in the H$\alpha$ line blue wing.

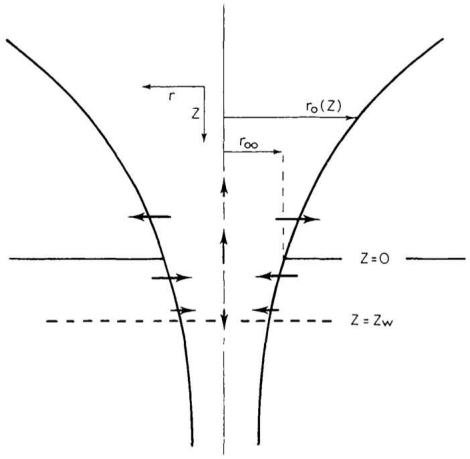


(a) Model by Spruit (1976).

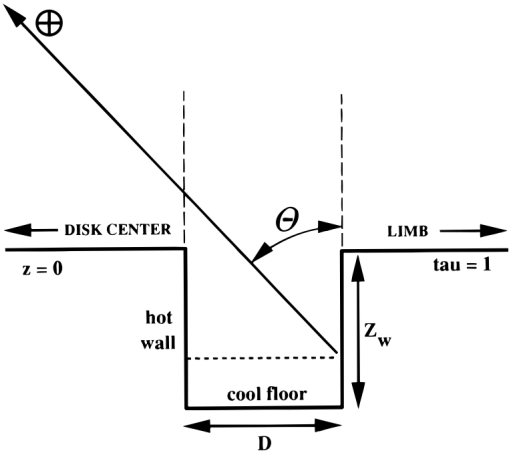


(b) Geometric model of 'hotwall', by Topka et al. (1997).

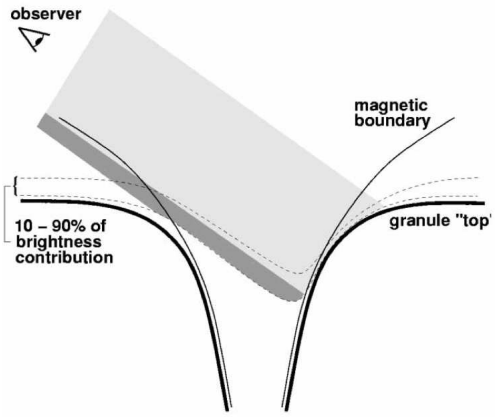


(c) Facular model by Keller et al. (2004).

FIGURE 1.6— Various magnetic flux tube models.

Since G and CN bands are very popular for the observation of BPs, some explanation about the formation and characteristics of these bands are mandatory. The CH band or G-band is populated by electronic transitions $A^2\Delta^+ - X^2\Pi^+$ in the band, and the central wavelength is at 430.5 nm. The bandhead is formed by the line overlapping of the mentioned transitions. CN is a molecular band at 388.33 nm mostly populated by electronic transitions in the CN $B^2\Sigma^+ - X^2\Sigma^+$ molecular band. G-band and CN are shown in Figure 2.3 on solid red lines (the scale can be found on the right).

Besides, the magnetic flux tube plays a role on this brightening further beyond of the pure idea of 'hot wall': since the density inside the magnetic flux tube is lower than outside, CN and CH are depleted, whose effect is less absorption and brighter structures (Kiselman et al., 2001). Since H is more abundant than N, there are more molecules of CH rather than CN. The strong decline in CN number density in deeper layers is the result of the temperature sensitivity to dissociation, which is exponential. In addition, the dissociation energy of CN is twice that of CH. These considerations are important on simulations to obtain synthetic contrasts to compare to observations. Zakharov et al. (2005) showed that CN synthetic filtergrams taken with a full width at half maximum (*FWHM*) of 0.8 nm – equivalent to the CN bandwidth in HINODE – give a contrast 1.4 times larger than the G-band contrast. However, other theoretical models (Uitenbroek and Tritschler, 2007) give CN-CH contrast ratio values of 0.96.

One of the most fundamental questions is if these structures are elementary or formed by smaller structures, such as a bunch of slender flux tubes or sheets. Berger et al. (2004) suggested that the forming blocks of larger magnetic features as 'filigree' are magnetic sheets (Deinzer et al., 1984). Other models consider that the striation of magnetic sheets is due to the fluting instability (Buente et al., 1993; Steiner, 2005b), fragmenting a flux sheet to form smaller flux units. Several authors, for instance Berger and Title (2001) reported cases of GBPs without associated magnetic field, and *vice versa*. In network and internetwork, GBPs can be further away from the main magnetic structures with $1''$ as maximum distance (Berger et al., 2004; Ishikawa et al., 2007). Thus an important question arises about the possibility of some 'activation mechanism', as the detectability of GBPs is high, but their magnetic counterpart sometimes is not. This can be because the magnetic field can reach values below the noise level because of instrumental or atmospheric issues. The 'activation mechanism' can be the intensification of the magnetic flux, i.e., convective collapse (detailed in Section 3.7.2). For this reason, sometimes GBPs were classified as 'magnetic' and 'non-magnetic' (Berger and Title, 2001; Bovelet and Wiehr, 2008). Beck et al. (2007) found 94% of the

GBPs (around a sunspot) having polarization signals over the noise level, and de Wijn et al. (2005) found 85% of the network bright points corresponding with Ca II BPs. With respect to Ca II BPs, a most recent point of view is offered by Jafarzadeh et al. (2010), who show the Ca II H bright points as temporally coincidental with magnetic concentrations, but not all the time.

Mean sizes for GBPs are approximately 200 km for most studies (Wiehr and Puschmann, 2005; Puschmann and Wiehr, 2006; Ishikawa et al., 2007; Beck et al., 2007; Utz et al., 2009), and slightly larger if these magnetic structures belong to faculae (Berger et al., 1995). On the attempt of counting such small structures, isolated GBPs can be successfully fitted to Gaussian functions. In Title and Berger (1996), the authors simulated GBPs by a double Gaussian. The positive component, with positive contrast, was modelled by a convolution of a Gaussian plus another one, whose *FWHM* corresponded to the resolution of the telescope. Also the dark intergranular lane was fitted to a negative Gaussian function. Other authors (Berger et al., 1995; Sánchez Almeida et al., 2004) used 2-D Gaussian functions. The *FWHM* of these structures derived with this method was approximately 200 km, the same value as obtained by the previously mentioned authors.

Mean lifetimes range from 3 to 5 min in internetwork areas, and in network areas, they can last up to 20 min. Their proper motion mean horizontal velocity is about 1 $\mathrm{km\,s^{-1}}$ (Berger et al., 1998; de Wijn et al., 2005, 2008). Very recent studies (i.e., Manso Sainz et al., 2011) show trajectories and paths, concluding that the diffusion is lower in magnetized structures than in the non-magnetized ones. Magnetic features show a superdiffusive behaviour into granules.

The area coverage of these small magnetic features is also an important magnitude. Values can oscillate, depending on the telescope used and the corresponding diffraction limit, and the segmentation method to count GBPs, among with *seeing* in ground based observations. Coverage does depend on the target region: when sought in the internetwork, it can yield a density as low as 0.2 $\mathrm{Mm^{-2}}$ (de Wijn et al., 2005). The area coverage peaks when network BPs are studied, at 9.3 $\mathrm{Mm^{-2}}$ (Berger et al., 1998).The GBPs area coverage is approximately 0.5% in Sánchez Almeida et al. (2004), increasing dramatically in Sánchez Almeida et al. (2010), with 0.99%. In Cabello García I., (PhD thesis, 2012), the coverage is 0.88% for disk centre on SST images. Other authors, like Balmaceda et al. (2009), obtain an area coverage of 0.26% and 0.22% respectively for G-band and CN.

#### 1.2.2.3 Faculae

Faculae are bright structures – as observed and coined by Galileo and Scheiner (Casanovas, 1997) – seen in the photosphere associated with magnetic fields ob-

served outside of disk centre, at $\cos\theta < 1$. At high resolution, they consist of many unresolved small bright structures, with diameters of about 100 km, called facular points. Several models for small flux tubes have been constructed (Spruit, 1976; Topka et al., 1997; Keller et al., 2004). Facular structures are brighter when going far off the disk centre because when increasing heliocentric angle the limbward side of the hot wall becomes visible, while the depressed cool floor disappears. Near the limb, a bright facula appears brighter because the 'hot wall' is viewed face-on while the surrounding non-magnetic atmosphere is strongly darkened. Flux tubes can be dark at disk centre because the 'hot wall' area is a minimum. If annihilation of convective energy transport into the tube is included, resulting in a cooling of the deeper layers (Spruit, 1976). Magnetic field strength also plays a role in the contrast: the larger the magnetic field strength, the darker the tube floor.

The facular brightening occurs on the disk-centre side of granules and can spread more than 0.″5 (Keller et al., 2004). The brightness enhancement of the facula originates mainly from a thin layer near the limbward interface between the magnetic flux concentration and the hot non-magnetic granule, in a shade of light gray in Figure 1.6(c). The opacity in the magnetic flux concentration is strongly reduced because of its low density thus providing a clear sight straight through the magnetic field onto the adjacent non-magnetic granule. If the tube is not too wide, the opacity reduction will not be enough to see a difference in the continuum intensity formed in the hot granule. Dark gray band marks the projection of the intergranular lane, i.e., the cooler downflow. Dashed lines enclose the area where the 80% of the continuum intensity is formed.

Many studies have been performed about how to discriminate between facular points and GBPs, as Kobel et al. (2008); Berger et al. (1998). The study of the flux tubes contrast and its dependence with the heliocentric angle is called the centre-to-limb variation (CLV) (Ortiz et al., 2002, 2003; Penza et al., 2004; Steiner, 2005a; Ortiz et al., 2006; Cabello and Domingo, 2006, among others).The dependence on wavelength affects strongly the facular contrast values. While in infrared the contrast is low, as in de Boer et al. (1997), Wang et al. (1998), ultraviolet observations yield higher values for the facular contrast (Centrone and Ermolli, 2003). Due to this fact, short wavelength contributions (Fröhlich, 2002) are fundamental to understand their role to the total solar irradiance and the Sun-as-a-star general behaviour.

## 1.3 Image processing

As the magnetic elements are the smallest structures that we can detect in the Sun, the dependence on the performance of the telescope is crucial. Solar light induces several effects on the image formation, as air turbulence damages the image quality, and indirectly, solar heat affects the post-focus instrument inducing defocus and problems on instruments. Therefore, in this Section, the theory of image formation, the principles of image degradation and image restoration procedures are discussed.

### 1.3.1 Image formation

The Earth's atmosphere affects the quality of the images in ground-based telescopes. Image degradation can be considered as a combination of three main effects, namely: image smearing (*blurring*), global displacements (*image motion*) and distortion of the structures caused by different atmospheric patches (*stretching*). All these effects together form the so-called *seeing*.

The basic ideal process describing the formation of images is shown in Figure 1.7. The object of study is placed on the so-called object plane represented by the coordinates system $(\xi, \eta)$, and another coordinate system $(x, y)$ called the image plane is situated right in the focal plane of the telescope. These two coordinate systems are linked by the magnification factor. The coordinates in the image plane are represented in vectorial notation as $\boldsymbol{q}$. The wave coming from a point source in the object plane passes through the atmosphere and part of it enters the telescope and forms the corresponding image (not a point anymore but a spot) centered at position $(x', y')$ in the image plane.

If the object source is the *impulse unit function*, its image corresponds to the *impulse response function* of the optical transmission system (atmosphere + telescope). This response is also named Point Spread Function (PSF) of the system[2]. The PSF can be viewed as the normalized distribution of intensity in the image of a point source and can be expressed as $s(x, y; x', y'; t)$, where $t$ represents the variability of the transmission system (e.g. atmospheric turbulence evolves at a fast rate) and $(x', y')$ reflects that the PSF is, in general, space variant, i.e. the distribution of intensity in the image of a point source changes with its location $(\xi, \eta)$ in the object plane. Note that $(x', y')$ is the image conjugated point of $(\xi, \eta)$.

Considering an extended object like the Sun as composed of a myriad of incoherent point sources, with individual intensities $i_o(\xi, \eta)$, we can estimate the resulting

[2]This concept is treated in more detail in Section §1.3.2.

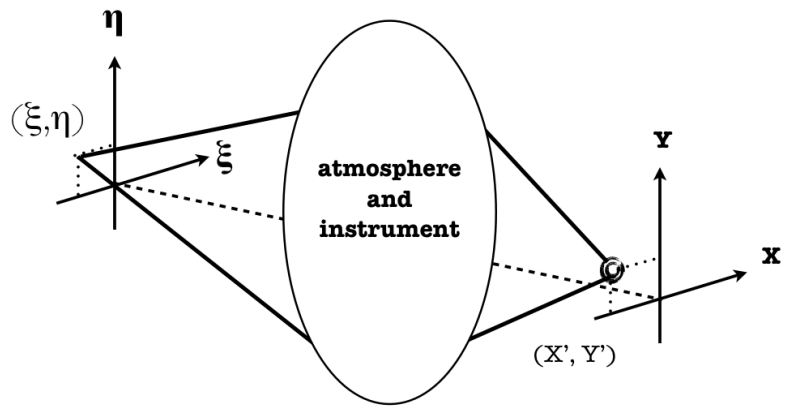


FIGURE 1.7— Image formation process diagram, showing the deformation process of a wavefront. A point source became blurred and it is represented by a circle.

intensity distribution in the focal plane of the telescope. Assuming a linear optical system and incoherent illumination, this intensity can be expressed as

$$i(x,y,t) = \iint i_o(x',y')\, s(x,y;x',y';t)\, \mathrm{d}x'\, \mathrm{d}y', \tag{1.2}$$

where $i_o(x',y')$ represents the intensity distribution in the ideal image (i.e. also in the object) that would produce a perfect system free from aberrations considering an infinite aperture, not limited by diffraction.

A concept inherited from the Kolmogorov statistics is the isoplanatic angle. Its projected region over the plane of the sky is called the isoplanatic patch, as the coherence of the same turbulence pattern over the sky: it is considered as the area where aberrations do not change significantly inside this region. In these patches, the PSF is considered space-invariant, which means that the images of point sources in the object plane change in location but do not change in functional form. Another interesting concept is the Fried parameter $r_o$. It is a parameter expressed in centimetres and corresponds to an area over which the root mean square wavefront error is less than 1 radian. It also can be interpreted as the equivalent diffraction-limited telescope aperture in the absence of atmosphere.

For an isoplanatic system having a spatially invariant PSF, i.e. $s(x,y;x',y';t) = s(x-x',y-y',t)$, the Equation 1.2 can be written as

$$\begin{aligned} i(x,y,t) &= \iint i_o(x',y')\, s(x-x',y-y',t)\, \mathrm{dx}'\, \mathrm{dy}' \\ &= \iint i_o(\boldsymbol{q}',t)\, s(\boldsymbol{q}-\boldsymbol{q}',t)\, \mathrm{d}\boldsymbol{q} = i_o(\boldsymbol{q}) * s(\boldsymbol{q},t), \end{aligned} \tag{1.3}$$

where $*$ stands for convolution. Using the convolution theorem (which states that the Fourier transform of the convolution of two functions is the product of their Fourier transforms), the Equation 1.3 can be transformed in 1.4.

$$I(\boldsymbol{u},t) = I_o(\boldsymbol{u})\, S(\boldsymbol{u},t), \tag{1.4}$$

where capital letters stand for the Fourier transforms of the functions in lowercase, $\boldsymbol{u}$ is the frequency vector in the Fourier domain and, $S$ is the so-called Optical Transfer Function (OTF) of the system. The amplitude of the OTF is called the Modulation Transfer Function (MTF): $\mathrm{MTF}(\boldsymbol{u},t) = |\mathrm{OTF}(\boldsymbol{u},t)|$. According to Equation 1.4, the MTF is a filter that attenuates the amplitudes of the Fourier components of the ideal image to form the observed image.

### 1.3.2 Diffraction limit and Point Spread Function

The resolution limit is the power of distinguishing two close point sources. The term resolution or minimum resolvable distance refers to the minimum distance between distinguishable objects in an image. The Rayleigh criterion defines this situation as stating that two point sources are regarded as just resolved when the principal diffraction maximum of one image coincides with the first minimum of the other. If the distance is larger, the two points are well resolved.

The limitation on the ability of distinguishing a point source of light with a given instrument is proportional to the size of its objective, and inversely proportional to the wavelength of the light being observed. For telescopes with circular apertures, the size of the smallest feature in an image that is diffraction limited is the size of the Airy disk. The diffraction pattern resulting from a uniformly-illuminated circular aperture presents a bright circle in the centre, known as the Airy disk which together with the series of concentric bright rings around it, is called the Airy pattern. Far away from the aperture, the angle at which the first minimum occurs, measured from the direction of incoming light, is given by the approximate formula – obtained by finding the first zero of the Fraunhofer diffraction pattern –:

$$PSF(\boldsymbol{q}) = \frac{1}{\pi}\left[\frac{J_1(\frac{D\pi}{\lambda f}\boldsymbol{q})}{\boldsymbol{q}}\right]^2 \tag{1.5}$$

$$\sin\theta = 1.22\frac{\lambda}{D} \Rightarrow \theta \approx 1.22\frac{\lambda}{D}\ [rad]. \tag{1.6}$$

The *seeing* parameter or Full Width at Half Maximum of the PSF is $0.976\lambda r_o^{-1}$, where $r_o$ is the Fried parameter. Furthermore, the *FWHM* is proportional to the integral of the quadratic index structure constant along the atmospheric height. The inverse of the *FWHM* corresponds to the atmospheric cutoff frequency $\boldsymbol{u}_c$, as stated in Equation 1.7:

$$\boldsymbol{u}_c = \frac{D}{\lambda f}, \tag{1.7}$$

where $f$ is the focal distance and $D$ is the diameter of the telescope aperture.

In the case of the telescopes used for this work, both Swedish Solar Telescope and SUNRISE, operating at the typical wavelength of G-band, $\lambda$430nm, the diffraction limit is 0.1 arcsec (0.″1). For HINODE, being its diameter 50 cm, the corresponding diffraction limit is 0.2 arcsec for the same wavelength (Wedemeyer-Böhm, 2008). We refer the reader to Chapter §2 for more information about these missions.

The impulse response of diffraction is the Fourier transform (squared) of the exit pupil. This impulse response is called the Point Spread Function (PSF).

The transfer function of diffraction is the Fourier transform of the PSF called the Optical Transfer Function (OTF). For an ideal telescope of diameter $D$ and focal length $f$, without aberration (phase delays are zero), the transmission pupil function is 1 for $r < D/2$. Therefore, the expression for the long-exposure OTF presents two parts: the $S_{tel}$ and the $S_{atm}$. These ones are defined in Equation 1.8 and Equation 1.9.

$$S_{tel}(\boldsymbol{u}) = \frac{2}{\pi}\left[\arccos(\alpha\boldsymbol{u}) - \alpha\boldsymbol{u}\sqrt{1-\alpha^2\boldsymbol{u}^2}\right], \tag{1.8}$$

where $\alpha = \lambda f/D$, that is the inverse of the cutoff frequency $\boldsymbol{u}_c$. The expression for the OTF related with the atmospheric turbulent effects is noted by the temporal average $\langle S_{atm}\rangle$:

$$\langle S_{atm}\rangle = e^{-3.44\boldsymbol{u}\frac{\lambda f}{r_o}^{5/3}}. \tag{1.9}$$

Let us consider a CCD image is with 1024×1024 pixels – the image is square as we have to use the Fourier transform – with G-band (430 nm) as the working wavelength for this case. The spatial sampling of the SST is 0.″034 pixel$^{-1}$ and for HINODE it is 0.″054 pixel$^{-1}$. The apertures are 100 cm and 50 cm, respectively. These two examples of ideal $S_{tel}$ are presented in Figure 1.8. The corresponding Optical Transfer Function of SST and HINODE are represented as surfaces.

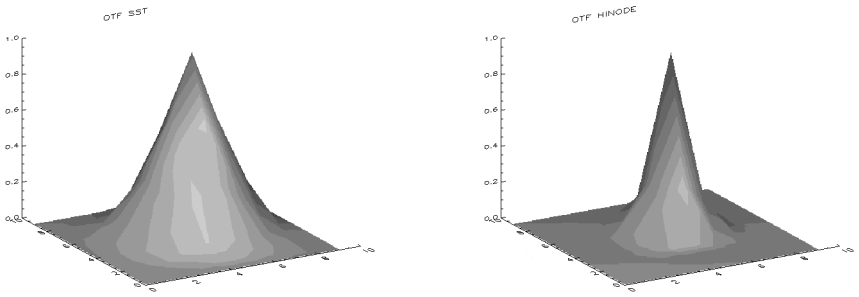


FIGURE 1.8— Ideal SST OTF *(left)* and HINODE OTF *(right)*, (units arcsec$^{-1}$), considering G-band (430 nm) as the working wavelength. The apertures are 100 cm and 50 cm, respectively. The typical cutoff frequency $\boldsymbol{u}_c$ of HINODE is approximately 3.5 arcsec$^{-1}$.

### 1.3.3 Phase Diversity

The Phase Diversity (PD) was first proposed by Gonsalves and Chidlaw (1979) as a method to infer phase aberrations working with images of extended objects. This technique of image reconstruction (Gonsalves, 1982; Paxman et al., 1992) requires to use at least two images from two channels of the object to be restored. One is the image degraded by the atmosphere and telescope aberration (unknown aberration) and the other image is affected by the same unknown aberration plus an intentionally induced aberration – for all cases described in this work this will be defocus –. This aberration can be created by just moving the camera forward/backward (along the optical axis of the system), the most common method in the SST; or placing a transparent plate in front of one of the cameras, as in IMaX/SUNRISE, or two plates, one transparent and another, a semi-reflective plate as in SuFI/SUNRISE. Investigations about the PD method were performed in Vargas Domínguez (2009). The formation of these two images can be expressed by (Equation 1.3 plus noise components):

$$\left.\begin{aligned} i_1(\boldsymbol{q}) &= i_o(\boldsymbol{q}) * s_1(\boldsymbol{q}) + n_1(\boldsymbol{q}), \\ i_2(\boldsymbol{q}) &= i_o(\boldsymbol{q}) * s_2(\boldsymbol{q}) + n_2(\boldsymbol{q}), \end{aligned}\right\} \tag{1.10}$$

where :

| | |
|---|---|
| $i_1(\boldsymbol{q}), i_2(\boldsymbol{q})$ | is the focused-defocused image pair that we observe. |
| $s_1(\boldsymbol{q}), s_2(\boldsymbol{q})$ | are the corresponding PSFs for each image channel. |
| $n_1(\boldsymbol{q}), n_2(\boldsymbol{q})$ | are the noise additive terms. |
| $i_o(\boldsymbol{q})$ | is the so-called *true object*. |

The system 1.10 has two equations and two unknowns, $i_o(\boldsymbol{q})$ and $s_1(\boldsymbol{q})$. If we do not consider the noise term, the system is determined. As $s_1(\boldsymbol{q})$ and $s_2(\boldsymbol{q})$ just differ in a well-known defocus value, these two terms are analytically related.

A least-squares solution for this system of equations was proposed by Paxman et al. (1992), considering the noise terms as Gaussian noise, allowing an statistical treatment. Operating in the Fourier space, all the convolutions can be treated as products. Therefore, the following error metric in the Fourier domain was proposed to be minimized:

$$L(I_o, S_1) = \sum_{\boldsymbol{u}} \Big\{ \big| I_1(\boldsymbol{u}) - I_o(\boldsymbol{u}) S_1(\boldsymbol{u}) \big|^2 + \gamma \big| I_2(\boldsymbol{u}) - I_o(\boldsymbol{u}) S_2(\boldsymbol{u}) \big|^2 \Big\}, \tag{1.11}$$

where capital letters stand for the Fourier transforms of the functions in lowercase in the system of Equations 1.10, and $\gamma = \sigma_1^2/\sigma_2^2$ was introduced by Löfdahl and Scharmer (1994) as a weighting factor to equalize the noise contributions when the noise variances $\sigma_1^2$ and $\sigma_2^2$ are not the same in both image channels. $S$ represents the OTF of the system which can be derived as the auto-correlation of the so-called *generalized pupil function* $H$,

$$S(\boldsymbol{u}) \propto \iint H(\boldsymbol{r}) H^*(\boldsymbol{r} - \lambda f \boldsymbol{u}) \mathrm{d}\boldsymbol{r}, \tag{1.12}$$

where $\lambda$ and $f$ stand for the working wavelength and the effective focal length of the optical system, respectively, and $\boldsymbol{u}$ is a vector with dimensions of spatial frequency. $H$, in turn, can be expressed in terms of the joint phase aberration $\phi(\boldsymbol{r})$ caused by the telescope and the turbulence as

$$H(\boldsymbol{r}) = |H(\boldsymbol{r})| e^{i\phi(\boldsymbol{r})}. \tag{1.13}$$

The phase aberration can be parametrized by using an expansion into the orthogonal circle Zernike polynomials[3]:

$$\phi(\boldsymbol{r}) = \phi(R\boldsymbol{\rho}) = \sum_{j=1}^{J} \alpha_j Z_j(\boldsymbol{\rho}), \tag{1.14}$$

where $R$ is the pupil radius, $\boldsymbol{\rho}$ is the vectorial notation for $(\rho, \theta)$ with $\rho$ defined in a unit circle $(0 \leq \rho \leq 1)$ and $\theta$ being the azimuthal angle, and $\boldsymbol{\alpha} \equiv \{\alpha_j, j = 1, 2, ..., J\}$ are the coefficients of the terms in the Zernike expansion.

Thus, Equation 1.13 can be then written as

$$H(R\boldsymbol{\rho}) = |H(R\boldsymbol{\rho})| e^{i\left[\delta(R\boldsymbol{\rho}) + \sum_{j=1}^{J} \alpha_j Z_j(\boldsymbol{\rho})\right]}, \tag{1.15}$$

where $\delta(R\boldsymbol{\rho})$ is the diverse phase, i.e. the induced defocus in our case. The final result is that the OTF (Equation 1.12) and therefore the error metric $L$ (Equation 1.11) are parametrized by the expansion in Zernike polynomials, so can be written: $L(I_o, \boldsymbol{\alpha})$. The diverse phase $\delta(R\boldsymbol{\rho})$ will be zero in the case of $S_1$ that corresponds to the focus image. In Bonet et al. (2004), up to 21 Zernike terms were used. In IMaX restoration, 45 Zernike polynomials are used (Martínez Pillet et al., 2011).

Part of the minimization of the Equation 1.11 can be performed analytically. The number of free parameters is $N \times N$ (pixels) plus the polynomial expansion of the aberration. Given a fixed aberration function, we can arrive to the solution of the Equation $\partial L / \partial I_o = 0$ for the real and the imaginary part yields an estimate of the object $\hat{I}_o(\boldsymbol{u})$ that minimizes the Equation 1.11,

$$\hat{I}_o(\boldsymbol{u}) = \frac{I_1(\boldsymbol{u})\, S_1^*(\boldsymbol{u}, \boldsymbol{\alpha}) + \gamma\, I_2(\boldsymbol{u})\, S_2^*(\boldsymbol{u}, \boldsymbol{\alpha})}{|S_1(\boldsymbol{u}, \boldsymbol{\alpha})|^2 + \gamma\, |S_2(\boldsymbol{u}, \boldsymbol{\alpha})|^2}. \tag{1.16}$$

[3]The Zernike polynomials belong to a basis defined over a circular support area, typically the pupil planes in classical optical imaging through systems of lenses and mirrors of finite diameter. Their advantage is the simple analytical properties inherited from the simplicity of the radial functions and the factorization in radial – developed from the Jacobi polynomials – and azimuthal functions (Noll, 1976); this leads for example to closed-form expressions of the two-dimensional Fourier transform in terms of Bessel Functions. Their disadvantage, in particular if high orders are involved, is the unequal distribution of nodal lines over the unit disk, which introduces ringing effects near the perimeter. For this reason, sometimes the Karhunen-Loève (KL to shorten) polynomials are used instead of Zernikes. KL functions are the optimal basis functions, since they present a diagonal covariance matrix.

Replacing $\hat{I}_o(\boldsymbol{u})$ in the Equation 1.11, we obtain a so-called *modified error metric* (Gonsalves, 1982; Löfdahl and Scharmer, 1994; Bonet et al., 2004):

$$L_M(\boldsymbol{\alpha}) = \sum_{\boldsymbol{u}} \frac{\left|I_1(\boldsymbol{u})\, S_2(\boldsymbol{u},\boldsymbol{\alpha}) - I_2(\boldsymbol{u})\, S_1(\boldsymbol{u},\boldsymbol{\alpha})\right|^2}{|S_1(\boldsymbol{u},\boldsymbol{\alpha})|^2 + \gamma\,|S_2(\boldsymbol{u},\boldsymbol{\alpha})|^2}. \tag{1.17}$$

Note that this modified metric is not explicitly dependent on the Fourier transform of the object $\hat{I}_o(\boldsymbol{u})$ but only includes the unknown $\boldsymbol{\alpha}$ vector. By means of non-linear optimization techniques, we find the $\boldsymbol{\alpha}$ vector, characterizing the aberration components, that minimizes the Equation 1.17. Once these components are determined, $\hat{S}_1$ and $\hat{S}_2$ can be calculated from Equations 1.15 and 1.12 and the object estimate can be eventually derived from Equation 1.16, completing in this way the restoration process.

### 1.3.4 Wiener filter

Considering noise uncorrelated with the level of signal (because solar fine structure has a low contrast), for a short exposure, the observed intensity is represented as follows:

$$i_n(\boldsymbol{q}) = \iint i_0(\boldsymbol{q'}) s(\boldsymbol{q}-\boldsymbol{q'}) \mathrm{d}\boldsymbol{q'} = i_0(\boldsymbol{q}) * s(\boldsymbol{q}) + n(\boldsymbol{q}), \tag{1.18}$$

where s$(\boldsymbol{q}-\boldsymbol{q'})$ is the smearing function of the atmosphere and telescope and $i_0(\boldsymbol{q'})$ is the true signal coming from the Sun. Its equivalent expression in the frequency domain is (Brault and White, 1971):

$$I_N(\boldsymbol{u}) = I_0(\boldsymbol{u}) S(\boldsymbol{u}) + N(\boldsymbol{u}) = I(\boldsymbol{u}) + N(\boldsymbol{u}). \tag{1.19}$$

Rearranging the Equation 1.19 yields:

$$\frac{I_N(\boldsymbol{u})}{S(\boldsymbol{u})} = \frac{I(\boldsymbol{u})}{S(\boldsymbol{u})} + \frac{N(\boldsymbol{u})}{S(\boldsymbol{u})}. \tag{1.20}$$

Treating the problem in this way, the consequence is that the restoration process will fail at high frequencies where the *signal-to-noise ratio* $(S/N)$ is small.

Therefore, a noise filter is essential to the process:[4]

$$I_F(\boldsymbol{u}) = I_N(\boldsymbol{u}) \Phi_N(\boldsymbol{u}) = [I(\boldsymbol{u}) + N(\boldsymbol{u})] \Phi_N(\boldsymbol{u}), \tag{1.21}$$

[4]From the notes on the postgraduate course *Técnicas de alta resolución para imágenes astronómicas* (2005). J. A. Bonet.

where $\Phi_N$ is a real function which weighs $I_N$ according to its $S/N$ ratio at each frequency. The optimum filter results in the closest smooth approach of the true signal and the filtered signal:

$$\delta = \int \varepsilon^2 \mathrm{d}\boldsymbol{u} = \int [I(\boldsymbol{q}) - I_F(\boldsymbol{q})]^2 d\boldsymbol{q} \Leftrightarrow \int |I(\boldsymbol{u}) - I_F(\boldsymbol{u})|^2 d\boldsymbol{u}, \tag{1.22}$$

This expression should be minimum in the root-mean square error sense. Equation 1.22 is equivalent in both sides of the symbol ($\Leftrightarrow$) by the Parseval's theorem, which states that the square of a function is equal to the integral of the square of its transform. Substituting Equation 1.21 in 1.22, it yields:

$$\delta = \int |I(\boldsymbol{u})[1 - \Phi_N(\boldsymbol{u})] - N(\boldsymbol{u})\Phi_N(\boldsymbol{u})|^2 \mathrm{d}\boldsymbol{u}, \tag{1.23}$$

Considering that $i(\boldsymbol{q})$ and $n(\boldsymbol{q})$ are uncorrelated and therefore their cross products are zero, we can rearrange Equation 1.23:

$$\delta = \int \varepsilon^2 \mathrm{d}\boldsymbol{u} = \int \{|I(\boldsymbol{u})|^2 [1 - \Phi_N(\boldsymbol{u})]^2 + |N(\boldsymbol{u})|^2 \Phi_N(\boldsymbol{u})|^2\} \mathrm{d}\boldsymbol{u} \tag{1.24}$$

Minimizing the Equation 1.24 yields:

$$\frac{\partial \varepsilon^2}{\partial \Phi_N} = -2|I(\boldsymbol{u})|^2 [1 - \Phi_N(\boldsymbol{u})] + 2|N(\boldsymbol{u})|^2 \Phi_N(\boldsymbol{u}) = 0. \tag{1.25}$$

Therefore, the filter $\Phi$ is:

$$\Phi_N(\boldsymbol{u}) = \frac{|I(\boldsymbol{u})|^2}{|I(\boldsymbol{u})|^2 + |N(\boldsymbol{u})|^2} = \frac{|I_N(\boldsymbol{u})|^2 - |N(\boldsymbol{u})|^2}{|I_N(\boldsymbol{u})|^2}. \tag{1.26}$$

The optimum filter does not present an explicit dependence of the smearing function. The function is real and even in both remains. This filter is applied to the restoration process in IMaX data (Chapter §2, Section 2.2.7).

### 1.3.5 General reduction and post-processing

The data reduction was performed with IDL (*Interactive Data Language*) and its package SolarSoftWare (SSW), which contains standard procedures for all the space missions (HINODE, SoHO, etc). For IMaX reduction data, no SolarSoftWare predesigned procedures were applied. Reduction were made with *ad hoc* procedures

described in Chapter §2, Section 2.2.7. For space missions, standard correction by subtraction of dark current, correction of imperfections and illumination gradients with flat-field images, and cosmic-ray despiking were made. For ground-based images, along with that, *destretching* is performed also, after the restoration process to avoid image deformation on different isoplanatic patches. the de-stretching algorithm was applied repeatedly in four subsequent steps, to completely eliminate residual effects (November, 1986). In every step, the size of the correlation tracking window was modified from greater to smaller sizes to ensure corrections at different spatial scales (Vargas Domínguez, 2009, PhD. thesis).

The main filtering performed in the data used on the HINODE, SST and IMaX data in this work (after the restoration in the last two cases) is subsonic filtering (Title et al., 1989). This filter acts as a p-mode filtering, setting all velocities larger than 4 $\mathrm{km\,s^{-1}}$ to zero. The wedge filter is actually a smooth wedge by apodization in the Fourier transformed space $k-\omega$ to avoid edge-effects on Fourier transforms on the limit of the wedge (Vargas Domínguez, 2009, PhD. thesis). This wedge presents a value on its generatrix of 4 $\mathrm{km\,s^{-1}}$ (cutoff velocity) and is designed not to affect any spatial scale of solar surface structures, such as small granules or large supergranules. The typical size of a granule is about 1000 km and its lifetime, 15 min approximately. This yields moderately high spatial (and time) frequencies. Supergranules have a size of around 35 000 km and their lifetime is around 1 day, so the spatial frequency is lower than the granular frequencies. These considerations make the p-mode filter more sophisticated than a mere pass-band filter. A sketch of this filter in the Fourier domain can be seen in Figure 1.9.

The effect of the p-modes is revealed as 'shadows' seen in filtergrams (G-band, Ca II, continuum, etc.) and also velocity maps. Although their peak-to-valley is a small fraction of the absolute value, they can affect different measures.

## 1.4 Spectropolarimetry

In this Section some considerations on polarimetry, instruments and inversion codes will be discussed. Since the one of the topics of this Thesis is the study of the magnetism in the photosphere, this Section provides the theoretical background to understand polarimetry and its applications to Solar Physics. The solar light coming from the photosphere is unpolarized. However, when magnetic fields come into play, symmetries are broken (i.e., the degeneracy of atomic levels) and polarization appears. The objective of this Section is to relate the magnetic fields and the polarized light via Zeeman effect, and how to guess the original magnetic field from the observed polarized light.

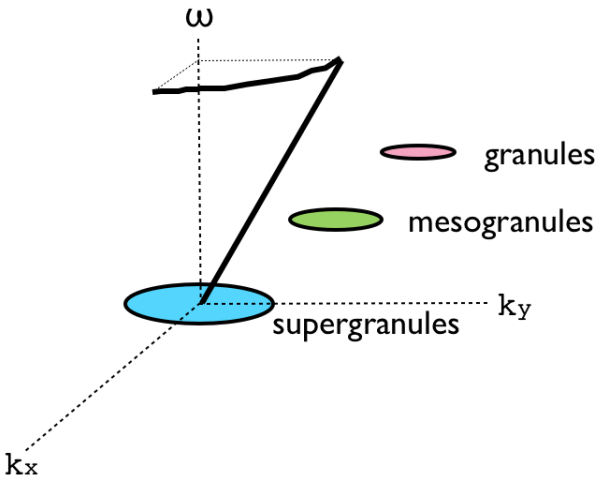


FIGURE 1.9— Wedge filter in the $k-\omega$ space for p-mode removal.

### 1.4.1 Basics of polarimetry

The principal optical elements involved in the treatment on the observed polarized light are presented here. Moreover, the physical mechanisms involved in the generation of magnetograms (as will appear in Chapter §2) and measurements of the magnetic field, as referred on Chapter §3 are also explained.

#### 1.4.1.1 Polarization optics

The electromagnetic field can be considered as linear superposition of monochromatic plane waves, creating a quasi-monochromatic beam of amplitude $\Delta\omega$. Consider a Cartesian coordinate system with directions $x, y$ and $z$ the propagation direction of a monochromatic, time-harmonic plane wave, since it comes from a very distant source:

$$\left.\begin{array}{c} E_x = a_x e^{i(kz-\omega t+\delta_x)} \\ E_y = a_y e^{i(kz-\omega t+\delta_y)} \\ E_z = 0 \end{array}\right\} \tag{1.27}$$

where $\omega$ stands for the frequency, $a_i$ for the wave amplitude, and $k$ is the wave number. Rearranging we arrive to the Equation 1.28, that yields the motion of the electric field on the plane perpendicular to the propagation direction (also called

the polarization ellipse):

$$\frac{E_x^2}{a_x^2} + \frac{E_y^2}{a_y^2} - 2\frac{E_x^2}{a_x^2}\frac{E_y^2}{a_y^2}\cos\delta = sin^2\delta, \tag{1.28}$$

where $\delta = \delta_x - \delta_y$, is called the *phase lag*.

This electric field describes an ellipse in a general case in the $XY$ plane. If the amplitudes in the two directions are identical and $\delta = \pm\pi/2$, a *circular polarized* wave is created. The sense is defined by the sign: if it is positive-signed, the wave is right-handed circularly polarized (symbolized with $\circlearrowright$); when negative, it is left-handed circularly polarized (as $\circlearrowleft$). When $\delta = 0$ or $\pi$, a linear polarized wave is produced (represented by an oriented symbol $\leftrightarrow$).

The optical devices designed to manipulate polarization are mainly divided into two categories, namely *polarizers* and *retarders*. An ideal linear polarizer (sometimes called analyser) is a device that transmits completely the electric vibration along a given axis (called the transmission or acceptance axis of the polarizer) and reflects or absorbs the electric vibration along the axis perpendicular to the former. An ideal retarder (sometimes called compensator) is characterized by the fact that the phase velocity of an electromagnetic wave propagating along the optical axis depends on the direction of the electric vibration. For an electric vibration parallel to the *fast axis*, the retarder is characterized by the index of refraction $n_f$, while for an electric vibration parallel to the slow axis the index of refraction is $n_s$, following the condition $n_s > n_f$. Depending on the retardance induced to the incident beam, retarders can be *quarter-wave plates* or $\lambda/4$-plates and *half-wave plates* or $\lambda/2$-plates. In the first case, the phase lag induced is $\pi/2$ and is indicated to change from linear to circular polarization and *vice versa*. In the second case, when using a *half-wave plates* or $\lambda/2$-plates, the sense of polarization is changed.

It is interesting to note that an ideal quarter-wave plate followed by an ideal linear polarizer whose transmission axis is directed at 45° from the *fast axis* in the counterclockwise direction (as seen by an observer facing the radiation source) behaves like an ideal filter that is totally transparent to positive (or right-handed) circular polarization and totally opaque to negative (or left-handed) circular polarization (Landi Degl'Inoccenti and Landolfi, 2005), as sketched in Figure 1.10. This optical setting is the basis to build magnetographs, as we will see later.

As a general case, we can consider a retarder with its *fast axis* located in the $X$ direction followed by a polarizer with the *optical transmission axis* rotated by an angle $\theta$. The electric field after passing the first element is the following, inducing a phase lag $\delta$ in the wave over the $Y$ component, it yields the Equation 1.29:

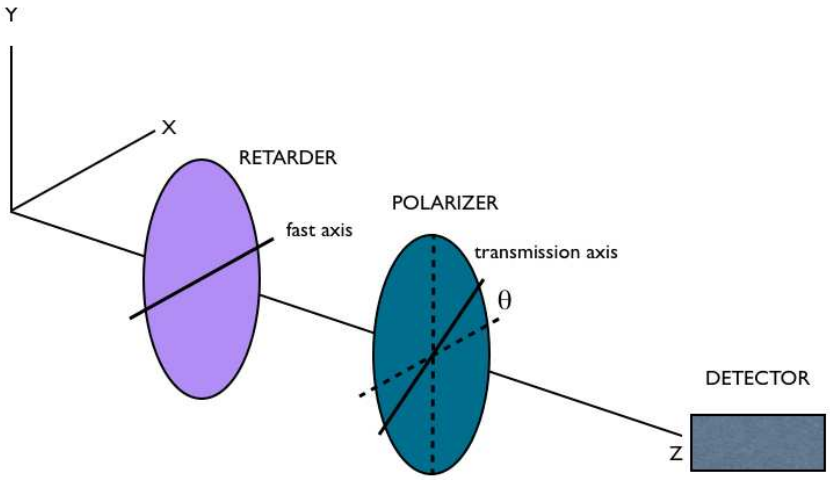


FIGURE 1.10— Sketch of a retarder-polarizer. When $\theta$= 45°, the left-circularly polarized light will be blocked, allowing to pass only the right-circularly polarized.

$$E'_x = E_x; \quad E'_y = E_y e^{i\delta} \tag{1.29}$$

At the end of this system, the amplitude of the electric vector will be:

$$E'_\theta = E_x \cos\theta + E_y \sin\theta e^{i\delta}. \tag{1.30}$$

Therefore, the intensity of the outgoing beam is:

$$\left.\begin{array}{c} I_{meas}(\theta,\delta) = \langle E_\theta E^*_\theta \rangle \\ I_{meas}(\theta,\delta) = \langle E_x E^*_x \cos^2\theta + E_y E^*_y \sin^2\theta + \\ \frac{1}{2} E_x E^*_y \sin 2\theta e^{-i\delta} + \frac{1}{2} E^*_x E_y \sin 2\theta e^{i\delta} \rangle \end{array}\right\} \tag{1.31}$$

Equation 1.31 contains all information needed to determine the polarization state of light uniquely, but cannot be directly employed. As a practical alternative for working with polarized light, Gabriel Stokes defined in 1852 the Stokes parameters $I, Q, U, V$ as a practical alternative for polarization work, because they are expressed in terms of total intensity (Equation 1.32). Symbols in the Equation regard to the polarization state and orientation, considering radiation facing the observer. In words, we can express the Stokes parameter $I$ as the total intensity; $Q$ as the

difference of horizontally and vertically linear polarized light; $U$ as the difference of intensity of linearly polarized light at 45° and the linear at -45°; and $V$ as the difference of right and left circular polarized light. In addition to this, if we rearrange the four terms appearing in Equation 1.31, we can get the four Stokes parameters as the combination of rotating plates (in Figure 1.10) (del Toro Iniesta, 2003), as shown on the right of the $\Rightarrow$ symbol.

$$\left.\begin{array}{c} I = \langle E_x^2 + E_y^2 \rangle = \updownarrow + \leftrightarrow \Rightarrow I_{meas}(0,0) + I_{meas}(\pi/2,0) \\ Q = \langle E_x^2 - E_y^2 \rangle = \updownarrow - \leftrightarrow \Rightarrow I_{meas}(0,0) - I_{meas}(\pi/2,0) \\ U = 2\langle E_x E_y \cos\phi \rangle = \nearrow - \nwarrow \Rightarrow I_{meas}(\pi/4,0) - I_{meas}(3\pi/4,0) \\ V = 2\langle E_x E_y \sin\phi \rangle = \circlearrowright - \circlearrowleft \Rightarrow I_{meas}(\pi/4,\pi/2) + I_{meas}(3\pi/4,\pi/2) \end{array}\right\} \quad (1.32)$$

The transformation matrix from one polarizing state of light – with the four Stokes parameters – to another is called *Mueller matrix*. The transformation of the intensity of the polarized light to the Stokes parameters is made via the modulation matrix. Finding the Stokes vector involves inverting the modulation matrix, that is called *demodulation*. Modulation can be performed spatially (using two detectors) or temporally, as achieved rotating the device or using electro-optical modulators, as liquid crystals, described below. The spatial modulation described above, simple in theory, becomes complicated by the fact of turning plates in the desired angles. Rotating plates in an effective and fast way is very complex mechanically. To overcome this issue, *liquid crystal variable retarders* (LCVRs) are used instead, which constitutes temporal modulation. Applying a voltage difference, these materials can generate a phase lag $\delta$ by aligning their molecules. Using them, we solve the mechanical problem of rotating, as the retardance becomes automated by a voltage power supply.

#### 1.4.1.2 The Zeeman effect

This effect was discovered in 1896 by the Dutch physicist Pieter Zeeman. From the observational point of view, is the splitting of a single spectral line into a group of lines when the gas producing a single line is subjected to a uniform magnetic field. The authors H. A. Lorentz and P. Zeeman explained it using the Lorentz model of the electron, involving the oscillator force and the Lorentz force. Let us consider the electron motion simplified to a linear oscillation in the $Z$ direction and a circular motion in the $XY$ plane. If an external magnetic field is applied in $Z$ direction, the Lorentz force, in turn balanced by the centripetal force, will act on the electron (Lorentz, 1910, and references therein). The anomalous Zeeman effect could not

be explained by this model; only the discovery of the electron's intrinsic spin led to a satisfactory explanation. According to the quantum theory, all spectral lines arise from electron transitions between different energy levels, with the frequency of the spectral line being proportional to the energy difference between the initial and final levels. Because of its intrinsic spin, the electron has a magnetic field associated with it. When an external magnetic field is applied, the electron's magnetic field may assume only certain alignments.

From the quantum theoretical framework, the approximation of $LS$ coupling is adopted as explanation of the Zeeman effect. $Russell - Saunders$ or $LS$ coupling is a simple coupling scheme because it allows one to use the same perturbation to the Hamiltonian as in an one-electron system. This approximation considers that the electrostatic interactions among the electrons are much more important than the spin-orbit interactions. It is valid for the range of magnetic fields found in the Sun. Thus, all the electronic orbital angular momenta $l_i$ couple to a total orbital angular momentum $L$, and the spin angular momenta $s_i$ couple to create the total angular momentum $S$. The total angular momentum is given by $\vec{\mathbf{J}} = \vec{\mathbf{L}} + \vec{\mathbf{S}}$. The projection of $M_J$ can range between $-j, -j+1 \ldots 0 \ldots j-1, j$. All the $(2j+1)$ states $M_J$ have the same energy in the absence of magnetic field. When a magnetic field $\vec{\mathbf{B}} \neq 0$ is present, $M_J$ is the projection of $J$ on the direction of the magnetic field and the degeneracy is broken. Under these conditions, the displacement of the line from the original position (by definition of Zeeman splitting) is:

$$\Delta\lambda_b = \lambda - \lambda_0 = \frac{e}{4\pi m_e c}\lambda_0^2 B(g_l M_l - g_u M_u), \tag{1.33}$$

with the well known constants $e$ as the electron charge, $m_e$ as the electron mass and $c$ as the speed of light. The Landé factors for the lower and upper transitions are represented by $g_l, g_u$; and $M_l, M_u$ are the corresponding quantum numbers.

The Landé factor is, basically, a constant that joins the magnetic moment of the electron with its angular momenta. The Landé factor plays a role on the line splitting: only the transitions with $g_L$ equal to unity lead to splitting into triplets, and this is considered the *normal* Zeeman effect. The *normal* Zeeman effect is actually the least common, as the *anomalous* effect is more frequent in different spectral lines. If the conditions mentioned before remain but a $g_L$ is different from unity, the splitting will be different, forming a multiplet. Also some cases of $pseudo - triplet$ can appear, if the total angular momentum have any value, but the $g_l = g_u = g$. Even some cases of $g_L < 0$ may appear, shifting the blue component to the red and the red component to the blue wing.

Also, since the solar lines are not Dirac's deltas but broad lines because of the observation, the components of a multiplet are usually not resolved. Anyway, it is not crucial for some cases: e. g., In the case of a weak field, a multiplet can be treated more easily as a triplet. To that end, an effective Landé factor, $g_{\rm eff}$, can be calculated from the weighted components of the multiplet. Analytically, it can be written as:

$$g_{\rm eff} = \frac{1}{2}(g_u + g_l) + \frac{1}{4}(g_u + g_l)\left[J_u(J_u+1) - J_l(J_l+1)\right]. \tag{1.34}$$

The combined effective Landé factor has a significant importance on the behaviour of the splitting: considering lines of different effective Landé factor, $g_{\rm eff}$, one larger than the other, the magnetic field saturates earlier in the one with a larger $g_{\rm eff}$. The magnetic field saturation happens for strong fields (>1000 G) and its consequence is that the Stokes $V$ lobes still separate but the amplitude does not increase.
Substituting the pertinent constants in Equation 1.33 we get:

$$\Delta\lambda = 4.7 \cdot 10^{-13} \lambda_0^2 g_{\rm eff} B. \tag{1.35}$$

This is the most often used formula for the Zeeman splitting, with $\lambda$ in Å, and $B$ in Gauss.

Let us consider a triplet. The three components can be described as follows: one corresponds to the $\Delta M_J = 0$ transition, or $\pi$ component, which is unshifted in wavelength. The other two correspond to the $\sigma$ components ($\Delta M_J = \pm 1$), which are shifted from the central position, one to the blue and the other to the red. It is produced between two levels of total angular momentum of 0 and 1.

The Zeeman components look different depending on the angle between the line-of-sight (hereafter, LOS) and the direction of the magnetic field. Let us consider the case of a magnetic field, parallel to the line of sight and perpendicular to the local surface, dependent of the heliocentric angle $\theta$, and a spectral line which will split forming a triplet. If the LOS is parallel to the field (the *longitudinal* Zeeman splitting, with $\theta$=0), only the $\sigma$ components, which have circular polarization of opposite sense, can be seen. With the LOS perpendicular to the magnetic field (*transverse* Zeeman effect, with with $\theta$=$\pi/2$), all three components can be detected: the $\pi$ component, linearly polarized parallel to the field, and the $\sigma$ components, linearly polarized perpendicular to the field. Generally, the magnetic field is oriented in-between these two extreme cases and the projection of the $\pi$ and $\sigma$ components along the LOS will be measurable as shown in Table 1.1 (del Toro Iniesta, 2003; Lorentz, 1910).

| Inclination | Blue component | Princ. component | Red component |
|---|---|---|---|
| $\theta$=0 | ↺ | | ↻ |
| $\theta$=$\pi/2$ | ↕ | ↔ | ↕ |

TABLE 1.1— States of polarization depending of the orientation of the source and the line-of-sight.

#### 1.4.1.3 Measurement techniques and instruments

This section is devoted to magnetograph fundaments. We describe the elements of some simple magnetographs. The most simple one probably is the photoelectric magnetograph that H. W. Babcock (Babcock and Babcock, 1952) developed in 1951, described as follows. This peculiar instrument retrieved 1-D magnetograms.

Two slits are placed in the red and blue wing of a chosen spectral line. The two longitudinal components of a line widened by Zeeman effect show circular polarization in opposite senses. If this circular polarized light crosses a rotating quarter-wave plate, these variations of signal in the two sensors (photomultipliers) behind the optical system can be amplified and recorded. By scanning the solar surface, we found a result of this instrument in Figure 1.11.

FIGURE 1.11— 1-D magnetogram made by Babcock, from the same website as Fig. 1.12.

With all these concepts on optical devices and polarization, a 2-D magnetograph can be devised; for instance, a simple one as in Leighton (1969). Figure 1.12 shows an sketch with the following components and some intermediate images. Let us suppose that we are observing two sunspots having opposite polarities, which emit right-circularly polarized light (↻) and left-circularly light (↺).

The circular polarized light from Zeeman splitting from the sunspot reaches to a $\lambda/4$-plate (L), that transforms it into linearly polarized light. The retarder is a quarter-wave plate ($\lambda/4$-plate), with the *fast axis* parallel to the $X$-axis, and its *slow* axis oriented in the $Y$-axis. This plate moves consecutively from the position sketched in 1.12 to a position where the *fast axis* is perpendicular to the former position. With a linear polarizer (P) acting as a analyser, maximum transmission is obtained and light goes out linearly polarized with an angle $\theta = \pi/4$, and intensity

equal to the incidental intensity. Turning the $\lambda/4$-plate, light becomes linearly polarized with an angle $\theta = -\pi/4$. Placing an slit (S), a line can be selected. Tuning on the blue and red wing in addition to subtract the first to the second image, is how a magnetograph image, called magnetogram, is created.

This simplified scheme is actually not used for achieving high polarimetric sensitivity, as it presents important drawbacks: the cross-talk is high; with this method, half of the photons are lost, and images are not acquired simultaneously. As we will see for IMaX, one of the most successful arrangement is the *dual-beam configuration*, which attenuates or eliminates these problems. Not only the optics (reflection in mirrors, stressed windows) can induce cross-talk and spurious signals, but also the atmosphere: one of the most significant sources of error in high-spatial-resolution ground-based solar polarimetry is noise caused by atmospheric *seeing*. Since *seeing* produces rapid image motion, blurring, and distortion, if the polarization modulation is slower than 1000 Hz, *seeing* causes false 'polarization signals'. Moreover, attaining high spectropolarimetric precision ($10^{-3}$ relative to the continuum intensity, $I_c$) at the telescope resolution demands integration times of at least several seconds to avoid noisy data (Ichimoto et al., 2008).

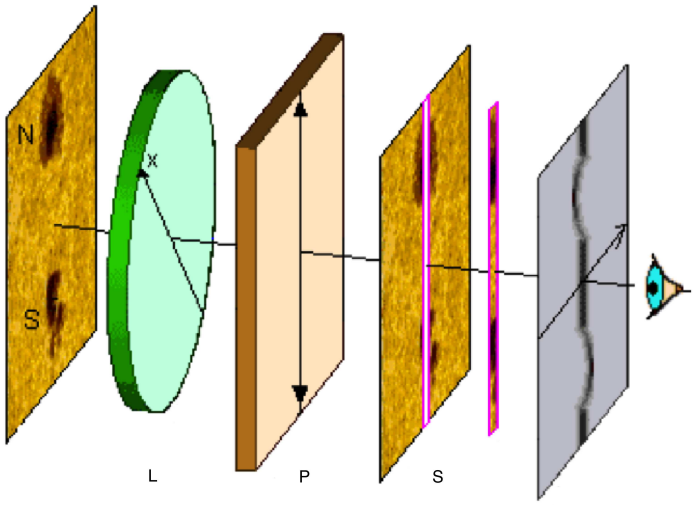


FIGURE 1.12— Scheme of a simple spectropolarimeter, from the website http://www.astrosurf.com/rondi/obs/shg/.

### 1.4.2 Retrieval of magnetic fields from observed polarization signals

Spectropolarimetric observations provide the spatially and spectrally resolved polarization state of the light in the form of $[I, Q, U, V]$. For polarization signals caused by the Zeeman effect, various methods can be used to derive the properties of the magnetic fields that have produced the polarization signal.

#### 1.4.2.1 Weak magnetic field approximation

The magnetic flux density[5] can be determined using the so-called *Weak field approximation* (Landi Degl'Innocenti, 1992; Landi Degl'Inoccenti and Landolfi, 2005). It is valid for weak fields ($<$ 600 G). This approximation is based on the assumption that the Doppler width of a line ($\Delta\lambda_D$) is larger than the Zeeman broadening, $\Delta\lambda_B$:

$$\Delta\lambda_B \lll \Delta\lambda_D = \frac{\lambda}{c}\sqrt{\frac{2kT}{m}}, \tag{1.36}$$

where $T$ is the temperature, $k$ is the Boltzmann constant and $m$ the mass of the particle, the atomic mass in this case. From the expansion in a Taylor series of the terms in the Radiative Transfer Equation (RTE) for polarized light, as explained also in Martínez González and Bellot Rubio (2009), we get

$$V(\lambda) = -\phi C \frac{\partial I(\lambda)}{\partial \lambda}, \tag{1.37}$$

where $\phi = fB\cos\gamma$ as the longitudinal magnetic flux density, $f$ is the filling factor, $\gamma$ is the inclination of the field with respect to the vertical, and $C = 4.6686 \cdot 10^{-13}\lambda_0^2 g_{\rm eff}$, with $\lambda_0$ expressed in Å. The longitudinal magnetic flux density $\phi$ has units of $Mx\ cm^{-2}$ or Gauss. The proportionality constant $C$ depends on the central wavelength $\lambda_0$ and the effective Landé factor of the transition, $g_{\rm eff}$.

The longitudinal magnetic flux density is obtained from a least-squares minimization:

$$\frac{\partial}{\partial\phi}\left[\sum_i \left(V_i + \phi C \frac{\partial I}{\partial \lambda_i}\right)^2\right] = 0, \tag{1.38}$$

[5] In this text and different works of Solar Physics, the magnetic field strength is used as an equivalent of the magnetic flux density.

This calculation is made for every pixel separately. The final result is:

$$\phi = -\frac{\sum_i \frac{\partial I}{\partial \lambda_i} V_i}{C \sum_i \left(\frac{\partial I}{\partial \lambda_i}\right)^2}. \tag{1.39}$$

#### 1.4.2.2 Centre-of-gravity method

The Centre-of-Gravity method (Semel, 1967; Rees and Semel, 1979) is used to estimate weak fields using only Stokes $I$ and $V$ profiles in the following way, calculating the differences of the centre-of-gravity position:

$$\lambda_{\pm} = \frac{\int [I_c - I_{\pm}(\lambda)]\, \lambda d\lambda}{\int [I_c - I_{\pm}(\lambda)]\, d\lambda}, \tag{1.40}$$

where $I_+ = \frac{1}{2} I_\lambda + V_\lambda$ and $I_- = \frac{1}{2} I_\lambda - V_\lambda$.
In its discrete form, it follows:

$$\lambda_{\pm} = \frac{\sum_i \lambda_i \left[1 - (I_i \pm V_i)/I_c\right]}{\sum_i \left[1 - (I_i \pm V_i)/I_c\right]}. \tag{1.41}$$

The proportionality law is given by:

$$B_{COG} = \alpha(\lambda_+ - \lambda_-) = 4.7 \cdot 10^{-13} \lambda_0^2 g_{\rm eff} B_{\rm eff}. \tag{1.42}$$

The constant $\alpha$ is different depending the spectral line, as it depends on $g_{\rm eff}$. For the 6301 Å, $\alpha$ is equal to 18 kG Å$^{-1}$; for the 6302 Å gets the value of 10.8 kG Å$^{-1}$ (Rees and Semel, 1979; Chae et al., 2007).

In this work we will also use a centroid method to obtain a central wavelength to calculate Dopplershifts, that is

$$\lambda_0 = \frac{\sum_i \lambda (1 - I/I_c) \Delta\lambda}{\sum_i (1 - I/I_c) \Delta\lambda} \tag{1.43}$$

This wavelength $\lambda_0$ is used to calculate Dopplershifts in Chapter §3.

$$v = \left(\frac{\lambda - \lambda_0}{\lambda_0}\right) c. \tag{1.44}$$

Defined in the astrophysical way, the movement of plasma going away from the observer is considered as redshifted. The sign, unless otherwise stated, is positive on downflows (going away) and negative in upflows.

#### 1.4.2.3 Inversion codes

The propagation of radiation through a medium is affected by absorption, emission and scattering processes. The fundamental quantity which describes a field of radiation is the spectral intensity, $I_\nu$. The spectral intensity experiences the emission (represented by $\epsilon$) and absorption ($\kappa$) processes along the beam path $s$, as written in Equation 1.45:

$$\mathrm{d}I_\nu = (\epsilon_\nu - \kappa_\nu I_\nu)\mathrm{d}s \tag{1.45}$$

Assuming that light passes by a plane-parallel stratified atmosphere, we can define the optical depth as:

$$\mathrm{d}\tau_\nu = -\kappa_\nu \mu \mathrm{d}s, \tag{1.46}$$

where $\mu$=cos $\theta$ is the heliocentric angle.
The radiative transfer theory describes these interactions mathematically by the Equation 1.47, known as RTE:

$$\mu \frac{\mathrm{d}I_\nu}{\mathrm{d}\tau_\nu} = I_\nu - \frac{\epsilon_\nu}{\kappa_\nu} = I_\nu - S_\nu, \tag{1.47}$$

with $S_\nu$ called the *source function*. When $S$ is known, the Equation 1.47 can be used to infer the emergent intensity $I_\nu$. This way of operating is the forward model: if we consider an atmosphere model and we know the source function $S$ and the properties of the medium, it is possible to know how the emergent intensity or the Stokes profiles are, in the case of a magnetized atmosphere. However, in observation, it is always the other way round: we just know the observed Stokes profiles and we have to guess the physical conditions of the medium and the magnetic field applied that can create the observed Stokes profiles. This is the *inverse* problem, and codes that solve it are named inversion codes.

The RTE (Eq. 1.47) in a magnetized atmosphere can be expressed now as:

$$\frac{\mathrm{d}\vec{I}(\tau_c)}{\mathrm{d}\tau_c} = \mathcal{K}(\tau_c)\left[\vec{I}(\tau_c) - \vec{S}(\tau_c)\right], \tag{1.48}$$

where $\tau_c$ represents the continuum optical depth at 5000 Å along the LOS, $\mathcal{K}$ is the total absorption matrix (a $4 \times 4$ matrix describing the absorption properties

of the atmosphere, including Zeeman effect). This matrix is important as it hosts three basic properties of the medium: absorption, dichroism and dispersion. The set of Stokes profiles is denoted by $\vec{I} = (I, Q, U, V)^\dagger$ and $\vec{S} = (S_I, S_Q, S_U, S_V)^\dagger$ the source function vector.
Since LTE conditions are assumed, the source function vector is given by $\vec{S} = (B_\nu[T], 0, 0, 0)^\dagger$, with $B_\nu[T]$ the Planck's function at the local temperature $T$.

Once $\mathcal{K}$ and $\vec{S}$ are computed, the Equation 1.48 can be solved. The RTE is integrated numerically for different wavelengths.

The integrand of the solution of the RTE is named Contribution Function:

$$C(\tau_c) = e^{-\int k(t)dt} k(\tau_c) S(\tau_c) \tag{1.49}$$

The Contribution Functions (CF) represent how much the different layers contribute to the observed spectrum. These functions are strongly dependent of the model atmosphere. We can take a first-order approximation of the CF: these linearized functions are called Response Functions. Response functions (RFs) $\mathbf{R}_x(\lambda, \tau)$ are computed for every optical depth and wavelength according to the Equation 1.50:

$$\mathbf{R}_x(\tau) = \mathcal{O}(0, \tau) \left\{ \mathcal{K}(\tau) \frac{\partial \vec{S}(\tau)}{\partial x} - \frac{\partial \mathcal{K}(\tau)}{\partial x} \left[ \vec{I}(\tau) - \vec{S}(\tau) \right] \right\},$$

where $\mathcal{O}(0, \tau)$ represents the evolution operator from $\tau$ to the surface. By definition, the modification of the emergent Stokes spectrum $\delta\mathbf{I}(\lambda)$ after perturbations $\delta x(\tau)$ of the atmospheric parameter $x$ at optical depth $\tau$ is given by:

$$\delta\mathbf{I}(\lambda) = \int_0^\infty \mathbf{R}_x(\lambda, \tau)\, \delta x(\tau)\, \mathrm{d}\tau. \tag{1.50}$$

Having a guess model atmosphere and the RTE, we can modify the atmosphere dependence between physical magnitudes provided by the CF until a set of Stokes profiles are created. When done so, the next step is to compare the artificial and the observed ones. The typical way is to minimize a merit function as the sum of differences squared between observed data and model predictions. The merit function in this case is $\chi^2$, and its mathematical definition is:

$$\chi^2 = \sum_i^m (y_i - Y_i)^2 \tag{1.51}$$

$$\chi^2(\mathbf{x}+\delta\mathbf{x}) \simeq \chi^2(\mathbf{x}) + \delta\mathbf{x}^T(\nabla\chi^2 + \mathbf{H}'\delta\mathbf{x}), \tag{1.52}$$

where $\mathbf{H}'$ is the Hessian matrix, containing the second order partial derivatives. If the second-order approximation is good enough and we are very near of the minimum of the merit function we can consider the Equation 1.52 to zero:

$$\nabla\chi^2 + \mathbf{H}'\delta\mathbf{x} = 0. \tag{1.53}$$

And the new $\mathbf{H}$ is the same $\mathbf{H}'$ for non-diagonal elements, and $H'_{ij}(1+\lambda)$ for the diagonal elements. $\lambda$ is the fudge factor.

However, if we are far from the minimum, it is better to consider stepping the function like this:

$$\delta\mathbf{x} = a\nabla\chi^2 \tag{1.54}$$

If the scaling factor is still too big, it can be divided by the fudge factor $\lambda$ and

$$\delta x_i = -\frac{1}{\lambda H'_{ii}}\nabla\chi^2 \tag{1.55}$$

All these elements are common to every inversion code: the RTE, the CF and the merit functions to minimize and helping to find the best solution. In this work, inversions have been performed, and the code used is LILIA. LILIA is the acronym for LTE Inversion based on the Lorien Iterative Algorithm, created by Socas Navarro Socas-Navarro (2001). Inspired by Ruiz Cobo and del Toro Iniesta (1992) and based on the concept of the SIR code, this code seeks for the model atmosphere which provides the best fit to the Stokes profiles. The underlying hypotheses are:

**1** Local Thermodynamic Equilibrium for the atomic level populations is assumed.

**2** No subpixel structure is taken into account.

**3** The observed Stokes profiles are induced by the Zeeman effect in transitions where L-S is a valid approximation (not extremely intense magnetic fields as in neutron stars, etc.)

**4** The hydrostatic equilibrium equation is used to calculate the gas pressure and the height scale in the atmosphere.

The code is written in Fortran90, but the output files are read and mapped in IDL. The necessary input settings are:

- Wavelength grid: for Hinode data inversion purposes, this grid has 112 points, from 6300.89 Å to 6303.28 Å, spaced on steps of 21.5 mÅ.

- Inputs of this inversion code are $[I, Q, U, V]$ in txt files, straylight files and $\mu$, and an atmosphere model (in this case, the Harvard-Smithsonian reference atmosphere, HRSA, Gingerich et al., 1971).

- Parameters of the atomic line to fit are used in a file. In this file, the central wavelength, the excitation potential of the lower level, ($\chi_l$), the Van der Waals damping factor and $log(gf)$ , logarithm of the oscillator strength $f$ with the statistical weight of the lower level $g$. Also the quantum numbers J, S, L for the transition are used.

- log$\tau$ is on the range [-6, 1.4]. Photospheric ranges are log$\tau$ = [-3, -1].

- Number of inversion iterations are set to 5 for every pixel. The derivatives of the profile with respect to the model parameters (response functions) are recomputed at each inversion iteration.

- The outputs of the program are the following 7 parameters depth-dependent of the model: temperature (K), electron pressure $P_e$ (in $dyn/cm^2$), microturbulence $v_{mic}$ (cm/s), magnetic field strength $|\mathbf{B}|$ (Gauss), line-of-sight-velocity $v_{LOS}$ (in cm/s), magnetic inclination $\gamma$ and azimuth $\phi$, both in degrees (°). Inclination is defined as the angle with respect to the solar surface, as $\mu$ was previously introduced for the inverted area. The depth-dependence is set by the nodes in the grid: 5 were set in temperature, 2 in velocity, 2 in magnetic field strength, 1 in inclination and azimuth, being the one of them in log$\tau$=-1.
- Also errors on these parameters are provided. Synthetic profiles appear in a different file, along with chi-square ($\chi^2$) of the fitting of the Stokes profiles with respect to the observed ones.To solve the inverse problem, singular value decomposition (SVD) for diagonalization of a quasi-singular matrix is applied (del Toro Iniesta, 2003). The minimization of $\chi^2$ is achieved by the Levenberg-Marquardt method aforementioned. $\chi^2$ should be always around 1 for a good fitting, since this merit function is normalized.

# 2

# Missions and data acquisition

This Chapter is focused on data acquisition, the missions used to achieve this purpose, data mining and data reduction, with special attention to the SUNRISE mission.

Fear of the Dark. (Iron Maiden,1992)

## 2.1 Ground-based telescopes

### 2.1.1 Swedish Solar Telescope

The Swedish Solar Telescope (SST, Scharmer et al., 2003a) is operated by the Institute for Solar Physics of the Royal Swedish Academy of Sciences and located at the Observatorio del Roque de los Muchachos of the Instituto de Astrofísica de Canarias (IAC) on the island of La Palma, Spain. The SST replaced the previous 50-cm Swedish Vacuum Solar Telescope (SVST). The clear aperture of the front lens of the SST has a diameter of just under 1 metre, becoming the largest optical solar telescope in Europe at this moment.[1] The resolution of this telescope is 0.″1, achieved with the use of adaptive optics, as described below. Modern solar telescopes cope with the atmospheric turbulence through two designs: open structures or vacuum telescopes/filled with helium. Vacuum telescopes cannot be built with very large apertures because such a design requires a vacuum window of extremely

[1] The telescope GREGOR, having a 1.5 m of aperture, is operated by KIS. Its first light is programmed at the end of 2011. The European Solar Telescope (EST), with an aperture of 4 metres, will open the way for the very large solar telescopes.

high optical quality. Obtaining such large windows is difficult because of the window thickness needed to cope with the enormous difference in pressure between the exposed surface to the atmosphere and inner face of the vacuum window has to be of about one tenth of the diameter (Stix, 2002). The practical limit for vacuum telescopes is probably a little over 1 metre in diameter, i.e., slightly larger than the SST. Stress on the glass leads to birefringence, which introduces spatial cross-talk between linear and circular polarization. Filling the telescope with helium instead of air, thanks to its larger thermal conductivity, reduces the effects of heat inside the telescope although not as much as by vacuum. While being filled avoids the large forces on vacuum windows, nevertheless it still requires an optical window of high quality but of a much smaller thickness than for a vacuum telescope.

The SST presents a corrector optical setup named Schupmann focus, which avoids chromatic aberration, astigmatism and favours the reduction of the stray-light. In this telescope, it consists of a 305 mm fused silica lens and a 300 mm Zerodur mirror. The field mirror deflects the beam upwards and away from the optical axis of the telescope. Light passing through and arriving to the optical bench is split by a dichroic beamsplitter (splitting at 500 nm approximately) in the so-called *Red Beam*, which feeds the spectropolarimeter SOUP (Solar Optical Universal Polarimeter) or CRISP (CRisp Imaging SpectroPolarimeter), and the *Blue Beam*, composed of a set of cameras and filters where the PD optical set is arranged to acquire images which will be restored afterwards.

The *Red Beam setup* comprises cameras and the instrument SOUP (Title et al., 1986), from the Lockheed Martin Laboratory (LMSAL). SOUP was a tunable polarization-interference monochromator Lyot filter which operated by rotating a set of linear polarizers and half-wave plates placed between calcite optics. Two bandpass modes, a broad one ($>$100 mÅ) and a narrow one ($<$100 mÅ) could be selected for any given line. The setup had two liquid crystal variable retarders (LCVRs) for measuring polarization states and generating magnetograms. This instrument was active until 2008.

For the season 2009 and 2010, the *Red Beam setup* was optimized for polarimetry with the new CRISP instrument. It consists of 0.3-0.9 nm wide prefilters, modulation with liquid crystals, a dual Fabry-Pérot tunable filter system, and a polarizing beam splitter located close to the final focal plane feeding two 1K$\times$1K Sarnoff CCD cameras with a spatial sampling of $0\farcs0651$ pixel$^{-1}$. The Fabry-Pérot system has a telecentric[2] optical design with a minimum number of optical surfaces and high transmission. About 10% of the light from the CRISP prefilter is directed

[2]The definition of telecentricity is explained in Section §2.2.5.2. An example of a telecentric setup is shown in Figure 2.14.

towards another Sarnoff camera used for broad-band context and the post-facto image restoration MOMFBD (Multi-Object Multi-Frame Blind Deconvolution).

The *Blue Beam* is based on four MegaPlus II 4020 2K×2K cameras. These cameras can collect about 8.5 frames per second. They are electronically shuttered and synchronized to allow co-processing of images from all cameras with MOMFBD image restoration methods. Two cameras are used for Phase Diversity of the same object, one in focus and another slightly defocused.

The typical filter selection intended for Ca II H/K observations is a broadband filter centered on the quasi-continuum between the K and H lines. One camera is used with a narrow band Ca II H wing filter, and another camera is used with a tunable Ca II H core filter. A G-band and a G-continuum filter can be placed as well in combination with some Ca II filter, depending on the campaign requisites.

The SST adaptive optics (Scharmer et al., 2003b) comprises the measurement of the wavefront perturbation, the extraction of a correlation signal from these measurements and the application of this signal to an active (tiltable or deformable) optical mirror, in order to compensate for the deformations of the wavefront. An important device in the SST is the Shack-Hartmann sensor. This is a type of wavefront sensor, commonly used in adaptive optics systems, optometry and metrology, and the most widespread used in adaptive optics. It consists of an array of 37 lenslets of the same focal length. Each of them is focused onto a part of the same CCD. If the wavefront were perfect, a pinhole image would be located in the same position for every lenslet image. On a real perturbed image, every pinhole image is shifted a different amount, and a local tilt is calculated. Any phase aberration can be approximated to a set of discrete tilts. By sampling an array of lenslets, all of these tilts can be measured and the whole wavefront approximated.

The wavefront is estimated with the Shack-Hartmann sensor, and a deformable mirror allows to correct the wavefront. The AO of the SST uses a deformable bimorph mirror with electrodes in the back side, allowing parts of the mirror to move and create the shape to counteract the distorted wavefront. The present 37-electrode deformable mirror was designed for correcting approximately the first 30 KL modes. A good match between the deformable mirror and the wavefront sensor allows straightforward and accurate calibration procedures. To measure the control matrix of the correlating wavefront sensor, a large pinhole for use with solar light is inserted at the primary focus, before the deformable mirror. With the bimorph mirror, for each of the 37 electrodes, a low-frequency sawtooth wave is introduced while the AO software determines all KL coefficients for each frame. KL functions are evaluated much better than Zernike coefficients for hexagonal sensors, due to the fact that the KL functions have smaller gradients close to the pupil perimeter

and that structures close to the perimeter extend further into the pupil area. For the same reason, bimorph mirrors can more easily produce KL than Zernike modes. In addition to that, this kind of mirrors can generate low-order aberrations with large amplitude, and high-order aberrations with smaller amplitude (Scharmer et al., 2003b).

The correlation tracker (CT) plays a role on reducing the image turbulent motion. This device employs a detector to get images separated in very short time intervals. Two consecutive images are shifted relative to each other until the maximum correlation is found through FFT cross-covariance. The shift is then interpreted as image motion and accordingly compensated in real time.

After collecting and pre-processing the data acquired at SST by means of dark current and flat-field correction, Multi-Object Multi-Frame Blind Deconvolution (MOMFBD) is applied. MOMFBD is an image restoration method by van Noort et al. (2005), based on the Multi-Frame Blind Deconvolution (MFBD) with Linear Equality Constraints (LECs) algorithm by Löfdahl (2002). For the season 2007 data, MOMFBD was applied in the reduction. Two objects are necessary for the MOMFBD restoration process: G-band, focused and defocused. In two channels, G-band ($\lambda$=430.56 nm and *FWHM*=1.3 nm) and its defocused pair generate images on the two Kodak Megaplus cameras 1.6 of 1536×1024. A third channel was employed on G-continuum ($\lambda$=436.3 nm and *FWHM*=1.1 nm) with the same chip size; and the fourth channel a Ca II H filter centered in $\lambda$=396.88 nm with a *FWHM* of 0.3 nm was placed. The plate scale was $0\farcs034$ pixel$^{-1}$ in the *Blue Beam*, with cameras of 2048×2048 pixels rendering an image size of $69'' \times 69''$.

## 2.2 Space missions

### 2.2.1 HINODE

FIGURE 2.1— Artistic view of the HINODE spacecraft.

The Solar-B satellite (renamed HINODE after its successful launch) was set on orbit on 2006, 22 September (Kosugi et al., 2007). HINODE is a Japanese mission developed and launched by ISAS/JAXA, collaborating with NAOJ as a domestic partner, NASA and STFC (UK) as international partners. The scientific operation of the HINODE mission is conducted by the HINODE science team organized at ISAS/JAXA. This team mainly consists of scientists from institutes in the partner countries. Support for the post-launch operation is provided by JAXA and NAOJ (Japan), STFC (UK),


FIGURE 2.2— MV2 rocket, similar to the MV7 model, where HINODE was launched.

NASA, ESA, and NSC (Norway).

This telescope was launched by the M-V Launch Vehicle number 7 (as in Figure 2.2). The circular polar orbit of Solar-B along with the contact with Svalbard ground station in Norway (ESA) allows downlink of data nearly every orbit; therefore, observations are possible 24 hours a day for about 8 months of the year. The orbit altitude is about 680 km, the inclination of the orbit is 98° and its period is 98 minutes. Data downloaded are available in the DARTS server, http://hinode.nao.ac.jp/hsc_e/darts_e.shtml.

HINODE is equipped with three telescopes: the Solar Optical Telescope (SOT), the EUV imaging spectrometer (EIS) and the X-ray telescope (XRT). EIS is briefly defined below, while SOT and XRT are described in Sections §2.2.1.1 and 2.2.1.4.

The Extreme-ultraviolet Imaging Spectrometer (EIS) is one of the three major scientific instruments of Solar-B. It utilizes an off-axis parabolic primary mirror and a toroidal diffraction grating in a normal incidence optical layout with high-reflectance Mo/Si multi-layer coatings. The multi-layer coatings have high reflectance in two wavelength ranges, 170-210 Å and 250-290 Å, and these wavelength ranges are simultaneously observed with two large back-illuminated CCDs. Many EUV events from the transition region, the corona, and flares display emission lines that can be studied with these two wavelength ranges, and observers can select an amount of spectral windows up to 25 in the imaging area of two CCDs. There is a slit/slot

exchanger that contains two narrow slits (1″ and 2″ width) and two wide slots (40″ and 266″ width).

#### 2.2.1.1 Solar Optical Telescope

The 50-cm diameter SOT (Tsuneta et al., 2008) can obtain continuous series of diffraction-limited images (0.″2-0.″3 or about 150 km on the surface of the Sun) in the 388-668 nm range. The images are acquired under very stable conditions (stability requirement $< 0.''09$) achieved by a combination of structural design and active image stabilization. The image stabilization system consists of a piezo-driven tip-tilt mirror in a closed-loop servo using a displacement error estimated from correlation tracking (CT) of solar granulation.

The Optical Telescope Assembly (OTA) consists of the primary mirror, secondary mirror, heat dump mirror, collimator lens unit, secondary field stop, tip-tilt fold mirror, and the polarization modulator. The optical telescope presents a Gregory configuration. The Focal Plane Package (FPP) includes the narrow-band (NFI) and broad-band (BFI) filtergraphs, plus the Stokes spectropolarimeter (SP). Some descriptions of the performance can be found in Suematsu et al. (2007). The CT is a high speed (580 Hz) CCD camera used to detect motions of the images in the focal plane by looking at the solar granulation pattern. The displacement of the live images with respect to the reference image, updated every 40 seconds, is computed, and the calculated displacement is fed to the closed loop controller.

The first subinstrument, BFI, holds a CCD of 4k×2k which yields $0.''0544$ pixel$^{-1}$, that subtends $224'' \times 111''$ with binning 1×1. It allows high cadence series, and six broadband filters are available (the corresponding filter *FWHM*s appear in brackets): the CN bandhead on 388.35 (0.7) nm, Ca II H on 396.85 (0.3) nm, CH I, whose bandhead corresponds to 430.50 nm (0.8), and blue, green, red continuum at 450.45, 555.05 and 668.40 nm with a *FWHM* of 0.4 nm for all three. Some of these filters and their corresponding spectral lines are presented in Figure 2.3, as the chromospheric Ca II H, and the photospheric bands CN and CH in black.

The NFI has a full field-of-view of $328'' \times 164''$, and with the same CCD size than BFI, the corresponding plate scale is $0.''08$ pixel$^{-1}$. Filters are tunable 0.6 nm to enable to get at least two positions inside a given spectral line (usually the red and blue wing of the line) to create longitudinal magnetograms. The filter wavelengths are the following: Mg I b (517.2 nm), Fe I (525.0 nm), Na I D (589.6 nm), a tunable one centered on 630.0 nm allowing Ti I (630.38), Fe I (630.15 and 630.25 nm) and H$\alpha$ (656.3 nm) observations. Fe I lines are used to construct photospheric magnetograms, and Mg I and Na I for low-chromospheric magnetograms and Dopplergrams. Only one spectral line can be used at a time in

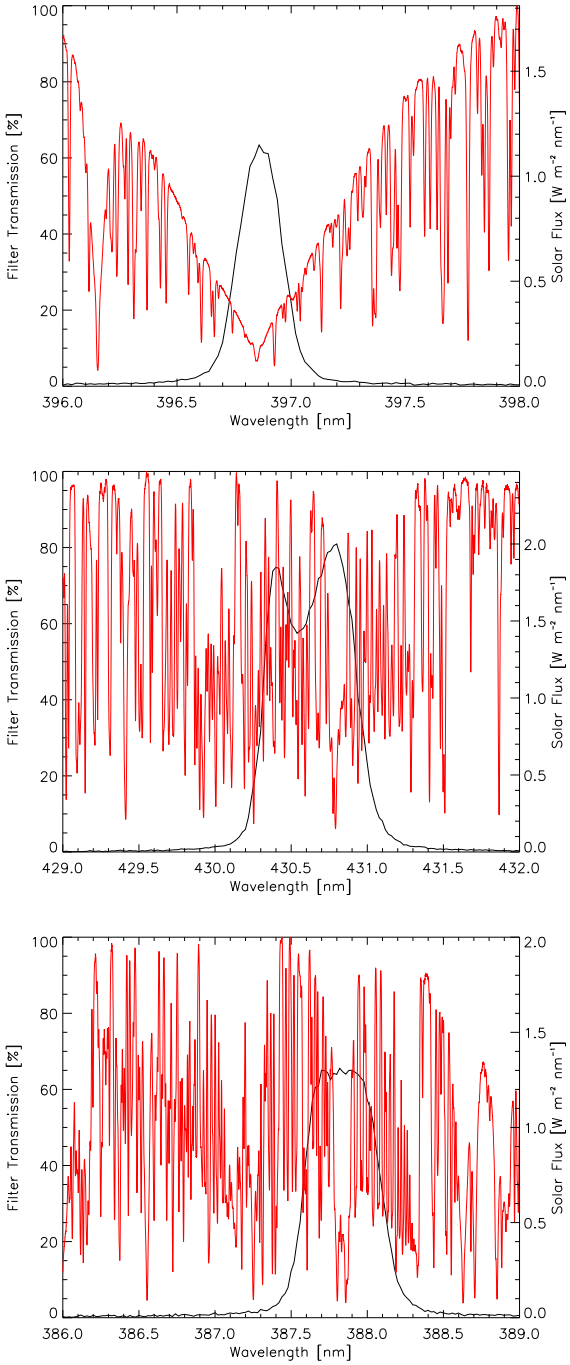


FIGURE 2.3— Transmission functions of HINODE BFI Ca II H, G-band and CN filters are depicted as black solid lines. Red lines mark the corresponding wavelengths of the spectral line/band along the wavelength filter range, whose scale is placed on the right side of the plot. Spectral data are taken from the Sacramento Peak atlas.

the NFI in an observing program. This is because frequent use of the tunable filter sometimes causes appearance of blemishes (bubbles) obscuring an image over part of the field of view.

#### 2.2.1.2 Filters and spectral lines of interest

Part of the SST and HINODE observation data are acquired with CN, G-band and Ca II filters. These filters produce high contrast images of the slender magnetic tubes, as explained in Section §1.2.2. The filter spectral ranges and the CN, G-band and Ca line are depicted in Figure 2.3. We would like to emphasize the importance of the filters used for studying small magnetic elements: the narrower the filter *FWHM* is, the higher the contrast may be (Uitenbroek and Tritschler, 2006, 2007).

#### 2.2.1.3 SOT-SP: Spectro-Polarimeter

The SpectroPolarimeter (SP, Ichimoto et al., 2008) obtains line profiles of the two magnetically sensitive lines at 630.15 and 630.25 nm, from the range 6300.89 to 6303.28 nm. The spectral sampling is 0.0215 mÅ pixel$^{-1}$ with 112 wavelength points, and the maximum spatial sampling is 0.″16 on both directions. The slit width is also 0.″16, and the maximum length of the slit projected on the sky is 164″. The Spectro-Polarimeter provides the line profiles in all Stokes parameters. For a typical exposure time, the sensitivity of the SP is 1-5 G in the longitudinal direction and 30-50 G in the transverse direction (Kosugi et al., 2007).

The SP has four modes of operation: Normal Map, Fast Map, Dynamics, and Deep Magnetogram. The Normal Map mode yields a polarimetric accuracy of $0.001 I_c$ with the spatial sampling mentioned of 0.″16 $\times$ 0.″16 (spending 4.8 s per slit position). The Fast Map mode of observation can provide scans every 3.6 s per slit position, with the same polarimetric accuracy but a spatial sampling of 0.″32, which is useful for studying dynamics of small magnetic features, but sacrificing spatial sampling. The Dynamics mode of observation provides higher cadence, of 1.6 s per slit position with 0.″16 sampling. Although at lower polarimetric accuracy, as its *signal-to-noise* ratio is lower than 600, this mode is useful to study highly dynamic small magnetic structures. In the Deep Magnetogram mode, photons may be accumulated over many rotations of the polarization modulator to achieve a better *signal-to-noise* ratio.

#### 2.2.1.4 X-Ray Telescope

An important issue in Physics is how to focus X-ray without letting them pass. The grazing incidence telescope are the most common ways of focusing X-ray photons.

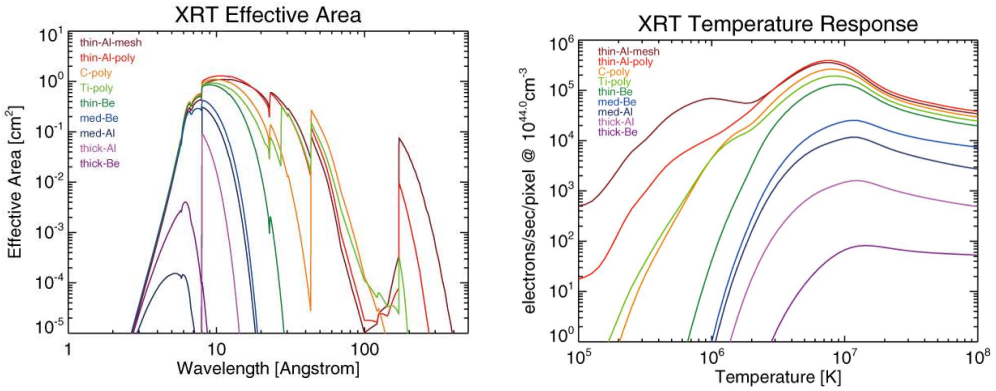


FIGURE 2.4— *Left*: The effective area for different filters (see legend) and their dependence on wavelength are shown in this panel. *Right*: XRT temperature response functions. From http://hinode.nao.ac.jp/index_e.shtml.

When a X-ray photon hits a surface in normal incidence, it crosses through it. However, in grazing incidence, photons can be focused varying the trajectory angle by grazing reflections, usually with parabolic or hyperbolic mirrors. With one mirror, the effective area is small, since only a narrow ring is the collecting area. To increase the area, the customary use is placing nested mirrors. Optimized Wolter-I-Schwarzschild grazing incidence optics is the telescope setting for XRT. The focal length of this telescope is close to 2 metres.

The XRT uses a back-illuminated three-phase CCD with 13.5 micron pixel-size and 2048×2048 array cooled to -43°C. If the spacecraft is pointed to the center of the solar disk, the largest field-of-view (2048×2048 pixel = 34'×34') can cover the full solar disk.

HINODE-XRT has a variety of filters available. The thin filters can saturate sometimes, so for the areas outside active regions, the choice of medium width filters is more adequate.

Some of the most used filters are C_poly (Carbon) and Medium_Be (Berilium), and their names stand for the optical coatings in each filter. The first one is intended to take images in a temperature response range $3\times10^5$-$10^7$ K, i.e. from the transition region to the corona, with a wavelength bandpass about 2-11 Å, while the second takes images in a temperature response range of $10^6$ -$10^7$ K with maximum transmission in $5\times10^6$ K and wavelength bandpass of 10-100 Å. The brightness ratio between two different filters provides a measure of the plasma temperature, considering it isothermal. The temperature response of the filters, along with the

effective area as function of the wavelength is displayed in Figure 2.4.

### 2.2.2 SUNRISE

#### 2.2.2.1 Mission concept

SUNRISE (Barthol et al., 2011; Solanki et al., 2010) was designed as a stratospheric balloon-borne solar observatory in the frame of NASA LDB (Long Duration Balloon) program. A zero pressure helium balloon with a volume of about 1 million cubic metres lifted a science payload of about 2 tons to an average altitude of 36000 m. This means above 99% of the Earth's atmosphere, where the wavefront distortions due to atmospheric turbulence are negligible. This provided *seeing*-free and continuous (without night interruptions) observation. In addition, the access to the UV window (not accessible on ground-based observatories due to atmospheric absorption), on the range of 200-300 nm, is an asset. Compared to space-borne missions the lower costs are also advantageous.

SUNRISE is a cooperative project of the Max Planck Institut für Sonnensystemforschung (MPS), Katlenburg-Lindau, with the Kiepenheuer Institut für Sonnenphysik (KIS), Freiburg, Germany, the High-Altitude Observatory (HAO), Boulder, USA, the Lockheed-Martin Solar and Astrophysics Lab. (LMSAL), Palo Alto, USA, and the spanish IMaX consortium comprising the Instituto de Astrofísica de Canarias (IAC), the Instituto de Astrofísica de Andalucía (IAA), the Instituto Nacional de Técnica Aeroespacial (INTA), and the Grupo de Astronomía y Ciencias del Espacio (GACE)[3]. The launching site of SUNRISE was located in Sweden and it was operated by NASA LDB at the Columbia Scientific Ballooning Facility (CSBF), Palestine, Texas, USA.

Solar mission balloons have been long used throughout the XX century. In the solar field, it started with the project *Stratoscope* (Schwarzschild, 1959), launched in 1957. It acquired white-light (545 nm) film photographs of granulation and sunspots with a 12-inches telescope. The flight lasted 4 hours. Some years later, the *Spektro-Stratoskop* (Mehltretter, 1976) took granulation images with a telescope of the same diameter. From 1966 to 1973, there were several flights of the *Soviet Stratospheric Solar Station*, carrying 50-cm and 1-m telescopes in different flights, taking filtergrams in the visible range (e.g., Krat et al., 1972). UV imaging was attempted in the range of 200-300 nm with a 20-cm telescope (among others, Samain and Lemaire, 1985). More recently, the *Flare Genesis* flew in 1996 and 2000, using an 80-cm telescope, providing magnetograms and Ca I 612.22 nm

[3]Currently it is part of the IPL (Image Processing Laboratory), University of Valencia, where the author developed her work.

filtergrams (Rust et al., 1996; Bernasconi et al., 2000).

The central scientific question that SUNRISE endeavoured to solve is the origin and properties of the magnetic structures. It also sought for answers of fundamental issues about how the magnetic flux appears and is removed from the surface and its relation with the solar dynamo, the relation of the magnetic flux and irradiance, and the heating of the upper solar layers. The technical requirements were to attain near diffraction-limited spatial resolution, on a sufficiently large field-of-view (FOV), over long uninterrupted periods and quasi-simultaneous in different heights in the solar atmosphere.

The SUNRISE telescope was a light-weight Gregory-type reflector with approximately 25 m effective focal length. A parabolic mirror (M1) of 1010 mm outer diameter and 1000 mm of clear aperture created a real image of the Sun in the first focus F1 of the telescope, 2423 mm in front of the M1 vertex. A field stop at F1 limited the telescope FOV so a small fraction reached the elliptical secondary mirror M2. M2 had a diameter of 245 mm and a focal length of 505 mm. M2 magnified the image in F1 by a factor of ten and refocused the light to a secondary telescope focus, located in the postfocus instrumentation package. Two plane fold mirrors M3 and M4 redirected the light: they helped in adjusting the incoming beam position (lateral position and focus), and beam direction (pupil position). Another field stop in the secondary focus limited the telescope FOV to 180″. The FOV of the instruments onboard SUNRISE were determined by different field stops and optical elements, therefore every science instrument had a different available FOV. More details about the optical setup of SUNRISE are offered in Barthol et al. (2011). All the relevant FOVs are sketched in Figure 2.5 over a MDI continuum image.[4]

The main mirror had a thickness of 178 mm and weighted about 47 kg. The rear side of the mirror presented three-fold symmetry with a triangular honeycomb structure. The mirror coating was 100 nm aluminum. Thermal studies were carried out to reduce deformations and provide the best wavefront error (WFE) at 22°5 elevation. Baffle blades cooled the mirror to the cold sky and against Earth's IR radiation.The front ring of the frame carried the secondary mirror and the heat rejection wedge (HRW). The HRW was an important piece since it received 1 kW, which was concentrated in F1 over 22 mm, rejecting 99% of the incoming radiation and conducting to two radiators, connected by ammonia pipes. Also the fine guiding sensor LISS (Lockheed Intermediate Sun Sensor) as pointing reference in flight was located on that ring. On its rear side, the tertiary plane folding mirror was placed.

[4]MDI operations concluded while writing this text, on April 12, 2011.

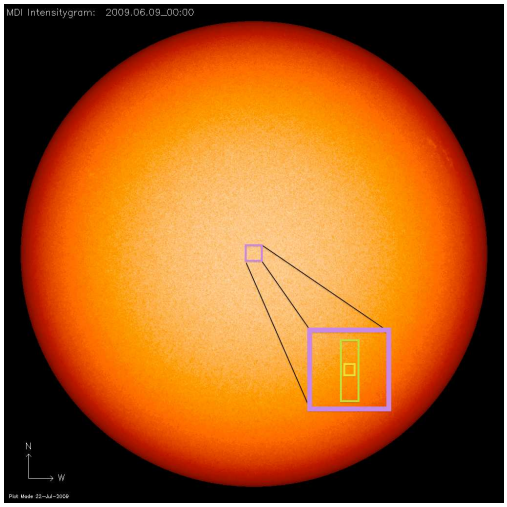


FIGURE 2.5— Sketch of the SUNRISE FOV depicted over a SoHO/MDI image. Purple centered square indicates the $50'' \times 50''$ IMaX FOV in scale. The larger purple box shows the same field with the scaled FOV of SuFI in green, and the scaled FOV of the CWS in yellow.

The secondary mirror, polished to a residual WFE of 6 nm, was isostatically mounted on bipods and attached to a three-axis stage. Focusing the entire postfocus assembly was done by moving the secondary mirror, located in F2. A 2.8 mm aperture and an slightly undersized stop in the conjugate image plane in F2 defined the usable telescope FOV, that was $180''$. Both M1 and M2 had a constant focus ratio even under thermal loads and telescope elevation, thanks to a Serrurier arrangement. The design was created in 1935 by Mark Serrurier when he was working on the 5-metre Hale telescope at Mt. Palomar. This design solved the problem of truss flexing by supporting the primary objective mirror and the secondary mirror by two sets of opposing trusses before and after the declination pivot. The trusses, in this case, were designed to have an equal amount of flexure, which allowed the optics to stay on a common optical axis. When flexing the top truss resisted tension and the bottom truss resisted compression, the optical elements are kept parallel to each other. The net result was that all of the optical elements stay in collimation regardless of the orientation of the telescope.

The PFI – postfocus instrumentation – included the intermediate instruments ISLiD and CWS, and the science instruments: the ultraviolet imager SuFI and the magnetograph IMaX. They are described in more detail in Sections §2.2.4 and §2.2.5, respectively.

The ISLiD, Image stabilization and Light Distribution System, was a panchromatic imager based on dichroic beamsplitter, diverting the different wavelength bands to the science instruments, maximizing the photon flux and preserving the polarization (designed to get minimum linear polarization at 525 and 854 nm), plate scale and pupil position. ISLiD was located in the center of the PFI and it covered its whole length. It also contained a tip-tilt mirror formed by a fast piezoelectric piece at a pupil plane of the optical system. A field stop in the telescope secondary focus projected the aperture stop of the primary mirror to the tip-tilt mirror. Reimaging (magnifying) of the secondary focus onto the instrument detectors was achieved by a two mirror Schwarzschild arrangement (this scheme will be explained in Section §2.2.4), before separating the UV range towards SuFI. ISLiD also contained the F2 calibration unit, which was a motorized filter with three positions: open, closed for dark calibration and a pinhole, used to control the relative alignment of the science instrument fields, and for CWS calibration.

The Correlating Wavefront Sensor, CWS, (Berkefeld et al., 2011; Schmidt et al., 2004), was located close to ISLiD in the central compartment of the PFI, in a non-pressurized chamber. This instrument was used for precision image stabilization (high frequency) and to control the telescope alignment (low frequency). The conceptual design was similar to the CWS of KAOS at the VTT, Tenerife. The components of the CWS were the Shack-Hartmann wavefront sensor, a high-speed camera, the control loop computer that converted the shifts measured with the wavefront sensor into actuator signals, the fast tip-tilt mirror and the slow secondary mirror M2. The Shack-Hartmann was composed of a 7-lenslet array in a pupil plane: 6 subapertures arranged in a ring, which formed 6 independent images on the detector, and the central lenslet produced an image of the secondary mirror. The Shack-Hartmann sensor carried out its own reduction process, such as dark and flat-field correction, intensity gradients removal, pinholes etc. to achieve the best performance. All the information derived from these six independent images was used to retrieve the coefficients of the Zernike polynomials of the wavefront error up to the third radial degree. The coefficients of tip, tilt, defocus and Seidel coma were used as error signals. A high speed camera with FOV of $12'' \times 12''$ and fast readout ($>$ 1 kHz) allowed detecting correlated images. The bandwidth of the closed loop was about 60 Hz with a correlation noise variance around $0\farcs003$. Undamped frequencies above 30 Hz could propagate from the gondola to the telescope, preventing from having a sensitivity better than $0\farcs002$. The non-optical components, as the gondola and the central structure were essential pieces of SUNRISE. The central frame was the main structure and carried the PFI on its top. The alignment between instruments had to be kept better than $\pm$ 0.1mm, with an angular

alignment of 3 arcmin in all directions. The PFI box was 1.4 metre wide and 2 metres long. The height of 350 mm is a trade-off between keeping the PFI center of gravity as low as possible and taking advantage of bending with height. This structure was made of honeycomb aluminum core with carbon fibers. One of the thermal requirements was to keep the temperature at 20$\pm$10°C along its 2 metres length. The gondola structure consisted of an aluminum/steel tube framework, relatively light but with the required stiffness and sufficiently high eigenfrequency ($>$10 Hz). As rigid body motion occurs when the lowest eigenfrequency of the moving parts is considerably higher than the excitation frequencies, the elevation and azimuth drives operated below 10 Hz and the gondola has been designed to achieve a minimum eigenfrequency of 15 Hz. The structure permitted an elevation of -5° to 50°, and also could be split in two halves for integration. Two ballast hoppers at the center of the gondola bottom carried 650 kg of steel grains, partly for compensating altitude losses due to night and day temperature differences. Shock absorbing cardboard crash pads reduced mechanical loads during touchdown and landing. A parachute of nearly 50 metres span was attached for this final moment. The balloon was made of polyethylene film filled with helium, weighting 2 tons and 0.5 ton, respectively. In total, a weight of nearly 6 tons flew away on SUNRISE.

Electrical power was provided by two solar photovoltaic arrays, generating 1.3 kW in total. These panels could reach 100°C on the surface, therefore they had to be placed far away to avoid generating thermal turbulence. The azimuthal control of the gondola was performed by a coarse azimuth drive, that decoupled the instrument from the rotating balloon, while the fine drive rotated a momentum wheel. The solar pointing was acquired by cells with a wide-field acceptance at the four corners of the gondola. Then mid range sensors with a field-of-view of $\pm$15° started operating. When pointing was achieved to an accuracy of 2°, LISS started functioning.

On the rear side of the gondola, shaded by the solar panels from direct illumination, the instrument control electronics was located. The largest part of SUNRISE electronics was located in two racks mounted left and right of the gondola structure. Only proximity electronics, such as the power supply of the tip-tilt mirror and mechanism controllers were located inside the PFI. These mentioned racks were inclined with respect to the structure in order to minimize radiative input from the Earth and the hot solar panels. The two data storage containers were located inside one of the upper side trusses of the core framework, spring-based protected for shocks. The truss framework provided protection and accessibility for recovery after landing. Data were stored in two racks with 24 disks of 100 Gb each.

The basic electronics architecture was the Instrument Control System (ICS)

FIGURE 2.6— The integration and final testing site was performed in the largest shed of the space facilities in Kiruna, shown here.

consisting of the Instrument Control Unit (ICU), the Data Storage Subsystems (DSS1 and DSS2), the PFI, the gondola Power Distribution Units, and the Line-of-Sight telemetry system.

The first plan was to launch SUNRISE from the base at Williams Field near McMurdo, Antarctica. As the decision of the trajectory to follow was changed to the Arctic Circle, NASA cooperated with the space facilities at ESRANGE, Kiruna, Sweden. The assembly and final tests were performed in these space facilities. The main hangar was used as integration and testing site, as shown in Figure 2.6.

### 2.2.3 SUNRISE flight

The first light was on April 30, 2009. The main task was checking the heat rejection wedge, the pointing under wind gusts and image stabilization. The SUNRISE flight window was opened on 2009, June 8. SUNRISE was successfully launched from ESRANGE (67.°89N, 21.°10E) near Kiruna, Sweden, on 2009, June 8 at 6:27 UT. It reached its float altitude of 37200 m after three hours. During the ascent, the instrument was in rotary mode to allow a constant heating for crossing the tropopause. This area is usually colder and the balloon pressure decreased, so the instrument lost altitude. An early failure of the 2 Mb/s LOS telemetry did prevent a full commissioning, then a link of 6 kb/s was used instead. The balloon flight followed the zonal wind system with a constant speed of 30 km/h on the Norwegian coastline to reach Greenland and Northern Canada on 2009, June 13. Somerset island was the landing spot after 137 hours. The trajectory is displayed as a red track in Figure 2.7. The primary mirror was found intact, so did most parts of IMaX (Barthol et al., 2011).

The disks storing data were recovered, and the data volume was about 415 Gb acquired by IMaX ($5\times10^5$ images) and 790 Gb recorded by SuFI ($1.5\times10^5$ images). The 37% of the SuFI images were acquired while the CWS control loop was closed. The 28% of these closed-loop images were collected near or at the limb ($\mu < 0.5$).

The total observation time was 130 hours. During 23% of the total time at float altitude the CWS loop was closed. Continuous time series longer than 1 min during 22% and time series longer than 10 min during 10% of the total observation time were acquired. The longest time series was 34 min, 19 min for the SuFI mode that included the shortest wavelength of 214 nm. This wavelength is by far the most sensitive to the air-mass along the LOS and was only observed around local noon (Solanki et al., 2010).

To complement the SUNRISE mission, coordinated ground and space-based observations were done with the SUMER instrument onboard SoHO (Solar Heliospheric Observatory, Domingo et al., 1995), also MDI (Scherrer et al., 1995) and HINODE. Ground-based observations were obtained by the Swedish Solar Telescope (SST) at la Palma, the Vacuum Tower Telescope (VTT) in Tenerife, the IRSOL facility in Locarno (Switzerland) and the Dunn Solar Telescope on Sacramento Peak, New Mexico, USA.

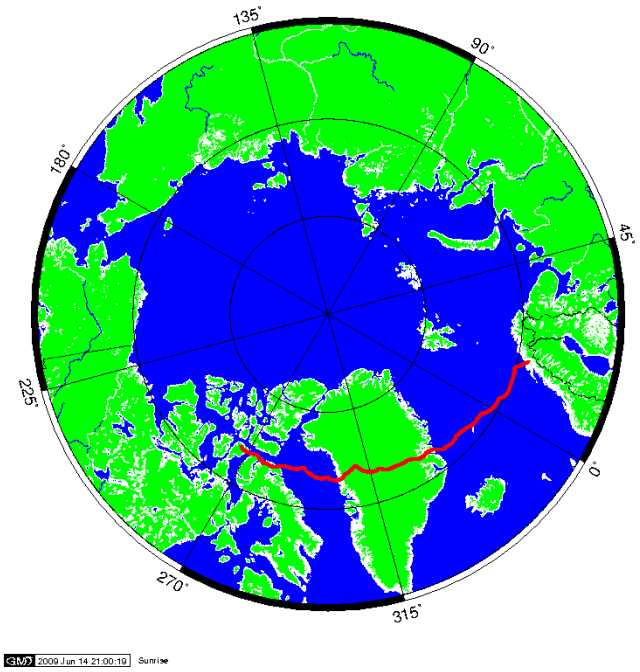


FIGURE 2.7— SUNRISE trajectory over the Arctic Circle, from http://www.iac.es/proyecto/IMaX/.

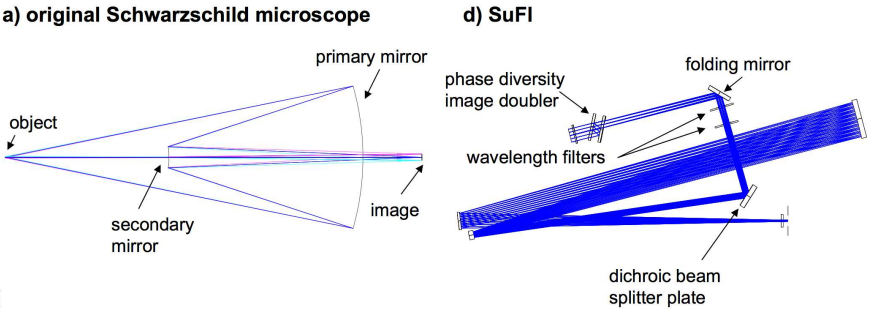


FIGURE 2.8— Schwarzschild microscope optical setup, from *Gandorfer et al. (2011)*.

### 2.2.4 SuFI/SUNRISE

SuFI – SUNRISE Filter Imager – (Gandorfer et al., 2011) provided high-resolution images of photospheric and chromospheric layers in the 5 wavelengths bands in visible and near UV. The optical arrangement was a Schwarzschild 2-mirror system – as a part of ISLiD – magnifying the telescope secondary focus by a factor of 5 onto the detector, resulting in an effective focal length of 121 m. The cameras were 2k×2k UV fast read-out CCD. The FOV was $15'' \times 40''$. Interference filters were used to isolate the wavelength bands of interest. They had transmission peaks at 214 (10) and 300 (5) nm together with OH and CN bands at 312 (1.2) and 388 (0.8) nm, and Ca II H line at 397.6 (0.18) nm, with brackets denoting their respective *FWHM*. The shorter wavelengths reached an angular resolution of $0''.05$, corresponding to 35 km on the Sun's surface.

One of the technical requirements of SUNRISE was that each instrument had to operate at their own resolution limit, and considering that SuFI operated on the shortest wavelengths, its science focus needed a 5 times larger plate scale than the telescope exit focus (allowing 3 pixel oversampling of the point spread function (PSF at 214 nm) so a magnification of 5 was required from F2 to SuFI focus.

SuFI's magnification was performed by a field lens near the telescope focus, which creates an image of the telescope aperture onto a folding mirror, where light was sent to the tip-tilt mirror afterwards. The original exit FOV of $180''$ had to be cut off to $20'' \times 40''$ by the CWS, therefore it presented an effective F-number of 121, larger than the telescope focus exit F-number of 24.2. For this kind of apertures, an off-axis scheme can be used, eliminating the central obscuration.

The Schwarzschild arrangement is common in UV microscopy. They can have large numerical apertures and cover a large FOV also. In SUFI, it had an achromatic field lens assembly in the focus of the Schwarzschild microscope. This lens

formed a real image of the instrument pupil. A second lens assembly reimaged the Schwarzschild focus with the required image plate (demagnification of about 5), creating a pupil at infinity.

The filters of SuFI were doubled. As light intensity decreases strongly towards shorter wavelengths, in the case of UV wavelength, two filters were necessary to suppress the unwanted contributions from longer wavelengths. So every selected wavelength used a two wheel filter, aligned and triggered properly. The exception was the Ca II H filter, because of straylight reasons, just had one. All filters were tilted by 0°5 to avoid ghost images. Filter wheels were mounted in two separate mounts with different rotation sense to avoid torque production.

The PD capability of SuFI was different from IMaX. As explained in Section §1.3.3, two images of the same object are acquired simultaneously at two different focus positions (one is in focus and the second defocused to create a new wavefront curvature of half a wave). From these two measurements, the object and the aberrations can be retrieved. This method was useful to correct for residual aberrations due to the thermoelastic deformations of the telescope during flight. The capability consisted of a PD image doubler: two plane-parallel plates in front of the focal plane, with a field stop on its front. The second plate was coated on half its surface with a 50/50 beamsplitter coating that transmitted half of the incoming light and reflected the other half. This arrangement produced one image that had crossed both glass plates without any reflection, and the other image had undergone two additional reflections: one at the beamsplitter plate, and the other at the back side of the first plate. The path difference was 28.15 mm.

The science camera was a PixelVision BioXight BV20CCD fulfilling the requirements of fast readout, being sensitive down to 210 nm, and a large area, 2048×2048 in this case. The frame rate was 2.64 frames per second. The camera head was cooled down with methanol heat pipes connected to the warm side of a Peltier element. The camera electronics was housed in a pressure vessel.

The observation modes were different depending which wavelength was used. For the shortest wavelength of 214 nm the observation should start when the Sun elevation was larger than 30 degrees, and the balloon altitude, more than 36 km. The exposure time could be modified from 1 second, the fastest, up to 40 seconds. However, in the shortest channel, exposure times resulted larger than calculated, due to the strong residual ozone extinction.

| SPECIFICATIONS | |
|---|---|
| SUNRISE aperture | 1 m |
| SUNRISE effective focal length | 45.00 m |
| **IMaX** | |
| Pixel size | 12 $\mu$m |
| Pixels | 1024 $\times$ 1024 |
| FOV | 50″$\times$50″ |
| Spatial sampling | 0.055 arcsec pixel$^{-1}$ |
| Working wavelength $\lambda$ | 525.02 nm (Fe I) |
| Spectral resolution $\delta\lambda$ | 65 mÅ (85 mÅ gaussian) |
| Wavelength drift over FOV | 28 mÅ |
| Lateral magnification | 1.8 |
| Image exposure time | 246 ms |
| $(S/N)_i$ (photon noise) | 850-1000 (5 G $B_L$, 80 G $B_T$) |
| IMaX weight | 75 kg |
| IMaX data rate | 996 kB s$^{-1}$ |

TABLE 2.1— Main IMaX specifications.

### 2.2.5 IMaX/SUNRISE

#### 2.2.5.1 Introduction

The instrument IMaX, Imaging Magnetograph eXperiment, (Martínez Pillet et al., 2011; Martínez Pillet et al., 2004) was devised to attain the maximum spatial and spectral resolution. Some of the basic design requirements were reaching a minimum of *signal-to-noise ratio* $S/N$ of about 1000, polarization sensitivity of 0.001 with respect to the continuum of Stokes $I$ ($10^{-3}I_c$), presenting a fast temporal polarization modulation. The spatial resolution was 0.″15-0.″18. The Fe I spectral line 5250.2 Å was selected (with a Landé factor $g$=3 and ionization energy $\chi_i$ equal to 0.121 eV). This instrument was entirely constructed by the IMaX consortium, presented in Section §2.2.2.1. The most relevant properties of this instrument are summarised in Table 2.1.

#### 2.2.5.2 IMaX optical setup

The optical setup can be found in Figure 2.9 and a photograph of the whole system in Figure 2.10. The optical path description is hereunder: F4 is the IMaX and SuFI light entrance from the SUNRISE optical system. Light passed through

the prefilter, crossed the modulation setup (liquid crystals) and a light baffle to avoid parasitic light. Then it entered the etalon, where wavelengths were selected. It turned back through the etalon (in a different position), fell onto a third mirror which deviated the light to the polarizing beamsplitter, which divided the beam to the two cameras. All the optical elements cited here are described below.

The prefilter presented a broad bandpass (1 Å), which permitted preselecting the IMaX spectral range. Other characteristics were a high transmission and wide acceptance angle, which provided maximum transmission at $2^{\circ}1$. The double cavity was designed to have a rapid attenuation of the prefilter transmission wings and almost eliminated the unwanted orders of the etalon placed behind the prefilter. The prefilter curve is slightly asymmetric, as it is shown in Figures 2.11 and 2.12. In the red wing side, the transmission is lower than 1% and in the blue-wing side shows an extended wing which includes the secondary etalon peak.

After passing through the prefilter which also protected the system from any residual UV light that could not be sent to SuFI, light travelled through the two LCVRs. Light reached the collimated lenses and made the first pass through the $LiNbO_3$ etalon. The enclosure windows of the etalon were made of fused silica, which provided optical thermal stability under temperature changes and low stress birefringence. Two 45° incidence folding mirrors turned the light backwards to enter again the etalon in a different point from the first pass through it. After leaving the etalon enclosure, light passed through the camera lenses and reached the cameras. The prefilter and the LCVRs shared the same mounting, and the folding mirrors were placed in another mounting. These two housings were thermally controlled.

The LCVRs and retarders were previously introduced on Chapter §1, Section §1.4.1. These liquid crystal variable retarders used voltages in the range of 10 V. However, not only voltage can induce retardance on these devices, but also temperature changes. The phase retardance dependence with temperature for IMaX went as in Equation 2.1 (Heredero et al., 2007),

$$\frac{\Delta\delta}{\Delta T} = -1.16 + 0.305V - 0.02V \text{ for } V < 8. \tag{2.1}$$

The voltages used in IMaX were therefore adjusted according to the expected temperature range during the flight.

An etalon, acting as a wavelength fine selector on IMaX, is considered as a plane-parallel plate with refractive index $n$ and thickness $\ell$. The physical fundaments of an etalon or Fabry-Pérot interferometer (FPI) are explained below. An incident beam at angle $\Theta$ is refracted at an angle $\Theta_1$ and then reflected between the two parallel surfaces with reflectance $R$. On each reflection, a fraction $T$ of the

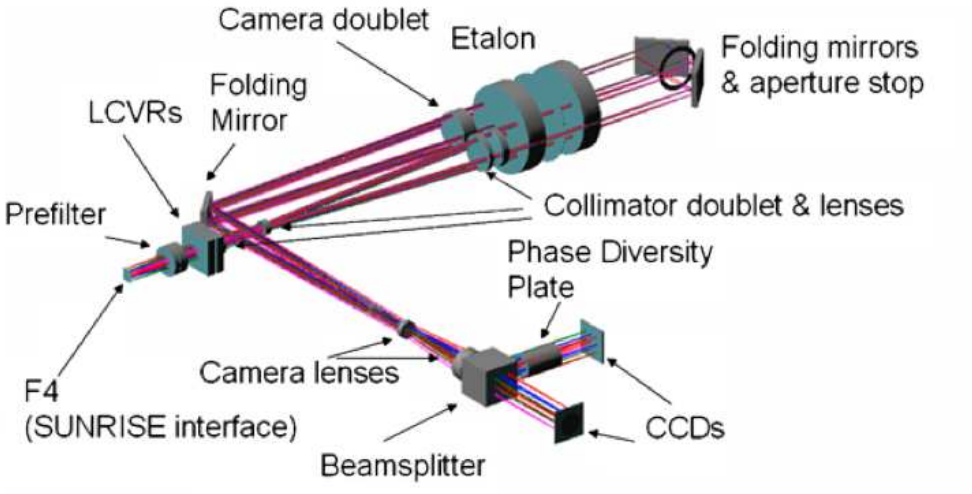


FIGURE 2.9— IMaX optical setup diagram, from *Martínez Pillet et al. (2011)*.

intensity is transmitted; the transmitted fraction interferes with the outgoing beam. Constructive interference occurs if the transmitted beams are in phase, and this corresponds to a high-transmission peak of the etalon. If the transmitted beams are out-of-phase, destructive interference occurs and it corresponds to a transmission minimum. Whether the multiply-reflected beams are in-phase or not depends on the wavelength ($\lambda$) of the light, the angle of incidence ($\Theta$), the thickness of the etalon ($\ell$) and the refractive index of the material between the reflecting surfaces ($n$). This process is depicted in Figure 2.13. The phase difference between each subsequent reflection is given by $\delta$ in Equation 2.2:

$$\delta = \left(\frac{2\pi}{\lambda}\right) 2n\ell\cos\Theta. \tag{2.2}$$

The interference condition for maximum transmission of an etalon is:

$$m\lambda = 2n\ell\cos\Theta, \tag{2.3}$$

where $m$ is the interference order.

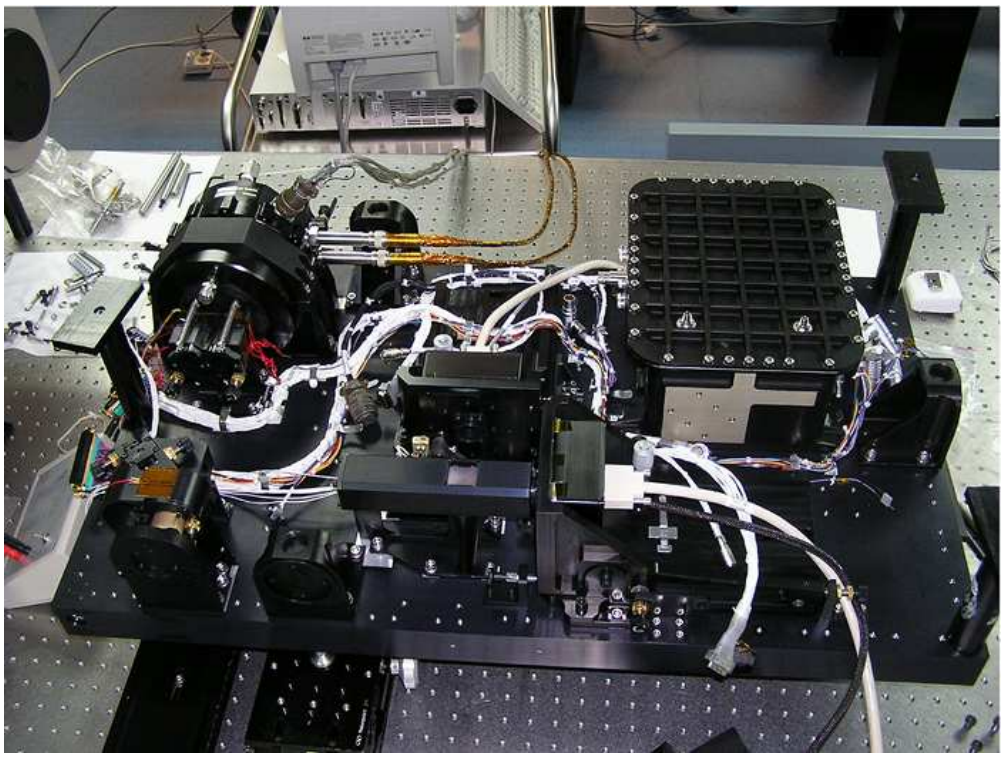

FIGURE 2.10— Setup of IMaX. Light entered the system through the prefilter, located in the lower-left part of the image. The black aluminum box was the enclosure that holds the electronics and the high voltage power supply. Courtesy of the *IMaX team*.

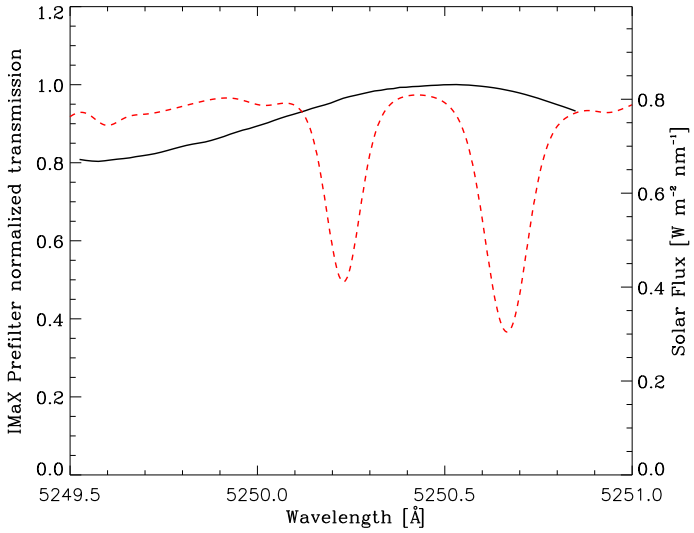


FIGURE 2.11— IMaX prefilter (solid line) and dashed red lines of Fe I of 5250.225 Å and 5250.5 Å, from the Fourier Transform Spectrometer (FTS) atlas (Brault & Neckel, 1987; Brault and Neckel, 1999).

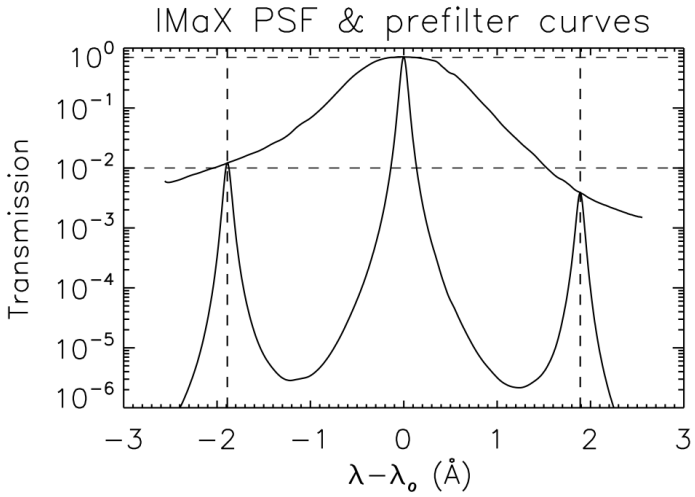


FIGURE 2.12— The upper solid line corresponds to IMaX prefilter. The lower line represents the spectral PSF convolved with a Gaussian of 85 mÅ. Figure adopted from *Martínez Pillet et al. (2011)*.

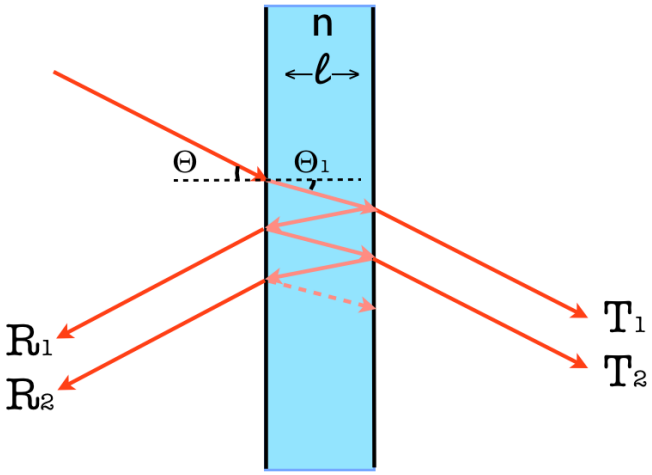


FIGURE 2.13— Transmission and reflection in a single etalon of thickness $\ell$ and refractive index $n$. The incident beam arrives to the etalon with an angle $\Theta$, and it is refracted inside the etalon on an angle $\Theta_1$. When the beam arrives to the second surface, part is reflected and part is transmitted.

IMaX FPI presented a collimated setup. This setup is not the only possible one; an etalon can be arranged on other optical designs, as in Figure 2.14. Some assets and drawbacks of these configurations are commented below.

These setups are presented in Kentischer et al. (1998). In the collimated configuration, shown in Fig. 2.14(a), the telescope aperture (PS, pupil stop) is imaged into the interferometer, being L2 the reimaging lens. At the Fabry Pérot location the beam is collimated. In the telecentric configuration, in Fig. 2.14(b), the lenses L1 and L2 project the solar image (FS, field stop) into the interferometer. Lenses L3 and L4 image the solar image onto the detector (FP2).

The telecentric configuration requires a trade-off between spectral resolution and effective FOV. Moreover, with a telecentric mounting, the beam becomes focused on the etalon's surface, and this fact can be a problem on the case of having dust or small imperfections of the flatness of the etalon surfaces which will shift locally the maximum transmission causing the 'orange peel pattern' (Kneer and Hirzberger, 2001; Blanco Rodríguez, 2008). These undesirable effects can be minimized by placing the telecentric etalon in the mounting slightly away from the focal plane. An advantage of this configuration is that the optical quality requirements can be less restrictive.

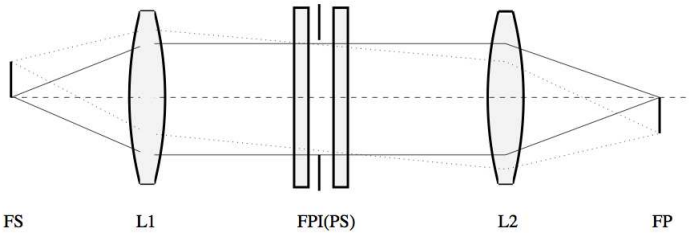


(a) Collimated setup

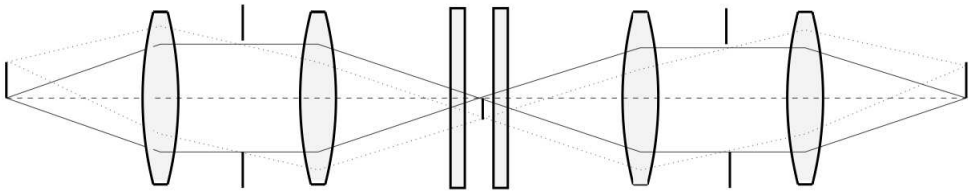

(b) Telecentric setup

FIGURE 2.14— Different Fabry-Pérot setups, from *Kentischer et al. (1998)*.

Collimated mountings have certain advantages; for instance, blocking ghost images can be much easier than in a telecentric configuration, but the requirements on the optical quality are more stringent. A caveat on collimated configuration is the wavelength drift over the FOV. This effect in collimated systems, called 'blueshift', affects differently depending on the wavelength, and refers to a shift of the maximum of wavelength transmission across the FOV. This drift over the FOV is represented by $\Delta\lambda$, which is the difference between the wavelength at the boundary of the etalon and the wavelength at the centre of the etalon:

$$\Delta\lambda = \lambda(\cos\Theta - 1) \approx -\frac{n\lambda}{2}\Theta^2, \tag{2.4}$$

Unless having the system in a telecentric mounting, this effect cannot be avoided. Taking the Equation 2.4, the theoretical maximum blueshift for the IMaX etalon is given by:

$$\Delta\lambda = \frac{\lambda_0}{2} \cdot \left(0.44\frac{\pi}{180n}\right)^2. \tag{2.5}$$

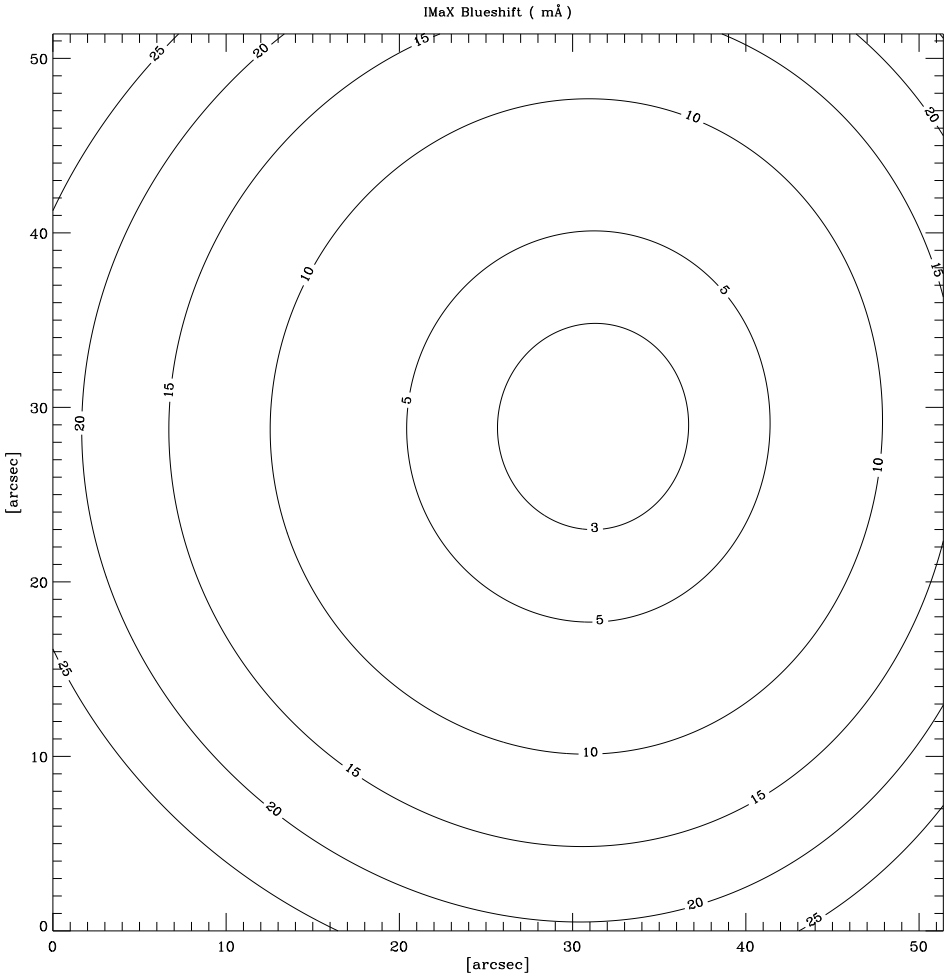


FIGURE 2.15— An example of wavelength drift over the FOV. Contour line units are mÅ.

The IMaX etalon thickness $\ell$ (at 25 mm aperture) was 281$\mu$m. The refractive index $n$ for $LiNbO_3$ is 2.327, and the angle of incidence on the etalon was 0°44. Therefore, the theoretical maximum blueshift was 28 mÅ. A blueshift contour plot is depicted in Figure 2.15. This value has to be kept in mind when correcting flat-field observations, in Section §2.2.7.

The $LiNbO_3$ (lithium niobate) etalon was connected to a high voltage power supply (HVPS). This high voltage in combination with the stratospheric pressure of

3 mbar, increased dramatically the probability of an electric discharge. This likely fact imposed a modification to the design: the power supply and the etalon had to be separated in pressurized chambers. These thermally controlled pressurized enclosures (TCPE) had an inside atmosphere of dry nitrogen at 1.2 bar.

The *FWHM* of the Airy function of the double etalon pass was 65 mÅ. The effective spectral resolution of the instrument, including spectral straylight from the side lobes, was degraded to 85 mÅ, as shown in Figure 2.12. This *FWHM* of the Gaussian was chosen among different *FWHM* used to convolve the FTS data until a satisfactory agreement with the observed spectrum was obtained.

The finesse of an optical resonator (cavity) is defined as its free spectral range divided by the *FWHM* bandwidth of its resonances. It is independent of the resonator length. The value of this magnitude in the IMaX etalon was about 20-25. The Free Spectral Range $FSR$, or separation of adjacent orders is defined in Equation 2.6:

$$FSR = \frac{\lambda^2}{2n\ell\cos\Theta} \tag{2.6}$$

The $FSR$ is related with the finesse as in the Equation 2.7:

$$F = \frac{FSR}{\delta\lambda}, \tag{2.7}$$

The total finesse is related to the fabrication finesse, $F_f$, and the reflective finesse, $F_r$ as in Equation 2.8:

$$\frac{1}{F^2} = \frac{1}{F_f^2} + \frac{1}{F_r^2}. \tag{2.8}$$

Considering a total finesse value of 22, and a $\delta\lambda$ of 50 mÅ, the IMaX $FSR$ was about 1 Å, which implied that a prefilter of half this width would be needed, complicating the mounting of the instrument. Instead, the choice was having an etalon with $\delta\lambda$ of 100 mÅ and force the light to pass twice through it. The $FSR$ would be 2 Å and the prefilter would be of 1 Å, as it eventually became.

One of the largest inconveniences of the $LiNbO_3$ technology is the tuning speed. The recommended speed was about 1500 V/s or 0.5 Å/s. As the typical spectral step was about 40 mÅ, the etalon spent 80 ms tuning each wavelength, quite long compared with piezo-stabilized optical devices. To give a hint about the voltages used, the continuum point at +227 mÅ used 3100 V on flight.

Other important pieces of the optical setup were the acquisition components. Light was bended by a mirror to a polarizing beamsplitter that divided light to the two Cameras. Camera 1 had the phase diversity (PD) plate in front of it. This plate was a fused silica slab of 27 mm thickness. It was designed to produce the specified amount of defocusing corresponding to $1\lambda$ at the edge of the pupil.

The focal plane detectors were two cameras Dalsa Pantera 1M30 with 1k×1k chips, of a pixel physical size of 12$\mu$m. The transfer time was about 4 ms. The typical working temperature of the cameras was 45°C and heat went through a thermal conductor to a cryostat cooled by a Peltier element. The quantum efficiency $QE$ was about 25%. The detectors were synced with the LCVR, and images were accumulated. Images were focused by a doublet and two lenses placed before each CCD.The cameras could reach 30 frames per second with 12-bit resolution. The rate during flight was 4 frames per second. Synchronicity between the two cameras was guaranteed.

PD is useful, not only for the post-facto calibration, but for the assembly and pre-launching phase. The etalon was found to show a significant astigmatism: the difference between sagittal and tangential foci is 1.6 mm. A trefoil factor – Zernike coefficients 9 and 10, probably from the mirror mounting – was also present. Spherical aberration was detected as well, but due to the gondola jittering, it might be an effect of the residual high frequencies (larger than 30 Hz) with amplitudes of 0.″03 or 0.″04 producing a blurring similar to the spherical aberration.

The optical system was carefully designed to avoid straylight by baffles painted of black. Ghost images were also considered as they were non-negligible due to the relatively large coherence length. To avoid their presence in the optical system, the etalon enclosure was rotated $0°36$.

#### 2.2.5.3 IMaX electronics

The IMaX electronics equipment was divided in three different subsets: the main electronics (ME), the optical bench electronics and the harness. In the optical bench, the proximity electronics (PE), the cameras and all the mechanical and optical actuators were included. The harness covers were chosen, like every component onboard SUNRISE, to minimize the outgassing in the quasi-vacuum flight conditions. Electronics were placed inside a pressurized enclosure.The harness electrical system included twisted pair wires to reject electronic noise.

The main electronics (ME) had five subsystems: the CPU board, the real time-image processing board (IPB), the interface (I/F) board, the etalon thermal control, and the power supply. The CPU unit possessed a processor, a flash memory disk, ethernet ports, a video card, among others. The IPB performed image accumula-

tion, demodulation and truncation. The I/F was kept for housekeeping signal of the main electronics box. The etalon thermal control unit kept its temperature constant with an accuracy of $\pm 0.03$°C, while the surrounding temperature was controlled within $\pm$ 0.5°C. The nominal temperature of the prefilter and the etalon were 35°C and 30°C, respectively. In the end they worked at temperatures of 31°C and 27°C with a diurnal fluctuation of $\pm 1$°C. This change on the expected temperature is considered for further calibrations.

The PE of the optical bench electronics (OBE) was in charge of the control of the LCVR, the etalon tilt motor and high voltage power control, synchronizing the etalon tuning with the LCVR retardance changes, among other tasks. The design of the PE was optimized to avoid excessive wiring and strong differences of voltages.

### 2.2.6 IMaX instrumental calibrations

This Section is mainly based on Martínez Pillet et al. (2011) and it is included in this text for completeness.

#### 2.2.6.1 Polarimetric description of the instrument

The polarimetric calibration of an instrument consists of estimating the demodulation and modulation matrices and efficiencies.

In vector polarimetry ($N_p = 4$, four polarization states), the modulation states $[S_1, S_2, S_3, S_4]$ are related with the Stokes vector $[I, Q, U, V]$ through the modulation matrix $\mathbf{M}$,

$$I_i = \sum_{j=1}^{4} M_{ij} S_j, \tag{2.9}$$

and the demodulation matrix as the inverse of the modulation matrix, $\mathbf{D} = \mathbf{M^{-1}}$.

The coefficients of $\mathbf{D}$ are used to determine the polarimetric efficiencies, $\varepsilon$:

$$\varepsilon_i = \left( N_p \sum_{j=1}^{4} D_{ij}^2 \right)^{-1/2}. \tag{2.10}$$

Ideally, the maximum achievable of $\varepsilon_1$ is equal to 1 and the maxima of $\varepsilon_1$ and $\varepsilon_{2,3,4}$ reach $1/\sqrt{3}$ (del Toro Iniesta and Collados, 2000; del Toro Iniesta, 2003).

For longitudinal polarimetry, just two states ($N_p = 2$) are needed, as combination of $I + V$ and $I - V$.

The two LCVR of IMaX were characterized separately and together with a fixed linear polarizer with the optical axis vertically oriented – as this direction is chosen for Stokes $Q$ orientation – plus a $\lambda/4$-plate in a rotating mount stepping 5°. When the LCVR were characterized and integrated, the characterization was performed for the beamsplitter and the prefilter. When the prefilter was set, since just 1 Å of visible light was allowed to enter, the exposure time and accumulation had to be raised. For shortening the measurement time, just the four polarization eigenstates were measured and tested: 0°, 90°, 45°, 135°. The $\mathbf{D}$ (demodulation) matrix obtained by IMaX calibration for the Camera 1 and 2 are:

$$\mathbf{D_{mod1}} = \begin{pmatrix} 0.250109 & 0.238974 & 0.260214 & 0.250423 \\ 0.455083 & 0.356425 & -0.377968 & -0.342087 \\ 0.678561 & -0.827494 & 0.0977504 & 0.0104520 \\ 0.0235024 & -0.140358 & -0.567420 & 0.690720 \end{pmatrix}$$

$$\mathbf{D_{mod2}} = \begin{pmatrix} 0.250067 & 0.239074 & 0.260436 & 0.250237 \\ -0.396238 & -0.307138 & 0.388434 & 0.338140 \\ -0.660712 & 0.794409 & -0.104223 & -0.0122207 \\ -0.0139619 & 0.126351 & 0.552859 & -0.672138 \end{pmatrix}$$

#### 2.2.6.2 IMaX Spectroscopic calibration

In the Assembly, Integration and Verification (AIV) phase, a iodine cell, chosen for its stability, was used for wavelength calibration. The iodine spectrum in the spectral range of interest (5250 Å) has lines of a few mÅ of *FWHM* that cannot be resolved by IMaX; however, when convolved with the Airy function of the double-pass etalon, it showed a blended spectrum very useful for Fe I calibrations. The aim was obtaining the relationship between the wavelength and the corresponding voltages applied. The final result was:

$$\lambda - \lambda_0 \; = \; a + bV \; = \; -0.701 + 0.0000335V, \tag{2.11}$$

where $\lambda_0$ =5250.225 Å is the nominal wavelength. The coefficient $a$ gives the difference to the nominal wavelength of the line when the etalon is at 0 V. This parameter is also important because it is the reference to the wavelength centre of

the line at disk centre. If observing at any $\mu$ rather than 1, the coefficient varies and has to be set. This fact is of crucial importance for flat-field calibrations and will be explained in Section §2.2.7. The coefficient $b$ remains practically the same regarding different disk positions. However, since the flight temperature was lower than expected, $a$ was around $-0.783$, i.e, nearly a 'thermal blueshift' of 80 mÅ. Solar rotation has to be considered also on the wavelength shift. Due to this fact, $a$ can vary by $\pm$ 0.0325 Å.

### 2.2.7 IMaX Observing Modes and data processing

This Section constitutes the summary of IMaX reduction data from scratch to restored data, still in progress.

IMaX observed in a variety of modes that differ in the number of Stokes parameters observed, the number of wavelength points and the number of accumulations at each wavelength. Modes can be Longitudinal *L*, when only $[I, V]$ are involved, and the Vectorial *V* modes, with full Stokes vector. The notation follows the number of wavelength points (3, 5 and 12 were used on this flight) and the number of accumulations per wavelength (2, 3, 6). These accumulations are performed to increase the $S/N$ ratio. The most widely used mode is V5_6, i.e. full Stokes vector measured on 5 wavelengths (4 in the line and 1 in the continuum), with 6 images accumulated per wavelength point. A summary of all the different Observing Modes is listed in Table 2.2. IMaX data are denoted as follows: observation number and the cycle number go in square brackets, i.e., 260, [108]. Every observation number typifies an observation mode, in longitudinal or full Stokes mode on science cases; or calibration observation, as pinholes, darks, flat-fields, and PD. The summary of the Observing Modes for June 10 and 11 can be found in Appendix A and Appendix B.

The reduction also depends on the magnetogram mode used. If *V* (vectorial mode) was performed, further calibration was applied. For *L* (longitudinal mode), 4 images were also recorded in every set $[I+V, I-V, I+V, I-V]$, resembling V-modes that have non-demodulated intensity images to get $[I, Q, U, V]$. As L-modes cannot be corrected with Mueller matrices, V was multiplied by a factor of 1.8 (Martínez Pillet, V., private communication).

SUNRISE observations were kept in timeline. However, the wind gusts affecting the gondola were strong enough to reduce the pointing performance. Then, for data mining tasks, we have had to find the images with correct pointing and separate calibration frames from science images. A quick look to the plots in Figures 2.16 and 2.17 allows us to manage this task. The intensity (in counts) is plotted on

TABLE 2.2— IMaX Observing Modes. In each mode, the amount of polarization states, wavelengths and accumulations are designated by $N_p$, $N_\lambda$ and $N_{acc}$, respectively.

| Obs. mode | $N_p$ | $N_\lambda$ | $N_{acc}$ | Duration [s] | $S/N$ | Sampling and Cont. [mÅ] |
|---|---|---|---|---|---|---|
| V5_6 | 4 | 5 | 6 | 33.25 | 1000 | $\pm$ 40, $\pm$ 80, +227 |
| V5_3 | 4 | 5 | 3 | 18.27 | 740 | $\pm$ 40, $\pm$ 80, +227 |
| V3_6 | 4 | 3 | 6 | 20.12 | 1000 | $\pm$ 60, +227 |
| L3_2 | 2 | 3 | 2 | 10.10 | 1000 | $\pm$ 60, +227 |
| L12_2 | 2 | 12 | 2 | 29.01 | 1000 | -192.5 to +192.5 (each 35) |

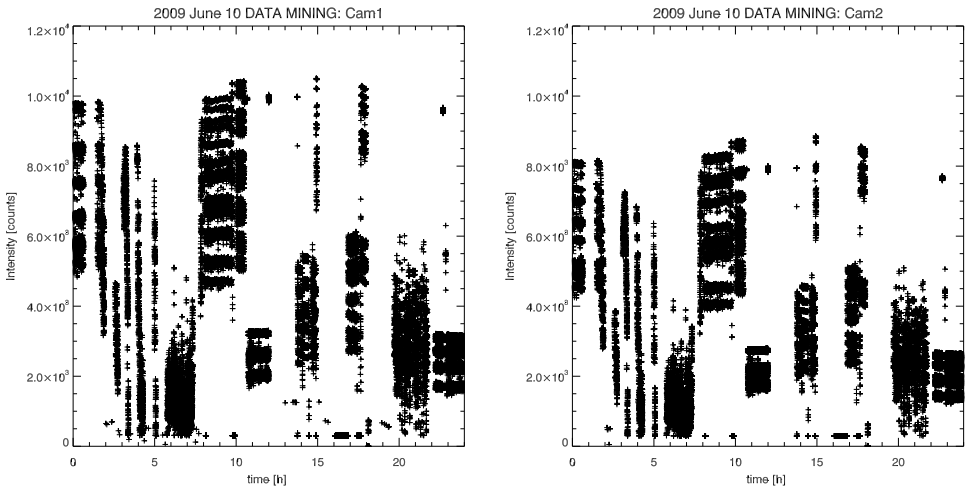


FIGURE 2.16— Intensity versus time, 2009 June 10.

$Y$ axis, as displayed in Figures 2.16 and 2.17. Camera 1 presents an average of 10000 counts in quality images, while Camera 2 counts average is approximately 8000. At first glance, intensity drops are manifest at moments when SUNRISE lost its pointing. These intensity diagrams are useful to discriminate calibration images from science data. Some reduction images can be found easily, as dark current images usually have 300 counts, and pinhole images – used to check the alignment between the two Cameras and calculating the image sampling – present similar count values.

The calibrations were always performed at disk centre, for line calibration rea-

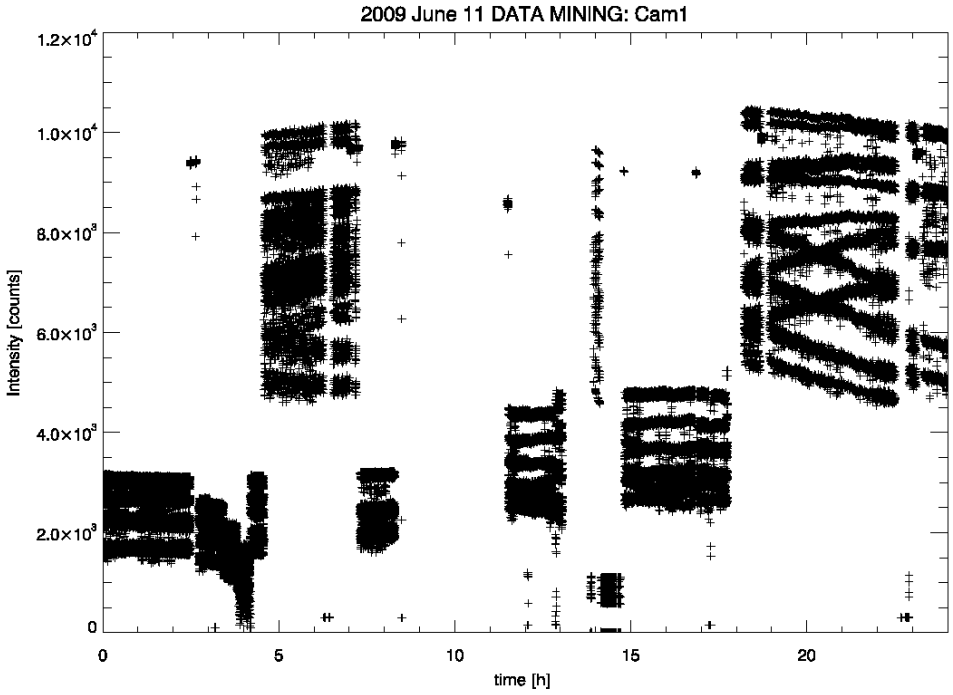


FIGURE 2.17— Intensity versus time, 2009 June 11.

sons. It consisted of flat-fielding series, with the telescope moving in a radius of 100″ around disk centre, with the tracking disabled in these series (of wavelength and polarization state), moving constantly the telescope during exposure at high speed. Flat-fields cannot be detected easily on an intensity plot as the counts amount are not different from a science image, but their contrast (since they are smeared by the telescope motion) are certainly lower than science images, of about 0.05. A way of tracking down flat-fields is locating the pointing in the header and check if the pointing was around the disk centre and followed a nonagon. This way of executing flat-fields is common in ground-based solar telescopes, since flat-fielding on a dome or surface could cool the tube and heating it again by focusing onto the Sun, creating turbulence inside the optical system and loss of focus by thermal expansion, among other effects.

For PD calibration, sets of 30 continuum images with the same number of accumulations were acquired together with series of 50 cycles of flat-field for phase diversity (one wavelength, without modulation). The closest temporal PD set to

the science image, along with its corresponding flat-field and dark-current images have to be identified. The PD calibration consists of inferring the instrumental PSF described by a set of 45 Zernike coefficients. The description of the PD method can be found in Paxman et al. (1996), and Löfdahl and Scharmer (1994), and it is summarised in Chapter §1, Section §1.3.3. As the anisoplanatism is regarded as negligible along the field of view, the Zernike coefficients can be averaged to obtain a mean wavefront for the whole FOV and its corresponding PSF.

A number of corrections are performed to the flat-field. Since the flat-field images have different wavelengths and polarizations, care has to be taken to correct from the blueshift effect (wavelength drift over the FOV, Equation 2.5). An image of this effect is shown in Figure 2.15. The blueshift calibration has two important outputs: the $a$ coefficient corresponding to the pointing of the flat-field, and the set of 16 coefficients that defines the blueshift, fitting a 3-degree polynomial for a surface.

The wavelength calibration is one of the most computer time-consuming tasks to be carried out. As flat-fields still have the blueshift contribution, it has to be removed. Depending in which part of the disk centre the flat-fields were obtained, this effect is corrected by the aforementioned coefficient $a$ in Equation 2.11. When all the wavelength points in the flat-field data are considered, a Gaussian is fitted to the whole set, and the wavelength calibration is completed. An example is displayed in Figure 2.18. In this Figure and the following, the spectral Fe I line is displayed by a solid line, the wavelength points of the whole dataset are clustered around the nominal centre of $\pm$0.04 Å, $\pm$0.08 Å and the continuum point $+$0.227 Å. Dotted lines mark the end of the each wavelength point group. A good Gaussian fit of the wavelength wings and continuum points can be assumed, as indicated by the agreement between the observed points and the solid line. Figure 2.19 is a corrected case, as wavelength points clearly depart from the solid reference line, so a new Gaussian with broader wings has to be fitted (dotted curve). This was caused by a non disk-centre observation for flat-field acquisition, which broadens the line wings. The Gaussian fitting is always a time consuming process, and we shall remind it is conducted to every pixel. For observation with less than five wavelength points, Gaussian fits to lines are not possible, so as first approximation, an estimation of the line centre was performed with the two core line points (-60 and $+$60 mÅ).

The presence of interference fringes from some of the optical elements (the polarizing beamsplitter and the prefilter) that also show thermal drift following the diurnal thermal changes forces one to use the flat-field closer in time to the observing run. The interference pattern does not remain exactly the same: it evolves while the etalon is changing the wavelength, since the angle of incidence of

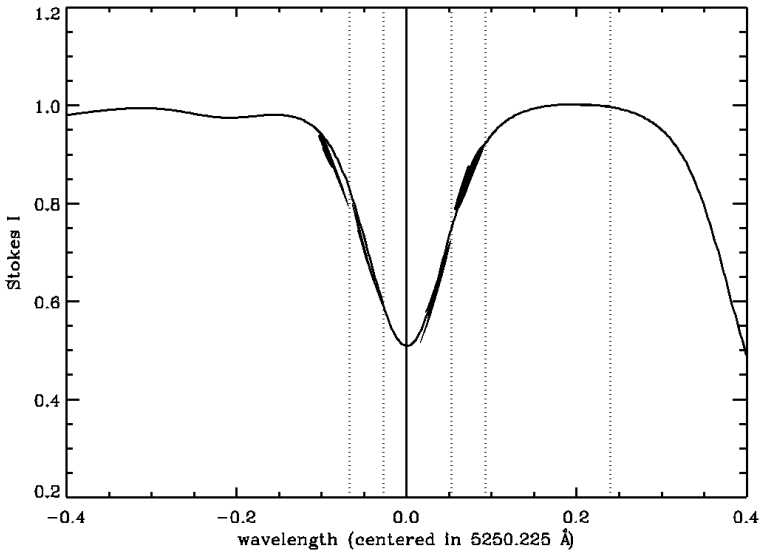


FIGURE 2.18— Example of line fitting for a flat. Solid line indicates the Fe I line. Dotted vertical lines mark the end of the each wavelength point group, five in this case. Wavelengths of the different cycles conforming the flat-field observation span along the dotted vertical line to the left.

the light rays is slightly altered.

A set of images more strongly affected by fringes and drift of dust particles is selected for each observation. The mean power spectrum of this chosen sequence is used to create a mask in the Fourier domain showing where the residual fringes appear. The mask is applied to every image in the cycle and the mask boundaries are weighted to be interpolated with a weighting function describing the excess of power within these masked areas. This function filters out the excess of signal in the real and imaginary domains. Two displays of the mean power spectrum in Camera 1 and Camera 2 of IMaX are presented in Figure 2.20. The removal of the first and second harmonics (seen in Figures 2.20 and 2.21) caused by the high-frequency fringes is accomplished.

This procedure has also the purpose of masking out the dust particles present in IMaX cameras. Their positions are replaced by interpolating at their boundaries, relieving the instrument from this effect.

The field stop removal is performed as well. A field stop was placed in F4 to reduce the straylight, as previously mentioned. This fact reduces the size from the original 1024×1024 to 936×936 pixels. During the PD restoration, an apodiza-

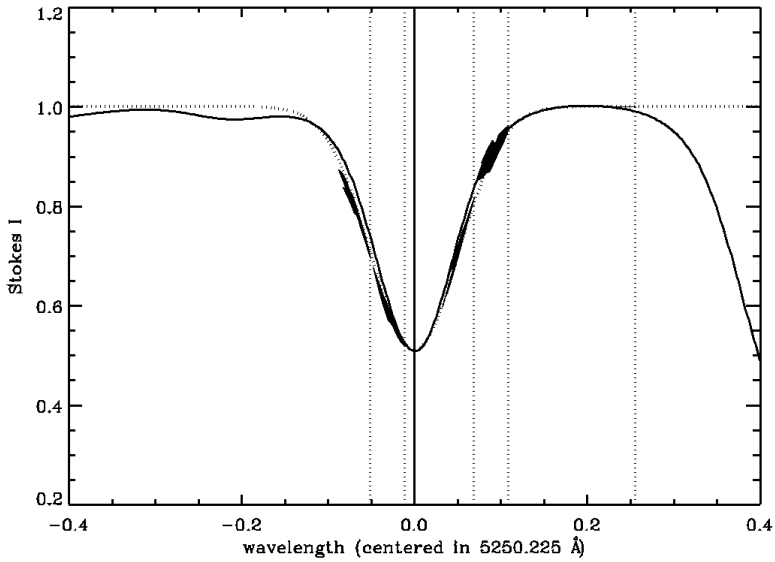


FIGURE 2.19— Example of a bad line fitting for a flat-field taken on 2009, June 11. Similar figure to 2.18 but wavelength points not only spread but separate from the solid line. The dotted curve fits accurately to the profile. This discrepancy is due to a flat-field observation acquired outside the disk centre.

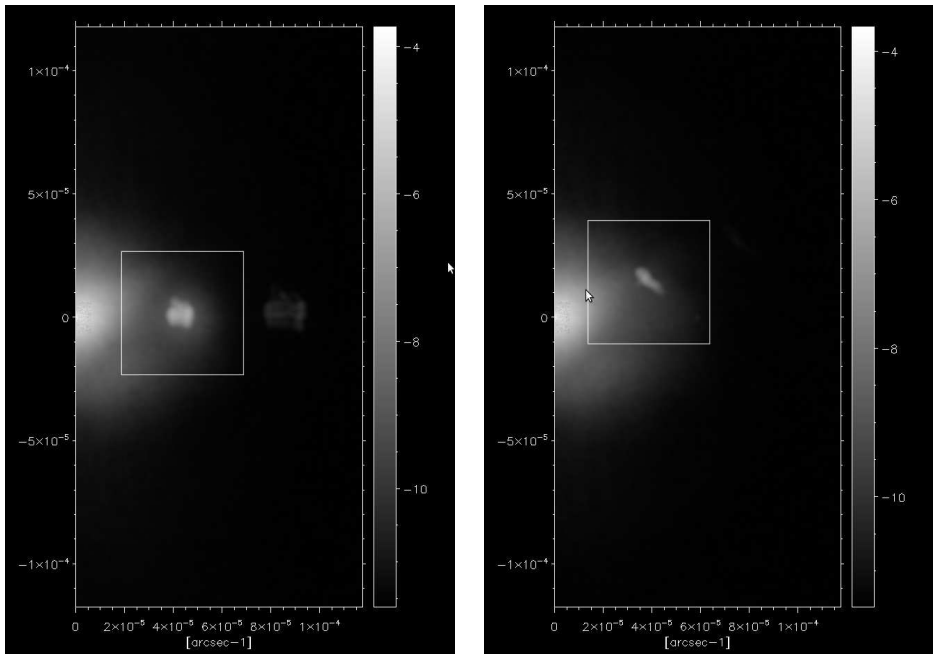


FIGURE 2.20— Mean power spectrum extracted from IMaX Cam1 (*left*) and Cam2 (*right*). White boxes enclose the first harmonics in each Camera.

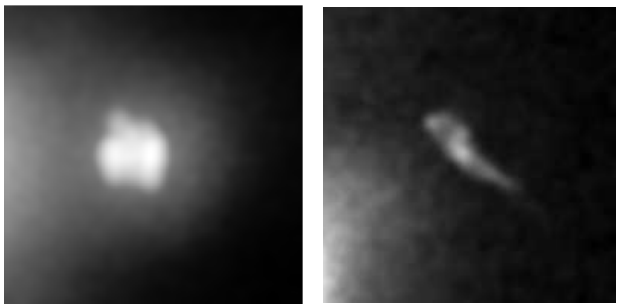

FIGURE 2.21— Details of the power spectrum displaying spatial first harmonics. The different shape of the harmonics and the camera orientation is noticeable.

tion window of 10% in each dimension is used, and leaves an usable final FOV of 842×842 or 46″×46″. Sometimes the treatment of images with apodization is cumbersome. Limb data in IMaX were fully reduced without introducing apodization to take full advantage of the limb data.

The data reduction process can be summarised as follows: images are corrected by the flat-field after the removal of the blueshift; the mask correction of the dust particles and fringes is applied; data are reconstructed using the PSF recovered by the PD method, and a modified Wiener optimum filter is applied, as originally proposed by Brault and White (1971) and mentioned in Chapter §1, Section §1.3.4. This is introduced to avoid high-frequency over-restoration, shown in images as opposite polarity haloes surrounding some large polarities features, usually solar network patches. The Equation 1.26 is modified by a regularization parameter.

Data are demodulated by $\mathbf{D_{flight}}$ matrix, which is the combination of all demodulation matrices of the instrument plus telescope. The intensity of the two Cameras are weighted, the relative displacement between the two pairs of images provided by the two Cameras is found, and the images are added to reduce the cross-talk created by the gondola jittering. Residual cross-talk from $V \rightarrow Q$ and $V \rightarrow U$ is calculated and the correction is then applied to the data. The output of this process is classified as Level 1 (unreconstructed) or Level 2 (reconstructed), and written in IDL **save** sets and **FITS** format. Once the data are reduced, they are ready to be scientifically usable. Gaussian functions are fitted to the spectral line for every pixel, allowing to obtain in an accurate way the so-called IMaX *parameters*: the *FWHM* and *Imin* or line minimum, fundamental for calculating Dopplershifts. On the other hand, with the whole set of Stokes parameters, longitudinal and transverse magnetograms were calculated as described in Section §1.4.1. For the longitudinal magnetograms, the two red wavelength points become sign changed to avoid cancellation, as in Equation 2.12, considering the components $a_i$ of $\vec{a}$ =[1, 1, -1, -1]. The formulae for the longitudinal and transverse signal are:

$$V_s = \frac{1}{4}\sum_{i=1}^{4} a_i V_i \tag{2.12}$$

$$L_s = \frac{1}{4}\sum_{i=1}^{4} \sqrt{Q_i^2 + U_i^2}. \tag{2.13}$$

A magnetogram calibration was also performed in Martínez Pillet et al. (2011), varying the field strength, and for the transverse field, the inclination angle was varied, and the azimuth angle was set to 0. In the weak-field range (in this case

[0,400] G), where the curve between the magnetic signal and the field strengths is linear, a linear least-square fit was performed, and the relations were:

$$B_{LON}(G) = 4762\frac{V_s}{I_s} \tag{2.14}$$

$$B_{TRA}(G) = 2526\sqrt{\frac{L_s}{I_s}}. \tag{2.15}$$

These equations can be used to obtain field strength estimates.

The $S/N$ ratio, as mentioned before, is about 800-1100 depending on the number of wavelengths and accumulations, and it changes randomly from pixel to pixel. Nonetheless, the reconstruction amplifies all frequencies but emphasizes the power at intermediate and high frequencies. This fact has an effect on amplification of the data noise, typically 2-3 times higher than the unreconstructed data. The polarization signals are higher by a factor 2. This yields a $S/N$ ratio slightly lower than the non-reconstructed images. The noise presents also an spatial pattern of 2-3 pixels because of the reconstruction, which affects high frequencies. For instance, a typical noise level value of $10^{-3}$ yields values of 4.5 G on $B_{LON}$ and 80 G in $B_{TRA}$ in non-restored images. For restored images, this noise level equivalence is 14 G on $B_{LON}$ and 135 G for $B_{TRA}$. Of course, the magnetogram equation is strongly dependent on the atmosphere model used. In this case, a kG field would correspond to $V_s$ of 0.21 and a internetwork field, to 0.08. We make a representative example. Using data from the observation number 200, cycle number 152, Observation Mode V5_6, we compare the flux obtained by IMaX calibration and the weak-field approximation in the Figure 2.22. In this figure, the relationship between the magnetogram calibration Equation 2.14 and the relation between the Equation 1.39 of the weak-field approximation is shown. The slope of the fitted line is 1.55, therefore the calibrated data are underestimating longitudinal flux.

Despite all these concerns, estimated magnetic flux increased by a factor of 2 (Solanki et al., 2010). Examples of reconstructed and non-reconstructed data are shown in Figure 2.23. These data are from 2009, June 11 at 17:25 UT. The mode is V5_3, from observation no. 260, cycle no. 108. On the left-hand side of the Figure, reconstructed images are presented, while the original are placed on the right-hand side. The linear polarization is displayed, among with continuum and circular polarization. In the linear polarization images, the difference between the linear polarization patches (white colour) and the traces of dust grains over the CCD window (in black) are quite evident. It is noticeable that the magnetic

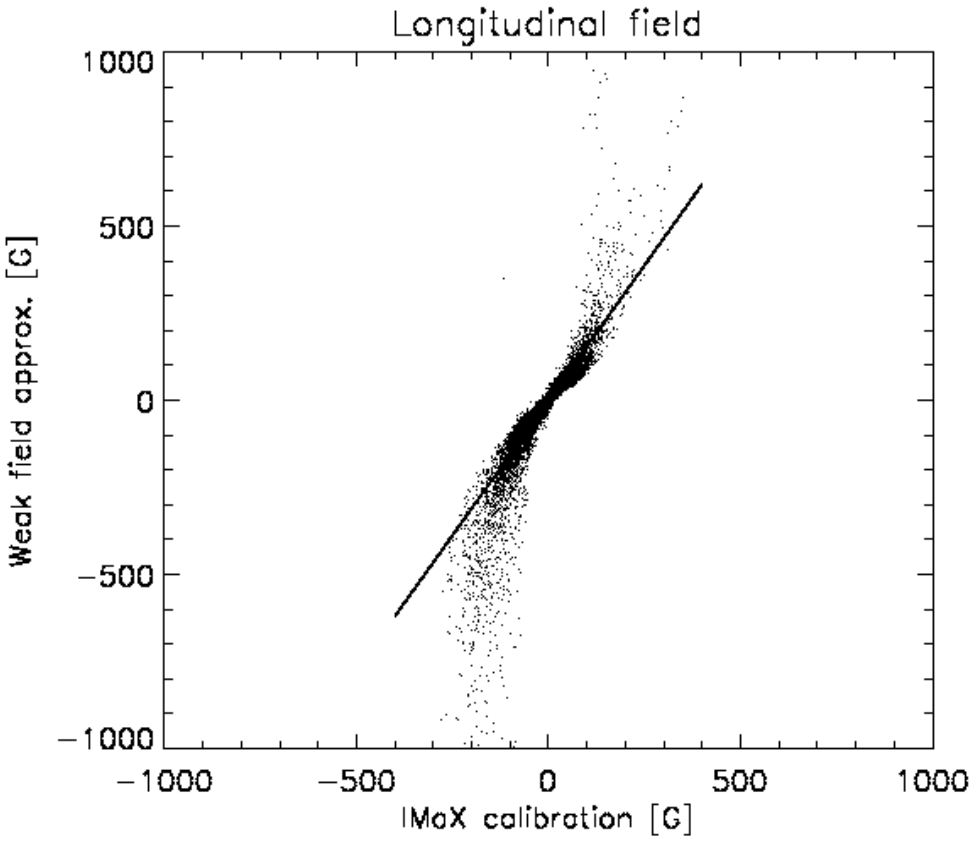


FIGURE 2.22— Weak field approximation versus IMaX calibration.

flux in non-reconstructed images is lower than the reconstructed, indicated by the corresponding colourbars.

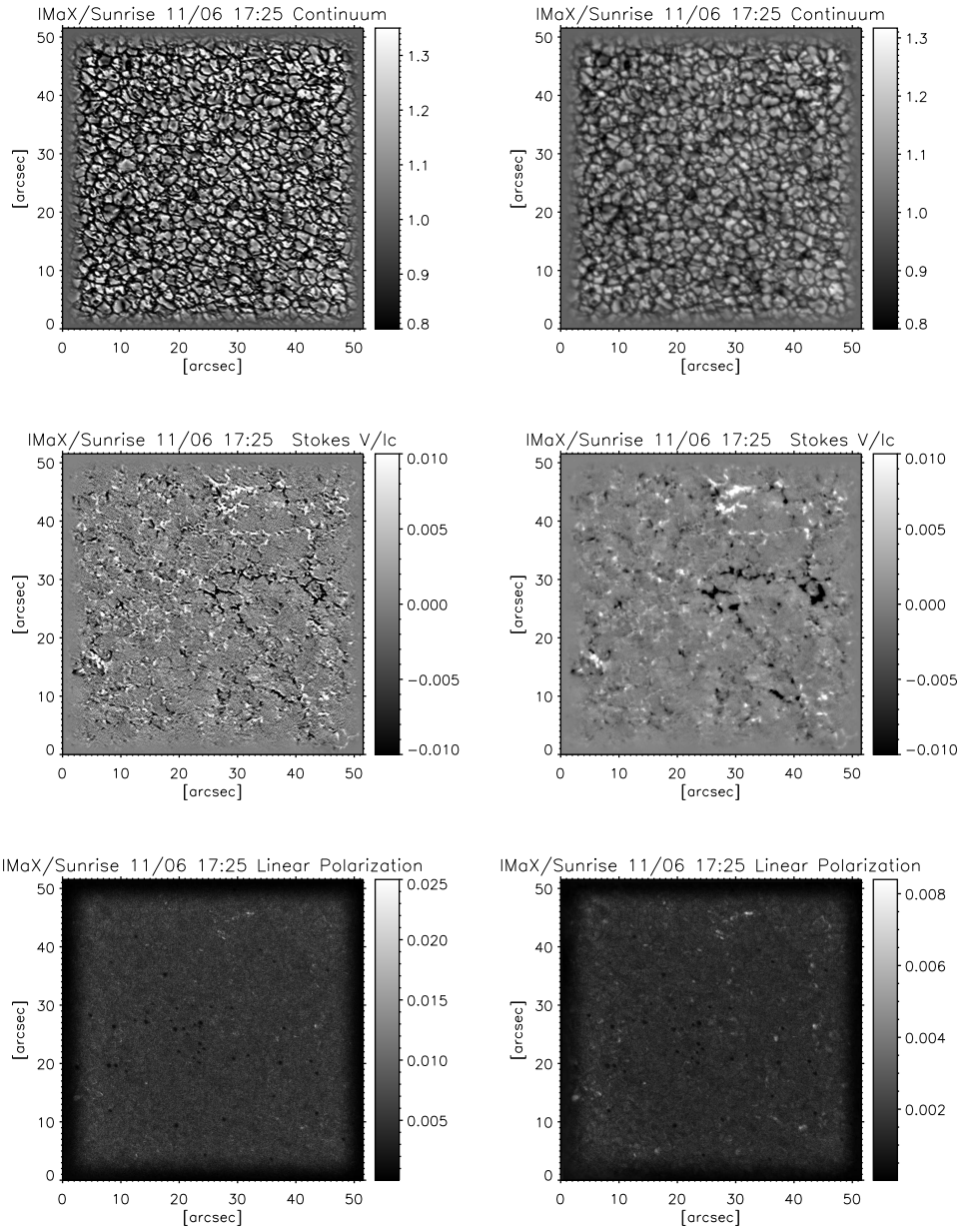


FIGURE 2.23— *Left*: V5_3 restored images of continuum, circular and linear magnetograms, from top to bottom. *Right*: non-restored images. The apodization window is clearly present.

# 3

# Dynamics of small magnetic elements with HINODE and SST

Vortex motion in the solar atmosphere affecting the small-scale magnetic concentrations will be described in this Chapter. These magnetic features appear as being dragged towards the centre of the vortex as evidenced by the analyses of solar magnetograms and throughout sequences of filtergrams at different heights in the solar atmosphere.[1]

Don't blame me, Sleeping Satellite. (Tasmin Ascher, 1992)

## 3.1 Introduction and historical overview

The dynamics of magnetic structures in the Sun are complex due to their different spatial and temporal scales. Small scale whirling movements – around 1Mm – will be the case studies in this Chapter and the following one. Here the turning motion of plasma in the intergranular lanes will be named *vortex* hereafter. In these downflows, the plasma starts turning around spiraling as in a bathtub drain moving towards the centre of the spiral motion that is denoted as *draining point*, and it is due to the passing of a fluid through a narrow hole. The conservation of angular momentum provokes this effect, making the fluid parcels rotate with similar angular speed. In a non-idealized case, fluid parcels can exhibit different angular speeds due to friction by viscosity. We shall remark that, opposite to the

[1] Parts of this Chapter are extended versions of *Balmaceda et al. (2009)*, *Balmaceda et al. (2010)*, *Palacios et al., ASP, (2011)*, and *Vargas Domínguez*, A&A, (submitted).

Earth's cyclones, the size of these vortices are small, from 0.5 Mm to 2 Mm. In this context the Coriolis force is negligible (Bonet et al., 2008). However, the Coriolis force tend to redistribute the angular momentum and generate rotational shear (Schriver and Siscoe, 2010), that may be the driver of the vortex-like flows Bonet et al. (2010). For larger scales, the Coriolis force is significant, as in the upper convection zone. In this region, large-scale convective cells were simulated, and strong vortices were found in the downflows (Miesch, 2005). These vortices conserved locally the angular momentum and showed counterclockwise direction in the Northern Hemisphere and clockwise direction in the Southern Hemisphere.

The small-scale vortices were predicted by Nordlund (1985) and first identified by the pioneering work of Brandt et al. (1988) and Wang et al. (1995). The analyses of simulations in Stein and Nordlund (1998), Kitiashvili et al. (2010) showed that granules rise and plasma flows to the intergranular lanes originating downflows. Several image sequences are shown in Figure 3.1. In an unstably stratified layer, buoyancy forces can preserve the swirling downflows, corresponding to Burgers vortices, which are stabilized by convective downflows (Cattaneo et al., 2001). Danilovic et al. (2010) observed strong downflows as consequence of the intensification of magnetic field in the context of a convective collapse, and these downflows helped the creation of small vortices. Vortices are found not only as photospheric downdrafts, but also as chromospheric swirling motion which may have a wave-related cause (Wedemeyer-Böhm and Rouppe van der Voort, 2009). Some authors theorize about the idea that the turning motion of GBPs leads to magnetic braiding and the field lines can act as guide lines to spread waves from the photosphere to the chromosphere (Jess et al., 2009; Goode et al., 2010). Very recently, Kitiashvili et al. (2011) simulated the turning motion and the subsequent appearance of waves.

The sizes of these events also vary, depending on the spatial scale of the study. The size of the vortex was more than 7 Mm and it persisted for several hours in Attie et al. (2009). These eddies were found in a variety of solar scales, from supergranular sizes to the medium-sized ones (Brandt et al., 1988; Balmaceda et al., 2010), to the smallest ones that are detected and tracked using G-band bright points (Bonet et al., 2008). The first case presented a mesogranular scale (due to the resolution achieved at the time), while the third had a size of 0.5 Mm. The simulated smallest vortices are presented in Danilovic et al. (2010), with a diameter of 0.2 Mm.

Dynamics of twisted field lines on sunspots are analysed by their helicity, a property first detected by Hale (1925). This sunspot turning motion and subsequent shear in the field lines can lead to reconnection, as in the Active Region of 13 Dec

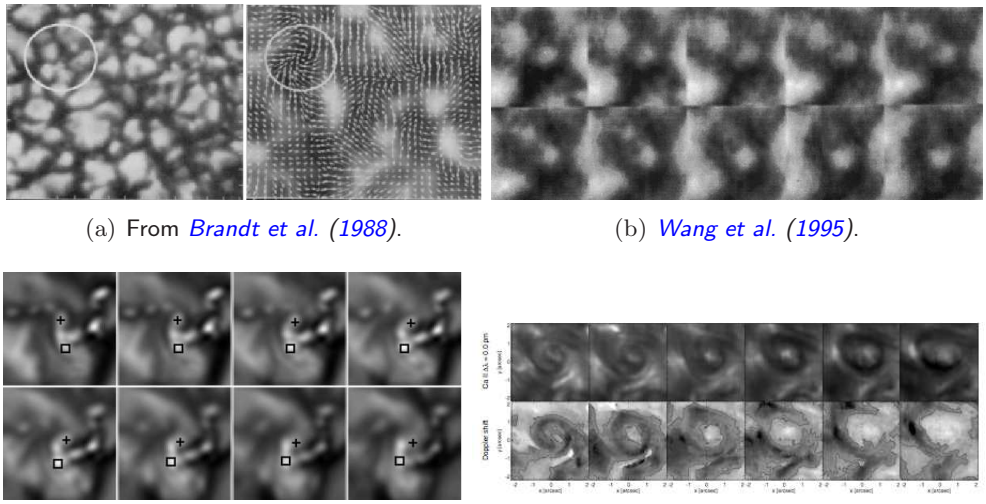

(a) From *Brandt et al. (1988)*. (b) *Wang et al. (1995)*.

(c) *Bonet et al. (2008)*. (d) *Wedemeyer-Böhm and Rouppe van der Voort (2009)*.

FIGURE 3.1— Several sequences of vortices in the literature.

2006 (Kubo et al., 2007; Yan et al., 2008). This kind of motion is completely linked to magnetic configuration and its nature is different from the motion observed and studied in this Chapter, with convection as the driving source. These surface movements are also different from the vertical vortices leading to bright edges in granules reported by Steiner et al. (2010). They are also uncomparable to the vorticity created by turbulence in shocks or mixing plasmas of different densities, as the shear vorticity reported for instance by Martínez-Sykora et al. (2008) and the Kelvin-Helmholtz instability reported by Foullon et al. (2011).

## 3.2 Methods applied to the analysis of vortices

As these movements are essentially convective, we can study the kinetics by several means: tracking the plasma when it is moving towards the intergranular lane to follow its spiral motion, or using the first technique with aid of some *tracers*. The most usual way to track these turning motions is the *Local Correlation Tracking* (LCT) (November and Simon, 1988) implemented by Yi and Molowny-Horas (1995). This technique calculates the displacement between consecutive pairs of images. A window function is applied, and the relative displacements that maximizes the correlation in this window are obtained. It presents a dependence of the

window size and its temporal averaging. These Gaussian boxcar windows are chosen accordingly depending on the size and time span of the event. LCT creates maps of horizontal velocities maps known as *flow maps*. Most studies use this procedure, as Brandt et al. (1988), Wang et al. (1995) or, some years later, Bonet et al. (2008). A particular benefit of the last studies mentioned was the usage of the GBPs in the area to track the movement, as *plasma tracers*, in Wang et al. (1995) and Bonet et al. (2008). G-band bright points are found to be tracers of the convective motion, as they mainly move along intergranular lanes. Attie et al. (2009) used some magnetic features to track the movement. Goode et al. (2010) combined the GBPs motion with LCT to conclude that some GPBs collide and a vortex is seen after the merging of GBPs. Other features are engulfed by the movement. Nisenson et al. (2003) also studied the GBP motion driven by convection and plot some of the tracks of these features. They estimate a maximum centrifugal acceleration of 0.4 km $s^{-2}$ on a vortex found in the field of view. Other magnitudes, as circulation, are calculated in Brandt et al. (1988) and Vargas Domínguez et al. (2011).

LCT is the basis to other strategies, like passive advected tracers – nicknamed as *corks* or *floaters* –. These tracers follow the flow maps generated by the LCT technique and reach places where they accumulate, which are called *sinks* in reference to negative divergences, as it will be shown later. The design of *corks* may vary depending the aim of the study: for instance, in van Ballegooijen et al. (1998), these tracers are disks that occupy a finite space and never overlap, which is very useful to trace network elements and analyse their dynamics.

A mixed technique is the *balltracking* method, which considers the continuum images of the granulation in a 3D representation where the intensity is seen as geometrical height. Spherical tracers of given mass are released in several positions and reach the local minima. As granules move, these balls trace the motion. The velocity fields are derived from this tracking, after averaging in space and time and recalibrating the velocities (since balls take some time on settling in minima, they can underestimate the velocity). This method was used in Attie et al. (2009) to reveal vortex flows in supergranular junctions.

Another procedure closely related to the application of passive advected tracers is the calculation of the divergence and vorticity of the flow maps obtained by LCT. These two magnitudes are defined as follows. The term *divergence* is used in this work as the divergence of the horizontal flow $\vec{v}_h(x, y)$ :

$$(\nabla \cdot \vec{v}_h) = \frac{\partial v_x}{\partial x} + \frac{\partial v_y}{\partial y}. \tag{3.1}$$

*Vorticity* is employed here as the vertical component of this magnitude:

$$(\nabla \times \vec{v})_z = \frac{\partial v_y}{\partial x} - \frac{\partial v_x}{\partial y}. \tag{3.2}$$

Note that the divergence is a scalar magnitude. Since horizontal velocities are computed, we can eliminate $v_z$ in the divergence. We should note that $v_z$ is equivalent to $V_{LOS}$ at disk centre. The vorticity is a vectorial magnitude, with a direction perpendicular to the $XY$ plane. In this case only the velocity components retrieved by LCT, $v_x$ and $v_y$, are used.

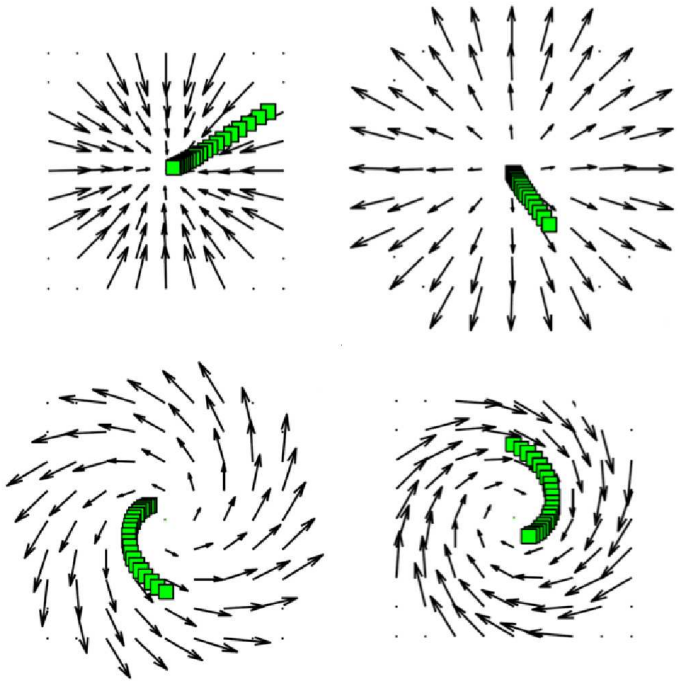

FIGURE 3.2— Divergence in the upper row. Left figure represents a converging flow with some passive tracers illustrated as green small squares. The vorticity effect, as the curl of the velocity, is depicted in the lower row. Right-rotating flow is mathematically meant by the negative curl, while left-rotating flow presents a rotating flow with positive curl.

Negative divergences represent *sinks* and positive divergences are taken as *sources*. Similarly, vorticity values larger than zero denote counterclockwise direction and areas with this magnitude below zero present a clockwise motion in

the velocity map, as shown in Figure 3.2. The computation of the vorticity and divergence (Pötzi and Brandt, 2005; Goode et al., 2010), among others, became other relevant method to probe and track this kind of phenomena.

Both divergence and vorticity are calculated in this Chapter by numerical differentiation using a three-point Lagrangian interpolation program by R. L. Molowny Horas (1992).

The divergence has also another useful advantage. In November and Simon (1988), a proportionality relation was established between the divergence and the *averaged* vertical velocities ($v_z \approx h_{\rm m} \nabla \cdot \vec{v}_h$) through the *scale height* factor. This factor is $h_{\rm m}$ = 150 km. This factor value has been rechecked for reliability in Márquez et al. (2006), yielding the same value.

## 3.3 Multi-wavelength observations of a vortex-like flow

Simultaneous data taken by HINODE and SST were used. Images were co-aligned and the common FOV in all wavelengths was selected.

An international campaign performed at the Canary Islands observatories was conducted during September-October 2007 and corresponded to an important collaboration among several European and Japanese institutions. For the first time, coordinated observations of ground-based facilities and the space solar telescope HINODE (Kosugi et al., 2007) were performed as part of the *Hinode Operation Program 14*. In the present Chapter, we make use of data recorded during a particular observing run on September 29, 2007. This selected region corresponded to a quiet sun area at the north part of the active region NOAA 10971, close to the solar disk centre ($\mu$=0.99), as shown in Figure 3.3.

*Ground-based observations* - The Swedish 1-m Solar Telescope (SST, Scharmer et al., 2003a) acquired high quality images with an effective field-of-view of 69″ × 69″CCD cameras with a size of $2048 \times 2048$ square pixels were employed (0.″034 pixel$^{-1}$). G-band images ($\lambda 430.56$ nm) and Ca II H ($\lambda 396.9$ nm, not shown) were recorded at a fast cadence. Post-processing of the images included the *Multi-Frame Blind-Deconvolution* (Löfdahl, 2002) restoration technique to correct for atmospheric turbulence and instrumental aberrations that degrade the image quality. The final product were two time series of images (*s1*: 08:47-09:07 UT and *s2*: 09:14-09:46 UT) with a cadence of 15 s. These two time series (*s1* and *s2*) of images present a time gap of 7 min between them, as shown in Table 3.1. Further steps in the data post-processing were applied, such as compensation for diurnal field rotation, rigid alignment of the images, correction for distortion and subsonic filtering to eliminate high frequency oscillations. The latter is explicitly defined in Chapter §1,

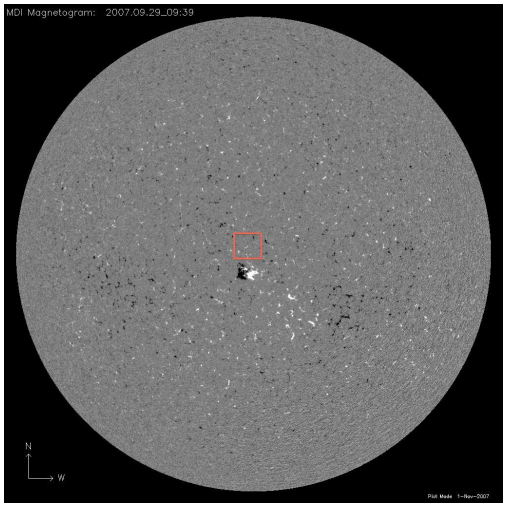


FIGURE 3.3— MDI full disk showing NOAA 10971

Section §1.3.5.

*Satellite data* - The Solar Optical Telescope SOT (Tsuneta et al., 2008) onboard the HINODE (Kosugi et al., 2007) satellite acquired filtergrams in CN ($388.35$ *FWHM* $0.7$ nm) and the core of Ca II H ($396.85$ *FWHM* $0.3$ nm) using the Broadband Filter Imager (BFI). A subsonic filter was applied also to BFI images. The observed FOV corresponds to $19\farcs18 \times 74\farcs09$, with a spatial sampling of $0\farcs05$ pixel$^{-1}$. Magnetograms in the Mg I line ($517.3$ nm) at a spatial sampling of $0\farcs08$ pixel$^{-1}$ were obtained with the Narrowband Filter Imager (NFI). A large region of the SST FOV is covered by HINODE observations. Data from the Spectropolarimeter instrument (Ichimoto et al., 2008) were acquired. This data set consists in Stokes $I, Q, U, V$ along a slit of 256 pixels, in raster scan of 18 scans from 08:20-09:44, with a sampling of $0\farcs15$ pixel$^{-1}$, and FOV of $2\farcs66 \times 40\farcs6$. The observed lines were the two Fe I lines, $630.15$ nm and $630.25$ nm. The SOT images were corrected for dark current, flat-field and cosmic rays with standard procedures, SP data were inverted using the full atmosphere inversion code LILIA (Socas-Navarro, 2001), based on the SIR code (Ruiz Cobo and del Toro Iniesta, 1992). The intrinsic 180°-ambiguity is resolved using the code Non-Potential magnetic Field Calculation (NPFC) method by Georgoulis (2005).

Figure 3.4 shows from bottom to top, time averaged Ca II H, CN and G-band filtergrams and Mg I magnetograms from 08:40 to 09:20 UT. Each frame corresponds to an average over 4 min. The averaging of the consecutive images

| Telescope | $\lambda$ | Time [UT] | Duration [min] | Images [No.] | Cadence [s] | FOV ["] |
|---|---|---|---|---|---|---|
| SST | G-band | 08:47-09:07 | 20 | 76 | 15 | 68.5×68.5 |
| | | 09:14-09:46 | 32 | 128 | 15 | 68.5×68.5 |
| HINODE | CN | 08:40-09:20 | 40 | 70 | 35 | 19.2×74.1 |
| | CaII H | 08:40-09:20 | 40 | 71 | 35 | 19.2×74.1 |
| | MgI | 08:40-09:20 | 40 | 143 | 20 | 15.4×65.3 |
| | SP FeI | 08:40-09:44 | 64 | 1954scans | 1.6 | 2.7×40.9 |

TABLE 3.1— Multi-wavelength data time series description.

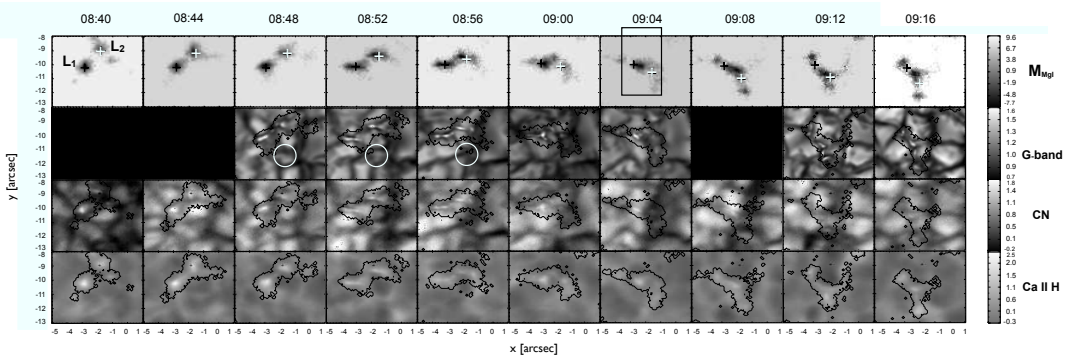


FIGURE 3.4— Quasi-simultaneous multiwavelength maps of the event. *From top to bottom*: Mg I magnetogram, G-band images, CN and Ca II. BPs are detected in all filtergrams and co-spatial with magnetic concentrations of Mg I magnetogram, overplotted to the filtergram images. Scale of the Mg I magnetogram $V/I$ is multiplied by $10^{-3}$.

still allows to easily identify the structures present in all images. Overlaid to the corresponding filtergrams are magnetogram contours that are useful to visualize the co-spatiality of the features observed at different wavelengths. The grayscale bars indicate the intensities normalized to the mean intensity of the whole data set for the respective wavelengths. The Mg I LOS magnetograms shown consist of masks obtained after applying a threshold of $3\sigma$ to remove the noise effects following Krivova and Solanki (2004). The good agreement between the magnetic features detected in these images and the bright elements present in the filtergrams gives us confidence to justify its use. Treatment of Spectropolarimetry data experience the same procedure to avoid noisy pixels, as commented in Section §3.4.

At first inspection, it is evident the apparent rotation that suffers the magnetic feature over the 40 minutes elapsed. We can see a magnetic structure with two main lobes, (denoted by L1 and L2 in the first frame of the top row of Figure 3.4,

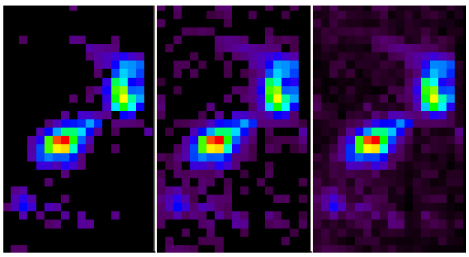

FIGURE 3.5— SP image of the sequence shown in Figure 3.6, at 08:40 UT. From left to right, the image showing a 5$\sigma$ mask, 3$\sigma$ and image without masking.

with one of them rotating around the other. This movement is also detected in the various wavelengths, i.e. different heights in the solar atmosphere. G-band and CN data provide information at photospheric level, while Ca II H images and Mg I magnetograms retrieve information from the low chromosphere. During the interval between 09:00 and 09:08, the L2 lobe seems to dissolve. Its magnetic signal appears to be decreasing, but increases again when the whole structure has rotated and L2 approaches the lower part of the FOV. An increase in intensity is observed in Ca II images and it is accompanied by the appearance of BPs in G-band, while in CN the signal is more diffuse. As a consequence of the rotation, small-scale processes of fragmentation and coalescence of BPs clearly discernible in G-band filtergrams take place along the intergranular lane. The BPs are also detectable in CN images, although the appearance is not so well defined as in the SST data, specially towards the end of the sequence. The good agreement between the small elements detected in Ca II H and the other wavelengths is also remarkable.

## 3.4 Spectropolarimetric analysis of the event

HINODE's *dynamic mode* was set to allow the study of extremely dynamic events by operating with an exposure time of 1.6 s per slit position. The noise level was $1.6 \times 10^{-3} I_c$ for Stokes $I$ and $1.8 \times 10^{-3} I_c$ for Stokes $Q$ and $U$. Due to the short exposure time, the noise level increases considerably. In order to remove the noise effects present in the data, we apply different thresholds to create masks. Depending on the purpose, a very restrictive selection can mask out the noisy pixels but also removes some small-scale structures. In Figure 3.5 the original image without removing any noise is shown at the right. The left and central panel show masks at 5$\sigma$ and 3$\sigma$ respectively. In the 5$\sigma$ image, is evident that the main magnetic structure remains unaltered as well as some conspicuous bright points

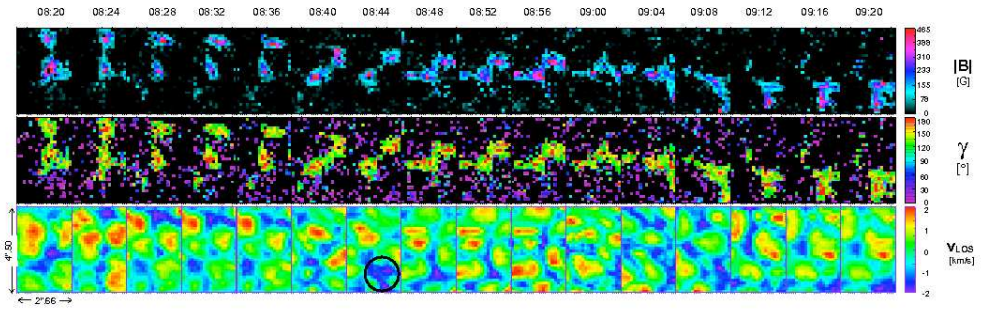


FIGURE 3.6— Spectropolarimetric map series. *From top to bottom*: magnetic field strength, inclination and LOS velocity single maps obtained by inverting SP data. As it is displayed, not all pixels are considered for inversion (see Figure 3.5) for details. The velocity is obtained by Stokes $I$ Dopplershift.

(see for instance the BP chain to the left of L2, or the ones located to the south of L1). However, in the $3\sigma$ image, we can trace better the aforementioned structures, in comparison with the G-band images and Mg I magnetograms.

Figure 3.6 displays the evolution of the magnetic structure in the sequence of individual maps of magnetic field strength $|B|$ and inclination $\gamma$ retrieved by LILIA (first and second rows) and LOS-velocity, $V_{LOS}$[2], obtained from the Dopplershift using the Stokes $I$ centroid calculation at the third row. The reader is referred to the Section §1.4.2.3 on Chapter §1 for explanations of these concepts and methods. Some pixels are eliminated when their signal is below the noise level to avoid the inversion of non-reliable pixels. However, the Stokes $I$ Dopplershift velocity is unmasked for a better visualization.

Similarly to what is observed in the Mg I magnetograms, the two magnetic lobes L1 and L2 are also clearly distinguished in the $|B|$ maps displayed in the first row. SOT-SP data started earlier than the filtergrams and magnetograms described above. The first five frames display the evolution of the magnetic structure prior to 08:40 where we can see that it is already rotating. There are not appreciable changes in the magnetic field strength throughout the whole sequence, the peak value being close to 600 G at 08:42 (though not included in the displayed images in the figure). The area of the structure seems to shrink with time. In particular, from 09:00-09:20 the magnetic patches evolve from binding together, when the two

[2]Note that the velocity signs in this Chapter are inverted, i.e., downflows have negative velocities.

structures lose their identity and part of them merge to an elongated shape. The Y-shape structure that is evident in the Mg I magnetogram (at about 09:12 UT) is not visible here, probably due to the lower resolution of the SP data. SP maps are available until 09:44 (though not shown in the figure) and show that the structure continues rotating after 09:20 when the SOT-NFI and BFI time series end, with L1 and L2 approaching each other towards the end of the observing interval. The inclination (second row of Figure 3.6) and azimuth (not shown here) remain stable during the whole observing period. Magnetic flux tubes are vertically oriented with inclination values close to 180 degrees. However, changes in the inclination can be seen at 08:44, when some BPs appear in between the magnetic lobes.

In the $V_{LOS}$ maps (third row of Figure 3.6), the granules are clearly distinguished as upflows with ranges from 1 to 2 $\mathrm{km\,s^{-1}}$ , and the intergranular lanes are the areas corresponding to downflows from -1.3 to -2.0 $\mathrm{km\,s^{-1}}$ . A strong downflow region appears at 08:44 UT (encircled area in Figure 3.6) that denotes the location where the photospheric vortex forms. It remains there for several minutes (until 08:56), and at 09:20 is observed again at the location of L2 at the end of the sequence though much less intense. The magnetic patches appear in the lanes, with a couple of exceptions where the magnetic areas do excursions into granules (at 09:00 and 09:07 UT). During the whole sequence, numerous small-scale processes take place leading to the formation of BPs.

Figure 3.7 shows the SP data sequence. From 08:20 UT to 09:20, images every 4 minutes are presented. The top row displays the LOS magnetograms obtained by computing the absolute value of $V/I$. In the middle sequence the integral of the absolute value of Stokes $V$ is shown, and in the bottom one the line-of-sight (LOS) velocity. The magnetic structure, as seen in the magnetograms and the unsigned Stokes $V$ maps, integrated from -29 pm to $+29$ pm – proportional to the magnetic flux – shows the same configuration than in the first row, and can be generally described as having two magnetic lobes. At 08:48, some bright points start developing between the two lobes, and some of them can be seen moving nearby the lower lobe. The apparent rotation of these magnetic structures, about 150° in one hour, is observed in this sequence. These magnetic patches follow a path whose common centre is a draining point. At 09:04, more GBPs develop in the lower right corner and the rotation becomes more evident.

## 3.5 Photospheric plasma flows

The G-band series from SST have been used to analyse the horizontal proper motions of structures in the FOV. Proper motions were measured by using the

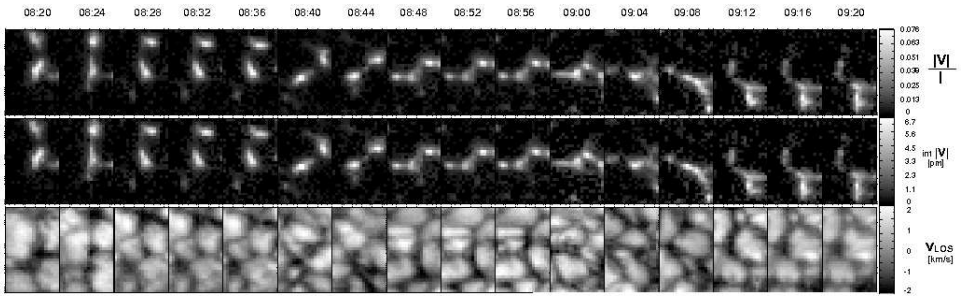


FIGURE 3.7— Figure displaying the maximum value of Stokes $V$ at the first row, and the unsigned Stokes $V$ maps in the second row. The $V_{LOS}$ is shown in the third row, resembling a continuum image.

LCT technique aforementioned. Maps of horizontal velocities are calculated for the time series by using a Gaussian tracking window of *FWHM* $1\farcs0$. Figure 3.8 shows the flow map computed from the first of the SST time series (*s1*). This map of horizontal velocities is calculated by averaging over the total duration of the series (19 min). The underlying background image represents in false-colour the normalized divergence field. Horizontal velocity magnitudes are averaging-dependent values (Vargas Domínguez, 2009), though the flow patterns yielded by the analysis of proper motions are commonly treated as representing plasma motions thus enabling the detection of general trends which are our main purpose here (e.g. sinks or granulation downdrafts where the cold plasma returns to the solar interior). The map of horizontal displacements is dominated by flows coming from granular explosive events and commonly associated to mesogranulation (Roudier and Muller, 2004; Bonet et al., 2005). Noticeably, we identified only a pair of examples where strong sinks are present at intergranular lanes (coordinates [6.5,3.5] and [8.5,7.5] in arcsec in Figure 3.8) but, different from other areas displaying downflows, these are characterized by being the draining point where all horizontal velocity vectors in the neighbourhood converge. Both vortex-type events last for several minutes ($> 20$ min). Nevertheless, the one framed in the two boxes in Figure 3.8 is less stable and has a defined onset in our data (at $\sim$08:48 UT) but also appears to be the final destination of the magnetic concentrations being dragged from an upper location (at coordinates [6.5,3.5] in the same figure), as shown in Figure 3.9. The latter vortex remains rather stable but disappears abruptly in the map of horizontal velocities computed for *s2* which is dominated by an organized flow coming from the lower right part of the FOV (Figure 3.9, right). Unfortunately, as commented before, there is a 7-min gap between *s1* and *s2* meaning that it is not possible to

determine exactly when the vortex disappears.

In Figure 3.9 we plot the trajectories followed by the *centroid* of the distribution of magnetic intensity for lobes L1 and L2. The *centroids* denoted with plus-signs and asterisks for the respective lobes are calculated for the individual maps obtained from SP data with a cadence of ∼36 s. Mathematically the centroids are defined by:

$$x_c = \frac{\sum_{i=1}^{N} x_i M(x_i, y_i)}{\sum M(x_i, y_i)} \tag{3.3}$$

$$y_c = \frac{\sum_{i=1}^{N} y_i M(x_i, y_i)}{\sum M(x_i, y_i)}, \tag{3.4}$$

where $(xi,\ y_i)$ are the coordinates of the $i$th pixel in the binary-object representation of each lobe and $M(x_i, y_i)$ is the SP magnetic signal for that given pixel. In spite of the lower resolution we make use of this data set because the time series extends until 09:44 UT, allowing to track the dynamics of the magnetic structure over a longer period. The trajectories are overlaid to both, the flow maps computed for the SST time series (*s1* and *s2*) and the divergence field for each series respectively. While the motion of L1 is confined to a radius of approximately 1″, L2 travels a much larger distance. In the time interval prior to 09:14 its motion seems to be strongly influenced by the vortex formed in the coordinates [3.5,1.5] in the left panel of Figure 3.9, increasing its velocity when it approaches this location. After the vortex has disappeared, L2 continues its movement probably influenced by the continuous evolution of the surrounding granules towards a new sink located at the coordinates [1.0,2.5] in Figure 3.9 (right). We suggest two possible scenarios explaining the observed event of magnetic concentrations being dragged towards the vortex centre. First, this could be the result of the stochastic evolution of granules which let the BPs approach closer to the radius of influence of the vortex, which accelerates their motions and eventually fall into it (*surface scenario*). On the other hand, the analysis of SP data suggests the presence of long lasting ($> 1$ h) vertical magnetic flux tubes. The rotation experienced by the magnetic structure anchored deep beneath the surface probably causes the twisting and the consequent formation/disappearance of photospheric BPs as observed in G-band and CN. The latter scenario might explain better the fact that we do not detect any BPs following trajectories towards the vortex located in the upper right corner of the FOV in Figure 3.8 that appears to be bigger, more stable and closer to the initial location of the BPs under analysis.

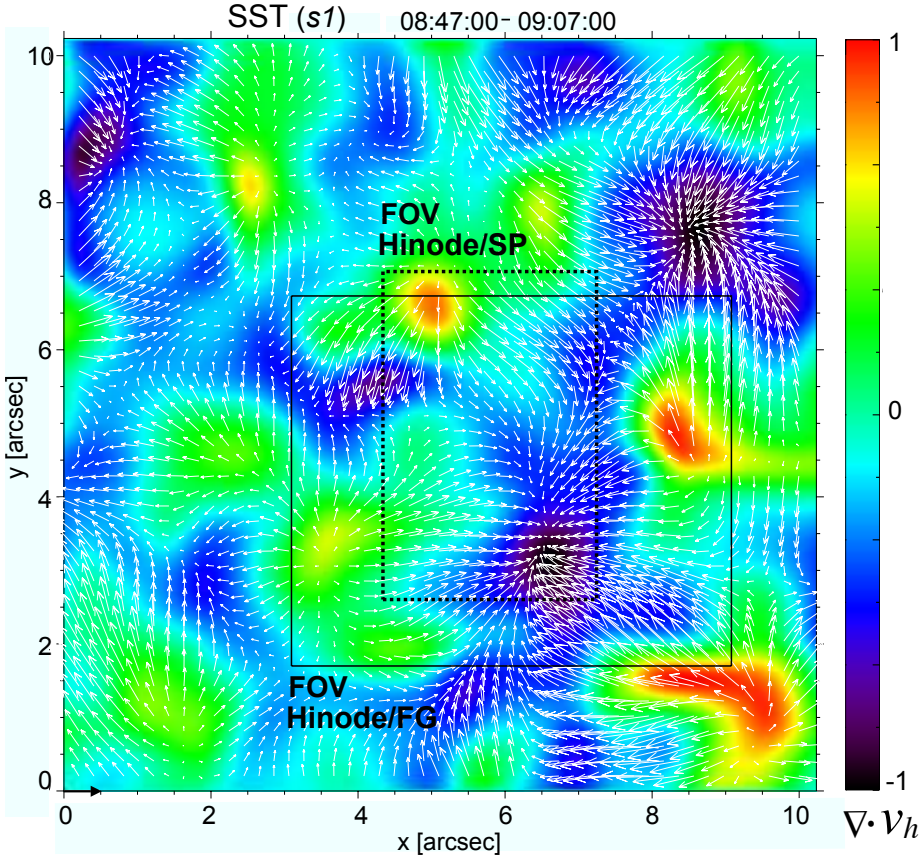


FIGURE 3.8— Map of horizontal velocities (*FWHM* 1.″0). The length of the black arrow at coordinates [0,0] corresponds to 1.5 $\mathrm{km\,s^{-1}}$. The background image represents the normalized divergence field. The solid/dotted boxes represent the FOV covered by the sequences of images in Figure 3.4 and Figure 3.6, respectively.

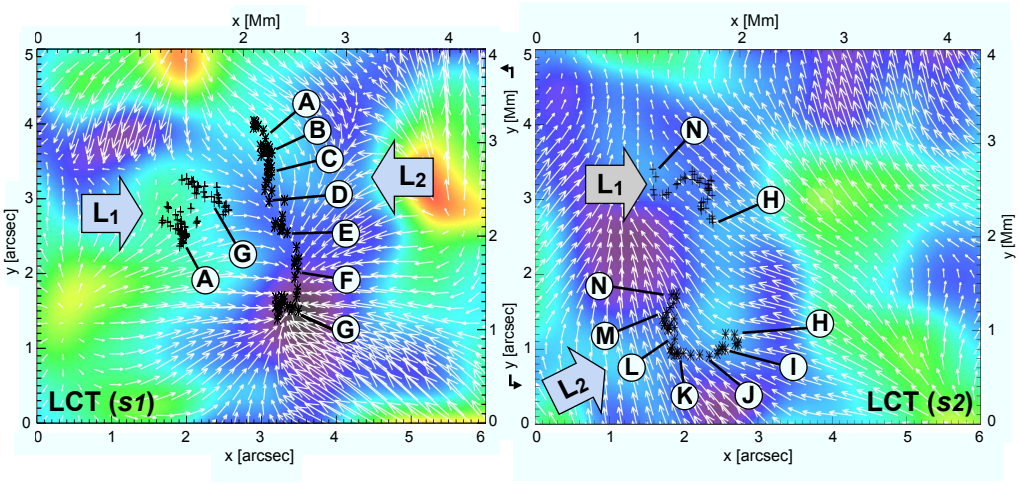


FIGURE 3.9— Temporal evolution of the magnetic centroid for both lobes ($L_1$ and $L_2$) in Figure 3.4. The trajectories followed by the centroids are plotted independently and against the flow maps computed for SST/G-band images in time intervals: *s1* (*left*) and *s2* (*right*). The background false-coloured image is the divergence field computed from each flow map respectively. Alphabet letters correspond to UT times as follows: **A**-08:40, **B**-08:48, **C**-08:56, **D**-09:00, **E**-09:04, **F**-09:08, **G**-09:12, **H**-09:21, **I**-09:24, **J**-09:28, **K**-09:32, **L**-09:36, **M**-09:40,**N**-09:44. The FOV is the same boxed in solid line in Figure 3.8.

## 3.6 Statistics of small magnetic elements

This Section appeared in Balmaceda et al. (2009). Bright points were identified in 40 HINODE CN images (one image per minute) using the $MLT4$ algorithm developed by Bovelet and Wiehr (2008). The technique consists in recognizing different levels of intensity and segmenting the image according to the level selection of features above a brightness threshold. The method performs a normalization of each cell to their maximum. A method of erosion or shrinking allows us to differentiate between the segments separated by dark lanes. Merging the structures afterwards permit fusing the structures that overlap, or discarding the very small features. Information about sizes and brightness of BPs could thus be obtained once segmented properly. The scaled intensities are calculated over the N-pixels of each BP:

$$I_{\rm scl} = \frac{1}{N} \times \sum_i \frac{I_i}{I_{\rm mean}}, \tag{3.5}$$

where $I_{\rm mean}$ represents the mean intensity for the whole image. Extensive and profound analyses of different segmentation methods are reported in DeForest et al.

(2007). Basically, segmentation methods are divided in three phases: finding the local minima through the second derivative to differentiate between bright structures (granules and BPs) and intergranular lanes; in the differentiation (segmentation), the structures can be convolved to be dilated (to eliminate too small structures) and merged, or eroded, depending if the segmentation is used for detecting small or larger features.

Typical values of the magnetic flux density are estimated of the order of hG in the small-scale magnetic elements. Most of the features have areas smaller than 0.1 square arcseconds, although these structures cover a wide range of values. The areas of BPs observed in G-band are considerably smaller than they are in CN, with peaks at 0.02 and 0.06 square arcseconds, respectively. The diameter of BPs can be calculated assuming a circular shape. The distributions of this parameter show peaks at $0\farcs27$ and $0\farcs14$ for CN and G-band BPs respectively. The apparent large difference between these properties derived from these two wavelengths can be attributed to the higher resolution of the telescope and the narrower passband width of the G-band filter in SST that makes possible to resolve individual small features when they are located in chains containing numerous BPs. In CN, instead, they appear blurred so they are often counted as a single feature. Probably for the same reason, BPs are more numerous in G-band. The coverage for BPs is 0.26% [3], while for CN it is 0.22%. Both distributions of the scaled intensities for BPs observed in CN and G-band show a maximum between 1 and 1.05. However, in G-band, some elements show values spanning from 0.9 to 1.8, while in the CN bandhead the highest scaled intensity is 1.25. A summary of these values can be found in Table 3.2.

| | CN | Gband | Small mag. elem |
|---|---|---|---|
| Lifetime [min] | 10 | 10 | 10 |
| Max. norm. intensity | 1.25 | 1.8 | 0.05 (mean(V/I)) |
| Area [$''^2$] | 0.06 | 0.02 | 0.05 |
| Diameter [$''$] | 0.27 | 0.14 | 0.1 |
| Surface coverage [%] | 0.22 | 0.26 | 0.31 |

TABLE 3.2— Summary table of properties of GBPs.

[3] Very recently, Cabello I. (PhD. thesis, 2012) shows a G-band BP coverage of 0.52%.

FIGURE 3.10— Comparison of longitudinal magnetograms from SP (*left*) and from SOUP (*right*).

## 3.7 Other spectropolarimetric studies

All these data sets obtained in such an extensive campaign are very rich, as they are quasi-simultaneous and co-spatial. In this Section, we establish comparison between other magnetograms, and study some events that exhibit convective collapse behaviour.

### 3.7.1 Comparison with magnetograms and weak-field approximation

In this Section we aim to verify the relatively low values obtained in previous Sections through two methods: comparison with a calibrated magnetogram and the application of the weak-field approximation.

A SOUP magnetogram taken at 09:04 UT on 2007, September 29, and co-temporal SP scans were selected for direct comparison. The MOMFD-restored longitudinal magnetogram acquired by the SST presents a pixel sampling of 0.″067, and noise level of $4 \times 10^{-3} I_c$. This magnetogram has been noise-filtered by a noise mask of $1\sigma$ or equivalently, 69 G. Taking advantage of the SP data, we can select a map with a time difference of less than 30 seconds with respect to SOUP data. Since we only have a SOUP magnetogram, we maximize the usable area of this magnetogram. Therefore SP data are cropped to a common FOV, which is the maximum area of the scan images (2.″66 $\times$ 40.″96). Then we can compare a calibrated SOUP magnetogram to the magnetic field strength obtained by inversions. The SOUP magnetogram and the SP longitudinal magnetogram are presented in Figure 3.10.

A magnetogram calibration for SOUP data was performed in the work of (Berger et al., 2004). It was carried out through the Equation which links the percentage

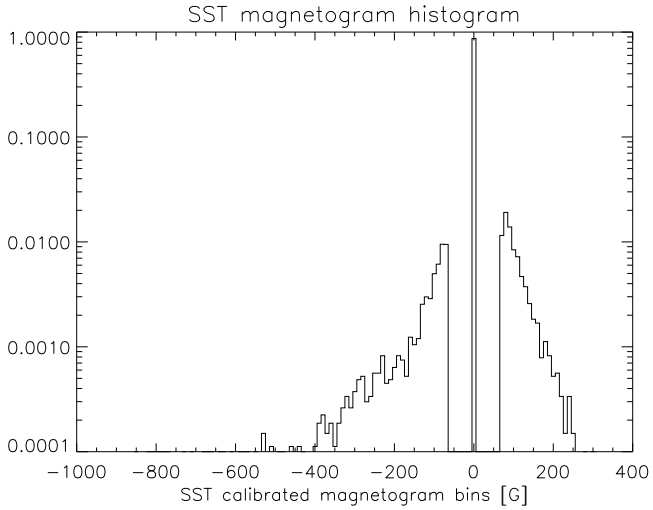


FIGURE 3.11— Histogram of a SST-SOUP calibrated magnetogram, in logarithmic scale. The data gap shown is due to $1\sigma$ filtering of the longitudinal magnetogram.

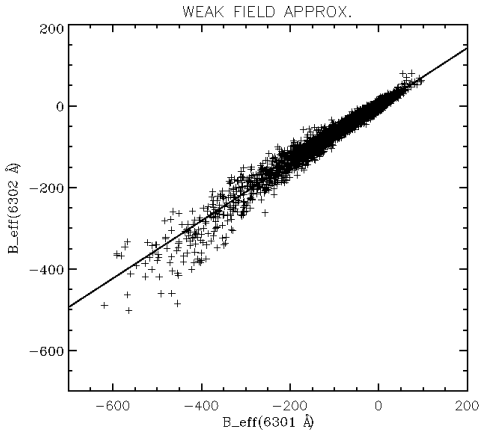


FIGURE 3.12— Weak field approximation ratio of Fe I 6301 and 6302 Å on HINODE-SP data.

of circular polarization $\mathbf{P}$ with the magnetic flux $\mathbf{M}$ (units are Gauss or Mx m$^{-2}$) is:

$$\mathbf{M} = \alpha \mathbf{P} \tag{3.6}$$

The calibration constant $\alpha$ is equal to 16551 Mx m$^{-2}$ (Berger et al., 2004). A limitation of this calculated factor is that the study was performed by comparison of MDI data, that exhibit a large pixel size, and whose working wavelength of MDI was Ni I 676.8 nm, different from the common Fe I lines of both SOUP and HINODE-SP. In Figure 3.11, a histogram of this calibrated magnetogram is shown. Using the previous factor $\alpha$, the histogram reach a value of -800 G, but the bulk of the values are around -200 G, which is in agreement with the inversions. The Weak-field approximation (Section §1.4.1) is also used for cross-checking the values of the effective magnetic field of these structures. The subset contains 20 minutes of HINODE SP scans of 4.″5. This FOV is selected in this way since it is the area under study for the vortex-like flow. The weak-field approximation is applied for both lines 630.1 and 630.2 nm, and plotted in Figure 3.12. The calculated slope is 0.70±0.04 in agreement with Martínez González et al. (2006), who retrieves 0.70±0.01 (for the line ratio) and Domínguez Cerdeña et al. (2003), which value is the inverse of 1.28±0.1, that is 0.78.

### 3.7.2 Magnetic field intensification

The magnetic field intensification can be produced by experiencing a *convective collapse*, or *convective intensification* (Grossmann-Doerth et al., 1998), also called *superadiabatic effect* by Parker (1978). A convective collapse is the theoretical phenomenon in which small-scale magnetic elements can concentrate magnetic flux and reach kilogauss magnetic field strength by the adiabatic downdraft inside the tube (Spruit, 1979). An initial downflow of mass is assumed during the process and its temperature increases adiabatically in contrast to the much steeper temperature gradient of the surroundings, leading to an enhancement of the downdraft (Fischer et al., 2009). In Nagata et al. (2008), cases of high speed downflows followed by an intensification of the magnetic field and the appearance of bright points were shown. In the cases presented here (see Figure 3.13), small magnetic patches experience a sudden strong downflow and some intensification of the magnetic flux. Since magnetic elements are actually present in the locations before the event (i.e. the strong downflow appearance), these cases are likely convective collapses of a part of the magnetic area or a flux intensification, and could be explained as unstable

flux tubes with high field strength (Spruit, 1979). The process of flux concentration is connected with strong redshifts, while the destruction of a magnetic structure is associated with large blueshifts (Bellot Rubio et al., 2001). In Narayan (2011), the increasing velocities in downflows correspond to magnetic field intensification. The Stokes profiles also experience changes in the case of magnetic field intensification. By the Zeeman effect, we can see the amplitude growth on Stokes $V$. But also asymmetries in the profiles of Stokes $I$ and $V$ can occur. These asymmetries can be explained in different contexts: when a strong gradient of velocity or magnetic field happen in a small magnetic element, the Stokes $V$ profiles can appear three-lobed (del Toro Iniesta, 2003; Orozco Suárez et al., 2008, and references therein). The Stokes $V$ area asymmetry becomes negative if the magnetic field increases with depth and the vertical flow speed increases in the direction of the velocity vector, which is a downflow whose speed increases with depth (Grossmann-Doerth et al., 1998). The three-lobed Stokes $V$ profiles could be explained also as several 'normal' profiles being redshifted (Bellot Rubio et al., 2001). Aborted convective collapses can cause upward shocks, which can generate asymmetries in $V$ profiles. Fischer et al. (2009) report convective collapses with a duration of about 10 min, where $2/3$ of them present strong downflows in Mg I Dopplergrams. The size of the ones presenting downflows varies from $0\farcs48$ of radius to $0\farcs38$ after the collapse has occurred. Some of these phenomena can lead to fragmentation and coalescence, similar to the events found in Viticchié et al. (2009).

In our HINODE observations, we found a few cases of events that could be convective collapses and we have investigated them below. These cases are interesting, since they can provide an observational counterpart to the simulations, for instance, of Danilovic et al. (2010). This particular region investigated show a vortex flow (see Figures 3.8 and 3.9), and afterwards the field magnification happens.

Figure 3.13 shows: **1)** Stokes $V$ profiles of 630.15 and 630.25 nm Fe I lines, **2)** maps displaying LOS velocities obtained by Dopplershift calculation on Stokes $I$ and **3)** co-temporal magnetograms in absolute value, for two cases (Case 1 and Case 2) of plausible convective collapse events.

In Case 1 (see row labeled **A** in Figure. 3.13), the Stokes $V$ profiles are plotted every 32 s, measured at the centre of the region encircled in white in the maps (at 09:22:08 UT). A green crosshair pinpoints the area where the profiles in **A** are obtained. Asymmetries between the two lobes are evident. In the fourth panel in **A**, a three-lobed profile appears in the 630.15 nm but not in the 630.25 nm line, suggesting the presence of stronger gradients of magnetic field strength or velocity higher up than in the lower photosphere (630.15 nm line). This phenomenon takes place during the period 09:22–09:25 UT, when the maximum LOS velocity

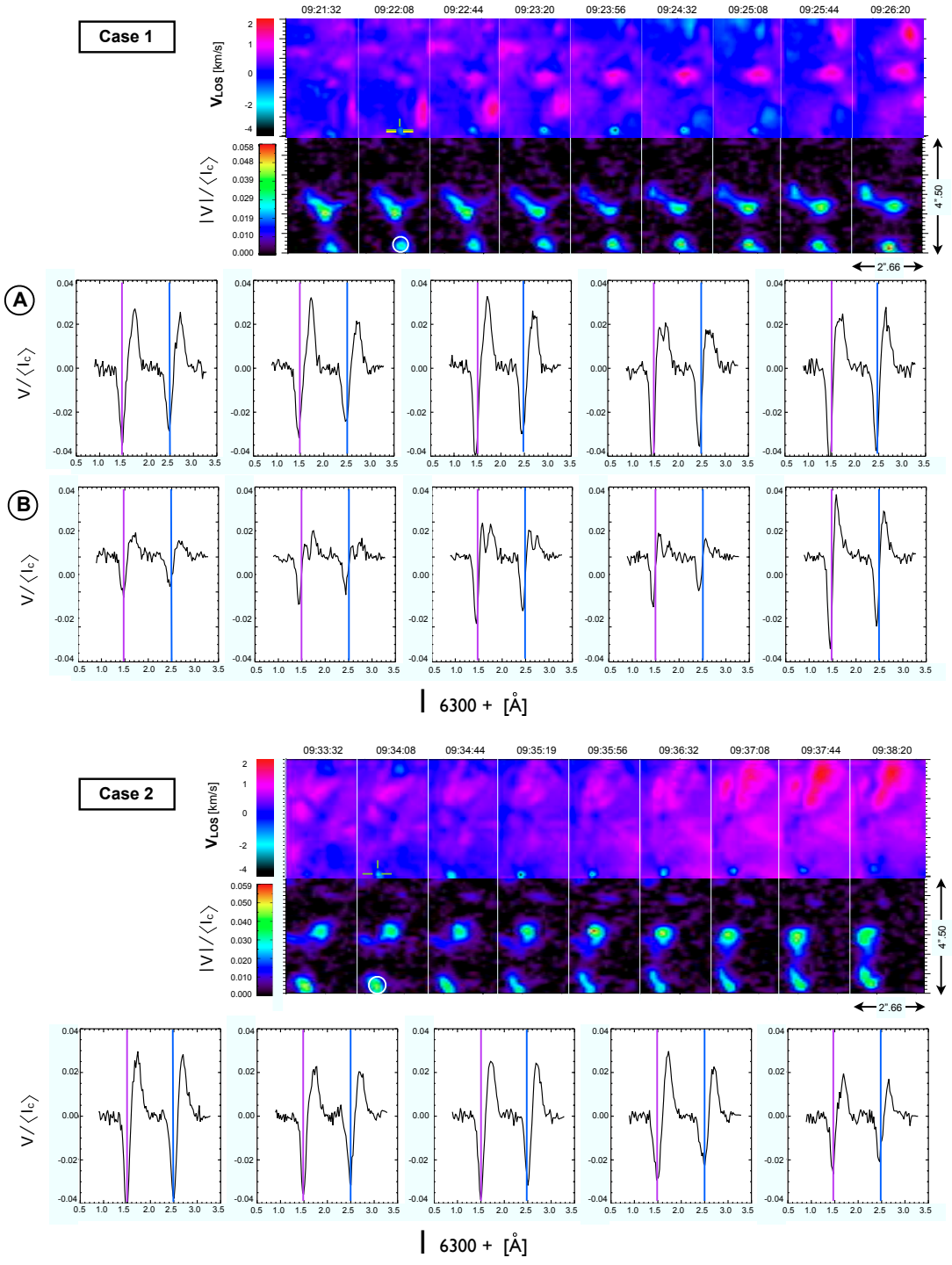


FIGURE 3.13— Detected cases of plausible convective collapse events in HINODE data on 2007, September 29. For every case the temporal sequence of LOS Doppler velocities (*upper row*) and magnetic signal (*lower row*) are simultaneously shown in false-colour maps. Encircled in white are regions displaying redshifts accompanied by an intensification in the magnetic field. Stokes $V$ profiles are correspondingly plotted for these regions (from the subpanel holding the white circumference to the following four ones), along with magenta and blue lines indicating the nominal wavelengths.

is about -3.5 $\mathrm{km\,s^{-1}}$ . The sequence in row **B** (Case 1) in the same figure shows the Stokes $V$ profiles for an adjacent pixel, pinpointed in yellow by a crosshair. Again, the appearance of three-lobed Stokes $V$ profiles indicate gradients of velocity. In the fourth panel, a sudden appearance of a more symmetric profile suggests 'stabilization' on the magnetic field or velocity gradients of the BP. In the G-band filtergrams, the presence of new BPs associated to this event are observed in this region (at 09:20).

Figure 3.13 (Case 2) displays the evolution of another probable case of convective collapse. The symmetric profiles, calculated for the encircled region in the corresponding maps at 09:34:08 and the pixel marked by a green crosshair, do not suggest strong changes in gradients and the magnetic region is rather stable over the time. However, during an interval of 66 s we observe a variation in velocity from -1.0 to -3.5 $\mathrm{km\,s^{-1}}$ . Similar to Case 1, BPs appear in this location in the G-band images (encircled in white at 09:34 simultaneously to the convective collapse event and lasting for about 8 min).

Velocities in the magnetized atmosphere can be estimated from a zero-crossing Stokes $V$. We can perform a rough guess from the Stokes $V$ profiles and their nominal wavelengths, marked with magenta for the 6301 Å and blue for the 6302 Å line. We estimate the wavelength shifts are about 0.1-0.15 Å, which lead to downflow velocities in the range of -4.7 to -7.1 $\mathrm{km\,s^{-1}}$ . Therefore, another element of the convective collapse, the supersonic downflow, appears into play.

Both cases extend over an area of about 4–6 pixels (0.″30 $\times$ 0.″30) and have lifetimes of the order of 5–8 min. For Case 1 the magnetic flux decreases about 50% from the corresponding initial profile to the middle one in Fig. 3.13 (**A**) and increases afterwards up to reach a value closer to the starting one.

Asymmetric profiles and downflows have been found and explained in different works, like in Orozco Suárez et al. (2008); Fischer et al. (2009); Nagata et al. (2008). Also Bello González et al. (2009) found asymmetric Stokes $V$ profiles where a BP showed flux intensification and downflows. Very recently, in Narayan (2011), a similar study has been performed in a network area close to pores with SST data, leading to large downflows lasting from 3 to 5 minutes. The estimated size on the figures is around 0.″2-0.″3. The field intensification is around 2-3 times the field estimated at the starting of the measurement, leading to kilogauss magnetic field density only with the introduction of straylight.

# 4

# Vortex flows observed by IMaX

Vortex flows observed by the instrument IMaX onboard SUNRISE are inspected by different methods, and some new approaches have been explored in this Chapter.

Vortex omnivium. Obscura (2011)

## 4.1 Introduction

This Chapter presents a characterization of the convectively driven vortex flows in the photosphere through their representative magnitudes, the divergence and the vorticity. Since these quantities are derived from Local Correlation Tracking, we study how the different parameters involved in it can influence the computation of the divergence and vorticity. We also study these quantities for finding vortices in different physical magnitudes, namely intensity (through continuum ima-ges) and longitudinal magnetic field, via magnetograms. We compare magnetic maps to simulations and offer an explanation to the discrepancy of the results on the divergence and vorticity estimated by observations and simulations. Moreover, statistics of vortices found in the field-of-view are carried out, and their relation with divergence, vorticity, and horizontal velocity azimuthal angles as well.

## 4.2 Data

Two IMaX data series acquired on 2009, June 9 were selected close to the solar centre. The mode used was V5_6 mode, which included full Stokes vector imaging at five wavelengths $\pm$ 40, $\pm$ 80 mÅ and the continuum at +227 mÅ with six

accumulations. The effective cadence was 33 seconds. These data were obtained in the observation number 163, the series from cycles [208-249] and [307-364], 00:36-00:58 UT and 01:31-02:02 UT, respectively. Data were reduced according to the mentioned steps in Chapter §2. Further processing, as alignment and p-mode removal, is applied. The effective FOV is $45'' \times 45''$. All the fundamental physical parameters are retrieved, such as magnetic field, line-of-sight velocity, line minimum intensity, and line width. The continuum intensity is also used. The second series was used in the work of Bonet et al. (2010). In this Chapter we refer to the first series.

## 4.3 Methods

The main method used in this Chapter is the Local Correlation Tracking. We analyse the different parameters and their effects on divergence and vorticity computations on full field-of-view maps. Moreover, for small vortical events, others techniques are used, as the calculation of magnetic centroids, zero-velocity points and azimuthal angles.

### 4.3.1 General properties of the estimated magnitudes by Local Correlation Tracking over the whole field-of-view

The Local Correlation Tracking generates different patterns depending, as we mentioned before, on the boxcar window and the averaging interval. When we consider small tracking windows (*FWHM* smaller than $1''$) or averaging interval lower than 5 minutes, patterns can be more fluctuating and inaccurate than when large windows and averaging intervals are used. In the following Subsections we analyse the effects of these variables on continuum images and longitudinal magnetograms.

#### 4.3.1.1 Effects of windows size and averaging on LCT

The aforementioned dependencies are tested in this Section. With series of continuum intensity images of a total duration of about $\sim$21 minutes, we average over 2.5, 5, 10, 15 and 20 minutes, with window sizes of $1''$ and $1''.5$. In the Figures 4.1 and 4.2 we can appreciate the effect on the divergence and vorticity for different time averages and correlation windows. While for smaller time intervals, divergence and vorticity are larger, values are reduced when the average used is 20 minutes. A surprising effect is that the spatial patterns in both magnitudes do not vary dramatically within the range of time average from 5 to 20 minutes. However, for the 2.5 minutes averaged, the pattern and values are less reliable. For the divergence, the standard deviation between the 5-min and 20-min average is 0.001 for the

1″window size and 0.0006 for the 1.″5 window size. For the vorticity, the standard deviation is 0.0009 between the 5-min and 20-min average for the 1″window size and 0.0005 for the 1.″5 window size.

The effects on the average window are evident again in the Figures 4.1 and 4.2. Albeit the pattern is more diffuse with a window of 1.″5 size, the main features are coincidental for all divergence and vorticity maps. As previously mentioned, an average of 2.5 minutes can reach the most extreme values combined with the smallest window size (in this case, with *FWHM* of 1″).

In Figures 4.3 and 4.4, histograms of the studied magnitudes and their dependence of the variable are presented. The size of the histogram bins are condensed in Table 4.1.

| *FWHM* | 1″ | 1.″5 |
|---|---|---|
| div. | 0.0005 | 0.0005 |
| vort. | 0.0002 | 0.0001 |

TABLE 4.1— Binsizes for the histograms in Figure 4.3 and Figure 4.4.

The histograms in Figure 4.3 and Figure 4.4 represent the time average on different line styles, studied with two different correlation windows, i.e., 1″ and 1.″5. They show that the distributions of the shortest time average are wider than the longest ones. Some statistical properties, as the median, display values slightly lower than zero for the divergence. Vorticity shows an asymmetry on the right tail of the histogram, corresponding to positive vorticity (i.e, counterclockwise motion). This asymmetry on the tail for positive values is perceptible on both histograms for distributions corresponding to 5, 10 and 20 minutes. The skewness present positive values, in the order of $10^{-3}$ for the 1″ window size and of 0.04 for the 1.″5 window size.

In Figures 4.5 and 4.6, the dependence of the divergence and vorticity with time averaging is analysed. For the divergence, the longer the average, the larger the area that present sinks (divergence lower than zero), as areas covered by exploding granules or important emergences smooth with time and a larger correlation window. The areas of negative divergence dilate with a larger time average. This behaviour differs when studying the vorticity: when we try to find values (in absolute values) larger than 0.001, the number of pixels which meet this condition decrease. This can be also explained by the shape of the distribution, for both divergence and vorticity maps: the larger the average, the narrower the distribution, meaning that we can find less values over this particular threshold.

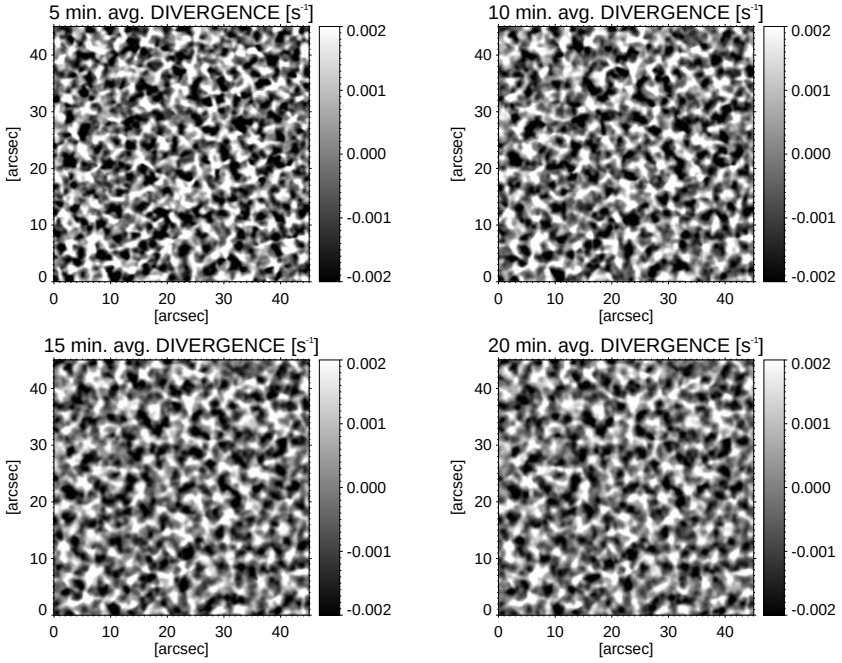


(a) Divergence maps with *FWHM* 1″.

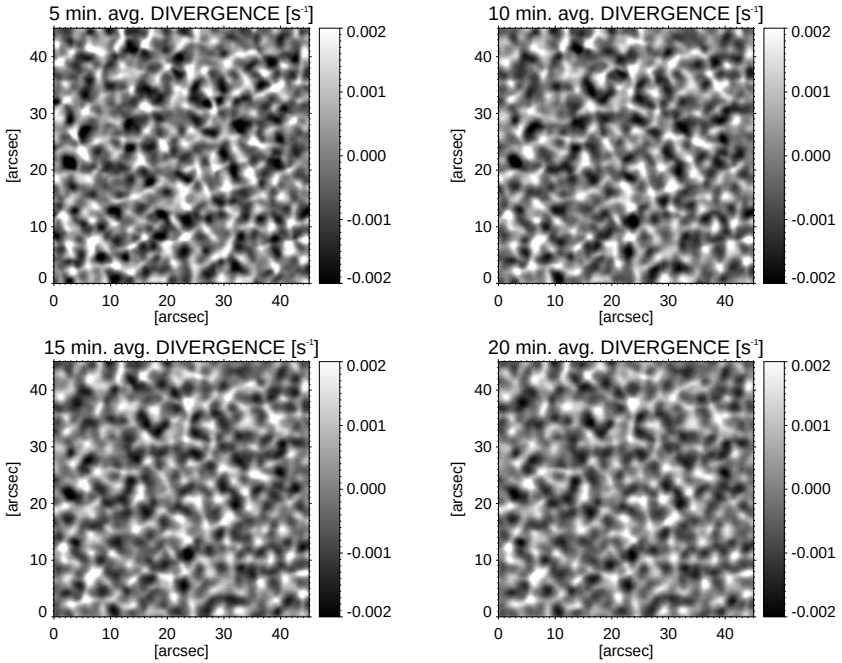


(b) Divergence maps with *FWHM* 1.″5.

FIGURE 4.1— Divergence maps, considering the time averaging and the window size. The four top images were made with *FWHM*=1″. The bottom four images were made with an *FWHM*=1.″5.

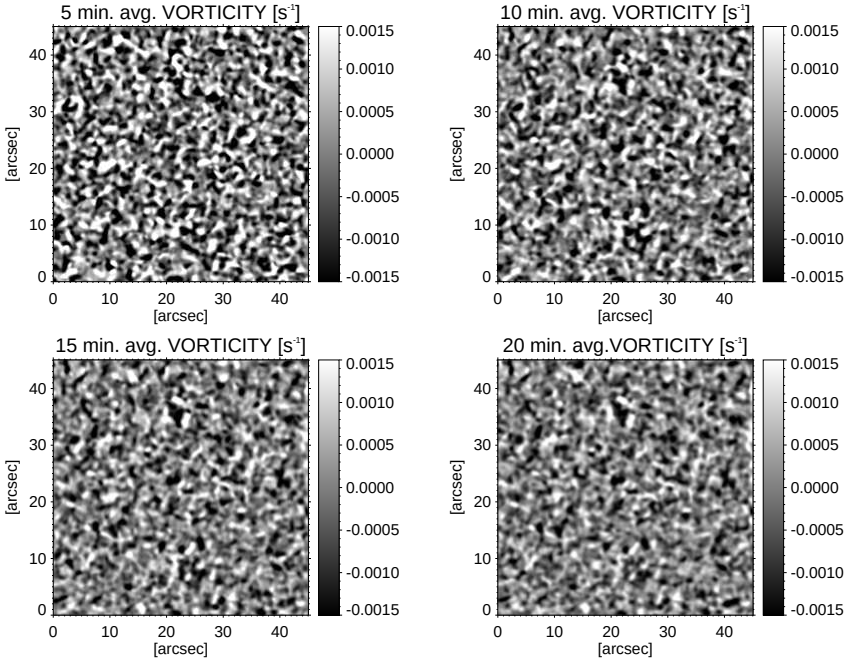


(a) Vorticity maps with *FWHM* 1″.

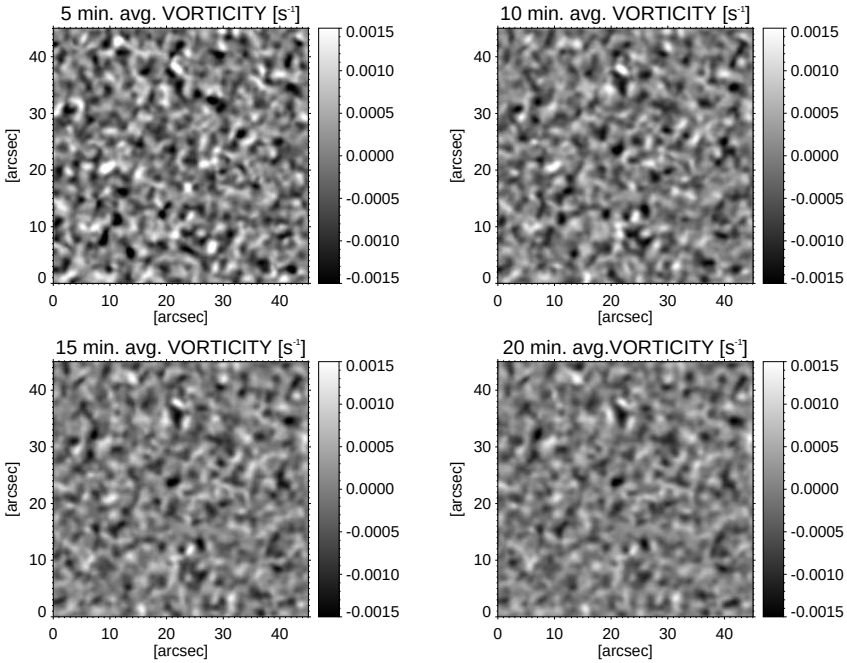


(b) Vorticity maps with *FWHM* 1.″5.

FIGURE 4.2— Vorticity maps, considering the time averaging and the window size. The four top images were made with *FWHM*=1″. The bottom four images were made with a *FWHM*=1.″5.

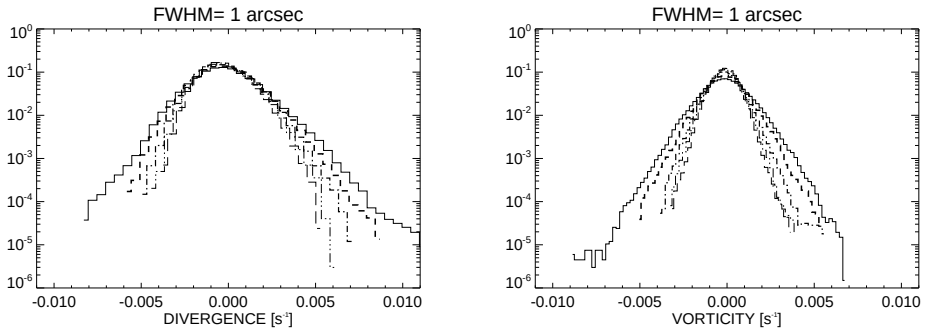


FIGURE 4.3— Distribution of the divergence and vorticity considering a window size of 1″. Lines represent the time average applied: the 2.5-minute average is represented in solid line (——). 5-minute average is symbolised by dashed lines (– – –). The 10-minute average, on thick dotted-dashed lines (· –). The 15-minute, with dot-dot-dot-dashed lines (· · · –). Last, the 20-minute average, is represented with long dashed lines (— —).

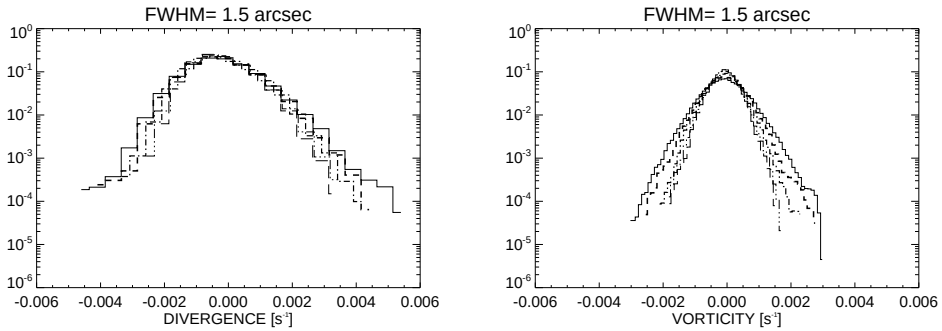


FIGURE 4.4— Distribution of the divergence and vorticity considering a window size of 1.″5. Lines represent the time average applied: the 2.5-minute average is represented in solid line (——). 5-minute average is symbolised by dashed lines (– – –). The 10-minute average, on thick dotted-dashed lines (· –). The 15-minute, with dot-dot-dot-dashed lines (· · · –). Last, the 20-minute average, is represented with long dashed lines (— —).

#### 4.3.1.2 Effects on magnetic field thresholding for LCT and comparison to different simulations

Another question that arises when using the LCT is the performance of its application in magnetograms. While in continuum the method works, sometimes we can find false positives in magnetograms, since the program is tracking noise. For this reason, the aim of this Section is analysing the effects of using masks in longitudinal magnetograms to reduce the noise on the LCT. Again, histograms of divergence and

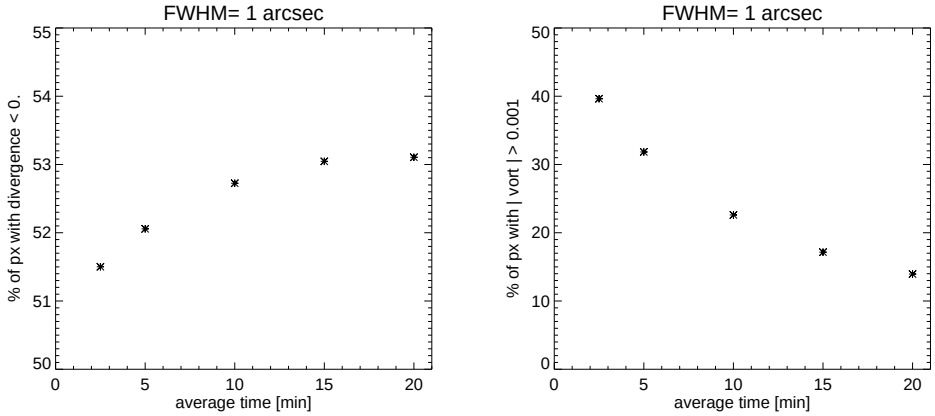


FIGURE 4.5— Proportion of surface with negative divergence and non-zero vorticity depending on time average with *FWHM*=1″.

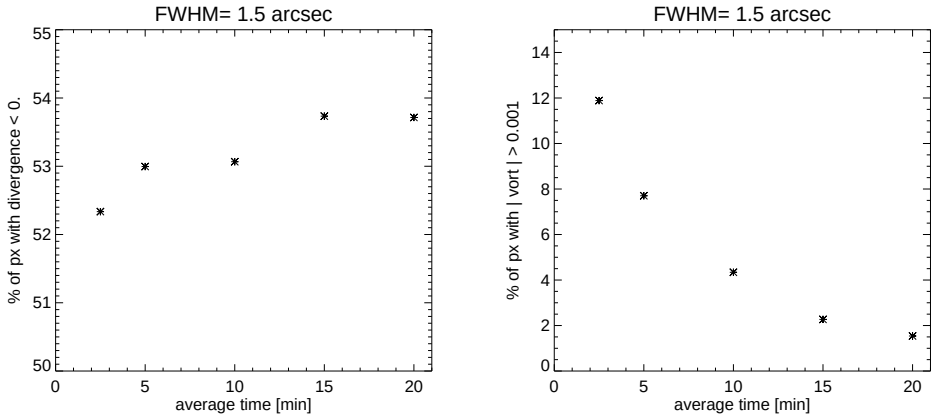


FIGURE 4.6— Proportion of surface with negative divergence and non-zero vorticity depending on time average with *FWHM*=1.″5.

vorticity have been computed. This time the longest series (20 min) and a *FWHM* window of 1.″5 was used. When we use masks for the magnetic field over one, two and three times the noise value to avoid the noise effects, we find the following distributions, shown in Figure 4.7. The $1\sigma$ histogram curve is very narrow, located in the center of the Figure. We shall remind that the maximum and minimum values are about $\pm 0.002$. However, when masking to $2\sigma$ and $3\sigma$, the distributions broaden substantially, reaching values up to $\pm 0.2$. These high values are typical

for numerical simulations. Indeed, simulations have the advantage that divergence and vorticity can be computed directly from the synthetic data, without having the flaw of averaging in time and being smoothed in the spatial range; therefore the calculated magnitudes are always higher than the obtained from observations.

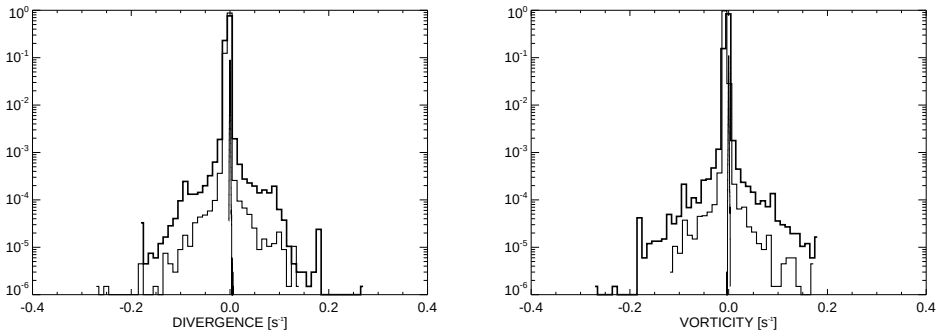


FIGURE 4.7— Histograms of divergence and vorticity for thresholded magnetic maps (in thicker lines: 1, 2, 3$\sigma$).

To check the last statement, we use a simulation appearing in Cheung et al. (2008). All details regarding this numerical simulation can be found in Section §5.3.4. Here we refer only to the results concerning divergence and vorticity. We analyse two case examples: the original synthetic longitudinal magnetograms, with a sampling of 0.″034, and a second, smoothed version of these longitudinal field frames. The LCT is applied with a *FWHM* of 1.″5 to both cases on these series, whose temporal average is their temporal span, i.e., 20 min. In Figure 4.8, these results are shown. The distribution of the original synthetic magnetograms is more spread and reaches higher values ($\pm$ 0.2) than the smoothed one, which reach up to $\pm$0.004. We can therefore conclude that the divergence and vorticity of the simulation give similar values and distribution than the divergence and vorticity of a real observation, with 2$\sigma$ and 3$\sigma$. For smoothed synthetic magnetograms, the distributions of divergence and vorticity can be compared to a 1$\sigma$-thresholded observational data.

Besides the synthetic magnetograms, the simulation in continuum is compared with observational data. The simulation and the observational data have been analysed through LCT with 1.″5. In Figure 4.9, similar distributions to Figure 4.8 are shown. The divergence and vorticity of the continuum intensity distributions are wider in the case of simulations than in observational data. However, in continuum, maximum values never reach the maximum values for magnetograms, thresholded

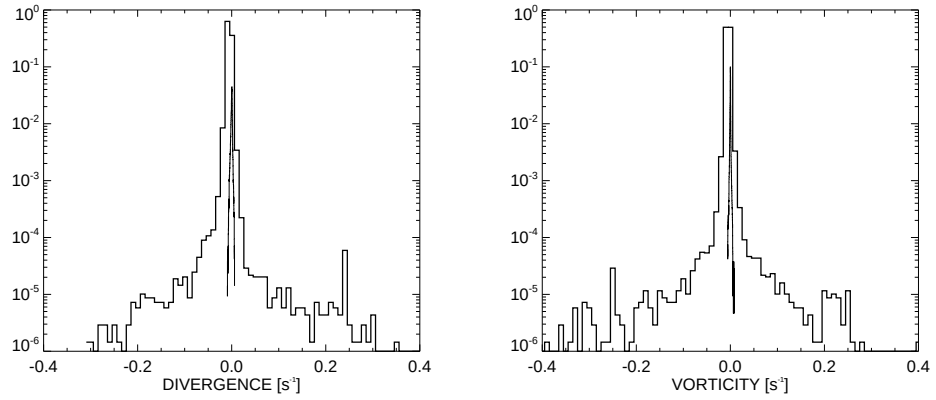


FIGURE 4.8— Histograms of divergence and vorticity in a simulation. The thick line represents the magnitudes for the synthetic magnetogram, and the thin line, for the degraded magnetogram. The bin size of the narrowest distribution is 0.0001, and for the all the wider ones, are 0.01.

or synthetic ones.

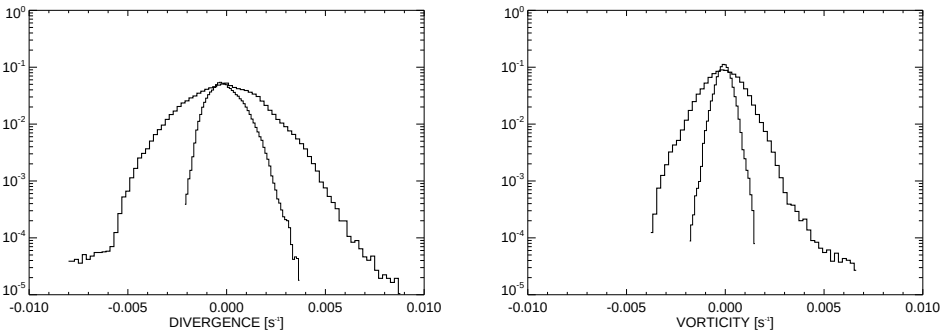


FIGURE 4.9— Histograms of divergence and vorticity in a synthetic continuum images and observed images. The thick line represents the magnitudes for the synthetic images, and the thin line, for the observed data. The bin size of the narrowest distribution is 0.0005, and for the all the wider ones, are 0.001.

#### 4.3.1.3 Another coordinate system for divergence and vorticity

When studying the divergence and vorticity, we can perceive that is difficult to describe a non-pure circular motion only with vorticity: large velocity components describing an ample arch can lead to same values than a proper circular motion.

Therefore, it is necessary to uncouple the curvature of the trajectory on the vorticity. Changing the coordinate system can be useful to achieve this uncoupling. Divergence and vorticity can be described on the *natural* coordinate system, that is, using the tangential and normal components instead of the Cartesian components for the velocity (see, for instance, Holton, 2004; Kundu, 1990). This reference system is displayed in Figure 4.10.

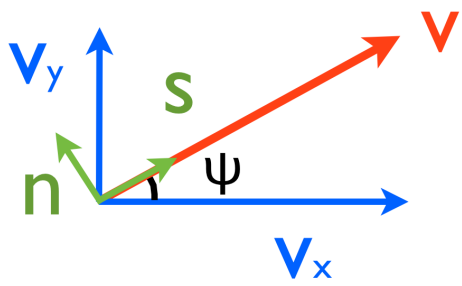


FIGURE 4.10— Reference system for velocity: in blue, Cartesian coordinates. In green: Natural normalized coordinates.

Therefore we have $\vec{v} = (v, 0)$ and the divergence can be expressed as:

$$\nabla \vec{v} = \frac{\partial v}{\partial s} + v\frac{\partial \psi}{\partial n}, \tag{4.1}$$

where $\psi$ is the direction relative to the coordinate system. The first part of the equation, $\frac{\partial v}{\partial s}$, is a measure of the stretching or shrinking of the velocity field (strain). The second part, $\frac{\partial \psi}{\partial n}$ indicates the *diffluence* or field vectors that become more separated when this quantity is positive. When field vectors *confluence* and mark proper convergence, with field vector shortening while approaching the zero-velocity point, this quantity is negative. A very visual case of diffluence on a diverging rotating fluid is presented in Figure 3.2, showing in the lower left panel a representation of positive vorticity, and also the flow lines are displayed separating from each other.

Vorticity can be also decomposed and analysed in this coordinate system as:

$$\nabla \times \vec{v} = v\frac{\partial \psi}{\partial s} - \frac{\partial v}{\partial n}, \tag{4.2}$$

where $\psi$ is the direction relative to the coordinate system. The quantity $v\frac{\partial \psi}{\partial s}$ indicates the shear vorticity, that is a measure for the change of the field vector perpendicular to the vector at that point. The shear vorticity can indicate where

is a center with velocity equal to zero, and its topology. The curvature vorticity, $-\frac{\partial v}{\partial n}$ takes into account the curvature and the sense of rotation (clockwise or counterclockwise).

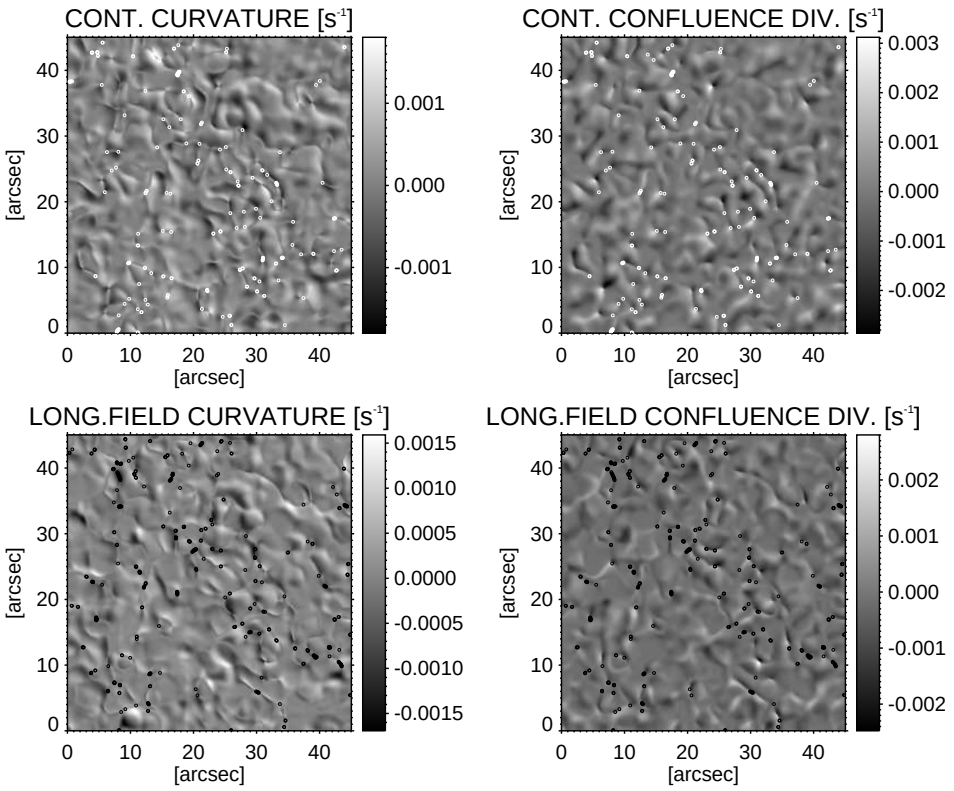


FIGURE 4.11— Curvature and confluence for continuum and longitudinal field.

Now the plots presented in Figure 4.11 are the curvature derived from the vorticity and the confluence, for maps calculated for a time average of 20 minutes and a *FWHM* of 1.″5. The places where the velocity is zero are marked by black circumferences for the longitudinal field and with white circumferences for the continuum maps. The confluence, or negative divergence, marks the pure convergence, removing the effect of velocity lines stretching or shrinking. The curvature diagrams show the vorticity without the contribution of the shear. An application of this decomposition for the vortex-like flow search would be trying to find them in locations with negative divergence, negative confluence and high curvature close to zero-velocity points.

#### 4.3.1.4 Zero-velocity and azimuth computation

From a idealized point of view, we can consider the vortex flow pattern as a point of null velocity (we can think on a hurricane to get the picture), and a convergent round pattern of non-zero velocity. We also can define and calculate the velocity vector angle, whose origin is the positive $X$-axis and spans from 0° to 360°. The horizontal velocities retrieved by LCT can be plotted regarding its angle. Employing this graphical method, potential centers of vortices can be found. Unfortunately, every structure with a circular flow pattern will be detected, as exploding granules.

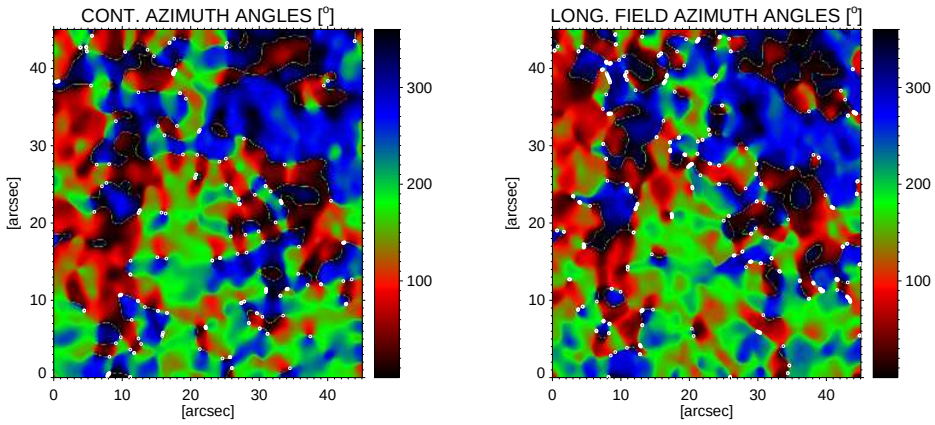


FIGURE 4.12— Azimuth angle of the horizontal flows for continuum and longitudinal magnetic field maps.

The zero-velocity map consists of plotting these quiet points with help of the horizontal velocity map obtained by the LCT. This is an advantageous way of knowing the final destination of *corks* without the need of developing a long-duration *cork* movie. Calculating the zero-velocity map for the duration of the time series is equivalent to wait for all the passive tracers to stop.

In Figure 4.12, these azimuthal angles are plotted, for a pattern of continuum images and magnetograms, computed with a *FWHM* of 1.″5 and 20-min average. The main directions are signalled by different colours: 0° in black, 90° in red, 180° in green and 270° in blue. Moreover, the centers with zero-velocity are marked with white circumferences in the continuum maps and white circumferences in the longitudinal field maps. The vortex-flow candidate patterns are the areas with a zero-velocity point surrounding by a pattern from 0° to 360°.

Another study performed consists of locating the zero-velocity points for dif-

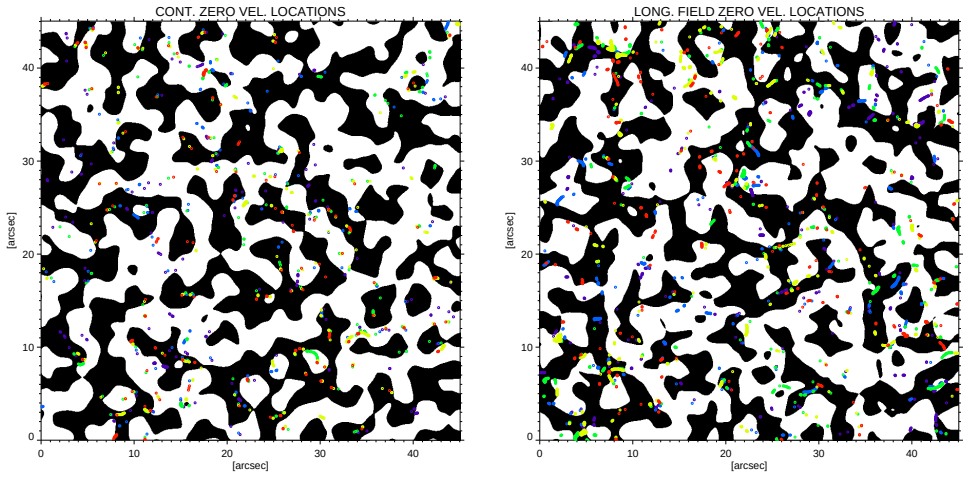


FIGURE 4.13— Zero-velocity points calculated for continuum (*left*) and longitudinal field maps (*right*). Colours denote the zero-velocity points for 2.5-min average, in purple; for 5-min, in blue; for 10-min in green; for 15-min., in yellow, and for 20-min average, in red. These points are overplotted to a map of negative/positive divergence (in white/black).

ferent temporal averages, in the case of the continuum images and longitudinal magnetograms. The result is shown in Figure 4.13. Zero-velocity points are plotted in purple for the 2.5-min average, in blue for the 5-min, in green for the 10-min average, in yellow for the 15-min and red for the 20-min average. These points cluster in areas where finding vortices of different durations is more likely. If we plot over the negative divergence areas, these regions are the most probable ones to find vortices.

### 4.3.2 Analysis of small vortical events

The preliminar detection of the vortex flow events is mainly based on visual inspection of longitudinal magnetograms movies. With these movies we set the spatial scale and temporal duration of the event. Once the whirlflow is detected, it is separated in a cube whose spatial dimension is a subfield of $5\farcs5 \times 5\farcs5$, (100 IMaX pixels). The third dimension is the duration of the event. A better performance of the LCT method can be achieved by interpolating images in the sequence to study, hence reducing the effective cadence from 33.25 to 11.0 seconds, and rebinning images to half the spatial sampling (from $0\farcs055$ to $0\farcs027$). The typical size of the Gaussian boxcar is $0\farcs6$. Large velocities are saturated to 5.3 $\mathrm{km\,s^{-1}}$ . Applying the

LCT method, we obtain the horizontal velocity maps, and divergence and vorticity are calculated. In this case, only the longitudinal magnetograms are used for the detection; however, continuum, FWHM and Doppler velocity are also checked. The criteria includes all sizes of vortices (i.e., mesogranular-size vortices are not excluded). In Figure 4.14, a map showing the vortices is displayed. Events turning clockwise are represented by $\diamond$ and the counterclockwise motion is represented by $\triangle$. Using the mean velocity field, we track the evolution of passively advected tracers (*corks*) with the algorithm of Yi, (PhD. Thesis, 1992). The corks are white squares that move over the photospheric flow and they are allowed to overlap each other. It uses the nearest velocity vector to move the *corks*, in a grid of 81 $\times$ 81 pixels. The velocity vectors are obtained by the LCT. The time interval used is 2 minutes (4 frames) and the step can be as long as 1000 iterations (1000 different positions of the cork grid). Some unusual behaviour is detected in some cases: the recurrent vortices may or may not keep the same sense of rotation. In the latter case, however, we cannot consider the vortices to be strictly recurrent.

The Figure 4.15 is created using the LCT with a *FWHM* of 1.″5 on an average of 20 minutes in continuum images, and calculating the divergence and vorticity afterwards. The left panel shows a binary mask where white color signals the areas of negative divergence, which are the most probable area to find vortices. All the events but one appear inside this area. The right panel represents the vorticity in a binary map. The area of positive vorticity are marked by light gray, the dark gray identify the negative vorticity, and the black regions represent the zero-vorticity (irrotational) areas. The proportion of vortical events that are out of the corresponding zone (an event marked with positive vorticity in a negative area or vice-versa) is about 10%. These events may change direction, or they can be short-lived events with a different vorticity. We are aware that these binary images are an average of the longest possible case, and it may be at variance with short-lived events.

#### 4.3.2.1 Statistics of small vortex-like flows

Considering the convergent or curved patterns in the flow maps of the magnetograms and continuum images, we can estimate some properties of these events, such as mean lifetimes or sense of rotation. We detected 74 events. Lifetimes are 9.8$\pm$6.5 min. The space-time density is $3.2\times10^{-3}$ vortices Mm$^{-2}$ min$^{-1}$, since the series lasts 21.5 min. Multiplying for the average lifetime, the density is $3\times10^{-2}$ vortices Mm$^{-2}$. We also find that 35% of the vortex flows turn clockwise, and 65% turns counterclockwise. This is a noteworthy result concerning the position of the FOV in the Sun. If we consider the shear caused by the differential rotation, this

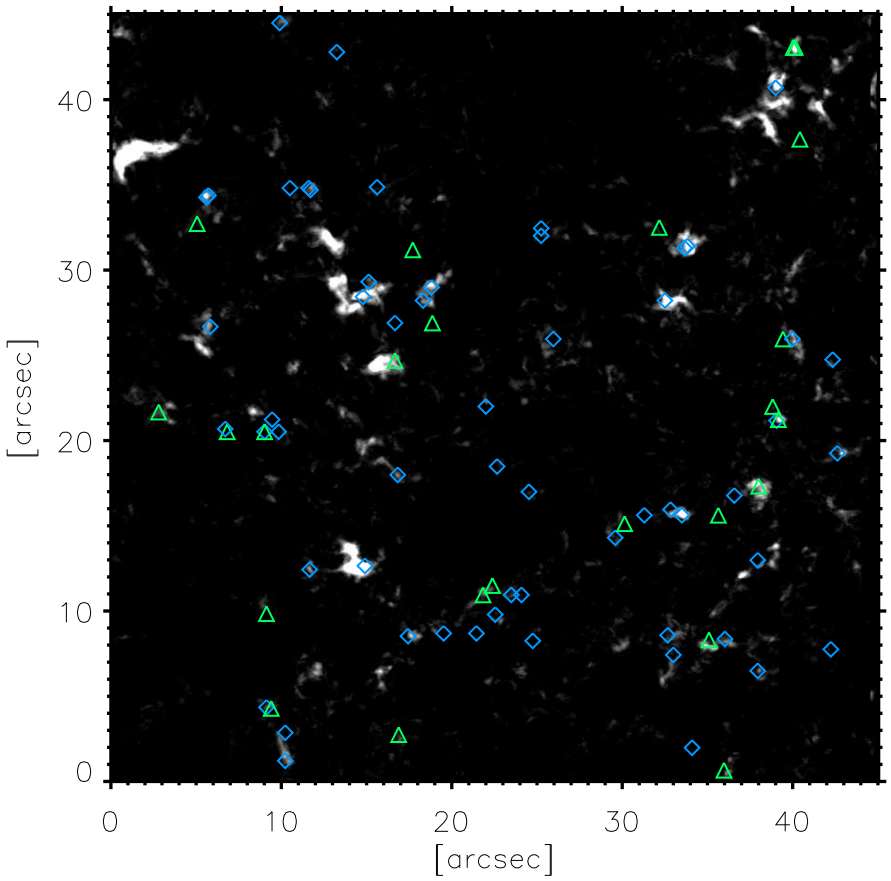


FIGURE 4.14— Map showing vortex distribution. They are marked as turning counterclockwise with green triangles and turning clockwise symbolized as blue diamonds. They are mostly concentrated on mesogranular and supergranular boundaries. The background is an average image of the magnetic concentrations over $3\sigma$, in absolute value.

fact may lead to a larger probability of finding vortices in the Northern Hemisphere in counterclockwise sense and in the opposite sense in the Southern Hemisphere.

The histogram in Figure 4.16 reveals a distribution whose main peaks are around 5 and 20 min. The 20-min events (12 out of 74) correspond to very conspicuous sinks, where plasma and magnetic field disappear on their centres.

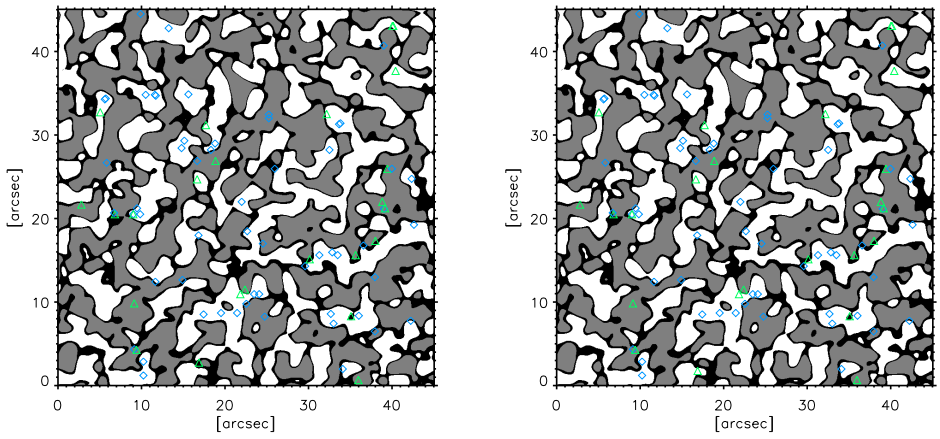


FIGURE 4.15— *Left*: The background is a binary image of the divergence. In white, areas with divergence lower than zero are displayed. All the events found are located in this area. *Right*: similar map, this time marking the vorticity. The different shades of gray indicate the vorticity sign: light gray correspond to positive vorticity, and dark shade indicate negative vorticity. Black areas are the areas with vorticity equal to zero (irrotational).

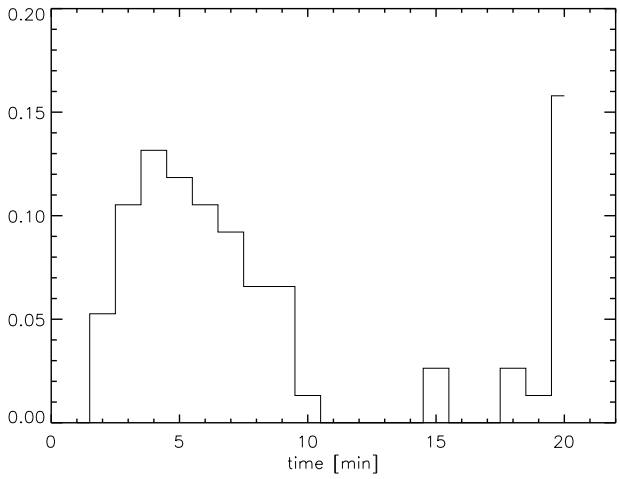


FIGURE 4.16— Vortex lifetime histogram.

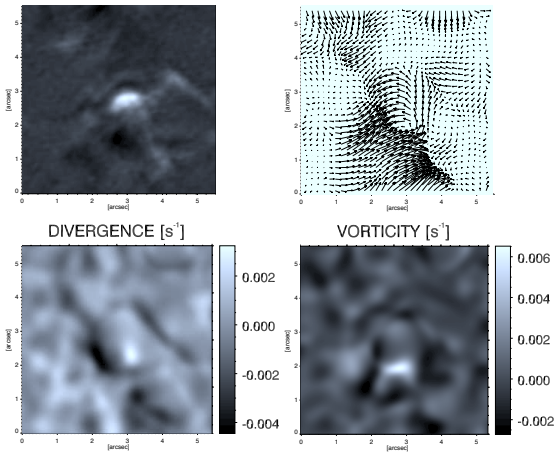


FIGURE 4.17— Panel showing, from the upper-left figure in clockwise direction, an average image, flow map, vorticity and divergence of the longitudinal field maps.

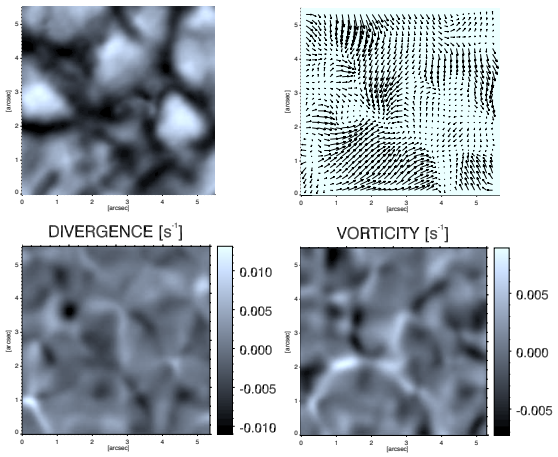


FIGURE 4.18— Panel showing, from the upper-left figure in clockwise direction, an average image, flow map, vorticity and divergence of the continuum maps.

#### 4.3.2.2 Centre of rotation and zero-velocity points on LCT

Other interesting method to find small-scale vortices is via the centre of curvature. This technique was implemented for the first time in Bonet et al. (2010).

A mathematical analysis that can be performed to find the centre of curvature can be interpreted in terms of the local angular velocity since plasma in pure rotational motion meets the condition $(\nabla \times \vec{v}) = 2\omega$, considering $\omega$ the angular velocity. Bearing this fact in mind, a definition of the curvature can be established as:

$$\kappa = \frac{1}{2}\frac{|\nabla \times \vec{v}_z|}{|\vec{v}|}. \tag{4.3}$$

This definition leads to a very similar spatial pattern than the one derived from the vorticity (Equation 4.2). In addition to that, the radius of curvature is determined calculating $\kappa^{-1}$. The curvature maps are reliable because they enhance the areas where the curvature radius is small.

An example of a vortex analysed in shown in Figure 4.17 and 4.18. In the four panels, the flow map is shown along with an average image, and the corresponding divergence and vorticity. Taking this example, we calculate the centre by different methods and different *parameters*: not only the continuum and the longitudinal magnetic field is used, but also the Doppler velocity and the line *FWHM* map.

The passively advected tracers yield a centre in the coordinates x=2.″76 ± 0.″19, y=2.″04 ± 0.″10. By the radius of curvature, we find x=2.″74 ± 0.″23, y=2.″14 ± 0.″22. The centre of zero-velocity yields to mark the centre on coordinates x=2.″72 ± 0.″11, y=1.″98 ± 0.″08.

#### 4.3.2.3 Magnetic centroids

Sometimes we detect GBP turning motions, that in their stochastic evolution can trace spiral movements. If they are in a vortex or not depend on whether they are tracked by other means, for instance, the permanence in a negative divergence area (sink). In Figure 4.19, it is shown the trajectories of the magnetic centroids for three individual examples. The colour code indicates the starting (in black) and end (in red) of the measured trajectory, marking with coloured asterisks the position of the centroid. In some frames, the magnetic field falls or smears out, then the centroid is calculated through its corresponding GBP. Taking into account the number of positions in every panel, and knowing the cadence of the images (33.25 s), we deduce a duration of these swirling motions from 4 to 7 minutes, and velocities from 0.7 to 3 $\mathrm{km\,s^{-1}}$ . In the middle panel of the Figure, it is evident that

the centroid describes three closed trajectories in 7 minutes, in clockwise direction. For these cases shown, the GBPs are located in a convergence area but they are too small, and their trajectories too short to be tracked by the LCT.

We note the small scale of the swirling motions, on the limit of resolution of IMaX. However, in Moll et al. (2011) the simulated trajectories are in agreement to this range of distances and rotation periods, as they find vortices which swirl twice during their lifetimes.

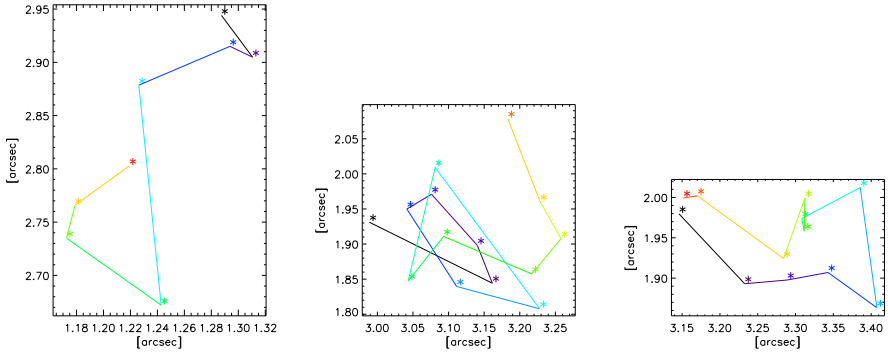


FIGURE 4.19— Trajectories of the computed magnetic centroids.

## 4.4 Discussion and conclusions

In this Chapter we have analysed the divergence, vorticity and their spatial patterns. The area covered by common divergence and vorticity pattern does not vary significantly by averaging from 5 minutes to 20 min, in Section §4.3.1.1. Due to a relatively large average times and *FWHM* sizes, the patterns tracked are very likely to be mesogranules, which have a lifetime, at least, of 10 minutes (Matloch et al., 2010).

Typical vorticities over the whole FOV range from $\pm 0.002$ for continuum images, in agreement with Bonet et al. (2010); Vargas Domínguez et al. (2011) that also yield similar values.

The divergence histograms are in accordance to the histograms in Vargas Domínguez et al. (2011), in which the median is always negative. The same histogram shapes can be inferred from Pötzi and Brandt (2005). Divergence values are also in agreement to Vargas Domínguez et al. (2011) and the values in the Figures 4.1 and 4.2 are very close to the images shown as vertical velocities in that work. Using the relationship of the *scale height* factor in Section §3.1, the

divergence is estimated in ±0.006. However, in Vargas Domínguez et al. (2011) the vorticity histograms are very symmetric, and this fact can reflect that the probability of clockwise-counterclowise is close to 50% (52% counterclockwise, 48% clockwise). Bonet et al. (2008) found 50.4% turning counterclockwise, 49.8% clockwise in the same FOV.

In Section §4.3.2 we found a larger occurrence of vortices rotating counterclockwise than in clockwise sense. From the vorticity histogram shapes in Figure 4.3 and 4.4 complemented with skewness slightly larger than zero, we can conclude that the studied area presents an slight positive vorticity, which can imply that the FOV is located in the solar Northern Hemisphere. In Bonet et al. (2010), some very slight differences between the left and right-hand side of the histogram may lead to the same conclusion. Both elements are in agreement with the fact the IMaX FOV of $45'' \times 45''$ may be located in the Northern hemisphere, since the actual position of the FOV on the Sun is unfortunately unknown.[1]

With respect to the small vortex flows investigated, they are always located in downdrafts, whose divergence is negative. Different methods to detect the centre of rotation, that are *corks* and null velocity points yield the same result within $0\farcs1$. These last two methods offer an approximation of the maximum and minimum number of events that we can find in a given FOV.

In Section §4.3.1.2, one of the most puzzling facts related with divergence and vorticity computation is presented: the typical ranges are usually around ± 0.005 without masking the noise; however, with a threshold of $2\sigma$ and $3\sigma$ for the magnetic field, values as high as ± 0.2 are reached. Values in simulations are as large as those ones (Stein and Nordlund, 1998; Danilovic et al., 2010; Shelyag et al., 2011). This result is relevant when comparing divergence and vorticity obtained by simulations to the observational data: removing the noise implies reaching values as the ones in simulations. Nevertheless, synthetic continuum images yield larger values of the divergence and vorticity, but lower than the obtained with magnetograms.

The density of these events are in the order of $10^{-2}$ vortices $Mm^{-2}$, in fully agreement to Bonet et al. (2010); Vargas Domínguez et al. (2011) and triple than Bonet et al. (2008). Vortices lifetimes (9.8±6.5 min) are slightly larger than in other similar works Bonet et al. (2010), (7.9±3.2 min), therefore it is the reason to obtain here a larger density. Spatial-time density are in the order of $10^{-3}$ vortices $Mm^{-2}$ $min^{-1}$ in this work and these two references. The FOV is comparable to all these works, $\sim 50'' \times 50''$. Probably the trend to find slightly larger lifetimes

[1] (Rubio F., private communication) has estimated the pointing of these data series from 2009, June 10 on should be corrected by (-70.″9, 69.″3). Therefore, the actual pointing may be (-70.″1, 69.″3). We shall remind that these series used are from 2009, June 9.

may imply larger spatial scales (i.e., mesogranulation) because the downdrafts are particularly strong on the mesogranular lanes (Stein and Nordlund, 1998).

# 5

# Study of mesogranular flows in IMaX data

Two large exploding granules hosting magnetic flux emergences are characterized. The granular flows display mesogranular scale and the evolution of the magnetic field emergences are described. After a while, mixed polarities start appearing. The duration of these features is around 20 min. LCT analyses show coherent spatial structures. In comparison to a MHD simulation, we found a similar behaviour to the emergence events.[1]

Watermelon man. (Herbie Hancock, 1973)

## 5.1 Introduction

In spite of having a large Reynolds number, the solar photosphere does not show large turbulent patterns. Instead, a neat pattern of convective cells is noticeable. Granulation, as the smallest spatial scale of the solar convection, drives the motion of plasma and also the small magnetic elements embedded into them. These cells are formed by hot plasma ascending in the centre of the granule and descending, when plasma has cooled down, to the dark intergranular lanes.

The SUNRISE balloon-borne mission (Barthol et al., 2011) was launched in June 2009. Having 1-m clear aperture Gregory-type telescope, this state-of-the-art mission provided high resolution images. The campaign was a continuous 5-day observation. At a cruise altitude around 36000 metres, the mission eluded 99% of

[1] This Chapter is an extended version of *Palacios et al.*, A&A, (2012), 537, A21.

the perturbations induced by the Earth's atmosphere (Solanki et al., 2010). The remains of these atmospheric effects were live corrected by the CWS (correlation wavefront sensor, Berkefeld et al., 2011). The Imaging Magnetograph eXperiment IMaX (Martínez Pillet et al., 2011) onboard SUNRISE acquired longitudinal and full-Stokes magnetograms, among other physical quantities. Considering that most part of the atmosphere and the ozone was beneath the balloon, ultraviolet observations could be attained by the SUNRISE filter imager SuFI (Gandorfer et al., 2011).

Although mesogranulation, an intermediate scale between granulation and supergranulation (3-10 Mm and lifetimes between 3-10 hours, November et al., 1981), has been thoroughly studied, the question whether it is a natural convection scale remains unanswered (Cattaneo et al., 2001; Yelles Chaouche et al., 2011; Ploner et al., 2000). This scale often manifests itself when temporal series of about 20 min to 1 hour are smoothed or approached through correlation tracking. Mesogranulation is sometimes identified as patches of positive divergence. Matloch et al. (2010) concluded that these patterns do not exhibit intrinsic size or time scales. This particular convection scale can indicate the relation to exploding granules and their fragmenting granule families. Bonet et al. (2005) performed a deep analysis of the granulation scales around a sunspot, focusing on the trees of splitting granules. Roudier and Muller (2004) matched families of fragmenting granules with prominent divergences. Passively advected tracers seem to coincide with these families. Mesogranules are considered as structures likely related to exploding granules, whose splitting is preceded by the formation of a dark hub due to buoyancy braking (i.e., Massaguer and Zahn, 1980). This effect caused by compressibility of the gas (Spruit et al., 1990) takes place when the mass excess in the centre of the granule reduces the upward velocity until its collapse. If energy losses cannot be compensated, the centre of the granule cools down, and the dark core emerges. When an incompressible plasma is considered, exploding granules do not develop, and mesogranulation arises as interaction between granules (Cattaneo et al., 2001). Compressibility and radiative cooling seem to be the factors which mark the maximum size for a granule.

The relationship between mesogranulation and vertical magnetic fields, as network, has been analysed by a number of authors. It is generally believed that the magnetic network is pulled out to the supergranular boundaries. de Wijn and Müller (2009) found trees of fragmenting granules devoid of magnetic elements, as they are dragged to the boundaries of the supergranule. Domínguez Cerdeña (2003) concluded that mesogranular structures in the network are smaller than those in the internetwork. Mesogranulation has been recently studied and related to the

distance to the network by Yelles Chaouche et al. (2011).

In this Chapter we characterize two events of magnetic flux emergence within mesogranular-sized cells. These emergences, unipolar at first, drift to the intergranular lane where the magnetic field intensifies. In or very close to the lane opposite polarities appear also. Transverse field is almost negligible over the granules' top, except when an opposite polarity becomes apparent and consequently the feature shows a loop topology, as described by Centeno et al. (2007) and Martínez González and Bellot Rubio (2009) and Gömöry et al. (2010). These emergences seem to be carried passively by the horizontal flow of the exploding granule. Previously, magnetic field emergences over granules were found in De Pontieu (2002); Orozco Suárez et al. (2008). Numerical simulations by Tortosa-Andreu and Moreno-Insertis (2009) showed large abnormal granules lasting 15 minutes and containing a magnetic field in the form of magnetic loops, as the ones presented here. We compare our detected emergence events with simulated data by Cheung et al. (2008) although the spatial scale of the latter corresponds to supergranular size.

## 5.2 Observations

The instrument IMaX was designed to observe the solar surface in polarized light at very high spatial resolution. IMaX achieved a spectral resolution of 85 mÅ and a spatial resolution of 0.″15-0.″18, observing at different wavelengths in the Fe I 5250 Å line. The restored data present an effective FOV of 45″×45″, with a spatial sampling of 0.″055. IMaX has several Observing Modes, two of which were used in this study: V5_6 and L12_2. With six accumulations, the V5_6 Mode includes full Stokes imaging polarimetry at four wavelengths ± 40, ± 80 mÅ from line centre and a continuum point at +227 mÅ, with 33 s cadence. Also the L12_2 Mode was employed, where Stokes $I$ and $V$ are observed at twelve wavelengths, from -192.5 to +192.5 mÅ in steps of 35 mÅ, and two accumulations, with 29 s cadence. The noise level is below $10^{-3} I_c$ in both Modes.

The data used in this work were collected by IMaX/SUNRISE close to the solar disk centre and consist of two series in two different Modes, acquired on 2009, June 10. Physical quantities are obtained by different means. The first series (hereafter referred to as emergence event $v10$) is obtained in IMaX V5_6 Mode, from UT 08:29 to 08:50 (∼21 min). In this case, longitudinal magnetograms are obtained by the weak-field approximation method (Landi Degl'Innocenti, 1992). Transverse magnetograms and Dopplergram calibrations are used as described in Martínez Pillet et al. (2011), along with the description of the IMaX Observing Modes and image restoration process. The second data series (emergence event

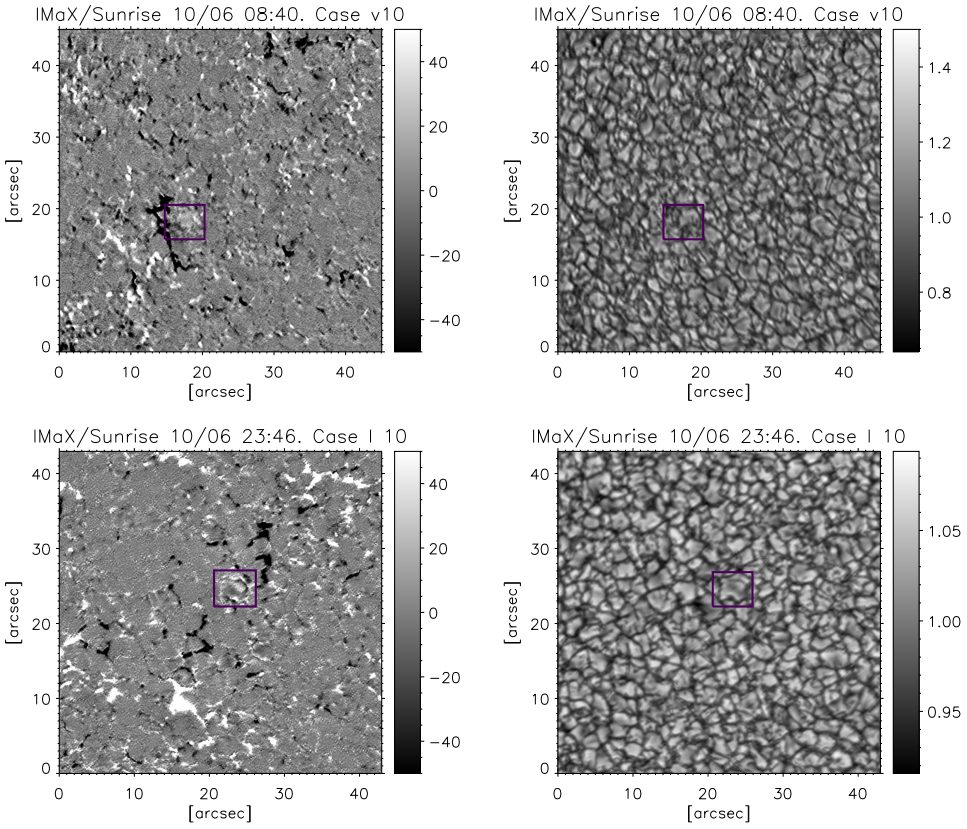


FIGURE 5.1— Full field-of-view longitudinal magnetic field maps (*left*) and continuum images (*right*) for the $v10$ event (*top row*) and the $\ell 10$ event (*lower row*). The dark purple squared boxes mark the exploding granules and their corresponding magnetic emergence. The box dimensions are $6\farcs9 \times 6\farcs9$. Longitudinal magnetograms are saturated to $\pm$ 50 G.

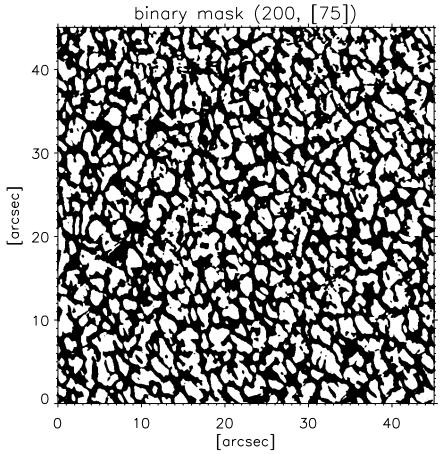


FIGURE 5.2— Binary mask of the frame showing the exploding granule of the $v10$ event before fragmentation, i.e., reaching its maximum size. Its dark centre is located at coordinates [18, 19].

$\ell 10$) is acquired in the Longitudinal Mode L12_2, from UT 23:42 to 23:59 ($\sim$18 min). In the $\ell 10$ case, line-of-sight magnetic field strength is obtained by $\mathbf{1}$) the centre-of-gravity (COG) method (Semel, 1967; Rees and Semel, 1979) and $\mathbf{2}$) SIR inversion (Ruiz Cobo and del Toro Iniesta, 1992). Line-of-sight (LOS) velocities are obtained from the SIR inversion. All data are subsonic filtered, hence *p-mode* removal is applied, following the space-time filtering by Title et al. (1989). In Figure 5.1, the full field-of-view images are shown. The dark purple squared boxes mark the exploding granules and their associated magnetic emergence over their respective longitudinal magnetograms and continuum images.

## 5.3 Analysis

The granule which hosts the magnetic emergence $v10$ presents a large scale, as confirmed by Fig. 5.2. An image of the granule is chosen before it splits into three granules, and area and effective radius histograms are plotted. The granule size lies into the last bins of the histograms, as evidenced by its large diameter, 2300 km ($>3''$).

### 5.3.1 Host exploding granules

Two emergence events ($v10$, $\ell 10$) are followed until the host exploding granules lose their identity and their fragments develop into three and four granules, respectively.

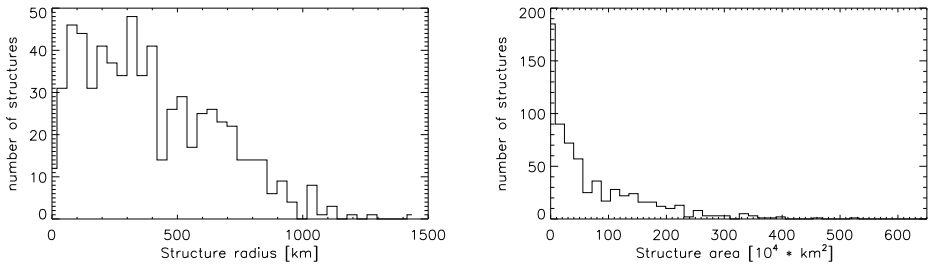


FIGURE 5.3— Histograms of radius and area of an image segmented by a binary mask. The emergence case is one of the largest, with 2300 km of diameter in that image.

Unfortunately neither of the two time series covers the full development and decay of the fragmenting granules. The granule hosting the magnetic emergence *v10* presents a large spatial scale. An image of the granule is chosen before it splits into three granules (shown on Figure 5.2). With this particular frame we produce a binary mask via thresholding (which separates granules from intergranular lanes) to estimate granules size. Areas are estimated and the equivalent radius is defined considering that areas correspond to circular granules. Hence histograms of the granular area and the equivalent granule radii are computed, in Figure 5.3. Spruit et al. (1990) and references therein state that the maximum size of granules before the onset of buoyancy braking is around 3″. We use the aforementioned binary mask for each frame to compute the number of granules with equivalent diameter larger than 3″, finding only around 1%, i.e, 3 granules per each IMaX frame (FOV of 45″×45″). We calculate the average granule coverage for the whole FOV of the *v10* series and the corresponding equivalent diameter is around 1.″22 for regular granules. Besides, in this work we found that the occurrence rate of granules with diameter larger than 3″ is approximately $5.7\times10^{-11}$ $\mathrm{km^{-2}\,s^{-1}}$, yielding a similar value as in Title et al. (1989), where the occurrence rate of exploding granules is found to be $7.7\times10^{-11}$ $\mathrm{km^{-2}\,s^{-1}}$.

The expansion velocity of the host granules is estimated by measuring the area and calculating the equivalent radius for every frame in both series. Then, velocity is calculated by least-squares fitting to the equivalent radius growth rate, in Figure 5.4 (top). The expansion velocity is $0.94 \pm 0.02$ $\mathrm{km\,s^{-1}}$ for *l10* and $0.95 \pm 0.02$ $\mathrm{km\,s^{-1}}$ for *v10*. Expansion velocities of the magnetic patch covering the exploding granules are also estimated, in Figure 5.4 (bottom). Results are $0.61 \pm 0.04$ $\mathrm{km\,s^{-1}}$ for *l10* and $0.68 \pm 0.03$ $\mathrm{km\,s^{-1}}$ for *v10*. Considering a threshold of 15 G for reconstructed images (see Martínez Pillet et al., 2011) we measure

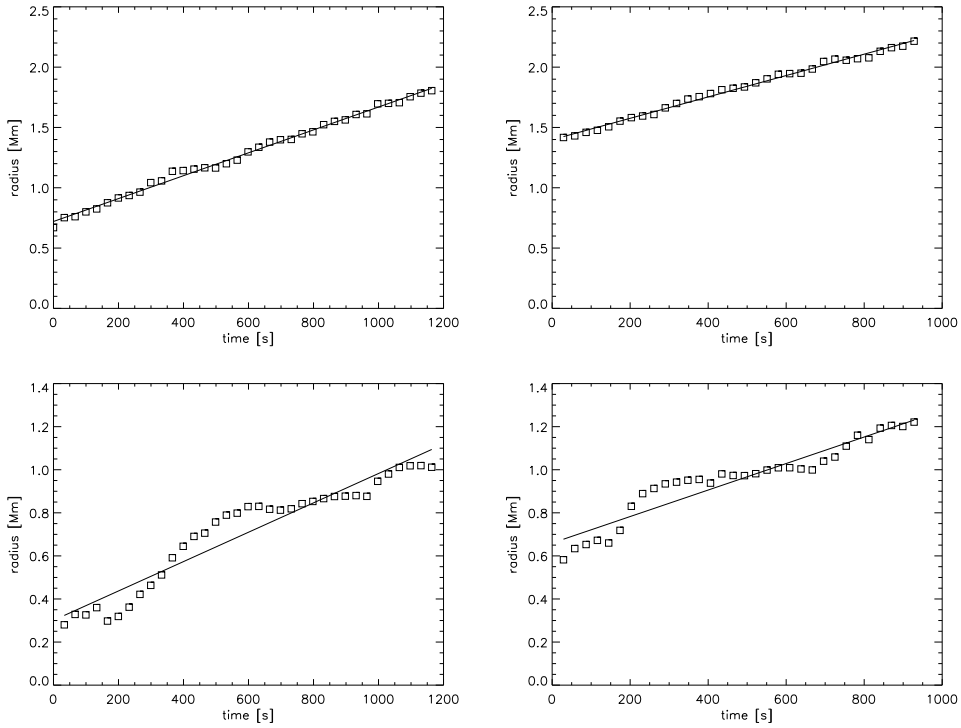


FIGURE 5.4— *Top row*: Granule effective radius versus time of the $v10$ and $\ell 10$ cases. Squares indicate the effective radius in each frame. Solid lines represent the least-squares fit. *Bottom row*: magnetic patch effective growth rate in both cases.

the area and calculate the equivalent radius for the magnetic patches.

### 5.3.2 Associated magnetic field emergences

Emergence event $\ell 10$ starts with a host granule of 3.″3 diameter, as shown in the first panel of the time sequence in Fig. 5.5. The thresholded patch of 15 G (in yellow) covers the central part of the granule in the first frames. This threshold is chosen to highlight the unipolar character – positive in both $\ell 10$ and $v10$ – of the emerging structures. As the granule grows and starts showing dark patches and crinkles that will become intergranular lanes, the magnetic patches overlie these dark areas. At 319 s from the start of the series, the buoyancy braking darkening is clearly visible (signaled by an arrow). This darkening is related to low velocities toward the observer, ending with moderate downflows of 0.5 $\mathrm{km\,s^{-1}}$.

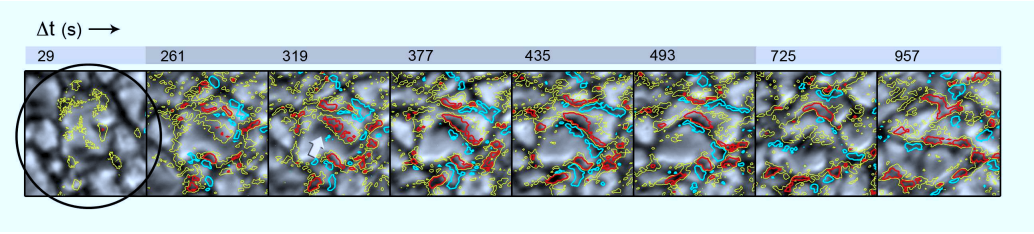


FIGURE 5.5— Sequence of continuum images for emergence event $\ell 10$. Overlaid to each image are the corresponding contours of longitudinal magnetic field (15 G in yellow; 45 G in red, and blue outlines -45 G). Corresponding times are labelled for each frame in the top bar, where dark gray are displayed every 58 s. The FOV is cropped to a size of $6\farcs9 \times 6\farcs9$. The black circumference presents a diameter of $8\farcs3$ (6 Mm). A white arrow in the third frame points to the buoyancy braking darkening (see text for details). The corresponding movies for the $\ell 10$ and $v10$ emergence are provided as electronic material in ftp://helio.uv.es/pub/THESIS_Judith/.

The unipolar magnetic concentrations with strengths larger than 45 G (red/blue for positive/negative polarities) which develop into the recently created intergranular lanes do not remain unipolar for more than 2 frames (1 min), appearing an opposite polarity nearby (see third and fourth panels in Fig. 5.5). This central intergranular lane drifts as the granule grows, and another dark spot appears at 725 s, when the granule finally splits into four, becoming a recurrent exploding granule. The area covered by the 15 G contours ranges from 18% to 32% of the granular area. Unfortunately, as the $\ell 10$ emergence is taken without $Q$ and $U$ Stokes profiles, we cannot establish whether or not these positive and negative patches are actually linked as loop footpoints.

In emergence event $v10$ we study a granule of initial diameter around $2''$ (sequence shown in the electronic material, movie $v10$). At 231 s from the start of the series, the centre of the granule presents a significant area covered by longitudinal magnetic fields larger than 15 G. At 561 s, a slightly darker spot arises in the granule, together with a longitudinal magnetic patch of value larger than 45 G. The 15 G contours start forming a trefoil shape, covering from 15% to a peak of 42% of the granular area. The time span of this structure is 600 s approximately. It partially covers a granule, until the moment it approaches an intergranular lane or a breaking granule spot, where the longitudinal magnetic field migrates and intensifies (from 45 G to more than 80 G). LOS-velocities mark slight upflows while the magnetic field at the centre of the granule is emerging. Maximum values of the longitudinal magnetic field peak around 100 G, while the transverse field is about 250 G. The maximum value of the transverse field is reached on the loop described below. Note that it seems a high value, but the noise is quite large (see Martínez

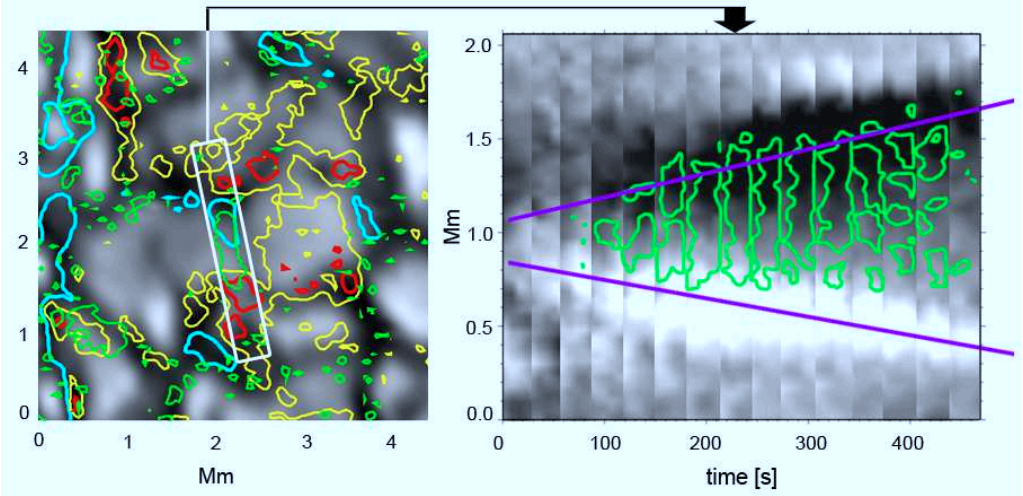


FIGURE 5.6— Emergence event *v10*. *Left*: Continuum image with contours of transverse magnetic field in green ($>$ 180 G) and yellow, blue and red contours as in Fig. 5.5. A region showing the emergence of a loop is outlined with a white box. *Right*: Corresponding timeslices of the magnetic loop emergence. The background image displays the longitudinal field with positive/negative polarities in white/black. Superimposed in green is the transverse field. Reference lines in purple mark the footpoint separation. Time in this panel is counted from the start of the first footpoint emergence, i.e., 698 s after the start of the series.

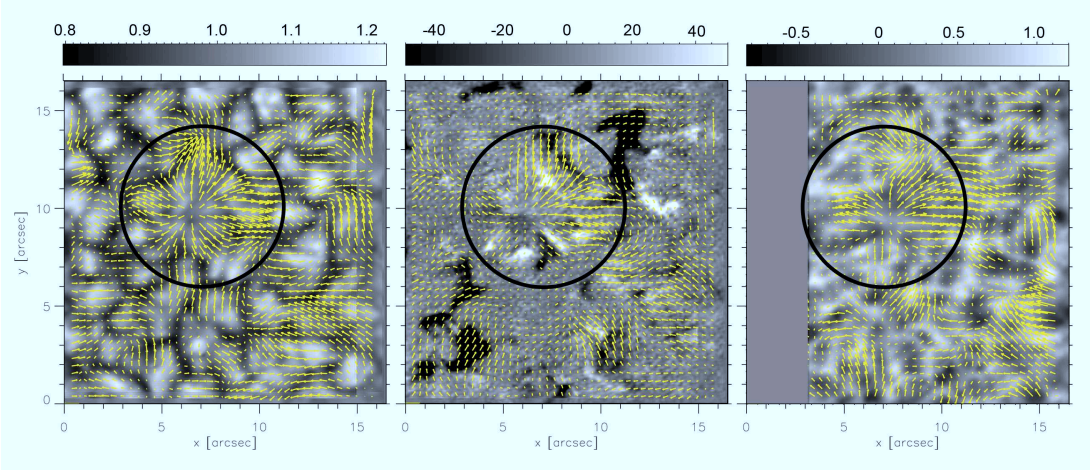


FIGURE 5.7— *From left to right*: flow maps of the continuum, COG longitudinal field and LOS-velocity of the $\ell 10$ emergence. The background images are averages of the following quantities: average normalized continuum image; longitudinal magnetic field, saturated to $\pm$ 50 G; and LOS-velocity ($\mathrm{km\,s^{-1}}$). The full FOV is 16.″5×16.″5. Separation length between tickmarks is equivalent to a velocity magnitude of 1.5 $\mathrm{km\,s^{-1}}$. A circle of diameter 8.″3 (same as in Fig. 5.5) is overplotted for comparison. See text for more details.

Pillet et al., 2011), then it is thresholded to 180 G. A positive polarity emerges at the edge of a previously fragmented portion of the granule followed by a transverse field patch at 764 s, indicating a magnetic loop top, lasting for around 90 s before the second footpoint becomes visible in our data. This dipole presents the semi-major axis parallel to the intergranular lane. The total duration over which the whole loop, including its apex is visible, is 396 s, also shown in Fig. 5.6 $(right)$, where a time series of the images in the region outlined by the white rectangle is presented. Green contours outline the transverse field while the background image corresponds to the longitudinal magnetic field. Positive/negative polarities are represented in white/black. Footpoints reach a maximum separation of 1.5 Mm, and the separation velocity is 3 $\mathrm{km\,s^{-1}}$, much larger than the granule expansion rate, bearing in mind that the velocity computed between any two points is usually larger than its average. LOS-velocities at the footpoints range from 0.5 $\mathrm{km\,s^{-1}}$ at the emergence of the first footpoint to 1.5 $\mathrm{km\,s^{-1}}$. The $v10$ event estimated flux ranges around 0.4-2.0 $\times 10^{18}$ Mx considering magnetic elements over 45 G.

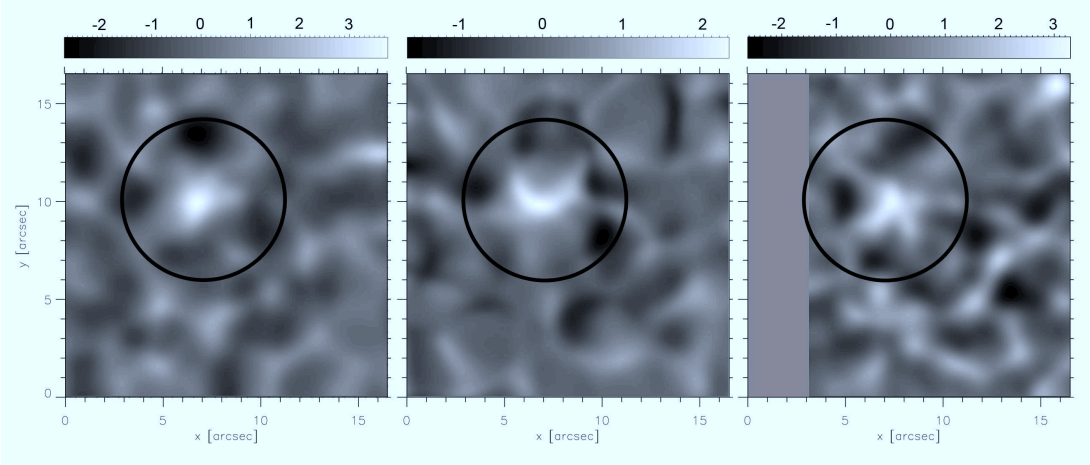


FIGURE 5.8— *From left to right*: continuum, longitudinal field and LOS-velocity divergences (resulting from the corresponding flow maps in Fig. 5.7) of $\ell 10$ emergence. Bars indicate the divergence value in units of $10^{-3}$ $s^{-1}$. The same circle of Fig. 5.5 and 5.7 is overplotted for comparison.

### 5.3.3 Flow maps of the magnetic and non-magnetic features

In this study, the Local Correlation Tracking (LCT, November and Simon, 1988) method implemented by Yi and Molowny-Horas (1995) is performed using a correlation window with *FWHM* of 1.″5 (28 IMaX pixels) averaged over the duration of the events (17 min for $\ell 10$ and 21 min for $v10$). Flow maps for continuum, the centre-of-gravity longitudinal field and LOS-velocity are computed. The time average LOS-velocity peaks between -2.5 and 2 $\mathrm{km\,s^{-1}}$. Figure 5.7 displays the results for emergence event $\ell 10$. Mean values of horizontal velocities in the continuum, longitudinal field and LOS-velocity maps are 0.63, 0.49 and 0.54 $\mathrm{km\,s^{-1}}$, respectively. Velocities obtained with LCT are lower than expansion velocities because of the long duration of the series and the size of the *FWHM*. In addition, the flow pattern is remarkably similar in all the three panels of Fig. 5.7. COG magnetic field flow maps show exactly the same pattern as the inversion magnetic field flow maps (not shown). The gray box in the last panel corresponds to a more stringent clipping of the inverted data (with respect to the non-inverted) to avoid influence from the apodized FOV, remnant of the reduction process. A circle of diameter 8.″3 is overlaid as visual indicator enclosing the exploding granule and its fragments. The divergence maps resulting from the LCT computation are shown in Fig. 5.8. Maxima are found for each panel and averaging the position, we find an accu-

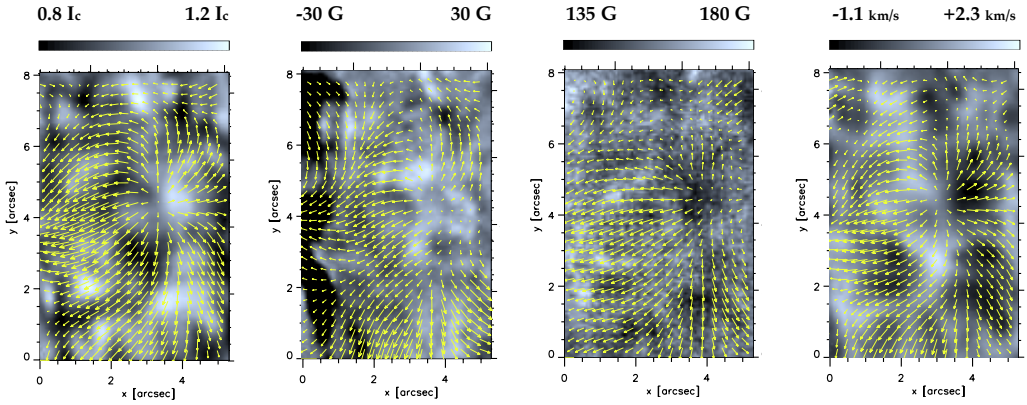


FIGURE 5.9— Flow maps of the continuum, longitudinal magnetic field, transverse magnetic field and velocity of the mesogranular emergence in V5_6. The FOV is $5\farcs55 \times 7\farcs92$, narrowed to avoid saturation in the magnetogram of a network element closeby. The tickmark arrow represents 1.20 $\mathrm{km\,s^{-1}}$. Magnetic field values are saturated to $\pm$ 30 G, and the transverse field values are restricted to a range from 135 to 180 G. Continuum and velocity values are the maxima and minima in the area.

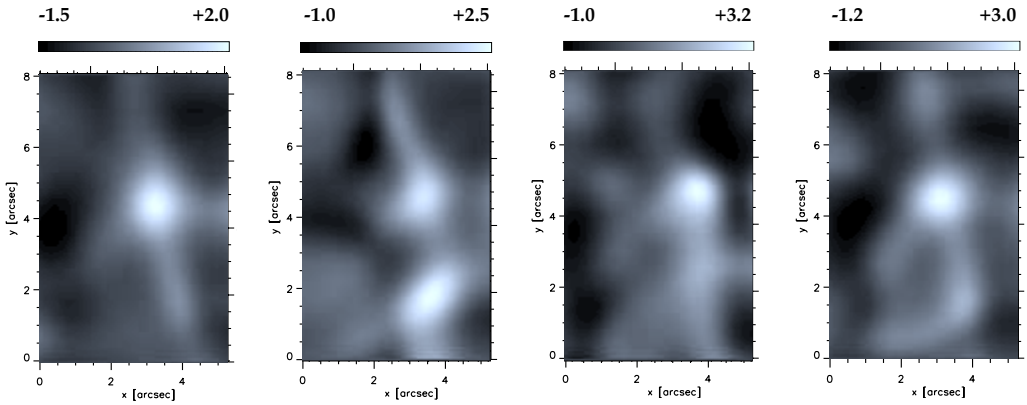


FIGURE 5.10— Divergence of the continuum, longitudinal magnetic field, transverse magnetic field and velocity of the mesogranular emergence in V5_6. Bars indicate the divergence value in units of $10^{-3}$ $\mathrm{s^{-1}}$.

rate centre of the mesogranular flow. The coordinates averaged are x=6.″56±0.″30, y=9.″84±0.″11. Divergences peak around $3\times10^{-3}$ s$^{-1}$, which is a moderately high value for a 17-min average. Results for emergence event *v10* are comparable and shown in Figures 5.9 and 5.10. The average velocity values for images of continuum, longitudinal field, transverse field and Doppler velocity are 0.60, 0.47, 0.44 and 0.48 $\mathrm{km\,s^{-1}}$ on *v10*. We can calculate the maxima in the different parameters for the main divergence feature, obtaining x=3.″72 ± 0.″15, y=4.″63 ± 0.″28.

### 5.3.4 Simulations

A simulation performed by Cheung et al. (2008) is used for comparison. Carried out with the MURaM code (Vögler et al., 2005), which solves the radiative MHD equations on a Cartesian grid, this numerical experiment places a rising fluxtube with a twist parameter $\lambda$ =0.25 at $z = -3.9$ Mm. The simulation domain has horizontal dimensions of 24 Mm × 18 Mm and a height of 5.76 Mm, with a total magnetic flux of $10^{20}$ Mx. A pixel of the simulation covers 25 km × 25 km or equivalently, 0.″034 pixel$^{-1}$, smaller than the IMaX sampling, which is 0.″055 pixel$^{-1}$. The flux tube placed at the bottom of the simulation box expands and rises and becomes turbulent. The continuum images and corresponding synthetic magnetograms at $\tau_{500}$=0.1 are degraded by smoothing with a 0.″17 wide boxcar window, equivalent to 3 IMaX pixels. A movie of the simulation is available in the electronic material. This movie shows a continuum image with red and blue contours representing longitudinal fields larger than 15 G and lower than -15 G respectively. Maximum and minimum of the simulation are 220 G and -350 G. Similarly to the observed cases, some large unipolar blobs covering granules appear, and also mixed polarities while the region evolves. Contrary to the observed cases, the longitudinal magnetic field seems to evolve more independently over the granules' top than in the analysed events, where granules develop and magnetic flux is apparently dragged by the plasma. Figure 5.11 shows a frame of the synthetic continuum overplotted with the aforementioned contours. The magnetic concentration centered in (14, 12) Mm is further measured to estimate the expansion velocity.

To analyse the behaviour of the simulation features with respect to observation, we apply the same methods for expansion velocity calculation and LCT. We computed the expansion velocity by means of effective radius measurement over time. The expansion velocity of the whole magnetic emergence, thresholded to ±15 G, is shown in Figure 5.12 (bottom). A negative patch covering some granules actually expands at a rate of 1.2 $\mathrm{km\,s^{-1}}$ (Figure 5.12, top), considering the features with a pixel averaged field strength above the threshold of -15 G. LCT (*FWHM* 1″ in this case) is applied also to the simulation. Fig. 5.13 displays the flow maps of

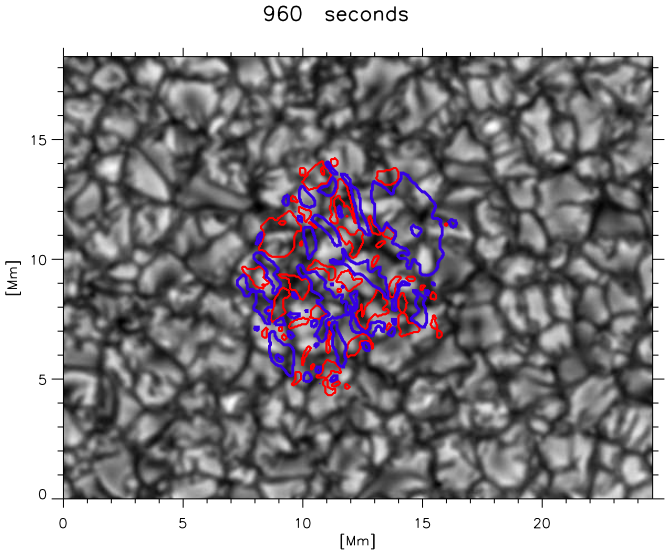


FIGURE 5.11— Synthetic continuum snapshot overplotted with contours coloured in red and blue, denoting 15 G and -15 G, respectively.

the synthetic longitudinal magnetogram (left) and the continuum intensity (right). The average longitudinal magnetogram is contoured over the continuum flow map (thick black line). While in the observed data a smaller window size does not provide more information, as tracked features are slower, in the simulation it highlights different features such as the divergence centres. Positive divergence centres are clearly spotted in red, while blue lanes indicate fragments of long-duration intergranular lanes, likely to be tracing mesogranular lanes (right panel). Most divergence features are well reproduced in both flow maps, e.g., strong negative divergence patch at coordinates [9, 9] Mm, although more marked and the overall expanding behaviour more obvious in the left panel in Fig. 5.13, i.e., when tracking magnetic features. Some differences arise when comparing the flow maps, as in [11,9], where the emergence of magnetic field starts and creates a large flow that wipes out the growing of smaller structures. Comparing with granules, these last ones present a different behaviour due to their smaller size compared with the largest magnetic blobs, making divergence centers appear sharper.

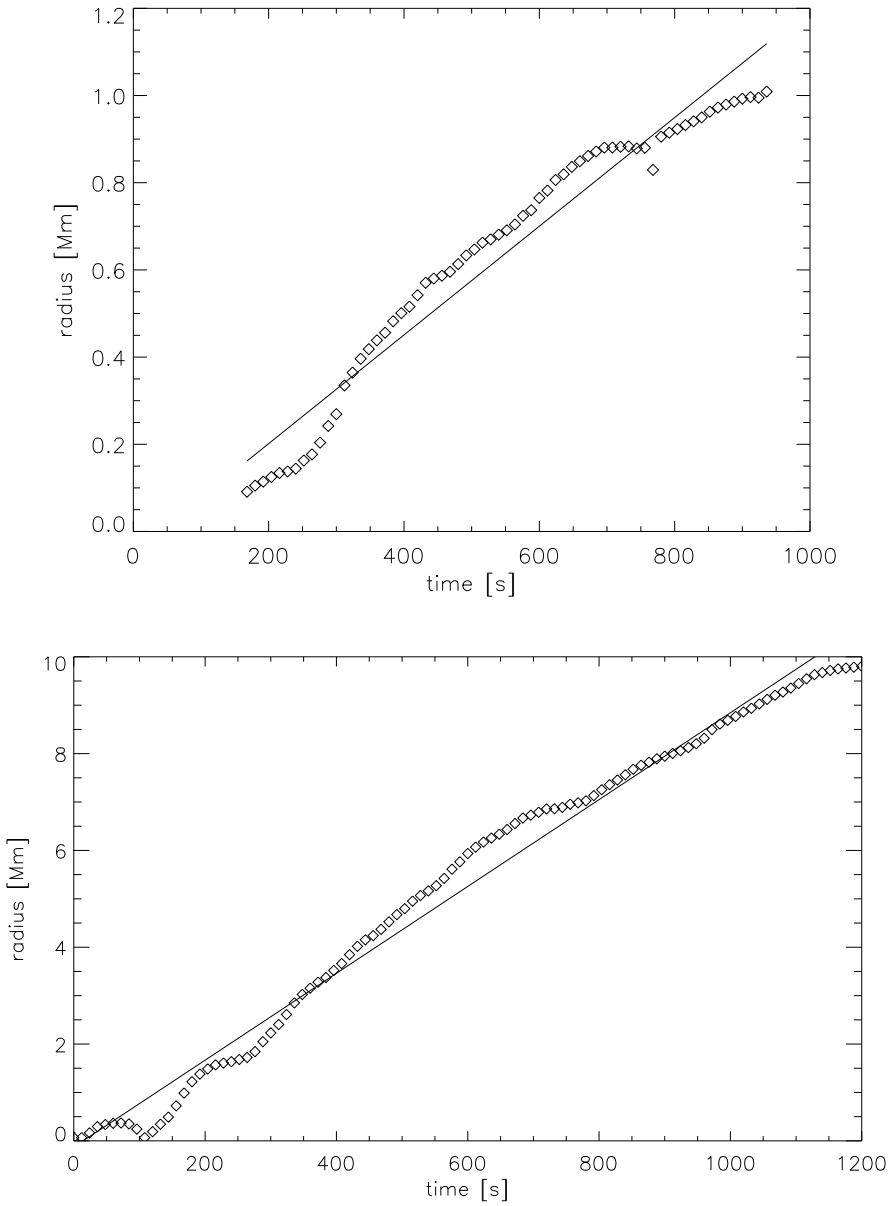


FIGURE 5.12— *Top*: Expansion velocity of the simulation, measured for a large magnetic concentration. *Bottom*: Expansion velocity of the simulation, measured over the whole synthetic magnetogram.

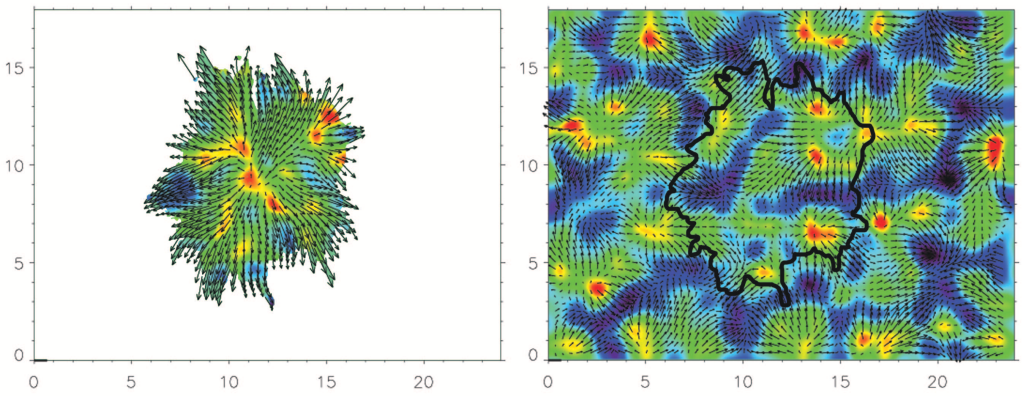


FIGURE 5.13— Local CorrelationTracking flow maps of the longitudinal magnetogram of the smoothed simulation (left) and its corresponding continuum image (right). Units in axes are Mm. Separation length between tickmarks is equivalent to a velocity magnitude of 1.1 $\mathrm{km\,s^{-1}}$. The background image represents the normalized divergence field in every case, with positive values (in red), marking clearly the emergence areas, and negative divergences (in blue), featuring long-duration lanes and probably mesogranular lanes. Black contour delimits the magnetic field over the divergence in the right panel.

## 5.4 Discussion and conclusions

Thanks to the high resolution and cadence of SUNRISE/IMaX, we obtained co-spatial and co-temporal magnetic field and continuum images, which allow these events to be studied. For the first time we found magnetic loops embedded in the fragments of large exploding granules, which are covered by magnetic longitudinal field patches. The origin of these magnetic structures is still uncertain, although the similarity of the observed features with the simulations of Cheung et al. (2008) suggests that they originate by a turbulent rising flux tube. The emerging magnetic flux features are advected by the exploding granule. In this scenario the magnetic flux concentrations act as tracers.

In both emergence events, the underlying granules expand at a rate of 0.95 $\mathrm{km\,s^{-1}}$ and the magnetic patches at 0.65 $\mathrm{km\,s^{-1}}$. Average horizontal velocities are about 0.60 $\mathrm{km\,s^{-1}}$ for continuum and 0.46 $\mathrm{km\,s^{-1}}$ for magnetic fields, in agreement with the typical granular expansion velocity estimated by LCT of 0.5-1.0 $\mathrm{km\,s^{-1}}$ (November and Simon, 1988). The velocities are lower when magnetic structures are involved. This lower mobility of the magnetic features seems to be real and not a consequence of tracking faint features. This phenomenon was observed by Manso Sainz et al. (2011) as well.

The emergence event *v10* seems to be a long-lived recurrent exploding granule

(*active* granule, Oda, 1984), as it is rechecked in other four short series (about half an hour in total) shown in Table 5.1. Roudier and Muller (2004) observed trees of fragmenting granules tracked over hours but no magnetic field information was available. Both cases presented here show magnetic field over granules, in agreement with De Pontieu (2002); Orozco Suárez et al. (2008). Furthermore, dark hubs have been observed in granules by Bello González et al. (2009). Regarding the flow dynamics, the emergence event $v10$ occurs close to a network element. The recurrent exploding granule and associated emergence event $\ell 10$ also harbours a network element in its surroundings. These facts could signify that these mesogranular emergences are close to a supergranular boundary.

Simulations used for comparison show a resemblance to the emergence $\ell 10$, as the positive and negative polarities become visible very close to each other, albeit the field emergence is by far faster in the supergranular simulation than in the observed data. Considering a synthetic magnetic field concentration, the expansion velocity is in agreement to Tortosa-Andreu and Moreno-Insertis (2009), who report expansion values of 4 $\mathrm{km\,s^{-1}}$ on their simulations. While in Cheung et al. (2008) supersonic downflows are revealed, probably related to convective collapses, we find no evidence of supersonic up- or downflows in Stokes V continuum using V5_6 data (event $v10$) similar to those found by Borrero et al. (2010).

Taking advantage of the $v10$ emergence that presents transverse field, we found a magnetic loop emerging in the FOV, whose associated footpoints separate from each other with a velocity of $\sim$3 $\mathrm{km\,s^{-1}}$, in agreement with Martínez González and Bellot Rubio (2009). The footpoints exhibit downflows, which may indicate mass draining along the legs of the loops, making their ascent to less dense layers possible. As only one footpoint and the loop apex appear first, this may indicate the emergence of an inclined loop, or significant differences between the field strength of the two footpoints. As a general fact, the transverse field is almost negligible in the exploding granule, while longitudinal field covers portions of the granule before drifting to the intergranular lane where it intensifies.

## 5.5 Flow maps over the field-of-view

This Section is not an addendum but it does provide an observational framework for this Chapter. It is justified as one of the events related in this Chapter is found in this FOV. From IMaX data of 2009, June 10, five series were selected, mode V5_6. These sequences were aligned and *p-mode* filtered. In the previous Sections, data from the Series 1 for studying the event $v10$ are used. Also the L12_2 series are presented, since data are interpolated and treated as a whole in $\ell 10$. Details

of these Series are presented in Table 5.1.

| Mode | Cadence [s] | Observation no. [No.] | Cycle obs. [No.] | Duration [min] |
|---|---|---|---|---|
| V5_6 | 33.25 | 200 | [48, 85] | 20.95 |
| | | 200 | [94, 107] | 7.65 |
| | | 200 | [114, 121] | 4.33 |
| | | 200 | [130, 145] | 8.76 |
| | | 200 | [155, 172] | 10.00 |

| Mode | Cadence [s] | Observation no. [No.] | Cycle obs. [No.] | Duration [min] |
|---|---|---|---|---|
| L12_2 | 29.01 | 225 | [89, 92] | 2.05 |
| | | 225 | [93, 96] | 2.03 |
| | | 225 | [97,103] | 3.62 |
| | | 225 | [104, 122] | 9.90 |

TABLE 5.1— Data series description for the events $v10$ and $\ell 10$.

In all these sequences we observe a conspicuous unipolar – negative – network feature surrounded by some small positive polarity elements. Local Correlation Tracking is applied to the different *parameters* obtained by reduction: the continuum images, longitudinal and transverse magnetograms, and Dopplergrams. The *FWHM* of the averaging window is $1\farcs5$. The temporal averages of the LCT are the series duration themselves. LCT yields similar results over the different maps that was applied. There are some areas that present recurrent exploding granules (active granules), as displayed in Figure 5.14. In the first three panels, the exploding granules are displayed very clearly, located at the left and right of the network element. However, large flows from the north-east in Panel 4 and north-west in Panel 5 move the structure and modify the network element shape. In Series 5, another small flux emergence appears above the network element, on coordinates [12,12]. This one also constitutes a small magnetic field emergence over an exploding granule.

Some concluding remarks can be drawn, as probably all the exploding granules on the area contribute to shape the network element and avoid the dispersal over nearly one hour. Since all these exploding granules are close to the network element, we should rule out the idea of these granules can fragment and drag some magnetic field structures from the network element, as the network has negative polarity and

all the emergences found are positive.

Although a whole computation of cancellation is beyond the scope of this work, some hints can be provided. The context is appropriate, as the data series present a unipolar network element, of about -200 G, surrounding by small positive concentrations, which magnetic field strength larger than $3\sigma$, ranging 75 G. Some approximation can be performed through the so-called *cancellation magnetograms*. A *cancellation magnetogram* is computed subtracting the absolute value of the true sign average image from the absolute value average image (see Sainz Dalda and Martínez Pillet, 2005, for details.)

$$cancel = \langle|\phi|\rangle - |\langle\phi\rangle| \tag{5.1}$$

The values of these *cancellation magnetograms* range from zero to the maximum averaged value, in this case, around 55 G, as the first term in Equation 5.1 is always positive and the second term is always lower than the first. We can understand this Equation as follows: pixels presenting the same sign value will appear as zero, while values will be maximum at pixels which present high differences between positive and negative values on the magnetogram in the sequence approximately half of the duration of the sequence – bearing in mind that the result is highly dependent on time averaging – . Therefore, the maxima in these areas correspond to regions very close to a polarity change, and they mark polarity inversion areas. In this case, the effect is very clear, as the network patch is negative and many of the small structures that appear and disappear are mainly positive. In Figure 5.15, the network element appears in black, as its net change is zero, and the surroundings of the network and some specific patches show the maximum values, in orange/red. The areas presenting the maximum values of the cancellation magnetograms are always close to large flows detected by the LCT. We should note that these *cancellation magnetograms* do not have to indicate real cancellation, but highlighting the places where magnetic fields change sign and the equivalent areas to neutral lines.

When the flow maps and the *cancellation magnetograms* are compared, the correspondence of the flow maps and the 'magnetograms' is worth being remarked upon, as displayed in Figure 5.15. Flows are perpendicular, in many cases, to the magnetic cancellation structures, which suggests that magnetic fields are driven by plasma, and the final destination is the network element. If the positive structures suffer cancellation or disappear for other causes while coming close to the negative network element is something that deserves a deeper analysis in the future.

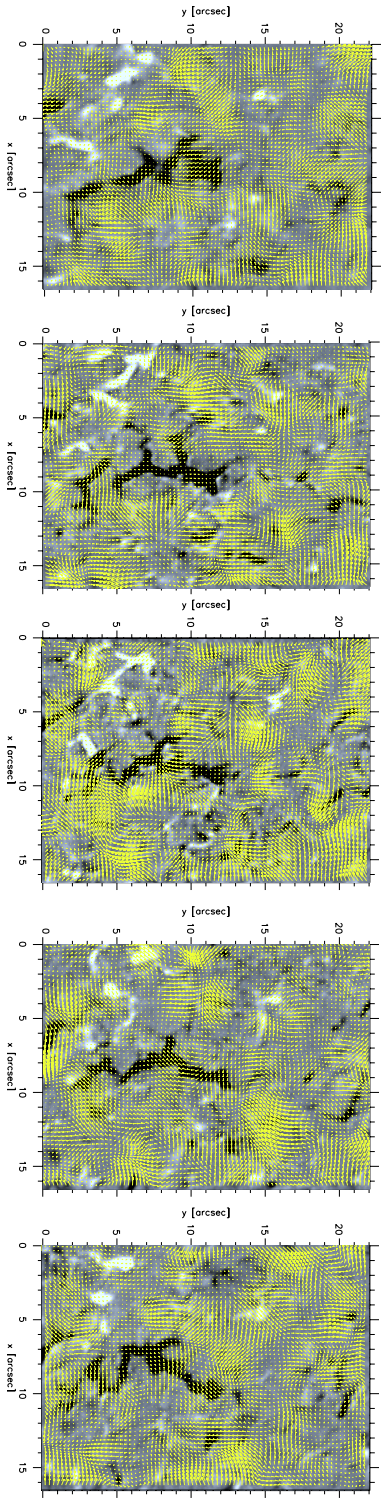


FIGURE 5.14— Longitudinal magnetogram flow maps for the five series. The background images are averaged magnetograms, saturated to ± 50 G. Tickmark distance represents a velocity magnitude of 1.2 $\mathrm{km\,s^{-1}}$ . Panels 2, 3 and 4 show very conspicuous positive polarity patches (size less than 1″) around the negative polarity of the network. In these cases the positive polarity concentrations are more evident as the temporal average is shorter.

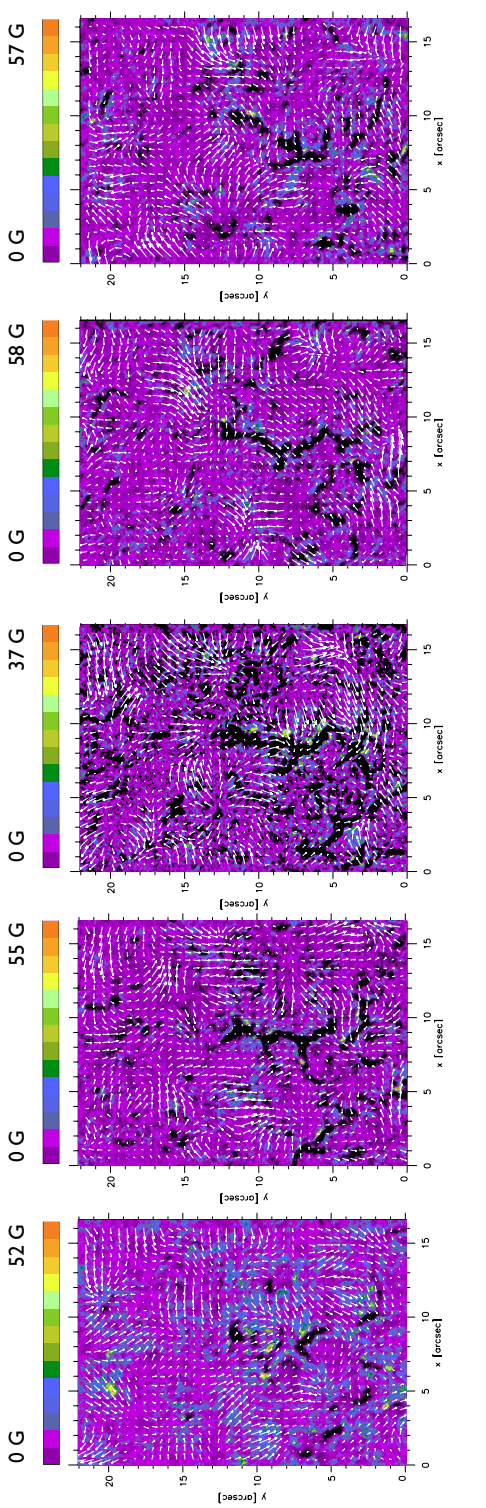


FIGURE 5.15— Flow maps (in white) superimposed to the *cancellation magnetograms* for the five series.

# 6

# Conclusions

General conclusions, remarks, and outlook.

Volaré bajito, a ras de suelo,
y sin perder de vista el horizonte. Presuntos Implicados, (1991)

In this work we have studied the dynamics of small magnetic elements in different contexts. In the first Chapter of the Thesis we describe several topics, such as the Sun's structure, and the photosphere as the layer of interest where these small magnetic elements are located. To learn about the magnetic field, several methods are used: inversions, weak-field approximation and centre-of-gravity method. When the application of these methods is not possible by some reason, magnetograph calibrations have been performed to estimate the magnetic field involved in these processes where the direct access to the Stokes parameters was not possible.

The data were acquired by the state-of-the-art instruments HINODE, SST and IMaX/SUNRISE. The ground-based facility SST provided G-band filtergrams, and Ca II filtergrams, magnetograms and SP-data were provided by the space telescope HINODE. The balloon-borne IMaX/SUNRISE supplied high-quality spectropolarimetric data during a 5-day uninterrupted campaign.

An important part of the work of the Thesis is done on the reduction of IMaX/SUNRISE data from scratch, correcting for defects by applying standard reduction procedures, such as flat-field, dark current corrections, and more novel techniques, as Fourier filtering to remove the excess of power corresponding to electronic and optical fringes and restoring them with the Phase Diversity method

to recover the best images up to the diffraction limit. The data products, such Doppler velocity maps and longitudinal and transverse magnetograms, were computed. These data are available now to the Solar Physics community for scientific use.

The scientific part of this Thesis is focused on dynamics of small magnetic elements and vortices i.e., whirling plasma flows. These phenomena, sometimes rather difficult to quantify, are found by different methods that lead to a common result. These techniques are based on the Local Correlation Tracking, which traces elements along time with a correlation window. The procedures are the divergence and vorticity calculation. In addition, the magnetic centroid computation allows us to track structures that are too small or fragmented to be followed by the Local Correlation Tracking.

The first vortex-like flow studied is analysed with independent procedures and, for the first time, in different wavelengths, including chromospheric lines, as Ca II, photospheric, as G-band and CN, and longitudinal magnetograms. Different techniques are applied, as LCT, divergence, calculation of magnetic centroids and inversion codes to retrieve magnetic flux density and velocities. This mesogranular-scale vortex display a slow rotation, however, magnetic elements are able to track its movement.

Some pure magnetic events are analysed, such as the convective collapse events, where an increase of magnetic field strength is linked to strong downflows (from -1 $\mathrm{km\,s^{-1}}$ to -5 $\mathrm{km\,s^{-1}}$ ) over a surface of $0\farcs30\times0\farcs30$, lasting around 3 minutes.

This swirling motions are located in downdrafts, where the cool, more dense, downflowing gas flows to the solar interior. Considering that Coriolis can cause rotational shear, the probability of finding these vortex-like motions turning counterclockwise in the Northern Solar Hemisphere is higher than in the opposite sense. This statement is true for large events; however, for small vortex events, more statistics is necessary. In this work, we have found an occurrence of 65% for counterclockwise swirling flows and 35% for the clockwise motion. The spatial density is $3\times10^{-2}$ vortices $\mathrm{Mm^{-2}}$ and lifetimes of $9.8\pm6.5$ min. Similar values have been found in the literature cited in this work.

The effects of the different parameters involved in the Local Correlation Tracking and their influence for finding vortical motions are also analysed in this text. A slightly positive trend on the vorticity is found in the observational data, by the occurrence of events and the shape of the histograms, whose skewness is positive. This fact may mean that the FOV is located in the Northern Hemisphere. This fact can be corroborated by the new pointing data of IMaX/SUNRISE (Rubio F. and SUNRISE team, private communication) who calculated that the pointing of the

data series of 2009, June 10 on have to be corrected by (-70.″9, 69.″3), therefore the pointing may be (-70.″1, 69.″3). Further studies about the pointing for all the IMaX/SUNRISE datasets have to be made in the future.

A decomposition of the divergence and vorticity is developed, namely, the shear vorticity and the diffluence divergence. These components clearly highlight the places where the horizontal velocity is zero, therefore marking a possible vortex centre. Moreover, the pattern is equal to the azimuth of the horizontal velocities.

The studied elements include the analysis of the emergence of magnetic field in mesogranular-sized granules. These magnetic field appearances over very large granules, that generate positive divergences on mesogranular scale, have been detected before, but in much smaller spatial scale. The study of two large exploding granules where magnetic field emerges, covering a significant part of them, expanding until reaching the intergranular lanes, where it intensifies. The expansion velocities of the large granules are $\sim 1\ \mathrm{km\,s^{-1}}$, while the magnetic patches expand at 0.6 $\mathrm{km\,s^{-1}}$. Magnetic loops are detected over the FOV, whose footpoints separate at 3 $\mathrm{km\,s^{-1}}$, in agreement to other works. These events have been compared to MHD simulations, degraded to IMaX/SUNRISE resolution. No supersonic downflows are noticed in the observational data; however, they are common in flux emergence simulations. More flux emergence events of granular size have been detected in the FOV, where the host granules become very active granules, driving exploding flows around a magnetic network element. These large features have been detected by IMaX/SUNRISE thanks to its high cadence, spatial and spectral resolution. The *cancellation magnetograms* is used to study the behaviour of small positive magnetic features that are dragged to a network element located in a confluence of intergranular lanes. This method prove to be a good tool to infer neutral lines and how they are usually perpendicular to the plasma flow, where the magnetic concentrations actually behave as tracers, following the plasma.

## 6.1 Future work

Thanks to the multi-spectral analyses carried in this Thesis, the employed methods can be applied to other observational cases. The accomplishment on combining of different techniques allows one to apply them in different studies, as looking for vortices on the chromosphere, or investigate the magnetic braiding from the photosphere up to higher layers. More vortices can be found along the high-quality series of IMaX/SUNRISE data, therefore the correlation between pointing and the sign of the vorticity can be attained.

A continuation on the research of the effects of LCT on divergence and vor-

ticity can lead to an automated technique to detect these vortices, in addition to constraint parameters as lifetimes and size.

Last but not least, the second flight of SUNRISE, programmed for 2013, and the project of the next cornerstone mission that is Solar Orbiter (around 2017), will complement notably our knowledge of the Sun at the finest resolution, as it will be the mission closest to the Sun ever launched.

# A

# Data mining June 10, 2009

The Table A is presented as the basis of IMaX data reduction for all data at 2009, June 10. The Modes found in this day were V5_6, L3_2 and L12_2. An example shown in Figure A.1 are data of the Longitudinal Mode L3_2, [207,3] showing the continuum image in Stokes $I$ and the continuum image in Stokes $V$. Some speckles are displayed in the image of Stokes $V$ in continuum, in the right panel: they are supersonic flows. The continuum wavelength point was chosen on the design as this wavelength point is located marking the lower limit of supersonic flows ($> 4\ \mathrm{km\,s^{-1}}$) when Dopplershifts are calculated (Borrero et al., 2010).

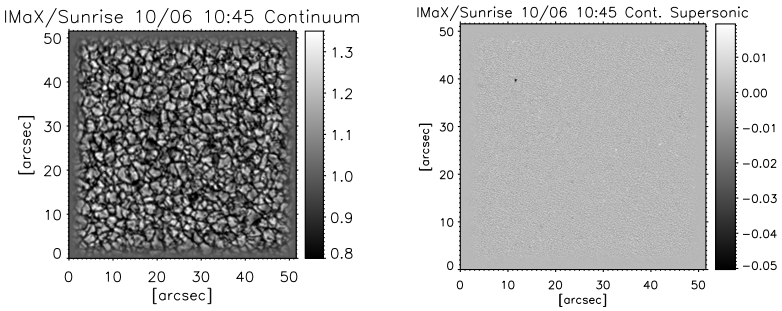


FIGURE A.1— Stokes $I$ continuum and Stokes $V$ continuum, L3_2 images.

| Obs. no. | Time init. | Time end | Cycle no. | Obs. Mode | Comments |
|---|---|---|---|---|---|
| 187 | 0.000 | 1.457 | 87-156 | V5_6 | |
| | | | 87 | | incomplete cycle |
| | | | 88, 91, 92, 152, 155 | | DATA: isolated ones |
| | | | 96-99, 103-112,123-137, 146-150 | | DATA: contrast 0.1 |
| | | | 89-90, 93-95, 100-102,113-122, 138-145,151,153-154,155 | | Not usable |
| 188 | 1.450 | 1.487 | 1-60 | V5_6 | PD. Good: [4,59] |
| 189 | 1.488 | 1.912 | 1-45 | V5_6 | |
| | | | 1-6 | | isolated ones |
| | | | 2-5, 7-10, 11-45 | | not usable |
| 190 | 2.576 | 2.604 | 1-60 | V5_6 | PD blurred and limb. Not for flats |
| 191 | 2.611 | 2.743 | 1-15 | V5_6 | Not usable |
| 192 | 3.082 | 3.111 | 1-60 | V5_6 | possible FF for PD |
| 193 | 3.112 | 3.391 | 1-31 | V5_6 | Not usable |
| 194 | 3.921 | 3.950 | 1-60 | V5_6 | possible FF for PD |
| 195 | 3.951 | 4.295 | 1-38 | V5_6 | Not usable but [23] (Wlimb) |
| 196 | 4.971 | 5.072 | 1-12 | V5_6 | Not usable |
| 197 | 5.770 | 6.132 | 1-40 | V5_6 | blurred or very unsharp |
| 198 | 6.161 | 7.344 | 1-129 | V5_6 | 107, 127-128=E limb good only |
| 199 | 7.812 | 8.223 | 1-12 | V5_6 | Not usable |
| 200 | 8.059 | 9.790 | 1-188 | V5_6 | |
| | | | 9-11,188 | | DARK in timeline |
| | | | 28-36,42,47-86,95-107,113-122,128-145 | | DATA |
| | | | 151-173 | | low contrast DATA |
| | | | 1-8,12-27, 37-41, 43-46, 87-94,108-112, 123-127, 146-150 | | lost and double locked |

TABLE A.1— 10 June data reduction table.

| Obs. no. | Time init. | Time end | Cycle no. | Obs. Mode | Comments |
|---|---|---|---|---|---|
| 201 | 9.792 | 9.809 | 1-2 | V5_6 | DARKS |
| 202 | 9.903 | 9.911 | 1 | V5_6 | PINHOLES |
| 203 | 9.915 | 9.922 | 1 | V5_6 | PINHOLES |
| 204 | 10.023 | 10.503 | 1-53 | V5_6 | FLAT FIELD |
| 205 | 10.506 | 10.530 | 1-50 | V5_6 | PD FF |
| 206 | 10.673 | 10.687 | 1-30 | V5_6 | PD[1,4] ok.[13,17] are blurred |
| 207 | 10.753 | 11.481 | 1-313 | L3_2 | |
| | | | 2-5, 60, 78-123,145-149 | | DATA |
| | | | 170-229 | | DATA $\mu \sim 0.5$ |
| | | | 2-5, 60, 78-123, 145-149 | | DATA $\mu \sim 1$ |
| | | | 232-236, 239-244, 253-267, 286-287 | | DATA |
| | | | 151-152, 237-238, 245-249, 251-252 | | double locked |
| | | | 1, 6-59, 61-79, 124-144, 150, 230-231, 268-285, 288-300 | | not usable |
| | | | 230-231, 268-285, 288-300 | | |
| 208 | 11.489 | 11.8521 | 1-157 | L3_2 | contrast 0.10 |
| | | | 1-4,14-21 | | DATA:long seq.Not good=64,95,105 |
| | | | 23-23, 143-157 | | Not usable |
| | | | 5-13 | | blurred |
| 209 | 11.854 | 11.988 | 1-58 | L3_2 | not usable and not suitable for FF |
| 210 | 11.990 | 12.014 | 1-50 | L3_2 | PD FF. granul noticeable |
| 211 | 13.747 | 13.775 | 1-60 | L3_2 | PD. [1-16] double locked |
| 212 | 13.771 | 14.468 | 1-75 | V5_6 | |
| | | | 5-29 | | DATA. W limb $\mu \sim 0.1$ |
| | | | 3, 4, 34-71 | | unsharp DATA. $\mu \sim 0.3$ |
| | | | 1-2, 30-33 | | not usable |
| | | | 74-75 | | Out disk. Fake darks. |

TABLE A.2— Continued.

| Obs. no. | Time init. | Time end | Cycle no. | Obs. Mode | Comments |
|---|---|---|---|---|---|
| 213 | 14.658 | 14.964 | 1-34 | V5_6 | contrast cam1=0.08 |
| | | | 15-25 | | DATA: blurred W-limb $\mu\sim$ 0.2 |
| 214 | 16.072 | 16.101 | 1-60 | V5_6 | PD DARKS |
| 215 | 16.103 | 17.970 | 1-203 | V5_6 | |
| | | | 1-81 | | DARKS |
| | | | 82-142 | | FLAT FIELDS not at disk center |
| | | | 143-162 | | DARKS |
| | | | 164-166, 169-185 | | FLAT FIELDS |
| | | | 163-164, 167-168, 186-203 | | blurred |
| 216 | 18.099 | 18.131 | 1-80 | V5_6 | CORRUPTED PD |
| 217 | 19.690 | 21.231 | 1-167 | V5_6 | W limb data $\mu \sim 0.2$ |
| | | | 1-7, 17, 23-32, 41-50, 54-68, 77-81, 89-92 | | W limb DATA |
| | | | 96-103, 107-139 | | 124 = bad; DATA: other diff. position in W-limb |
| | | | 143-144, 148-156, 163, 166-167 | | DATA: other position in W-limb |
| 218 | 21.031 | 21.327 | 1-55 | V5_6 | BLURRED LIMB. NOT usable for PD FF. |
| 219 | 21.395 | 21.408 | 1-26 | V5_6 | PD blurred limb. Not usable |
| 220 | 21.483 | 21.511 | 1-60 | V5_6 | PD LIMB good = [1,18]. LIMB not for PD!! |
| 221 | 21.513 | 21.738 | 1-25 | V5_6 | |
| | | | 2-6,10-15,19-24 | | Unsharp W-limb $\mu \sim 0.2$ |
| 222 | 22.224 | 22.681 | 1-53 | L12_2 | FLAT FIELD in timeline |
| 223 | 22.682 | 22.706 | 1-50 | L12_2 | PD FF |
| 224 | 22.843 | 22.857 | 1-30 | L12_2 | PD FF. Not usable for PD FF |
| 225 | 22.924 | 23.999 | 1-123 | L12_2 | |
| | | | 19-26, 89-92, 97-122 | | DATA |
| | | | 49-84 | | DATA. badcycl= [66-69] |
| | | | 1-16, 27-48, 85-88, 93-96, 123 | | not usable |
| | | | 17-18, 38 | | double locked |

TABLE A.3— Continued.

# B

# Data mining June 11, 2009

The table B is presented as the basis of IMaX data reduction for all data at 2009, June 11. On this date, the balloon SUNRISE passed by over Greenland, and this fact had some implications: a temperature increase was detected by the large albedo of Greenland, and this pass by over land provoked two altitude losses.

| Obs. no. | Time init. | Time end | Cycle no. | Obs. Mode | Comments |
|---|---|---|---|---|---|
| 225 | 0.000 | 2.020 | 125-154 | L12_2 | |
| | | | 137, 161, 199, 284, 290, 320, 336 | | isol ones |
| | | | 144-146,151-153,166-167,171-173,213-214,262-263 | | short sequences |
| | | | 126-132, 180-192, 218-243 | | long sequences |
| 226 | 2.025 | 2.481 | 1-52 | L12_2 | FLATS in timeline |
| 227 | 2.482 | 2.507 | 1-50 | L12_2 | PD flat fields |
| 228 | 2.644 | 2.658 | 1-30 | L12_2 | PD: all double locked but [4,9] |
| 229 | 2.724 | 3.098 | 1-43 | L12_2 | |
| 230 | 3.099 | 3.472 | 1-43 | L12_2 | |
| | | | 9,13 | | DARKS |
| | | | 14, 26 | | can be used as flatfield |
| 231 | 3.475 | 3.849 | 1-43 | L12_2 | not useful |
| 232 | 3.849 | 4.281 | 1-50 | L12_2 | 20-21 in S. hemisphere $\mu\sim0.8$ |
| 233 | 4.283 | 4.577 | 1-34 | L12_2 | FLATS in timeline.Used 1-31 |
| 234 | 4.579 | 6.308 | 1-188 | V5_6 | FLATS in timeline.Used 1-185 |
| | | | 185, 188 | V5_6 | DARKS |
| 235 | 6.312 | 6.329 | 1-2 | V5_6 | DARKS |
| 236 | 6.423 | 6.431 | 1 | V5_6 | PINHOLES |
| 237 | 6.434 | 6.441 | 1 | V5_6 | PINHOLES |
| 238 | 6.542 | 6.550 | 1-53 | V5_6 | FLATS in timeline.Used 1-52 |
| 239 | 7.026 | 7.049 | 1-50 | V5_6 | PD FLATS |
| 240 | 7.155 | 7.162 | 1-6 | V5_6 | lost PD.1-3 used as PD FF |
| 241 | 7.212 | 7.226 | 1-30 | V5_6 | PD FF |
| 242 | 7.268 | 7.283 | 1-30 | V5_6 | PD FF |
| 243 | 7.312 | 8.161 | 1-368 | L3_2 | |
| | | | 30,33,38,39,60,66-68,75,76,174-176,231,241-242,288,294 | | double locked |
| | | | 77, 232, 240 | | blurred |
| 244 | 8.162 | 8.297 | 1-59 | L3_2 | FLATS in timeline.Not useful. |
| 245 | 8.299 | 8.323 | 1-50 | L3_2 | PD FF |
| 246 | 8.484 | 8.498 | 1-30 | L3_2 | FF. DARKS: [21,30] |
| 247 | 11.488 | 11.516 | 1-60 | L3_2 | PD. Used: [27,43] |

TABLE B.1— 11 June data reduction table.

| Obs. no. | Time init. | Time end | Cycle no. | Obs. Mode | Comments |
|---|---|---|---|---|---|
| 248 | 11.518 | 13.071 | 1-306 | V5_3 | |
| | | | 13, 231, 290 | | isol. cycles |
| | | | 200-205, 213-216, 294-296, 304-306 | | sequences in south. hemisphere |
| | | | 42-88 | | Used as FLATS. |
| | | | 109-112 | | DARKS. |
| | | | 266-268 | | DARKS counts around 400. |
| 249 | 13.850 | 13.885 | 1-4 | V5_6 | bad demodul. |
| 250 | 13.946 | 13.951 | 1 | V5_6 | bad demodul. incomplete. |
| 251 | 13.986 | 14.022 | 1-4 | V5_6 | bad demodul. Good[1,6] |
| 252 | 14.061 | 14.118 | 1-7 | V5_6 | bad demodul. |
| 253 | 14.145 | 14.383 | 1-26 | V5_6 | bad demodul. |
| 254 | 14.402 | 14.554 | 1-17 | V5_6 | bad demodul. incomplete |
| 255 | 14.579 | 14.597 | 1-3 | V5_6 | bad demod. incomplete |
| 256 | 14.627 | 14.712 | 1-10 | V5_6 | bad demodul. incomplete |
| 257 | 14.794 | 14.822 | 1-60 | V5_6 | PD. Double locked. |
| 258 | 14.82410 | 16.82230 | 1-394 | V5_3 | $\mu$=0.5, 0.73 in logbook. |
| | | | 2-9, 17-48*, 56-69, 76-81, 237-244, 254-262 | | Short seq. * double=34,35,40 |
| | | | 91-190*, 199-230, 269-327, 335-361, 371-394 | | Long seq. * blurred = 181, 182, 188, 190 |
| 259 | 16.844 | 16.872 | 1-60 | V5_3 | |
| | | | 38,43 | | Good cycles |
| | | | 1,11 | | Used for FLATS |
| | | | 45-50 lil bit blurred; 50-59, slightly blurred | | |
| 260 | 16.875 | 17.753 | 1-173 | V5_3 | a=-0.773099 in logbook |
| | | | 68,77 | | DARKS not in timeline |
| | | | 1-23, 33-55, 64-67, 84-93, 98-131, 137-150 | | last 2 seq. with very good contrast |
| | | | 1, 38, 62, 63, 82, 83, 97 | | blurred |
| 261 | 18.215 | 18.699 | 1-53 | V5_6 | FLAT FIELDS. Used [1, 52]. |
| 262 | 18.698 | 18.722 | 1-50 | V5_6 | PD FF |
| 263 | 18.865 | 18.879 | 1-30 | V5_6 | PD: Used [1,12]; double locked [12,18] |

TABLE B.2— Continued.

| Obs. no. | Time init. | Time end | Cycle no. | Obs. Mode | Comments |
|---|---|---|---|---|---|
| 264 | 18.945 | 22.043 | 1-336 | V5_6 | |
| | | | 44-59, 64-66, 71-77, 81-95, 106-113, 117-120, 175-178 | | Short sequences |
| | | | 183-185, 190-203, 214-216, 315-316, 322-326 | | Good short seq. |
| | | | long seq=[126,168], [221,308*] | | *blurred=241-243,276 |
| | | | | | lost =251-253, 278-280, 299-302 |
| | | | 1,15, 63, 98, 104, 116, 173,174, | | blurred |
| | | | 182,189, 206, 212, 213, 220, 332 | | |
| 265 | 22.046 | 22.526 | 1-53 | V5_6 | FLATS. Used [1,52] |
| 266 | 22.673 | 22.687 | 1-30 | V5_6 | DARKS in timeline |
| 267 | 22.812 | 23.116 | 1-54 | V5_3 | NO DARKS TO DO IT |
| 268 | 23.115 | 23.139 | 1-50 | V3_6 | FF PD |
| 269 | 23.276 | 23.289 | 1-30 | V3_6 | PD. [1,5] , 30 a bit blurred. |
| 270 | 23.320 | 23.997 | 1-88 | V3_6 | |
| | | | 13,24,79,80-84 | | double locked |
| | | | 43, 57, 65 | | blurred |

TABLE B.3— Continued.

# C

# Resumen en español

Este resumen presenta una descripción de los contenidos y trabajo elaborados en esta Tesis. No se incluyen Figuras ni Tablas, ya que nos referiremos a las incluidas en los Capítulos centrales.

## C.1 Introducción

### C.1.1 Objetivos de esta Tesis

El objetivo principal de esta Tesis es el estudio detallado de pequeñas concentraciones magnéticas en la fotosfera y baja cromosfera. Estas estructuras son importantes en tanto en cuanto son las más abundantes de la superficie solar y juegan un papel importante en las estimaciones de irradiancia, dínamo local y magnetismo superficial. Para el estudio de estos elementos, se han usado datos de telescopios en tierra, como el Telescopio Solar Sueco, y espaciales, como HINODE y SUNRISE. Asimismo, una buena parte del trabajo de esta Tesis se ha dedicado a la reducción de datos de IMaX/SUNRISE hasta dejarlos listos para su explotación científica.

### C.1.2 Estructura del Sol

El Sol es el astro más cercano a la Tierra. Por su indudable efecto sobre la biosfera terrestre, el Sol ha sido objeto de culto ancestral. Sin embargo, hasta la era telescópica que iniciaron Galileo y contemporáneos, – con algunos intentos previos de observación con cámara obscura u observación directa a través de nubes o humo –, la superficie solar era prácticamente desconocida. Como esta capa del Sol emite en longitudes de onda visibles, constituye la capa más estudiada actualmente.

Sin embargo, y como cualquier estrella, tiene un núcleo en el que se generan las reacciones de fusión en las cuales se libera energía. Sobre el núcleo está la zona radiativa en la que, debido a su alta densidad y opacidad, la energía se transmite por radiación. Cuando la opacidad baja, el transporte convectivo es mucho más eficiente, lo que genera la capa conocida como la zona de convección, y en la parte más externa de ésta, se sitúa la fotosfera. Por encima de ella se encuentra la cromosfera. La baja densidad de esta capa y siguientes y su creciente temperatura hacen que no se encuentren en equilibrio termodinámico local. En la corona, que es la parte de la atmósfera solar con menor densidad, se alcanzan temperaturas de millones de grados.

El plasma solar está en continuo movimiento. Es muy claro ver este movimiento en la fotosfera, observando la granulación. El movimiento de cargas genera un efecto, que es la creación de campos magnéticos. Podemos observar campos magnéticos desde la fotosfera hasta la corona, en diversas estructuras, tales como manchas solares, fáculas, *plages*... y también en diminutas estructuras, que centran el interés de este estudio. Estos elementos magnéticos se consideran formados por tubos de flujo. Estos tubos magnéticos están en equilibrio hidrostático y por ello, como las presiones de gas y magnética han de equilibrarse, la presión de gas dentro del tubo es menor que la de los alrededores, haciendo que tenga menos densidad. Debido a que también se cumple la hipótesis de equilibrio radiativo, se observa que las paredes son brillantes, ya que el tubo radía por las paredes. En la Figura 1.6 se observan varios esquemas gráficos de estos tubos. La baja densidad y alta temperatura hace que se disocien moléculas como el CH y el CN, haciendo que su contraste sea más alto en estas bandas. Es por ello que estos elementos magnéticos se observan principalmente en esas bandas. Estos tubos son los bloques que forman los elementos de red, la filigrana, los puntos brillantes (GBPs) y los puntos faculares.

### C.1.3 Procesado de imagen

Que estas concentraciones magnéticas puedan ser estudiadas dependen del poder resolutivo del telescopio y de la calidad de la atmósfera. La resolución de las imágenes, en casos ideales sin atmósfera, o aplicado en telescopios espaciales –y considerando telescopios perfectos –, dependen del diámetro de la apertura y de la longitud de onda utilizada. Los datos tomados por telescopios terrestres o estratosféricos sufren cambios provocados por la turbulencia atmosférica. Esta degradación de imagen se puede descomponer en diferentes componentes: desplazamientos globales de la imagen, y distorsión pura de las estructuras causadas por diferentes porciones de la atmósfera, suavizado y pérdida de detalle, etc. Para

mitigar estos efectos perjudiciales de la atmósfera, se llevan a cabo diferentes procesos de restauración, tales como el MOMFBD, la restauración por Diversidad de Fase (PD) y filtros óptimos que permiten minimizar los efectos del ruido y mejorar la señal. Asimismo se aplican filtros para eliminar los modos *p* solares que provocan diferencias en contraste, velocidad en la línea de visión, etc.

### C.1.4 Espectropolarimetría

En esta Sección se estudian los métodos principales para obtener estimaciones de campo magnético a través de la luz polarizada proveniente del Sol. Dado que los fotones sufren múltiples colisiones antes de emerger en la fotosfera, la luz solar en longitudes de onda visible no está polarizada. Sin embargo, esto no es así en presencia de un campo magnético: la luz se polariza por el efecto Zeeman. Este efecto da cuenta no sólo del desdoblamiento de líneas espectrales, si no también por qué esos desdoblamientos están polarizados (considerando el campo magnético paralelo a la línea de visión). Por ello, esta luz se puede recoger y transformar a través de retardadores o cristales líquidos en luz linealmente polarizada. Con un juego de polarizadores podemos extraer la señal y analizarla. Obviamente, para realizar todo este proceso, se necesita seleccionar una línea espectral magnéticamente sensible primero, lo que se realiza a través de un etalón u otro tipo de interferómetro.

Cuando ya tenemos la señal polarizada, podemos combinarla a través de una matriz de demodulación para obtener los parámetros de Stokes $I, Q, U, V$. Una vez tenemos los parámetros de Stokes, podemos inferir el campo magnético que creó la señal original a través de diversos métodos: la aproximación de campo débil (Ecuación 1.39), el centro de gravedad de la línea (Ecuación 1.41 y siguientes) o los métodos de inversión. Para este último, se usa un modelo de atmósfera solar ajustado a las condiciones físicas en particular, y junto a diferentes variables termodinámicas, se obtiene la magnitud del campo magnético local, además de la inclinación y el azimut, que posteriormente hay que desambiguar.

## C.2 Misiones y adquisición de datos

### C.2.1 Telescopio Solar Sueco

El Telescopio Solar Sueco (SST) está ubicado en el Observatorio del Roque de los Muchachos en La Palma. El diámetro de este telescopio solar es uno de los más grandes del mundo. Con 1 metro de apertura, la resolución que se alcanza es de $0\farcs1$. Este telescopio es de vacío, para evitar turbulencia dentro del tubo, aunque está relleno de helio para evitar las diferencias de presiones en la ventana de apertura. Este telescopio tiene un foco Schupmann que evita aberraciones

cromáticas, astigmatismo, y reduce la luz dispersa. Al final del tubo hay un divisor de haz, que divide la luz en longitudes superiores e inferiores a los 500 nm. Las longitudes de onda menores que 500 nm se mandan al 'canal azul', un conjunto de cámaras con filtros para Ca II H en las alas de la línea, en el centro, en banda G y continuo de la banda G. Para la temporada 2007, de la que se utilizan datos, el muestreo espacial es $0\farcs034$ píxel$^{-1}$. Las mayores de 500 nm se mandan al 'canal rojo', típicamente, un polarímetro. En las campañas anteriores a 2008 el polarímetro era SOUP, y posteriormente, el instrumento CRISP tomó su lugar. Por supuesto, un telescopio tan grande ha de llevar óptica adaptativa. En este caso, un sensor Shack-Hartmann permite saber la forma de las deformaciones del frente de onda y un espejo deformable que las compensa. Asimismo, el correlador de imagen reduce el movimiento global de las imágenes. Las imágenes obtenidas por la SST se han reducido con el algoritmo 'Multi-Frame Blind Deconvolution (MFBD) with Linear Equality Constraints (LECs)', como aparece en Löfdahl (2002).

### C.2.2 HINODE

Este telescopio espacial fue lanzado el 22 de septiembre de 2006. Esta misión japonesa, con colaboración de diferentes institutos, es un telescopio de 50 cm de apertura para el visible y ultravioleta, y consta de diferentes instrumentos: SOT y su subinstrumento SOT-SP, además de EIS y XRT. El primero es el telescopio óptico, que toma imágenes en CN, banda G, Ca II, y también genera magnetogramas longitudinales en Na I y Mg I. Los datos que usaremos aquí presentan unos muestreos espaciales de $0\farcs054$ píxel$^{-1}$ para los filtrogramas y de $0\farcs08$ píxel$^{-1}$ para los magnetogramas longitudinales. SOT-SP es el espectropolarímetro. Usando las líneas 6301 y 6302 Å, adquiere datos que, ya demodulados, ofrecen los parámetros de Stokes al usuario a través de su servidor DARTS. El muestreo espacial es $0\farcs16$ píxel$^{-1}$. EIS y XRT son los instrumentos para ultravioleta y de rayos X.

### C.2.3 SUNRISE

#### C.2.3.1 Descripción

La misión SUNRISE es una misión que consta de un telescopio solar de 1 metro de apertura y un globo que lo elevó a 36 000 m durante el vuelo polar sobre el Ártico, de Suecia a Canadá, del 8 al 13 de junio de 2009. Esta misión fue fruto de la colaboración de diferentes institutos, tales como NASA, MPS, KIS, HAO, LMSAL, IAC, IAA, INTA y UV. Como buena parte de la instrumentación está prácticamente intacta, se planea un segundo vuelo para el año 2013. Las ventajas de una misión estratosférica polar es que, al lanzarla en el verano polar, se tienen días con 24

horas de luz solar. Además, como vuelan casi por encima de la capa de ozono, la absorción de luz ultravioleta por esta molécula es mínima.

El telescopio de SUNRISE es un telescopio de tipo Gregory (con estructura Serrurier) de más de un metro de diámetro, con un espejo parabólico como primario, que pesa 47 kg. Los espejos están aluminizados y concentran la luz sobre una cuña que disipa el calor, ya que recibe más de 1 kW de luz solar sobre ella. Este calor se traslada hacia unos paneles que lo radían fuera del telescopio. Otro instrumento intermedio es ISLiD, el sistema de distribución de luz y estabilización de imagen, que contiene un divisor de haz que lleva la luz hacia los instrumentos de ciencia, y también tiene el CWS o sensor correlador de frente de onda. El apuntado se realiza a través de LISS (sensor solar). El telescopio se abastece de energía a través de sus paneles solares. Los datos se almacenan en discos de 100 Gb.

Los instrumentos científicos de SUNRISE son IMaX, el magnetógrafo de imagen y SuFI, que obtiene filtrogramas en ultravioleta de la baja cromosfera. SuFI tiene 5 filtros diferentes en 312, 388, 397 nm, correspondientes a bandas de OH, CN, Ca II, además de los filtros en 214 y 300 nm. Estos filtros son dobles para evitar en lo posible las contribuciones fotosféricas en las imágenes. El campo de SuFI es de $15'' \times 40''$. SuFI tiene un sistema de Diversidad de Fase con el que se corrigen las imágenes tras su adquisición.

El instrumento IMaX se crea con la contribución de un consorcio de instituciones científicas españolas. IMaX es un espectropolarímetro que opera en la longitud de onda correspondiente al Fe I 5250.2 Å. El muestreo espacial es $0\farcs055$ píxel$^{-1}$ y el campo de IMaX es de $50'' \times 50''$.

El sistema óptico de IMaX es bastante complejo. La luz pasa por un prefiltro, con el que se selecciona 100 mÅ en el rango de 5250.2 Å. Esta luz pasa por los cristales líquidos, que cambian su retardo conforme se les aplica un determinado voltaje, actuando como retardadores y polarizadores. Posteriormente la luz incide en el etalón, y se vuelve a hacer pasar una segunda vez, para que la selección del interferómetro sea más fina. Esta luz va a un divisor de haz que la lleva a las cámaras. El diseño de las partes integrantes de IMaX y su conjunto fue determinante para su éxito. Por ejemplo, el retardo producido por los cristales líquidos se puede ver alterado por fluctuaciones de temperatura, por lo cual la estabilización de la misma dentro del sistema es fundamental. El etalón, a su vez, funciona con altos voltajes, por lo que había que aislar su fuente de alimentación para que no hubiera descarga en arco, ya que el instrumento va en vacío. También la configuración de un etalón es crítica: en la configuración colimada de IMaX se genera una deriva en las longitudes de onda (llamada *blueshift*, de la que se muestra un ejemplo en la Figura 2.15) que luego se ha de corregir en los datos.

#### C.2.3.2 Reducción de datos de IMaX

IMaX adquirió datos en diversos Modos de Observación: con los 4 parámetros de Stokes $[I, Q, U, V]$ para construir magnetogramas longitudinales y transversales, o sólo $[I, V]$, para magnetogramas longitudinales únicamente. En estos modos también se podía elegir el muestreo de la línea, que eran tres o cinco puntos. Ajustando a una gaussiana y deduciendo los diferentes parámetros de la línea, posteriormente se utiliza para sacar la velocidad en la línea de visión, etc. Estos modos están resumidos en la Tabla 2.2.

El primer paso de la reducción en sí es la localización de las imágenes de ciencia y auxiliares en los datos. La reducción de datos de IMaX comienza quitando las contribuciones de corriente oscura y de *campo plano*. Estos campos planos contienen la contribución del *blueshift*, que se ha de eliminar. Para ello, se ha de realizar la calibración de la longitud de onda: ajustando la línea espectral con los datos de cada imagen de *campo plano*, se usa para restar esta contribución. Como el campo está afectado de franjas, se genera una máscara en el dominio de Fourier donde aparecen de forma muy evidente, que hace desaparecer las franjas y algunas motas de polvo situadas en las ventanas de las cámaras (Figura 2.20). Posteriormente, se pasa a corregir las imágenes con Diversidad de Fase, que crea la OTF del telescopio con las aberraciones propias y de la atmósfera. Así la imagen queda restaurada. El resumen de datos encontrados está en las Tablas A y B, en los Apéndices A y B. Una muestra de la restauración de datos se presenta en la Figura 2.23.

### C.3 Dinámica de elementos magnéticos con datos de HINODE y SST

#### C.3.1 Introducción y métodos

La dinámica de las estructuras magnéticas en el Sol es compleja debido a su variedad de escalas espaciales y temporales. Los movimientos en remolino de la más pequeña escala, de alrededor de 1 Mm, son los casos que se estudian en este Capítulo y el siguiente. En estos sumideros que se encuentran en las zonas intergranulares, el plasma baja formando las paredes granulares y cuando llega a la zona intergranular, toda esa materia ha de bajar a la zona inferior de la capa convectiva a través de áreas muy pequeñas. Por conservación del momento angular, el plasma en movimiento comienza a rotar alrededor del sumidero, como el de una bañera. Este efecto se ha observado en simulaciones, y posteriormente se ha hallado en la fotosfera solar. Muy recientemente, también se han encontrado flujos vorticales en la cromosfera.

El modo de observar estos movimientos es a través, en general, de Seguimiento de Correlación Local. Esta técnica permite seguir diversas estructuras y generar un

mapa de flujo en el que aparecen las velocidades horizontales de estas estructuras, promediadas en una ventana espacial. Este método también es dependiente del promediado temporal que se use para seguir las estructuras.

Una vez tenemos los mapas de flujo, se puede calcular la divergencia y vorticidad con las Ecuaciones 3.1 y 3.2. La divergencia tiene un uso bastante particular, dado que, si se multiplica por un factor de escala, se puede obtener una estimación de las velocidades perpendiculares al flujo horizontal.

También se pueden utilizar *trazadores* que siguen los flujos horizontales. Estos trazadores pueden ser artificiales (comúnmente llamados *corchos*) o en la superficie del Sol, como GBPs. Se pueden observar trazando trayectorias alrededor del sumidero.

### C.3.2 Datos

Este estudio multiespectral incluye diferentes datos obtenidos el día 29 de septiembre de 2007 en la campaña internacional HOP 14 en la que participaron SST e HINODE, entre otros observatorios. Estos datos, correspondientes a $\mu$=0.99, son los siguientes:

- El telescopio SST obtuvo datos en banda G y Ca II con un campo efectivo de $69'' \times 69''$, con un muestreo espacial de $0\farcs034$ píxel$^{-1}$. Se restauraron utilizando el 'Multi-Frame Blind Deconvolution (MFBD) with Linear Equality Constraints (LECs)', obteniéndose dos series de datos (*s1*: 08:47-09:07 TU and *s2*: 09:14-09:46 TU) con una cadencia de 15 s. Estas dos series han sido filtradas para eliminar los modos *p*, y se ha corregido la posible distorsión post-restauración.
- El telescopio HINODE adquirió datos en CN y Ca II. El campo de estas imágenes es $19\farcs18 \times 74\farcs09$, con un muestreo espacial de $0\farcs054$ píxel$^{-1}$ y una cadencia de 35 s. Además, se tomaron magnetogramas en la línea de la baja cromosfera Mg I, con un muestreo espacial que es $0\farcs08$ píxel$^{-1}$, cada 20 s. Las secuencias se tomaron de 08:40 a 09:20 TU.
- Con el instrumento SOT-SP, se adquirieron 1954 scans, con un muestreo de $0\farcs15$ píxel$^{-1}$, y una cadencia de 1.6 segundos por posición de la rendija. La serie de datos va de 08:20 a las 09:44 TU. Las líneas observadas fueron 6301 y 6302 Å. Los datos fueron invertidos con el código LILIA. Un resumen de los datos se encuentra en la Tabla 3.1.

La Figura 3.4 muestra una secuencia en distintas longitudes de onda del evento. Cada imagen es un promedio de 4 minutos. Sobre los filtergramas se han superpuesto los contornos magnéticos que permiten identificar perfectamente la estructura. A los magnetogramas de Mg I se les ha aplicado una máscara con un umbral por encima de $3\sigma$ para eliminar el ruido. Se ve que la estructura está definida en

dos *lóbulos* (L1 el del sur y L2 el del norte) que se mueven respecto a un centro común a lo largo de 40 minutos. En diversos intervalos, los *lóbulos*, formados por GBPs, evolucionan, pierden estructuras o se unen.

### C.3.3 Análisis de datos espectropolarimétricos

Los datos de HINODE SOT-SP presentan un ruido de $1.6 \times 10^{-3} I_c$ para Stokes $I$ y $1.8 \times 10^{-3} I_c$ para Stokes $Q$ y $U$. Dado el corto periodo de integración de estos scans, presentan bastante ruido. Por ello, es necesario eliminar el ruido. Usaremos una máscara de $3\sigma$, como en los datos de Mg I. Se prueba el efecto de diferentes máscaras ($3\sigma$ y $5\sigma$) en una imagen. En la Figura 3.6 se observa la evolución de las estructuras magnéticas con los datos obtenidos por LILIA para el valor absoluto de la magnitud del campo magnético $|B|$, la inclinación y la velocidad. Hay dos velocidades que se han obtenido: una a través de LILIA, que da la velocidad de la atmósfera magnetizada y no magnetizada, y la obtenida por el parámetro de Stokes $I$, que da la velocidad de la atmósfera no magnetizada, que es en la que estamos interesados. En ese mapa se plasma la evolución de las estructuras magnéticas. A través de las inversiones y la aproximación de campo débil, se ve que los máximos valores del campo magnético se dan en los centros de los *lóbulos*, rondando los 600 G. Aparece un flujo intergranular descendente de velocidad alta, de 3 $\mathrm{km\,s^{-1}}$, en la parte inferior de la imagen, donde comienza a formarse un vórtice, como muestra la Figura 3.8.

También en este campo, al observarse coalescencia y separación de GBPs, podemos observar posibles colapsos convectivos. Determinadas estructuras magnéticas presentan una gran velocidad hacia el interior de la superficie solar acompañadas de un incremento en el campo magnético. En la teoría de formación de tubos de flujo, cuando éstos aparecen en la superficie solar, puede apreciarse cómo el gas en el interior del tubo se vacía, por la presión magnética (observable en el incremento de la velocidad), además de un incremento del campo magnético, hasta que el tubo se equilibra. El tamaño de las estructuras donde se dan son de unos $0\farcs3$. Además, y detectando esos gradientes de velocidad y campo en los perfiles $V$ de Stokes, se pueden apreciar perfiles con 3 lóbulos, además de velocidades descendentes de unos 7 $\mathrm{km\,s^{-1}}$. Estos gradientes duran unos 2 minutos.

### C.3.4 Estructura vortical con mapas de flujo y centroides

Las series en banda G se han usado para analizar los movimientos propios horizontales. Se ha usado la técnica de Seguimiento de Correlación Local usando una ventana gaussiana de $1''$ y promediado en 19 minutos. La Figura 3.8 muestra

ese mapa de flujo sobre un mapa de divergencia normalizado. Se observan dos sumideros en las coordenadas [6.5,3.5] and [8.5,7.5] . El primero es el centro del sumidero con respecto al cual giran las estructuras magnéticas L1 y L2.

Cuando se dibujan las trayectorias de L1 y L2 calculando el centroide de la distribución magnética con la Ecuación 3.4, se observa los arcos que describen (Figura 3.9), e incrementan su velocidad cuando se van aproximando al centro del sumidero.

### C.3.5 Conclusiones

Con respecto al vórtice, se sugieren dos posibles escenarios: los efectos observados pueden ser por la evolución estocástica de los gránulos, que han arrastrado a los GBPs hacia el centro del sumidero que hace acelerar sus movimientos. Sin embargo, no se siguen GBPs hasta el centro del vórtice, lo cual podría deberse al *trenzado magnético* entre los tubos de flujo principales que generan la aparición y desaparición de GBPs. También se ha hecho una estadística de los elementos magnéticos hallados en las imágenes de CN, G-band y magnetogramas de Mg I. Estos elementos magnéticos se han reconocido a través del método de segmentación MLT4, que consiste en reconocer diferentes niveles de intensidad y segmentar la imagen dependiendo del nivel de intensidad de la imagen por encima de un determinado valor umbral. Se observan que las concentraciones en banda G presentan un diámetro de 0.″14, mientras en CN su diámetro es de 0.″27. La cobertura de superficie de estas estructuras es de 0.26% y 0.22% respectivamente. Se puede ver un resumen de este estudio en la Tabla 3.2.

## C.4 Vórtices observados con datos de IMaX

### C.4.1 Introducción

Este Capítulo presenta una caracterización de los flujos convergentes que generan vórtices debidos a la convección en la fotosfera solar a través de sus magnitudes más representativas, que son la divergencia y la vorticidad. Como estas cantidades están derivadas de las velocidades horizontales extraídas de Método de Correlación Local, hemos de estudiar la influencia de diferentes parámetros sobre la divergencia y la vorticidad.

### C.4.2 Datos

Dos series de datos de IMaX se obtuvieron el día 9 de junio de 2009, cerca del centro solar. Se adquirieron en modo V5_6. Estos datos pertenecen a la observación número 163, con ciclos [248-249] y [307-364] 00:36-00:58 TU y 01:31-02:02 TU.

El procesado posterior fue el alineamiento subpíxel y la eliminación de *modos p*. El campo efectivo de visión es $45'' \times 45''$. La primera serie se ha usado en este Capítulo.

#### C.4.2.1 Métodos: efectos del promediado espacio-temporal

El método de Correlación Local genera diferentes patrones dependiendo de la ventana de promediado espacial y el promediado temporal. Cuando se consideran ventanas menores que $1''$ o intervalos temporales menores de 5 minutos, los patrones son más fluctuantes. Esto se prueban tomando la serie de $\sim$21 minutos, y promediando en los primeros 2.5 minutos, 5, 10, 15 y 20 minutos. Se observa en las Figuras 4.1 y 4.2 que el patrón espacial obtenido por la divergencia y la vorticidad no varía demasiado, cuando consideramos ventanas de correlación de $1''$y $1\farcs5$. En las Figuras 4.3 y 4.4 se puede ver la distribución de la divergencia y la vorticidad con las mencionadas ventanas y diferentes promedios temporales. Se observa que los valores de divergencia y vorticidad son mayores cuanto menor es el promediado espacio-temporal. Otras propiedades estadísticas relevantes, tales como las medianas, se observa que son siempre negativas para estas distribuciones de divergencia y siempre positivas en el caso de la vorticidad. En particular, la vorticidad muestra asimetrías en el lado positivo de la distribución, lo cual podría indicar que la Serie analizada está en el hemisferio norte solar.

#### C.4.2.2 Métodos: efectos de la eliminación de ruido en magnetogramas en el LCT y comparación con simulaciones

La Correlación Local puede dar falsos positivos en vorticidad si el método está siguiendo patrones espaciales de ruido en lugar de una señal real. Por tanto, hemos usado diferentes valores umbrales aplicados a los magnetogramas (de 1, 2 y $3\sigma$), y estudiado sus efectos, para el caso del promediado temporal de 20 minutos, y *FWHM* de $1\farcs5$. Los histogramas obtenidos son clarificadores: la distribución es más estrecha para $1\sigma$, bastante similar al caso sin valor umbral, y en el caso de los de 2 y $3\sigma$, la distribución es mucho más ancha, y llega hasta valores de $\pm$ 0.2, valores de divergencia y vorticidad muy altos sólo obtenidos en simulaciones. Para comprobar estos valores, hemos usado una simulación creada por Cheung et al. (2008) y que también se usa en la Sección §5.3.4. Analizamos los casos referentes a la simulación original, con un muestreo espacial de $0\farcs034$, y otra simulación, suavizada a través de una convolución. Considerando también un promediado de 20 minutos, y *FWHM* de $1\farcs5$, obtenemos distribuciones de divergencia y vorticidad, que se muestran en la Figura 4.8. La simulación original genera un histograma bastante similar a las

distribuciones de 2 y 3$\sigma$, y la suavizada presenta una distribución similar a la de 1$\sigma$. También se realiza la comparación entre una simulación en continuo y las observaciones. Los valores de la divergencia y la vorticidad son también altos, pero menores que en los casos de magnetogramas sintéticos.

#### C.4.2.3 Otro sistema de coordenadas para la divergencia y vorticidad

A la hora de estudiar la divergencia y vorticidad, especialmente esta última magnitud, podemos percibir que es difícil describir un movimiento de trayectoria curva no circular, ya que las velocidades horizontales que describen un arco pueden dar lugar a los mismos valores que un movimiento circular puro. Por tanto, es necesario desacoplar la curvatura de la trayectoria de la vorticidad. Cambiando el sistema de referencia es posible, y aparece la componente *cizalla* de la vorticidad (ver Ecuaciones 4.1 y 4.2), junto con la de la curvatura, con lo que quedan desacoplados en dos términos.

#### C.4.2.4 Análisis de pequeños vórtices

Realizando un recuento de vórtices sobre los magnetogramas, buscando patrones convergentes en los diagramas de flujos horizontales, obtenemos los siguientes resultados: las vidas medias son de 9.8$\pm$ 6.5 min, la densidad superficial es $3.2\times10^{-2}$ vórtices Mm$^{-2}$ y la densidad espacio-temporal es $3\times10^{-3}$ vórtices Mm$^{-2}$ min$^{-1}$. También se encuentra que 35% de los vórtices giran en sentido horario, y 65% giran en sentido antihorario. Este resultado tiene su importancia relacionada a la posición del campo de visión. Si consideramos la cizalla causada por la rotación diferencial, este hecho puede da lugar a mayor probabilidad de encontrar vórtices que giran en sentido antihorario en el hemisferio norte solar y en sentido horario en el hemisferio sur. Este hecho también está en acuerdo con las asimetrías observadas en los histogramas en las Figuras 4.3 y 4.4.

A veces es posible detectar de modo visual el movimiento giratorio de GBPs en zonas de divergencia negativa. Sin embargo, en general son demasiado pequeños para ser seguidos por medios de Correlación Local. Hay otros métodos válidos para seguir estos elementos magnéticos, como los centroides magnéticos. En la Figura 4.19, se muestran tres trayectorias de centroides magnéticos, dos que giran en sentido antihorario, y uno en sentido horario. La trayectoria comienza en el segmento negro y termina en el rojo. La duración es de 4 a 7 minutos. Debemos hacer notar la pequeña escala de estos movimientos, del orden de la resolución de IMaX. Sin embargo, en Moll et al. (2011), las trayectorias de partículas prueba en una simulación están en acuerdo con este rango de distancias y de períodos

de rotación, ya que se encuentran vórtices que presentan giros dobles durante su duración.

## C.5 Emergencias de campo magnético en gránulos de escala mesogranular

### C.5.1 Introducción

Aunque la mesogranulación, como escala intermedia entre la granulación y la supergranulación se ha estudiado en profundidad, la pregunta de si es realmente una escala natural de la convección sigue sin respuesta. Esta escala particular se manifiesta cuando series temporales de más de 20 minutos y hasta 1 hora se promedian o se analizan por Correlación Local. También está relacionada con los los gránulos explosivos y las familias de gránulos explosivos, que generan grandes flujos de plasma. La mesogranulación también se identifica por zonas de divergencia positiva, que las generan los gránulos explosivos. Estos gránulos explosivos pueden alcanzar un gran tamaño, y antes de fragmentarse generan una estructura más oscura que el gránulo medio debido al frenado de la flotabilidad del plasma, ya que el exceso de masa sobre la parte superior del gránulo reduce la velocidad de ascenso del plasma hasta su colapso. Otras claves para entender la emergencia de estos gránulos es la compresibilidad: en plasmas incompresibles, estas estructuras no aparecen, por lo cual la mesogranulación no se desarrolla. La relación entre la mesogranulación y los campos magnéticos también ha sido analizada en la literatura. Se cree que los elementos magnéticos de red son empujados a los límites supergranulares, por lo que se pueden encontrar familias de gránulos que han expelido los elementos magnéticos hacia los límites de las familias.

En este Capítulo se analiza la relación de grandes gránulos explosivos de los que emergen campos magnéticos débiles que pueden llegar a cubrir una importante fracción del gránulo. Estos campos, al inicio son unipolares y cuando se va fragmentando, aparecen áreas de doble polaridad. Estas regiones se desplazan hacia las zonas intergranulares, donde el campo magnético se intensifica. El campo magnético transversal es casi despreciable sobre la estructura magnética principal, salvo en bucles magnéticos que aparecen cuando el gránulo explosivo está en proceso de fragmentación.

### C.5.2 Análisis

Los datos usados han sido obtenidos por el instrumento IMaX/SUNRISE el día 10 de junio de 2009 en dos modos de observación diferentes. La primera serie, (referida al evento $v10$) se ha adquirido en el modo de V5_6, de 08:29 to 08:50 TU ($\sim$21 min). En este caso, se usado la aproximación del campo débil para los

magnetogramas longitudinales, mientras los campos transversales y dopplergramas se obtuvieron siguiendo la calibración en Martínez Pillet et al. (2011). La segunda serie de datos, y cuyo evento denominaremos $\ell 10$, se ha adquirido en el modo longitudinal L12_2, from 23:42 to 23:59 TU (∼18 min). En el caso $\ell 10$, el campo magnético se obtiene por $\mathbf{1}$) el método de centro de gravedad y $\mathbf{2}$) inversiones SIR. Todos los datos han sido filtrados para eliminar los modos *p*.

### C.5.2.1 Descripción de los gránulos explosivos

Los dos eventos $v10$, $\ell 10$ se siguen hasta que los gránulos explosivos se fragmentan y pierden su identidad. Para estimar el tamaño del gránulo justo antes de su fragmentación, se crea una máscara binaria para medir el área. Se calcula el radio equivalente considerando la estructura como circular. Los gránulos tienen un tamaño de $> 3''$ en ese momento. También se infiere una densidad superficial alrededor de 1% para estas estructuras convectivas, que son unos 3 gránulos explosivos en cada imagen de IMaX. Hallando la tasa de ocurrencia de estos eventos, se obtiene $7.7{\times}10^{-11}\ \mathrm{km^{-2}\,s^{-1}}$. Hallando el área del gránulo en cada imagen, se calcula la velocidad de expansión ajustando por mínimos cuadrados a una recta, obteniendo $0.94 \pm 0.02\ \mathrm{km\,s^{-1}}$ para $\ell 10$ y $0.95 \pm 0.02\ \mathrm{km\,s^{-1}}$ para $v10$. Asimismo, se calcula el área cubierta por la zona magnética considerando un límite inferior de 15 G. Calculando el radio equivalente de estas estructuras, obtenemos $0.61 \pm 0.04\ \mathrm{km\,s^{-1}}$ para $\ell 10$ y $0.68 \pm 0.03\ \mathrm{km\,s^{-1}}$ para $v10$. Estos ajustes se exponen en la Figura 5.4.

### C.5.2.2 Emergencias de campo magnético asociadas a los gránulos

Las emergencia asociada al evento $\ell 10$ sucede en un gránulo de $3\farcs3$ de diámetro. Se observa cómo las emergencias cubren las zonas por donde el gránulo se fragmentará. Instantes después, se observa el centro de fragmentación con una velocidad hacia abajo de $0.5\ \mathrm{km\,s^{-1}}$. El área cubierta va de 18% a 32% de la proporción de la superficie del gránulo. Cuando la emergencia de flujo se va hacia la zona intergranular, se observa un incremento de flujo desde el umbral de 15 G hasta el de 45 G, con valores máximos de 90 G. Este proceso se puede apreciar en la Figura 5.5.

La emergencia $v10$ sucede de un modo similar, con un gránulo de tamaño inicial de $2''$. El área cubierta va de 15% a 42% en proporción a la superficie del gránulo. La particularidad de este caso es que tiene campo magnético transversal, que nos permite encontrar un bucle magnético, encontrando primero los dos pies y posteriormente la zona horizontal más alta. Una secuencia temporal explicativa se

muestra en la Figura 5.6.

### C.5.2.3 Mapas de flujo de las estructuras

Se ha utilizado Seguimiento de Correlación Local en todos los mapas de las magnitudes físicas relevantes de estas estructuras, tales como el continuo, el campo magnético longitudinal, transversal y la velocidad para crear los mapas de flujo, además de sus divergencias. Los valores medios de los campos de velocidades horizontales de estas magnitudes son, para $\ell 10$ 0.63, 0.49 y 0.54 $\mathrm{km\,s^{-1}}$. En el caso de $v10$, son 0.60, 0.47, 0.44 y 0.48 $\mathrm{km\,s^{-1}}$. Estas velocidades son más bajas que las propias de expansión porque dependen del promediado temporal y el tamaño de la caja de correlación. Con respecto a las divergencias, al tener un centro muy definido, podemos calcular el máximo de la divergencia, que en el caso $\ell 10$ es x=6.″56±0.″30, y=9.″84±0.″11, y en el $v10$ está centrado en x=3.″72 ± 0.″15, y=4.″63 ± 0.″28. Nótese que el error es bastante bajo, dando una posición bastante exacta del centro del gránulo explosivo. Estos centros se observan claramente en las Figuras 5.7, 5.8, 5.9 y 5.10.

### C.5.2.4 Simulaciones

Para esta Sección se ha utilizado una simulación creada por Cheung et al. (2008) consistente en colocar un tubo magnético en la parte de abajo de una caja computacional que se expande, asciende y se vuelve turbulento. La caja computacional presenta los siguientes parámetros: dimensiones horizontales de 24 Mm × 18 Mm y altura de caja de 5.76 Mm, con un flujo magnético total en el tubo de $10^{20}$ Mx. El píxel en esta simulación cubre 25 km × 25 km o equivalentemente, 0.″034 píxel$^{-1}$. Las imágenes de continuo y el magnetograma longitudinal obtenidas en la simulación se degradan con una ventana de 0.″17, equivalente a 3 píxeles de IMaX. Posteriormente se opera con Correlación Local para obtener mapas de flujo, obteniendo también las divergencias. Estos mapas revelan diversos centros de emergencias positivas coincidentes en el continuo. También se observa una red de zonas intermesogranulares en el mapa de divergencias del continuo, que aparece en azul en la Figura 5.13. A continuación, se toma una concentración magnética en la simulación y se calcula su velocidad de expansión, que es 1.2 $\mathrm{km\,s^{-1}}$.

## C.5.3 Conclusiones

El origen de estas estructuras magnéticas es incierto, pero por comparación con una simulación, la idea de un tubo magnético que emerge de modo turbulento está de acuerdo con los datos. También a través de estas simulaciones se observa

un comportamiento común, como es la emergencia de una zona unipolar que, al fragmentarse, se vuelve multipolar. La emergencia en $v10$ parece un gránulo explosivo recurrente o activo. Por primera vez se ha informado del hallazgo del bucles magnéticos en gránulos explosivos.

### C.5.4 Mapas de flujo sobre todo el campo

El elemento de red que aparece cerca de $v10$ nos sirve para alinear cinco series. Esta estructura es muy característica por ser unipolar negativa, y estar rodeada de pequeñas concentraciones positivas. Se estudia por Correlación Local estas cinco series y se observa un patrón de gránulos explosivos en las cercanías del mencionado elemento. Se detecta otra pequeña emergencia de flujo en la última serie.

Asimismo, también se define una magnitud llamada 'magnetograma de cancelación' para estudiar cualitativamente las diferentes polaridades de las estructuras. Estos 'magnetogramas' no señalan cancelación magnética como tal, pero sí líneas neutras, los lugares donde los píxeles cambian de polaridad magnética. Combinando los mapas de flujo de velocidades con estos 'magnetogramas de cancelación', se observa que las áreas de máximo cambio en polaridad se encuentran atravesadas perpendicularmente por el flujo de velocidades, indicando que, probablemente, las concentraciones positivas han sido arrastradas hasta coincidir con la negativa.

## C.6 Conclusiones finales

En este trabajo hemos estudiado la dinámica de los pequeños elementos magnéticos en diferentes contextos. En el primer Capítulo se encuentran temas variados, tales como la estructura solar, y elementos de formación de imagen. Para la estimación del campo magnético se han usado diferentes métodos, tales como inversiones, aproximación de campo débil y método de centro de gravedad con los parámetros de Stokes $I$ y $V$. Cuando la aplicación directa de estos métodos no ha sido posible (por no disponer de los parámetros de Stokes de los que se obtuvieron los magnetogramas), se han llevado a cabo calibraciones con la ecuación del magnetógrafo.

Una parte importante de la Tesis llevada a cabo durante el periodo predoctoral ha sido el de la reducción de datos de IMaX, desde las imágenes obtenidas por el globo, pasando por todos los procesos pertinentes de calibración. Estos datos están disponibles para la comunidad de física solar para su uso científico.

La segunda parte de esta Tesis está centrada en la detección de vórtices, que son flujos de plasma que desciende por las paredes del gránulo hasta las zonas intergranulares y comienza a rotar, por el momento angular, generando un efecto de torbellino en un sumidero. Estos fenómenos, a veces un poco difíciles de cuantificar,

se intentan encontrar a través de diferentes métodos que dan un resultado común. Estas técnicas están basadas en Seguimiento Local de Correlación, que encuentra elementos para trazar a través de una ventana de correlación. Otras magnitudes se estiman a través de este modo, obteniendo las velocidades horizontales y calculando la divergencia y la vorticidad. A veces, estos elementos, al ser mucho más pequeños que la ventana de correlación, no se pueden encontrar. Entonces, el cálculo de centroides magnéticos ayuda a la tarea.

Se ha dedicado un capítulo a analizar los efectos de los diferentes parámetros del Seguimiento de Correlación Local, tales como la ventana espacial y el promediado temporal.

El estudio de elementos magnéticos incluye el análisis de grandes emergencias de campo magnético débil sobre gránulos explosivos de gran tamaño (escala mesogranular). Estos campos magnéticos habían sido detectados antes, pero en un tamaño más moderado. También se encontraron pequeños bucles magnéticos en el campo estudiado.

Los principales hallazgos de este trabajo se pueden resumir en:

- Las concentraciones magnéticas han sido analizadas en un estudio multiespectral, que con un análisis de seguimiento de estructuras, nos ayudó a encontrar un flujo vortical con los elementos girando alrededor de un centro que corresponde al centro del sumidero. Un cálculo de centroides magnéticos ha ayudado a ver estos elementos girar.

Las propiedades de los flujos horizontales tales como la divergencia y la vorticidad han sido estudiadas en detalle, concluyendo que:

- Los patrones de divergencia y vorticidad no varían en intervalos de promediado de 5 a 20 minutos.

- Una tendencia de la vorticidad ligeramente positiva (en los histogramas y su sesgo) y el conteo del sentido de rotación de los vórtices, nos permite concluir que el campo estudiado estaba en el hemisferio norte solar (las coordenadas de apuntado eran desconocidas hasta ahora), que muestra una preferencia en los vórtices con sentido antihorario. Rubio F. y equipo SUNRISE, (comunicación privada) han estimado el apuntado de los datos de IMaX a partir del día 10 de Junio de 2009 y deberían ser corregidos un factor (-70.″9, 69.″3). Por tanto, el apuntado real debería ser (-70.″1, 69.″3), lo que implica el hemisferio norte solar.

- Se ha desarrollado una descomposición de la divergencia y la vorticidad, que son las componentes de cizalla de la vorticidad, y de confluencia en la divergencia. Cuando se muestran los diagramas de estas magnitudes, se observan patrones que marcan el centro del posible vórtice. Además, los patrones de estas dos magnitudes son similares a las de los azimutes de las velocidades horizontales.

• Se han estudiado dos grandes gránulos explosivos donde emerge campo magnético que cubre porciones significantes de los mismos, y se expanden hasta las zonas intergranulares, donde el campo se intensifica. También se detectan bucles magnéticos en la superficie estudiada. Se han detectado más eventos como éstos en otras series, donde los gránulos se convierten en gránulos activos y generando flujos explosivos alrededor de un elemento de red.

### C.6.1 Trabajo futuro

Gracias al análisis multiespectral llevado a cabo en esta Tesis, los métodos pueden ser aplicados a otros casos observacionales. El logro de combinar las técnicas mencionadas nos permite usarlo en multitud de estudios, como por ejemplo, el trenzado magnético en estructuras vorticales, o vórtices que se encuentren en capas superiores a la fotosfera. Además una continuación en el estudio de la divergencia y la vorticidad puede dar lugar a un método automatizado de búsqueda de vórtices, además de una mejor comprensión de las magnitudes utilizadas.

Y sin olvidar las misiones futuras, el segundo vuelo de SUNRISE, programado para 2013, y el proyecto de una misión fundamental como es Solar Orbiter (lanzamiento alrededor de 2017), complementará nuestro conocimiento sobre estas estructuras elusivas. Esta misión es la más cercana al Sol nunca enviada antes.

# Bibliography

M. Aschwanden. *Physics of the Solar Corona. An Introduction with Problems and Solutions*. Praxis Publishing Ltd.-Springer, second edition, 2005. ISBN 3-540-30765-6.

R. Attie, D. E. Innes, and H. E. Potts. Evidence of photospheric vortex flows at supergranular junctions observed by FG/SOT (Hinode). *A&A*, 493:L13–L16, January 2009.

H. W. Babcock and H. D. Babcock. Mapping the Magnetic Fields of the Sun. *PASP*, 64:282–+, December 1952.

L. Balmaceda, S. Vargas Domínguez, J. Palacios, I. Cabello, and V. Domingo. Evidence of small-scale magnetic concentrations dragged by vortex motion of solar photospheric plasma. *A&A*, 513:L6+, April 2010.

L. A. Balmaceda. *Solar variability and solar irradiance reconstructions on time scales of decades to centuries*. Copernicus GmbH, Germany, first edition, 2007. ISBN 978-3-936586-68-8.

L. A. Balmaceda, J. Palacios, I. Cabello, and V. Domingo. Observations of Magnetic Elements in the Quiet Sun Internetwork. In B. Lites, M. Cheung, T. Magara, J. Mariska, & K. Reeves, editor, *Astronomical Society of the Pacific Conference Series*, volume 415 of *Astronomical Society of the Pacific Conference Series*, pages 156–+, December 2009.

P. Barthol, A. Gandorfer, S. K. Solanki, M. Schüssler, B. Chares, W. Curdt, W. Deutsch, A. Feller, D. Germerott, B. Grauf, K. Heerlein, J. Hirzberger, M. Kolleck, R. Meller, R. Müller, T. L. Riethmüller, G. Tomasch, M. Knölker, B. W. Lites, G. Card, D. Elmore, J. Fox, A. Lecinski, P. Nelson, R. Summers,

A. Watt, V. Martínez Pillet, J. A. Bonet, W. Schmidt, T. Berkefeld, A. M. Title, V. Domingo, J. L. Gasent Blesa, J. C. del Toro Iniesta, A. López Jiménez, A. Álvarez-Herrero, L. Sabau-Graziati, C. Widani, P. Haberler, K. Härtel, D. Kampf, T. Levin, I. Pérez Grande, A. Sanz-Andrés, and E. Schmidt. The Sunrise Mission. *SolPhys*, 268:1–34, January 2011.

C. Beck, L. R. Bellot Rubio, R. Schlichenmaier, and P. Sütterlin. Magnetic properties of G-band bright points in a sunspot moat. *A&A*, 472:607–622, September 2007.

N. Bello González, L. Yelles Chaouche, O. Okunev, and F. Kneer. Dynamics of small-scale magnetic fields on the Sun: observations and numerical simulations. *A&A*, 494:1091–1106, February 2009.

L. R. Bellot Rubio, I. Rodríguez Hidalgo, M. Collados, E. Khomenko, and B. Ruiz Cobo. Observation of Convective Collapse and Upward-moving Shocks in the Quiet Sun. *ApJ*, 560:1010–1019, October 2001.

T. E. Berger and A. M. Title. On the Relation of G-Band Bright Points to the Photospheric Magnetic Field. *ApJ*, 553:449–469, May 2001.

T. E. Berger, C. J. Schrijver, R. A. Shine, T. D. Tarbell, A. M. Title, and G. Scharmer. New Observations of Subarcsecond Photospheric Bright Points. *ApJ*, 454:531–+, November 1995.

T. E. Berger, M. G. Loefdahl, R. S. Shine, and A. M. Title. Measurements of Solar Magnetic Element Motion from High-Resolution Filtergrams. *ApJ*, 495:973–+, March 1998.

T. E. Berger, L. H. M. Rouppe van der Voort, M. G. Löfdahl, M. Carlsson, A. Fossum, V. H. Hansteen, E. Marthinussen, A. Title, and G. Scharmer. Solar magnetic elements at 0.1 arcsec resolution. General appearance and magnetic structure. *A&A*, 428:613–628, December 2004.

T. Berkefeld, W. Schmidt, D. Soltau, A. Bell, H. P. Doerr, B. Feger, R. Friedlein, K. Gerber, F. Heidecke, T. Kentischer, O. v. D. Lühe, M. Sigwarth, E. Wälde, P. Barthol, W. Deutsch, A. Gandorfer, D. Germerott, B. Grauf, R. Meller, A. Álvarez-Herrero, M. Knölker, V. Martínez Pillet, S. K. Solanki, and A. M. Title. The Wave-Front Correction System for the Sunrise Balloon-Borne Solar Observatory. *SolPhys*, 268:103–123, January 2011.

P. N. Bernasconi, D. M. Rust, H. A. Eaton, and G. A. Murphy. Balloon-borne telescope for high-resolution solar imaging and polarimetry. In R. K. Melugin & H.-P. Röser, editor, *Society of Photo-Optical Instrumentation Engineers (SPIE) Conference Series*, volume 4014 of *Society of Photo-Optical Instrumentation Engineers (SPIE) Conference Series*, pages 214–225, June 2000.

J. Blanco Rodríguez. *Magnetic Activity at The Poles of The Sun*. Copernicus GmbH, Germany, first edition, 2008. ISBN 978-3-936586-80-0.

J. A. Bonet, I. Márquez, R. Muller, M. Sobotka, and A. Tritschler. Phase diversity restoration of sunspot images. I. Relations between penumbral and photospheric features. *A&A*, 423:737–744, August 2004.

J. A. Bonet, I. Márquez, R. Muller, M. Sobotka, and T. Roudier. Phase diversity restoration of sunspot images. II. Dynamics around a decaying sunspot. *A&A*, 430:1089–1097, February 2005.

J. A. Bonet, I. Márquez, J. Sánchez Almeida, I. Cabello, and V. Domingo. Convectively Driven Vortex Flows in the Sun. *ApJL*, 687:L131–L134, November 2008.

J. A. Bonet, I. Márquez, J. Sánchez Almeida, J. Palacios, V. Martínez Pillet, S. K. Solanki, J. C. del Toro Iniesta, V. Domingo, T. Berkefeld, W. Schmidt, A. Gandorfer, P. Barthol, and M. Knölker. SUNRISE/IMaX Observations of Convectively Driven Vortex Flows in the Sun. *ApJL*, 723:L139–L143, November 2010.

J. M. Borrero, V. Martínez-Pillet, R. Schlichenmaier, S. K. Solanki, J. A. Bonet, J. C. del Toro Iniesta, W. Schmidt, P. Barthol, A. Gandorfer, V. Domingo, and M. Knölker. Supersonic Magnetic Upflows in Granular Cells Observed with SUNRISE/IMAX. *ApJL*, 723:L144–L148, November 2010.

B. Bovelet and E. Wiehr. The quiet Sun's magnetic flux estimated from Ca II H bright inter-granular G-band structures. *A&A*, 488:1101–1107, September 2008.

P. N. Brandt, G. B. Scharmer, S. Ferguson, R. A. Shine, and T. D. Tarbell. Vortex flow in the solar photosphere. *Nature*, 335:238–240, September 1988.

J. W. Brault and H. Neckel. Announcement Spectral Atlas of Solar Absolute Disk-Averaged and Disk-Center Intensity from 3290 TO 12510Å (Brault and Neckel, 1987) now Available from Hamburg Observatory Anonymous FTP Site. *SolPhys*, 184:421–421, February 1999.

J. W. Brault and O. R. White. The Analysis and Restoration of Astronomical Data via the Fast Fourier Transform. *A&A*, 13:169–+, July 1971.

M. Buente, O. Steiner, and V. J. Pizzo. On the interchange instability of solar magnetic flux tubes. I - The influence of magnetic tension and internal gas pressure. *A&A*, 268:299–308, February 1993.

I. Cabello and V. Domingo. Solar Photospheric Magnetic Elements Dimension and Radiance. In *SOHO-17. 10 Years of SOHO and Beyond*, volume 617 of *ESA Special Publication*, July 2006.

J. Casanovas. Early Observations of Sunspots: Scheiner and Galileo. In B. Schmieder, J. C. del Toro Iniesta, & M. Vazquez, editor, *1st Advances in Solar Physics Euroconference. Advances in Physics of Sunspots*, volume 118 of *Astronomical Society of the Pacific Conference Series*, pages 3–+, 1997.

F. Cattaneo, D. Lenz, and N. Weiss. On the Origin of the Solar Mesogranulation. *ApJL*, 563:L91–L94, December 2001.

R. Centeno, H. Socas-Navarro, B. Lites, M. Kubo, Z. Frank, R. Shine, T. Tarbell, A. Title, K. Ichimoto, S. Tsuneta, Y. Katsukawa, Y. Suematsu, T. Shimizu, and S. Nagata. Emergence of Small-Scale Magnetic Loops in the Quiet-Sun Internetwork. *ApJL*, 666:L137–L140, September 2007.

M. Centrone and I. Ermolli. The center to limb variation of photospheric facular contrast. *Memorie della Societa Astronomica Italiana*, 74:671–+, 2003.

J. Chae, Y.-J. Moon, Y.-D. Park, K. Ichimoto, T. Sakurai, Y. Suematsu, S. Tsuneta, Y. Katsukawa, T. Shimizu, R. A. Shine, T. D. Tarbell, A. M. Title, B. Lites, M. Kubo, S. Nagata, and T. Yokoyama. Initial Results on Line-of-Sight Field Calibrations of SP/NFI Data Taken by SOT/Hinode. *PASJ*, 59:619–+, November 2007.

M. C. M. Cheung, M. Schüssler, T. D. Tarbell, and A. M. Title. Solar Surface Emerging Flux Regions: A Comparative Study of Radiative MHD Modeling and Hinode SOT Observations. *ApJ*, 687:1373–1387, November 2008.

S. Danilovic, M. Schüssler, and S. K. Solanki. Magnetic field intensification: comparison of 3D MHD simulations with Hinode/SP results. *A&A*, 509:A76+, January 2010.

C. R. de Boer, G. Stellmacher, and E. Wiehr. Three colour photometry of solar limb faculae. *A&A*, 324:1179–1182, August 1997.

B. De Pontieu. High-Resolution Observations of Small-Scale Emerging Flux in the Photosphere. *ApJ*, 569:474–486, April 2002.

B. de Pontieu, S. McIntosh, V. H. Hansteen, M. Carlsson, C. J. Schrijver, T. D. Tarbell, A. M. Title, R. A. Shine, Y. Suematsu, S. Tsuneta, Y. Katsukawa, K. Ichimoto, T. Shimizu, and S. Nagata. A Tale of Two Spicules: The Impact of Spicules on the Magnetic Chromosphere. *PASJ*, 59:655, November 2007.

A. G. de Wijn and D. Müller. On the Relationship Between Magnetic Field and Mesogranulation. In B. Lites, M. Cheung, T. Magara, J. Mariska, & K. Reeves, editor, *The Second Hinode Science Meeting: Beyond Discovery-Toward Understanding*, volume 415 of *Astronomical Society of the Pacific Conference Series*, pages 211–+, December 2009.

A. G. de Wijn, R. J. Rutten, E. M. W. P. Haverkamp, and P. Sütterlin. DOT tomography of the solar atmosphere. IV. Magnetic patches in internetwork areas. *A&A*, 441:1183–1190, October 2005.

A. G. de Wijn, B. W. Lites, T. E. Berger, Z. A. Frank, T. D. Tarbell, and R. Ishikawa. Hinode Observations of Magnetic Elements in Internetwork Areas. *ApJ*, 684: 1469–1476, September 2008.

C. E. DeForest, H. J. Hagenaar, D. A. Lamb, C. E. Parnell, and B. T. Welsch. Solar Magnetic Tracking. I. Software Comparison and Recommended Practices. *ApJ*, 666:576–587, September 2007.

W. Deinzer, G. Hensler, M. Schussler, and E. Weisshaar. Model Calculations of Magnetic Flux Tubes - Part Two - Stationary Results for Solar Magnetic Elements. *A&A*, 139:435–+, October 1984.

J. C. del Toro Iniesta. *Introduction to Spectropolarimetry*. Cambridge University Press, United Kingdom, first edition, 2003. ISBN 0-521-81827-3.

J. C. del Toro Iniesta and M. Collados. Optimum Modulation and Demodulation Matrices for Solar Polarimetry. *AO*, 39:1637–1642, April 2000.

V. Domingo, B. Fleck, and A. I. Poland. SOHO: The Solar and Heliospheric Observatory. *Space Science Reviews*, 72:81–84, April 1995.

I. Domínguez Cerdeña. Evidence of mesogranulation from magnetograms of the Sun. *A&A*, 412:L65–L68, December 2003.

I. Domínguez Cerdeña, F. Kneer, and J. Sánchez Almeida. Quiet-Sun Magnetic Fields at High Spatial Resolution. *ApJL*, 582:L55–L58, January 2003.

R. B. Dunn and J. B. Zirker. The Solar Filigree. *SolPhys*, 33:281–304, December 1973.

C. E. Fischer, A. G. de Wijn, R. Centeno, B. W. Lites, and C. U. Keller. Statistics of convective collapse events in the photosphere and chromosphere observed with the Hinode SOT. *A&A*, 504:583–588, September 2009.

C. Foullon, E. Verwichte, V. M. Nakariakov, K. Nykyri, and C. J. Farrugia. Magnetic Kelvin-Helmholtz Instability at the Sun. *ApJL*, 729:L8+, March 2011.

C. Fröhlich. Total solar irradiance variations since 1978. *Advances in Space Research*, 29:1409–1416, 2002.

A. Gandorfer, B. Grauf, P. Barthol, T. L. Riethmüller, S. K. Solanki, B. Chares, W. Deutsch, S. Ebert, A. Feller, D. Germerott, K. Heerlein, J. Heinrichs, D. Hirche, J. Hirzberger, M. Kolleck, R. Meller, R. Müller, R. Schäfer, G. Tomasch, M. Knölker, V. Martínez Pillet, J. A. Bonet, W. Schmidt, T. Berkefeld, B. Feger, F. Heidecke, D. Soltau, A. Tischenberg, A. Fischer, A. Title, H. Anwand, and E. Schmidt. The Filter Imager SuFI and the Image Stabilization and Light Distribution System ISLiD of the Sunrise Balloon-Borne Observatory: Instrument Description. *SolPhys*, 268:35–55, January 2011.

M. K. Georgoulis. A New Technique for a Routine Azimuth Disambiguation of Solar Vector Magnetograms. *ApJL*, 629:L69–L72, August 2005.

O. Gingerich, R. W. Noyes, W. Kalkofen, and Y. Cuny. The Harvard-Smithsonian reference atmosphere. *SolPhys*, 18:347–365, July 1971.

P. Gömöry, C. Beck, H. Balthasar, J. Rybák, A. Kučera, J. Koza, and H. Wöhl. Magnetic loop emergence within a granule. *A&A*, 511:A14, February 2010.

R. A. Gonsalves. Phase retrieval and diversity in adaptive optics. *Optical Engineering*, 21:829–832, October 1982.

R. A. Gonsalves and R. Chidlaw. Wavefront sensing by phase retrieval. In A. G. Tescher, editor, *Society of Photo-Optical Instrumentation Engineers (SPIE)*

*Conference Series*, volume 207 of *Presented at the Society of Photo-Optical Instrumentation Engineers (SPIE) Conference*, pages 32–39, 1979.

P. R. Goode, V. Yurchyshyn, W. Cao, V. Abramenko, A. Andic, K. Ahn, and J. Chae. Highest Resolution Observations of the Quietest Sun. *ApJL*, 714: L31–L35, May 2010.

U. Grossmann-Doerth, M. Schuessler, and O. Steiner. Convective intensification of solar surface magnetic fields: results of numerical experiments. *A&A*, 337: 928–939, September 1998.

G. E. Hale. Nature of the Hydrogen Vortices Surrounding Sun-spots. *PASP*, 37: 268–+, October 1925.

R. L. Heredero, N. Uribe-Patarroyo, T. Belenguer, G. Ramos, A. Sánchez, M. Reina, V. Martínez Pillet, and A. Álvarez-Herrero. Liquid-crystal variable retarders for aerospace polarimetry applications. *AO*, 46:689–698, February 2007.

J. R. Holton. *An Introduction to Dynamic Meteorology*. Elsevier, fourth edition, 2004. ISBN 0-12-354015-1.

Douglas V. Hoyt and Kenneth H. Schatten. Overlooked sunspot observations by hevelius in the early maunder minimum, 1653-1684. *Solar Physics*, 160:371–378, 1995. ISSN 0038-0938. 10.1007/BF00732815.

K. Ichimoto, B. Lites, D. Elmore, Y. Suematsu, S. Tsuneta, Y. Katsukawa, T. Shimizu, R. Shine, T. Tarbell, A. Title, J. Kiyohara, K. Shinoda, G. Card, A. Lecinski, K. Streander, M. Nakagiri, M. Miyashita, M. Noguchi, C. Hoffmann, and T. Cruz. Polarization Calibration of the Solar Optical Telescope onboard Hinode. *SolPhys*, 249:233–261, June 2008.

R. Ishikawa, S. Tsuneta, Y. Kitakoshi, Y. Katsukawa, J. A. Bonet, S. Vargas Domínguez, L. H. M. Rouppe van der Voort, Y. Sakamoto, and T. Ebisuzaki. Relationships between magnetic foot points and G-band bright structures. *A&A*, 472:911–918, September 2007.

S. Jafarzadeh, J. Hirzberger, A. Feller, A. Lagg, S. K. Solanki, A. Pietarila, S. Danilovic, T. Riethmueller, P. Barthol, T. Berkefeld, A. Gandorfer, M. Knülker, V. Martínez Pillet, W. Schmidt, M. Schüssler, and A. Title. Relation between the Sunrise photospheric magnetic field and the Ca II H bright features. In *38th COSPAR Scientific Assembly*, volume 38, pages 2856–+, 2010.

D. B. Jess, M. Mathioudakis, R. Erdélyi, P. J. Crockett, F. P. Keenan, and D. J. Christian. Alfvén Waves in the Lower Solar Atmosphere. *Science*, 323:1582–, March 2009.

C. U. Keller, M. Schüssler, A. Vögler, and V. Zakharov. On the Origin of Solar Faculae. *ApJL*, 607:L59–L62, May 2004.

T. J. Kentischer, W. Schmidt, M. Sigwarth, and M. V. Uexkuell. TESOS, a double Fabry-Perot instrument for solar spectroscopy. *A&A*, 340:569–578, December 1998.

D. Kiselman, R. J. Rutten, and B. Plez. The formation of G-band bright points I: Standard LTE modelling. In P. Brekke, B. Fleck, and J. B. Gurman, editors, *IAU Symposium*, pages 287–+, 2001.

I. N. Kitiashvili, A. G. Kosovichev, A. A. Wray, and N. N. Mansour. Mechanism of Spontaneous Formation of Stable Magnetic Structures on the Sun. *ApJ*, 719: 307–312, August 2010.

I. N. Kitiashvili, A. G. Kosovichev, N. N. Mansour, and A. A. Wray. Excitation of Acoustic Waves by Vortices in the Quiet Sun. *ApJL*, 727:L50+, February 2011.

F. Kneer and H. Hirzberger. A Fabry-Perot spectrometer for high-resolution observation of the Sun. *Astronomische Nachrichten*, 322:375–378, December 2001.

P. Kobel, J. Hirzberger, A. Gandorfer, S. K. Solanki, and V. Zakharov. Discriminant Analysis of Bright Points and Faculae: Center-to-Limb Distribution, Contrast and Morphology. *12th European Solar Physics Meeting, Freiburg, Germany, held September, 8-12, 2008. Online at http://espm.kis.uni-freiburg.de/, p.2.60*, 12: 2–+, September 2008.

T. Kosugi, K. Matsuzaki, T. Sakao, T. Shimizu, Y. Sone, S. Tachikawa, T. Hashimoto, K. Minesugi, A. Ohnishi, T. Yamada, S. Tsuneta, H. Hara, K. Ichimoto, Y. Suematsu, M. Shimojo, T. Watanabe, S. Shimada, J. M. Davis, L. D. Hill, J. K. Owens, A. M. Title, J. L. Culhane, L. K. Harra, G. A. Doschek, and L. Golub. The Hinode (Solar-B) Mission: An Overview. *SolPhys*, 243:3–17, June 2007.

V. A. Krat, V. N. Karpinsky, and L. M. Pravdjuk. On the Sunspot Structure. *SolPhys*, 26:305–317, October 1972.

N. A. Krivova and S. K. Solanki. Effect of spatial resolution on estimating the Sun's magnetic flux. *A&A*, 417:1125–1132, April 2004.

M. Kubo, T. Yokoyama, Y. Katsukawa, B. Lites, S. Tsuneta, Y. Suematsu, K. Ichimoto, T. Shimizu, S. Nagata, T. D. Tarbell, R. A. Shine, A. M. Title, and Elmore David. Hinode Observations of a Vector Magnetic Field Change Associated with a Flare on 2006 December 13. *PASJ*, 59:779–+, November 2007.

P. K. Kundu. *Fluid Mechanics*. Academic Press, Harcourt Place, London, second edition, 1990. ISBN 0-12-428770-0.

E. Landi Degl'Innocenti. *Magnetic field measurements*, pages 71–+. Sanchez, F., Collados, M., & Vazquez, M., 1992.

E. Landi Degl'Inoccenti and M. Landolfi. *Polarization in Spectral Lines*. Kluwer Academic Publishers. Springer, Dordrecht, first edition, 2005. ISBN 1-4020-2414-2.

J. Leenaarts, R. J. Rutten, M. Carlsson, and H. Uitenbroek. A comparison of solar proxy-magnetometry diagnostics. *A&A*, 452:L15–L18, June 2006.

R. B. Leighton. Observations of Solar Magnetic Fields in Plage Regions. *ApJ*, 130: 366–1085, April 1969.

M. G. Löfdahl. Multi-frame blind deconvolution with linear equality constraints. In P. J. Bones, M. A. Fiddy, & R. P. Millane, editor, *Society of Photo-Optical Instrumentation Engineers (SPIE) Conference Series*, volume 4792 of *Society of Photo-Optical Instrumentation Engineers (SPIE) Conference Series*, pages 146–155, December 2002.

M. G. Löfdahl and G. B. Scharmer. Wavefront sensing and image restoration from focused and defocused solar images. *A&AS*, 107:243–264, October 1994.

H. A. Lorentz. On the theory of the Zeeman effect in a direction inclined to the lines of force. *KNAW Proceedings*, 12:321–340, January 1910.

R. Manso Sainz, M. J. Martínez González, and A. Asensio Ramos. Advection and dispersal of small magnetic elements in the very quiet Sun. *A&A*, 531:L9+, July 2011.

I. Márquez, J. Sánchez Almeida, and J. A. Bonet. High-Resolution Proper Motions in a Sunspot Penumbra. *ApJ*, 638:553–563, February 2006.

M. J. Martínez González and L. R. Bellot Rubio. Emergence of Small-scale Magnetic Loops Through the Quiet Solar Atmosphere. *ApJ*, 700:1391–1403, August 2009.

M. J. Martínez González, M. Collados, and B. Ruiz Cobo. On the validity of the 630 nm Fe I lines for magnetometry of the internetwork quiet Sun. *A&A*, 456: 1159–1164, September 2006.

V. Martínez Pillet, J. A. Bonet, M. V. Collados, L. Jochum, S. Mathew, J. L. Medina Trujillo, B. Ruiz Cobo, J. C. del Toro Iniesta, A. C. López Jiménez, J. Castillo Lorenzo, M. Herranz, J. M. Jerónimo, P. Mellado, R. Morales, J. Rodriguez, A. Alvarez-Herrero, T. Belenguer, R. L. Heredero, M. Menéndez, G. Ramos, M. Reina, C. Pastor, A. Sánchez, J. Villanueva, V. Domingo, J. L. Gasent, and P. Rodríguez. The imaging magnetograph eXperiment for the SUNRISE balloon Antarctica project. In J. C. Mather, editor, *Society of Photo-Optical Instrumentation Engineers (SPIE) Conference Series*, volume 5487 of *Society of Photo-Optical Instrumentation Engineers (SPIE) Conference Series*, pages 1152–1164, October 2004.

V. Martínez Pillet, J. C. Del Toro Iniesta, A. Álvarez-Herrero, V. Domingo, J. A. Bonet, L. González Fernández, A. López Jiménez, C. Pastor, J. L. Gasent Blesa, P. Mellado, J. Piqueras, B. Aparicio, M. Balaguer, E. Ballesteros, T. Belenguer, L. R. Bellot Rubio, T. Berkefeld, M. Collados, W. Deutsch, A. Feller, F. Girela, B. Grauf, R. L. Heredero, M. Herranz, J. M. Jerónimo, H. Laguna, R. Meller, M. Menéndez, R. Morales, D. Orozco Suárez, G. Ramos, M. Reina, J. L. Ramos, P. Rodríguez, A. Sánchez, N. Uribe-Patarroyo, P. Barthol, A. Gandorfer, M. Knoelker, W. Schmidt, S. K. Solanki, and S. Vargas Domínguez. The Imaging Magnetograph eXperiment (IMaX) for the Sunrise Balloon-Borne Solar Observatory. *SolPhys*, 268:57–102, January 2011.

J. Martínez-Sykora, V. Hansteen, and M. Carlsson. Twisted Flux Tube Emergence From the Convection Zone to the Corona. *ApJ*, 679:871–888, May 2008.

J. M. Massaguer and J.-P. Zahn. Cellular convection in a stratified atmosphere. *A&A*, 87:315–327, July 1980.

Ł. Matloch, R. Cameron, S. Shelyag, D. Schmitt, and M. Schüssler. Mesogranular structure in a hydrodynamical simulation. *A&A*, 519:A52+, September 2010.

J. P. Mehltretter. Observations of photospheric faculae at the center of the solar disk. *SolPhys*, 38:43–57, September 1974.

J. P. Mehltretter. The flight of Spektro-Stratoskop. *Sterne und Weltraum*, 15: 44–47, February 1976.

M. S. Miesch. Large-Scale Dynamics of the Convection Zone and Tachocline. *Living Reviews in Solar Physics*, 2:1, April 2005.

R. Moll, R. H. Cameron, and M. Schüssler. Vortices in simulations of solar surface convection. *A&A*, 533:A126, September 2011.

S. Nagata, S. Tsuneta, Y. Suematsu, K. Ichimoto, Y. Katsukawa, T. Shimizu, T. Yokoyama, T. D. Tarbell, B. W. Lites, R. A. Shine, T. E. Berger, A. M. Title, L. R. Bellot Rubio, and D. Orozco Suárez. Formation of Solar Magnetic Flux Tubes with Kilogauss Field Strength Induced by Convective Instability. *ApJL*, 677:L145–L147, April 2008.

G. Narayan. Transient downflows associated with the intensification of small-scale magnetic features and bright point formation. *A&A*, 529:A79, May 2011.

P. Nisenson, A. A. van Ballegooijen, A. G. de Wijn, and P. Sütterlin. Motions of Isolated G-Band Bright Points in the Solar Photosphere. *ApJ*, 587:458–463, April 2003.

R. J. Noll. Zernike polynomials and atmospheric turbulence. *Journal of the Optical Society of America (1917-1983)*, 66:207–211, March 1976.

A. Nordlund. Solar convection. *SolPhys*, 100:209–235, October 1985.

L. J. November. Measurement of geometric distortion in a turbulent atmosphere. *AO*, 25:392–397, February 1986.

L. J. November and G. W. Simon. Precise proper-motion measurement of solar granulation. *ApJ*, 333:427–442, October 1988.

L. J. November, J. Toomre, K. B. Gebbie, and G. W. Simon. The detection of mesogranulation on the sun. *ApJL*, 245:L123–L126, May 1981.

N. Oda. Morphological study of the solar granulation. III - The mesogranulation. *SolPhys*, 93:243–255, July 1984.

D. Orozco Suárez, L. R. Bellot Rubio, J. C. del Toro Iniesta, and S. Tsuneta. Magnetic field emergence in quiet Sun granules. *A&A*, 481:L33–L36, April 2008.

A. Ortiz, S. K. Solanki, V. Domingo, M. Fligge, and B. Sanahuja. On the intensity contrast of solar photospheric faculae and network elements. *A&A*, 388:1036–1047, June 2002.

A. Ortiz, V. Domingo, and B. Sanahuja. Contribution of the small photospheric magnetic elements to the long-term solar irradiance. In A. Wilson, editor, *Solar Variability as an Input to the Earth's Environment*, volume 535 of *ESA Special Publication*, pages 43–46, September 2003.

A. Ortiz, V. Domingo, and B. Sanahuja. The intensity contrast of solar photospheric faculae and network elements. II. Evolution over the rising phase of solar cycle 23. *A&A*, 452:311–319, June 2006.

E. N. Parker. Hydraulic concentration of magnetic fields in the solar photosphere. VI - Adiabatic cooling and concentration in downdrafts. *ApJ*, 221:368–377, April 1978.

R. G. Paxman, T. J. Schulz, and J. R. Fienup. Joint estimation of object and aberrations by using phase diversity. *Journal of the Optical Society of America A*, 9:1072–1085, July 1992.

R. G. Paxman, J. H. Seldin, M. G. Loefdahl, G. B. Scharmer, and C. U. Keller. Evaluation of Phase-Diversity Techniques for Solar-Image Restoration. *ApJ*, 466: 1087–+, August 1996.

V. Penza, B. Caccin, I. Ermolli, and M. Centrone. Comparison of model calculations and photometric observations of bright "magnetic" regions. *A&A*, 413:1115–1123, January 2004.

S. R. O. Ploner, S. K. Solanki, and A. S. Gadun. Is solar mesogranulation a surface phenomenon? *A&A*, 356:1050–1054, April 2000.

W. Pötzi and P. N. Brandt. Is Solar Plasma Sinking Down in Vortices. *Hvar Observatory Bulletin*, 29:61–70, 2005.

K. G. Puschmann and E. Wiehr. The flux-gap between bright and dark solar magnetic structures. *A&A*, 445:337–340, January 2006.

D. E. Rees and M. D. Semel. Line formation in an unresolved magnetic element - A test of the centre of gravity method. *A&A*, 74:1–5, April 1979.

T. Roudier and R. Muller. Relation between families of granules, mesogranules and photospheric network. *A&A*, 419:757–762, May 2004.

B. Ruiz Cobo and J. C. del Toro Iniesta. Inversion of Stokes profiles. *ApJ*, 398: 375–385, October 1992.

D. M. Rust, G. Murphy, K. Strohbehn, and C. U. Keller. Balloon-Borne Polarimetry. *SolPhys*, 164:403–415, March 1996.

A. Sainz Dalda and V. Martínez Pillet. Moving Magnetic Features as Prolongation of Penumbral Filaments. *ApJ*, 632:1176–1183, October 2005.

D. Samain and P. Lemaire. Solar High Resolution Balloon Spectra Obtained in the 190-300 nm Wavelength Band. In R. Muller, editor, *High Resolution in Solar Physics*, volume 233 of *Lecture Notes in Physics, Berlin Springer Verlag*, pages 123–+, 1985.

J. Sánchez Almeida, I. Márquez, J. A. Bonet, I. Domínguez Cerdeña, and R. Muller. Bright Points in the Internetwork Quiet Sun. *ApJL*, 609:L91–L94, July 2004.

J. Sánchez Almeida, J. A. Bonet, B. Viticchié, and D. Del Moro. Magnetic Bright Points in the Quiet Sun. *ApJL*, 715:L26–L29, May 2010.

G. B. Scharmer, K. Bjelksjo, T. K. Korhonen, B. Lindberg, and B. Petterson. The 1-meter Swedish solar telescope. In S. L. Keil & S. V. Avakyan, editor, *Society of Photo-Optical Instrumentation Engineers (SPIE) Conference Series*, volume 4853 of *Society of Photo-Optical Instrumentation Engineers (SPIE) Conference Series*, pages 341–350, February 2003a.

G. B. Scharmer, P. M. Dettori, M. G. Lofdahl, and M. Shand. Adaptive optics system for the new Swedish solar telescope. In S. L. Keil & S. V. Avakyan, editor, *Society of Photo-Optical Instrumentation Engineers (SPIE) Conference Series*, volume 4853 of *Society of Photo-Optical Instrumentation Engineers (SPIE) Conference Series*, pages 370–380, February 2003b.

P. H. Scherrer, R. S. Bogart, R. I. Bush, J. T. Hoeksema, A. G. Kosovichev, J. Schou, W. Rosenberg, L. Springer, T. D. Tarbell, A. Title, C. J. Wolfson, I. Zayer, and MDI Engineering Team. The Solar Oscillations Investigation - Michelson Doppler Imager. *SolPhys*, 162:129–188, December 1995.

W. Schmidt, T. Berkefeld, R. Friedlein, F. Heidecke, T. Kentischer, O. F. von der Lühe, M. Sigwarth, D. Soltau, and E. Walde. High-precision wavefront sensor for

the SUNRISE Telescope. In J. M. Oschmann Jr., editor, *Society of Photo-Optical Instrumentation Engineers (SPIE) Conference Series*, volume 5489 of *Presented at the Society of Photo-Optical Instrumentation Engineers (SPIE) Conference*, pages 1164–1172, October 2004.

C. J. Schriver and G. L. Siscoe. *Heliophysics: Evolving Solar Activity and the Climates of Space and Earth*. Cambridge, first edition, 2010. ISBN 978-0-521-11294-9.

M. Schwarzschild. Photographs of the Solar Granulation Taken from the Stratosphere. *ApJ*, 130:345–+, September 1959.

M. Semel. Contribution à létude des champs magnétiques dans les régions actives solaires. *Annales d'Astrophysique*, 30:513–513, February 1967.

S. Shelyag, P. Keys, M. Mathioudakis, and F. P. Keenan. Vorticity in the solar photosphere. *A&A*, 526:A5+, February 2011.

H. Socas-Navarro. Stokes Inversion Techniques: Recent Achievements and Future Horizons. In M. Sigwarth, editor, *Advanced Solar Polarimetry – Theory, Observation, and Instrumentation*, volume 236 of *Astronomical Society of the Pacific Conference Series*, pages 487–+, January 2001.

S. K. Solanki, P. Barthol, S. Danilovic, A. Feller, A. Gandorfer, J. Hirzberger, T. L. Riethmüller, M. Schüssler, J. A. Bonet, V. Martínez Pillet, J. C. del Toro Iniesta, V. Domingo, J. Palacios, M. Knölker, N. Bello González, T. Berkefeld, M. Franz, W. Schmidt, and A. M. Title. SUNRISE: Instrument, Mission, Data, and First Results. *ApJL*, 723:L127–L133, November 2010.

H. C. Spruit. Pressure equilibrium and energy balance of small photospheric fluxtubes. *SolPhys*, 50:269–295, December 1976.

H. C. Spruit. Convective collapse of flux tubes. *SolPhys*, 61:363–378, March 1979.

H. C. Spruit, A. Nordlund, and A. M. Title. Solar convection. *ARAA*, 28:263–301, 1990.

R. F. Stein and A. Nordlund. Simulations of Solar Granulation. I. General Properties. *ApJ*, 499:914–+, May 1998.

O. Steiner. Radiative properties of magnetic elements. II. Center to limb variation of the appearance of photospheric faculae. *A&A*, 430:691–700, February 2005a.

O. Steiner. Recent Progresses in the Physics of Small-Scale Magnetic Fields. In *The Dynamic Sun: Challenges for Theory and Observations*, volume 600 of *ESA Special Publication*, December 2005b.

O. Steiner, M. Franz, N. Bello González, C. Nutto, R. Rezaei, V. Martínez Pillet, J. A. Bonet Navarro, J. C. del Toro Iniesta, V. Domingo, S. K. Solanki, M. Knölker, W. Schmidt, P. Barthol, and A. Gandorfer. Detection of Vortex Tubes in Solar Granulation from Observations with SUNRISE. *ApJL*, 723:L180–L184, November 2010.

M. Stix. *The Sun. An Introduction*. Springer Verlag, Berlin Heidelberg, second edition, 2002. ISBN 3-540-20741-4.

Y. Suematsu, K. Ichimoto, Y. Katsukawa, M. Otsubo, S. Tsuneta, M. Nakagiri, M. Noguchi, T. Tamura, Y. Kato, H. Hara, M. Miyashita, T. Shimizu, M. Kubo, and Y. Sakamoto. Optical Performance of the Solar Optical Telescope aboard HINODE. In *American Astronomical Society Meeting Abstracts #210*, volume 38 of *Bulletin of the American Astronomical Society*, pages 217–+, May 2007.

A. M. Title and T. E. Berger. Double-Gaussian Models of Bright Points or Why Bright Points Are Usually Dark. *ApJ*, 463:797–+, June 1996.

A. M. Title, T. D. Tarbell, L. Acton, D. Duncan, and G. W. Simon. White-light movies of the solar photosphere from the SOUP instrument on Spacelab. *Advances in Space Research*, 6:253–262, 1986.

A. M. Title, T. D. Tarbell, K. P. Topka, S. H. Ferguson, R. A. Shine, and SOUP Team. Statistical properties of solar granulation derived from the SOUP instrument on Spacelab 2. *ApJ*, 336:475–494, January 1989.

K. P. Topka, T. D. Tarbell, and A. M. Title. Properties of the Smallest Solar Magnetic Elements. II. Observations versus Hot Wall Models of Faculae. *ApJ*, 484:479–+, July 1997.

A. Tortosa-Andreu and F. Moreno-Insertis. Magnetic flux emergence into the solar photosphere and chromosphere. *A&A*, 507:949–967, November 2009.

S. Tsuneta, K. Ichimoto, Y. Katsukawa, S. Nagata, M. Otsubo, T. Shimizu, Y. Suematsu, M. Nakagiri, M. Noguchi, T. Tarbell, A. Title, R. Shine, W. Rosenberg, C. Hoffmann, B. Jurcevich, G. Kushner, M. Levay, B. Lites, D. Elmore, T. Matsushita, N. Kawaguchi, H. Saito, I. Mikami, L. D. Hill, and J. K. Owens. The

Solar Optical Telescope for the Hinode Mission: An Overview. *SolPhys*, 249: 167–196, June 2008.

H. Uitenbroek and A. Tritschler. The Contrast of Magnetic Elements in Synthetic CH- and CN-Band Images of Solar Magnetoconvection. *ApJ*, 639:525–533, March 2006.

H. Uitenbroek and A. Tritschler. Narrow-band imaging in the CN band at 388.33 nm. *A&A*, 462:1157–1163, February 2007.

D. Utz, A. Hanslmeier, C. Möstl, R. Muller, A. Veronig, and H. Muthsam. The size distribution of magnetic bright points derived from Hinode/SOT observations. *A&A*, 498:289–293, April 2009.

A. A. van Ballegooijen, P. Nisenson, R. W. Noyes, M. G. Löfdahl, R. F. Stein, Å. Nordlund, and V. Krishnakumar. Dynamics of Magnetic Flux Elements in the Solar Photosphere. *ApJ*, 509:435–447, December 1998.

M. van Noort, L. Rouppe van der Voort, and M. G. Löfdahl. Solar Image Restoration By Use Of Multi-frame Blind De-convolution With Multiple Objects And Phase Diversity. *SolPhys*, 228:191–215, May 2005.

S. Vargas Domínguez. Study of horizontal flows in solar active regions based on high-resolution image reconstruction techniques. *ArXiv e-prints*, June 2009.

S. Vargas Domínguez, J. Palacios, L. Balmaceda, I. Cabello, and V. Domingo. Spatial distribution and statistical properties of small-scale convective vortex-like motions in a quiet-Sun region. *MNRAS*, 416:148–154, September 2011.

B. Viticchié, D. DelMoro, F. Berrilli, L. Bellot Rubio, and A. Tritschler. Imaging Spectropolarimetry with IBIS: Evolution of Bright Points in the Quiet Sun. *ApJL*, 700:L145–L148, August 2009.

A. Vögler, S. Shelyag, M. Schüssler, F. Cattaneo, T. Emonet, and T. Linde. Simulations of magneto-convection in the solar photosphere. Equations, methods, and results of the MURaM code. *A&A*, 429:335–351, January 2005.

H. Wang, T. Spirock, P. R. Goode, C. Lee, H. Zirin, and W. Kosonocky. Contrast of Faculae at 1.6 Microns. *ApJ*, 495:957–+, March 1998.

Y. Wang, R. W. Noyes, T. D. Tarbell, and A. M. Title. Vorticity and Divergence in the Solar Photosphere. *ApJ*, 447:419–+, July 1995.

S. Wedemeyer-Böhm. Point spread functions for the Solar optical telescope onboard Hinode. *A&A*, 487:399–412, August 2008.

S. Wedemeyer-Böhm and L. Rouppe van der Voort. Small-scale swirl events in the quiet Sun chromosphere. *A&A*, 507:L9–L12, November 2009.

E. Wiehr and K. G. Puschmann. The Size of Small-Scale Solar Magnetic Regions. In D. E. Innes, A. Lagg, & S. A. Solanki, editor, *Chromospheric and Coronal Magnetic Fields*, volume 596 of *ESA Special Publication*, November 2005.

X. L. Yan, Z. Q. Qu, and C. L. Xu. A Statistical Study on Rotating Sunspots: Polarities, Rotation Directions, and Helicities. *ApJL*, 682:L65–L68, July 2008.

L. Yelles Chaouche, F. Moreno-Insertis, V. Martínez Pillet, T. Wiegelmann, J. A. Bonet, M. Knölker, L. R. Bellot Rubio, J. C. del Toro Iniesta, P. Barthol, A. Gandorfer, W. Schmidt, and S. K. Solanki. Mesogranulation and the Solar Surface Magnetic Field Distribution. *ApJL*, 727:L30+, February 2011.

Z. Yi and R. Molowny-Horas. Correlation tracking technique for measurement of transverse chromospheric motions. *A&A*, 295:199–205, March 1995.

V. Zakharov, A. Gandorfer, S. K. Solanki, and M. Löfdahl. A comparative study of the contrast of solar magnetic elements in CN and CH. *A&A*, 437:L43–L46, July 2005.

J. Zhang, J. Ma, and H. Wang. Comparison of Magnetic Flux Distribution between a Coronal Hole and a Quiet Region. *ApJ*, 649:464–469, September 2006.

## Websites

http://www.iac.es/proyecto/IMaX/
http://star.mpae.gwdg.de/Sunrise/
http://www.solarphysics.kva.se/
http://dubshen.astro.su.se/wiki/index.php/Main_Page
http://www.lmsal.com/solarsoft/
http://soi.standford.edu
http://www.astrosurf.com/rondi/obs/shg/magnetogram_anglais.htm#histoire
http://hinode.nao.ac.jp/index_e.shtml
http://hinode.nao.ac.jp/hsc_e/darts_e.shtml
http://adswww.harvard.edu/
http://arxiv.org/

Some movies and more electronic material can be found in:
ftp://helio.uv.es/pub/THESIS_Judith/.

## Articles in refereed publications

**I** L. Balmaceda, S. Vargas Domínguez, **J. Palacios**, I. Cabello,V. Domingo. *Evidence of small-scale magnetic concentrations dragged by vortex motion of solar photospheric plasma*, A&A, 513, L6 (2010). DOI: 10.1051/0004-6361/200913584.

**II** J. A. Bonet, I. Márquez, J. Sánchez Almeida, **J. Palacios**, V. Martínez Pillet, S. K. Solanki, J. C. del Toro Iniesta, V. Domingo, T. Berkefeld, W. Schmidt, A. Gandorfer, P. Barthol, and M. Knölker. SUNRISE/*IMaX observations of convectively driven vortex flows in the Sun*, (2010), ApJL, 723, L139. DOI: 10.1088/2041-8205/723/2/L139.

**III** S. K. Solanki, P. Barthol, S. Danilovic, A. Feller, A. Gandorfer, J. Hirzberger, T. L. Riethmüller, M. Schüssler, J. A. Bonet, V. Martínez Pillet, J. C. del Toro Iniesta, V. Domingo, **J. Palacios**, M. Knölker, N. Bello González, T. Berkefeld, M. Franz, W. Schmidt, and A. M. Title. SUNRISE*: instrument, mission, data and first results*, (2010), ApJL, 723, L127. DOI: 10.1088/2041-8205/723/2/L127.

**IV** S. Vargas Domínguez, **J. Palacios**, L. Balmaceda, I. Cabello and V. Domingo. *Spatial distribution and statistical properties of small-scale convective vortex-like motion in a quiet Sun region*, (2011), MNRAS, 416, 148-154. DOI: 10.1111/j.1365-2966.2011.19048.x .

**V** Y. Cerrato, E. Saiz, C. Cid, W. D. Gonzalez and **J. Palacios**. *Solar and interplanetary triggers of the largest $Dst$ variations of solar cycle 23*, JASTP, accepted, (2011). DOI: 10.1016/j.jastp.2011.09.001.

**VI** S. Vargas Domínguez, **J. Palacios**, L. Balmaceda, I. Cabello and V. Domingo. *Evolution of a quiet Sun region under the influence of a small-scale convective vortex flow* A&A, (2010), submitted.

**VII J. Palacios**, J. Blanco Rodríguez, S. Vargas Domínguez, V. Domingo, V. Martínez Pillet, J. A. Bonet, L. R. Bellot Rubio, J. C. del Toro Iniesta, S.K. Solanki, P. Barthol, A. Gandorfer, T. Berkefeld, W. Schmidt, M. Knölker *Magnetic field emergence in mesogranular-sized exploding granules with* SUNRISE*/IMaX data*, A&A, (2012), 537, A21.

http://dx.doi.org/10.1051/0004-6361/201117936.

## Non-refereed articles

**1** Balmaceda L., **Palacios J.**, Cabello I., Domingo V. *Observations of Magnetic elements in the quiet Sun internetwork*. ASP (Astronomical Society of the Pacific Conference), 415, 156 (2009). IBSN: 978-1-58381-710-0.

**2** S. K. Solanki, P. Barthol, S. Danilovic, A. Feller, A. Gandorfer, J. Hirzberger, A. Lagg, T. L. Riethmüller, M. Schüssler, T. Wiegelmann, J. A. Bonet, V. Martínez Pillet, E. Khomenko, J. C. del Toro Iniesta, V. Domingo, **J. Palacios**, M. Knölker, N. Bello González, J.M. Borrero, T. Berkefeld, M. Franz, M. Roth, W. Schmidt, O. Steiner and A. M. Title. *The Sun at high resolution: first results from the* SUNRISE *mission*. Proceedings of the IAU Symposium, 273, (2011).

**3** S. K. Solanki, P. Barthol, S. Danilovic, A. Feller, A. Gandorfer, J. Hirzberger, S. Jafarzadeh, A. Lagg, T. L. Riethmüller, M. Schüssler, T. Wiegelmann, J. A. Bonet, V. Martínez Pillet, E. Khomenko, J. C. del Toro Iniesta, V. Domingo, **J. Palacios**, M. Knölker, N. Bello González, L. Yelles Chaouche, J. M. Borrero, T. Berkefeld, M. Franz, M. Roth, W. Schmidt, O. Steiner and A. M. Title. *First results from the* SUNRISE *mission*. ASP (Astronomical Society of the Pacific Conference), submitted, (2011).

**4 Palacios J.**, Balmaceda L.A., Vargas Domínguez, S., Cabello I., Domingo V. *Observations of vortex motion in the solar photosphere using HINODE-SP data*. ASP (Astronomical Society of the Pacific Conference), in press, (2011).

**5** Domingo V., **Palacios J.**, Balmaceda L.A., Vargas Domínguez, S., Cabello I. *Structure of small elements in the solar atmosphere*. ASP (Astronomical Society of the Pacific Conference), in press, (2011).

## Contributions to meetings

**1** Iballa Cabello, Vicente Domingo and **Judith Palacios**. *Quiet sun magnetism and irradiance* (Poster) CAWSES. Kyoto, Japan, 2007.

**2** **Judith Palacios**, Iballa Cabello, Laura Balmaceda and Vicente Domingo. *Small magnetic elements* (Oral contribution). COSPAR. Montréal, Canada, 2008.

**3** Iballa Cabello, **Judith Palacios**, Laura Balmaceda and Vicente Domingo. *Pequeños elementos magnéticos en la fotosfera y cromosfera* (Oral contribution). I Reunión Española de Física Solar y Heliosférica. Barcelona, Spain 2008.

**4** Laura Balmaceda, Vicente Domingo, Iballa Cabello and **Judith Palacios**. *Observations of magnetic elements in the Quiet Sun internetwork* (Poster). Second Hinode Science Meeting. Boulder, USA, 2008.

**5** Vicente Domingo, Laura Antonia Balmaceda, Iballa Cabello, **Judith Palacios**, Jose L. Gasent, Pedro J. Rodríguez. *Small magnetic elements and SO-PHI* (Poster). 3rd Solar Orbiter Workshop. Sorrento, Italy, 2009.

**6** **Judith Palacios**, Santiago Vargas Domínguez, Laura Balmaceda, Iballa Cabello and Vicente Domingo. *Pequeños elementos magnéticos en diferentes longitudes de onda* (Oral contribution). II Reunión Española de Física Solar y Heliosférica. Palma de Mallorca, Spain, 2009.

**7** **Judith Palacios**, Laura A. Balmaceda, Santiago Vargas Domínguez, Iballa Cabello and Vicente Domingo. *Observation of vortex motion in the solar photosphere using HINODE and SST data* (Poster). Third Hinode Science Meeting.Tokyo, Japan, 2009.

**8** Vicente Domingo, **Judith Palacios**, Iballa Cabello, Laura A. Balmaceda and Santiago Vargas Domínguez. *Structure of small magnetic elements in the solar photosphere* (Poster). Third Hinode Science Meeting. Tokyo, Japan, 2009.

**9** C. Cid, Y. Cerrato, E. Saiz, W. Gonzalez, **Judith Palacios**, A. Aran, H. Cremades, S. Dasso, C. Lathuillere, C. Mandrini, M. Menvielle, S. Poedts, L. Rodríguez, B. Sanahuja, B. Schmieder, A. Zhukov. *Solar sources related to the largest Dst variations of the solar cycle 23* (Oral contribution). JASTP. Brazil, 2010.

**10** Santiago Vargas Domínguez, **Judith Palacios**, Laura A. Balmaceda, Iballa Cabello and Vicente Domingo. *Small-scale convective vortex flow in the solar photosphere* (Poster). Fourth Hinode Science Meeting. Palermo, Italy, 2010.

**11** **Judith Palacios**, J. Blanco Rodríguez, S. Vargas Domínguez, V. Domingo, V. Martínez Pillet, J. A. Bonet, L. R. Bellot Rubio, J. C. del Toro Iniesta. *Magnetic field emergence in mesogranular-sized exploding granules with* SUNRISE*/IMaX data*. III Reunión Española de Física Solar y Heliosférica (Oral contribution). Granada, Spain, 2011.

**12** Vicente Domingo, Julián Blanco Rodríguez, Jose Luis Gasent, Pedro J. Rodríguez, **Judith Palacios**, Valentín Martínez Pillet. SUNRISE *first and second flight as context for Solar Orbiter/PHI* (Poster). Astromadrid. Madrid, 2011.

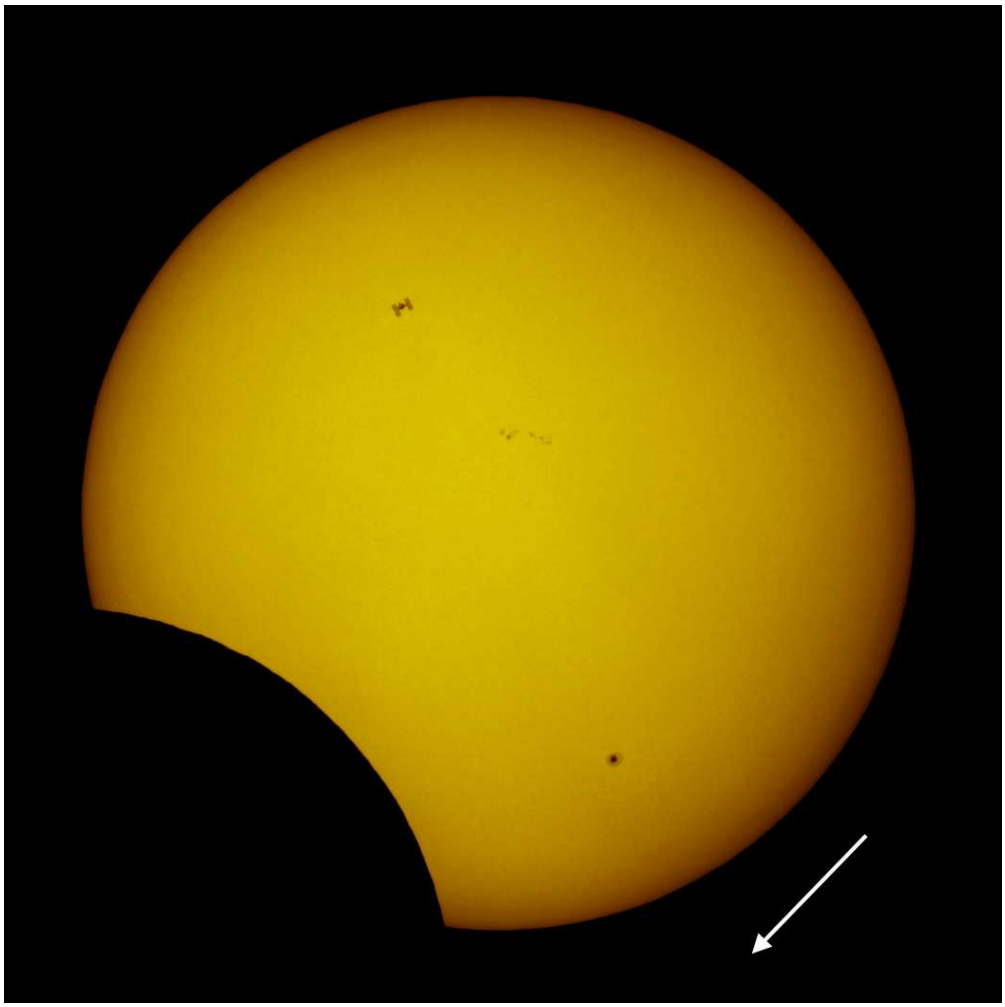

FIGURE C.1— Partial solar eclipse on 2011, Jan 4. ISS is visible passing in front of the Sun. The white arrow marks the direction of the North Solar Pole. A single developed sunspot and a F group appear as remarkable features on the surface. Credits: Thierry Legault.

# Agradecimientos
# Acknowledgements

I feel indebted to all people appearing in this last Section. This work is an enterprise that could not be possible without all of you. I learnt a lot about everyone and everything that has crossed my life in these four years in Valencia.

A Vicente Domingo, mi director, porque desde el principio apostó por mí, me dio esta oportunidad, y quiero expresar mi ms sincero agradecimiento por estos 4 años de dirección y atención constante. Y gracias a todo el equipo de IMaX en Valencia: José Luis Gasent, Pedro Rodríguez, y todos los ingenieros, que hace que este grupo sea tan multidisciplinar. Cómo no, a mi tutor, Juan Fabregat. A todos los compañeros del GACE-IPL, con quienes he compartido buenos momentos de café y conversaciones.

A Laura Balmaceda, Iballa Cabello y Santiago Vargas, por enseñarme a programar como se debe, y por enseñarme este oficio en general. Habéis estado ahí todas las veces que he dicho 'aquí me quedo' y no dejaron que el desaliento me venciera. Gracias por empujarme para seguir siempre hacia adelante. ¡Gracias, Santi, por estar al otro lado 24-7 en cualquier red, y la ayuda para hacer figuritas! Y sí, Iballa: he aprendido más contigo de lo que puedas creer.

También a Julián Blanco, de los últimos IMaXeros incorporados, que ha corregido incansable todas mis incoherencias al redactar, ayudándome con los innumerables problemas técnicos, además de haber hecho cambios sustanciales que han mejorado la reducción de IMaX. A Beatriz Sánchez, por realizar papeleo necesario en estos 4 años, y aportar ese toque de alegría que siempre necesitamos en el IPL. Gracias a Concha también en el tiempo que estuvo aquí. También al personal de mantenimiento de la UV que ha ayudado a tener siempre todo en buen estado.

My profound thanks are due to the SUNRISE and IMaX team, for all the hard work with the developing and flight that made this mission excellent, and for all the huge work on reducing and obtaining results. I am very honoured to have been an active member of this team. Thanks to all the SUNRISE team for all the improvements on the paper.

I want to acknowledge Mark Cheung for providing simulations so kindly, which were used in this work. Vielen Dank to Christian Beck, who made a substantial improvement of this work by his useful corrections. David Orozco, ¡gracias también por los comentarios y los ánimos!

También sin duda, al grupo de *spaceweather* de la Universidad de Alcalá, especialmente a Consuelo Cid, Elena Saiz, Yolanda Cerrato y colaboradores por la oportunidad que me han dado de colaborar en un tema tan interesante como la búsqueda de agujeros coronales relacionados con eventos en el medio interplanetario, y poder continuar profundizando en ello. A los PhD. students, que me llenan de ánimo en las últimas fases de esta tesis.

Thanks to all people on support at SST: for technical help (and coffee) to Rolf Kever; for computer help to Pit Sütterlin and for administrative tasks to IAC staff, at the Residence and offices.

To all people who helped me in my Short Stays around the world:

**1** To the staff of the Sterrenkundig Instituut at Utrecht University to make my life so pleasant there, on my first time before the PhD and while doing it. Thanks for having me there a second time, Christoph Keller and Rob Rutten. To Catherine Fischer, who introduced me on the field of inversion codes. And especially to my friends Sandra, Onno, Peter... and all my Utrechtse friends: Niki, Terhi,... May the Sun shine upon all of you.

Thanks, Peter for taking a look to the thesis, and always cheered me on!

**2** For all the help in my stay in Japan and help making me feel absolutely at home. Arigato gozaimasu to all the staff in the NAOJ, and especially to Tsuneta-san, David Orozco, Yukio Katsukawa & Marie Katsukawa, Yoshi Kato, Sergio Terzo and the staff of Kyoto University (Ichimoto-san, Hiroko Watanabe, Patrick Antolín...) and JAXA who treated me so well in all the visits... ganbatte!

**3** For the stay at the IAC learning how to reduce and use IMaX data. Thanks again to Valentín Martínez Pillet, Jose Antonio Bonet and all the SUNRISE team for the invaluable construction of the data pipeline, the useful advices for using them, and the collaboration and correction of the publications. Gracias a los paseos por Tenerife con Christian, Klaus y Andrei para conocer esa bella isla;

4 For the Solar School 'El Leoncito' and the stay there in the observatory. A Laura de nuevo, y al personal del CONICET que tan bien me trataron. A todos los chicos allá: Fernando, Damián, todas las Natalias que conocí allí, las gentes de Buenos Aires... ¡son recopados, ché! Gracias por todos los ricos asados! Y también, Vir & family, y ¡las sesiones de jazz en Kunst!

Some acknowledgement is necessary to the things that made my life easier and more pleasant, as *dexetify* and *PhD comics*. It is also fair to mention some beings that made, or still make me happy: the tiny AC & DC, running and chewing while i was writing during long nights; and in Utrecht, of course, to Sheri or *mijn koninginnekatje*.

Cómo podría dejar de mencionar a mis pequeñuelos sobris, Jon, Iván, Andrea y Sara. Por días llenos de sol, 'waka waka', hamsters, fútbol, bailes, pistas de hielo, patines: ¡Los expertos supremos en hacerme reír! Y cómo no, a 'la famiglia' (así tipo *El Padrino*). Gracias de corazón a mis padres por darme la educación y formación.

Otros seres humanos indispensables a los que les quiero dedicar esto es a todos los amigos de Madrid: Iñigo, Nora, Javi, Nuria, Fran, Marián, Raquel, Eva,... por haber creído siempre en mí. Sabéis que sin vuestro apoyo, esto hubiera sido imposible. Siempre en conversaciones a la distancia, pero siempre animándome, haciendo que no dejara nunca de soñar. ¡Espero que pueda disfrutar de vuestra amistad otros 1000 años!

A las chicas de Logroño, especialmente a Patricia, que creía que llegaría a la NASA y... bueno, ¡recorrí un cachito de mundo, que no es poco!

Y a los que ya no están, como Selene y Claudio... *wish you were here*. Ahí dejo una canción de Bryan Adams y una de la *streetlife queen* Billie Holiday, porque seguís viviendo en el corazón. Hora de marcarse un *Watermelon Man* en vuestro honor.

★ *THIS JOURNEY CONTINUES....* ★

And now ... Esc